

Characterization of low-temperature plasmas generated by dielectric barrier discharges for bacterial inactivation

Présentée le 12 avril 2024

Faculté des sciences de base
SPC - Physique des Plasmas de Base
Programme doctoral en physique

pour l'obtention du grade de Docteur ès Sciences

par

Lorenzo IBBA

Acceptée sur proposition du jury

Prof. M. Wyart, président du jury
Prof. I. Furno, directeur de thèse
Dr S. Starikovskaia, rapporteuse
Dr K. Stapelmann, rapporteuse
Dr B. Labit, rapporteur

Before I came here, I was confused about this subject.
Having listened to your lecture, I am still confused.
But on a higher level.

— Enrico Fermi

Acknowledgements

Desidero esprimere la mia più profonda gratitudine alla mia famiglia per il loro sostegno incrollabile lungo questo percorso impegnativo, ma gratificante. Grazie, papà, per avermi fatto innamorare della scienza, forse inconsciamente, e per le molte discussioni sugli aspetti filosofici della fisica, che, in fin dei conti, è ciò che più affascina. Grazie, mamma, per aver mostrato sempre interesse nel mio lavoro e per avermi sostenuto, anche nei momenti più bui, quando credevo che il fallimento fosse una fine, invece che un inizio. Grazie, fratello, per le tante risate che abbiamo condiviso su cose stupide e per avermi distratto nei momenti difficili, facendoli passare senza quasi accorgermene. Grazie, sorella, per l'orgoglio che mi fai provare sapendo il rispetto che nutri per me, ma soprattutto per le avventure che abbiamo condiviso e per quelle che so che condivideremo. Gli obiettivi che ho perseguito in questi ultimi anni sono stati possibili solo grazie al vostro incoraggiamento, amore e comprensione. Siete stati i miei pilastri di forza e la mia casa sicura, e sono veramente fortunato e grato ad avervi al mio fianco.

I am deeply indebted to Ivo, my supervisor, for his guidance, mentorship, and unwavering belief in my capabilities. Your invaluable feedback and constructive criticism have been fundamental in shaping the direction of my research and pushing me to strive for results. Despite your numerous responsibilities I never felt abandoned to face the challenges of research alone, and your passion and curiosity crucially inspired me to find answers and made the work of these years exciting and satisfying.

I extend my sincere appreciation to my collaborators, whose expertise has significantly contributed to the success of this research. Thanks to the Bio-plasma people, but also to the BPPA group, including Fabio, Brayden, Anna, Leonardo, Silvia, Sasha, Jia, Simon, Cyrille, Renat, Marcelo, Remy, Lyes, Philippe, Christine, Félicien, Alexandra, Alan, Riccardo, Marianna and Gennady. Your efforts and/or comments and feedback have not only enhanced the quality of my work but also made the time in the lab and office incredibly better. A special thanks goes to all the people of SPC that made these years in this unique place wonderful, whether it was a casual chat over a coffee in the cafeteria or enduring four years of shared academic pain.

Acknowledgements

A particular acknowledgment goes to Paolo Ambrico, unofficially my second mentor, without whom I would not have been able to perform half of the work presented in this thesis. His extensive technical knowledge enabled me to conduct cutting-edge experiments and advance the knowledge in the field.

Heartfelt thanks go to my friends, each one of them, all scattered around the world. If you are reading these acknowledgements, then know that I am referring to you. The time we shared is invaluable to me, and I believe that it is what everything is all about. Sharing time and experiences is what makes everything else significant, and for this, I thank you.

Last but not least, thank you, Rita, the person with whom I am happy to share most of my time. While you are acknowledged in almost all the other categories as a colleague and friend, you are much more than that. Your positivity, strength, and love for everything that makes life worth living have been a constant source of inspiration. Thanks for all the laughter and craziness that turned difficult times into joyful moments, especially towards the end of this journey. Thanks for the countless memories created during these years. Your belief in me has been a driving force and has helped me persevere during the most challenging times. I love you.

This thesis is a testament to the collective efforts and support of these wonderful individuals, and I am sincerely thankful for each one of you who has played a role, big or small, in this significant chapter of my life.

Lausanne, February 2024

L. I.

Abstract

Low-temperature plasmas (LTPs) at atmospheric pressure hold great promise for disinfection and sterilization applications. When compared to traditional sterilization technologies like autoclaving, LTPs may offer several benefits, including reduced energy consumption, lower operational temperature, absence of high pressure or vacuum requirements, shorter treatment times, and the absence of persistent hazardous compounds. Nevertheless, the understanding of the physics and chemistry of LTPs is still incomplete due to the numerous variables at play, particularly in air at atmospheric pressure. The aim of this dissertation is to improve the comprehension of the mechanisms responsible for bacterial inactivation in atmospheric pressure LTPs by conducting a thorough physical, chemical, and biological characterization. Special attention is given to performing measurements under conditions identical to those of biological treatments, addressing the often overlooked influence of the biological target on the plasma discharge. To examine the effects of indirect plasma treatments on *E. coli* an atmospheric pressure surface dielectric barrier discharge (SDBD) plasma in air, powered by a nanosecond pulse generator, is employed. The treatments demonstrate bacterial inactivation up to 4-log reductions after 10 minutes of plasma exposure. In-situ FTIR spectroscopy reveals the presence of O₃, NO₂, N₂O, and N₂O₅, while laser-induced fluorescence (LIF), employing a picosecond laser, is used to measure the kinetics of NO produced in the plasma on a two-dimensional area in front of the DBD surface. The results show a correlation between the concentration of reactive oxygen and nitrogen species (RONS) with the relative humidity (RH) and with the plasma discharge power, measured using Lissajous figures. The results suggest that NO is not a main factor contributing to the inactivation of *E. coli* in the plasma treatments examined in this study. To investigate direct plasma treatments, *Bacillus subtilis* spores on monolayer membranes are treated using a nanosecond volume DBD (VDBD) plasma at atmospheric pressure in humid air, reaching complete inactivation with >5-log reductions after 1 minute of plasma exposure. The membranes are treated in the VDBD plasma discharge on the ground side and on the high-voltage side, showing no difference in the treatment results. Both in-situ FTIR and NO LIF are performed on this setup, showing the presence of O₃, N₂O, and ~1 ppm of NO temporally decaying in between plasma discharges. To evaluate the impact of the electric field in direct plasma treatments, measurements of electric field induced second harmonic (EFISH) generation using a picosecond and a nanosecond laser

are performed. The ps EFISH measurements, owing to the improved temporal and spatial resolution, reveal features previously undetected by the ns EFISH measurements, including a different electric field evolution depending on the position in the plasma discharge. To understand the mechanisms of the nanosecond plasma breakdown in humid air, a comparison with a simplified kinetic model has been carried out. The results provide insights on the ion and electron kinetics, revealing differences with previously studied nitrogen plasmas and highlighting the importance of electronegative species in the breakdown dynamics. Finally, preliminary tests for achieving sterilization standards are performed.

Key words: Low-temperature plasmas, cold plasmas, non-thermal plasmas, Dielectric barrier discharge, Laser-induced fluorescence, Nitric oxide LIF, LIF spectroscopy, EFISH, Electric field, Second harmonic generation, in-situ FTIR, FTIR spectroscopy, Plasma sterilization, Plasma disinfection, Plasma decontamination, Biological applications of plasmas, E. coli, Bacillus subtilis spores

Abstract

I plasmi a bassa temperatura (LTPs) a pressione atmosferica offrono grandi promesse per applicazioni di disinfezione e sterilizzazione. Rispetto alle tecnologie tradizionali di sterilizzazione come l'autoclave, i LTPs possono offrire diversi vantaggi, tra cui un consumo energetico ridotto, una temperatura operativa più bassa, l'assenza di requisiti di pressione o vuoto, tempi di trattamento più brevi e l'assenza di composti pericolosi persistenti. Tuttavia, la comprensione della fisica e della chimica dei LTPs è ancora incompleta a causa delle numerose variabili in gioco. Lo scopo di questa tesi è migliorare la comprensione dei meccanismi responsabili dell'inattivazione batterica nei LTPs a pressione atmosferica mediante una caratterizzazione fisica, chimica e biologica approfondita. Particolare attenzione è dedicata alla realizzazione di misure in condizioni identiche a quelle dei trattamenti biologici, considerando l'effetto spesso trascurato dell'organismo biologico sulla scarica di plasma. È stato condotto uno studio per esaminare gli effetti dei trattamenti al plasma indiretti su *E. coli* utilizzando una scarica a barriera dielettrica di superficie (SDBD), alimentata da un generatore di impulsi al nanosecondo. I trattamenti dimostrano un'inattivazione batterica con riduzioni fino a 4 logaritmi dopo 10 minuti di esposizione al plasma. La spettroscopia FTIR in-situ rivela la presenza di O_3 , NO_2 , N_2O e N_2O_5 , mentre la fluorescenza indotta dal laser (LIF), utilizzando un laser al picosecondo, è utilizzata per misurare la cinetica dell'NO prodotto nel plasma di fronte alla superficie della SDBD. I risultati mostrano una correlazione tra la concentrazione delle specie reattive dell'ossigeno e dell'azoto (RONS) e l'umidità relativa (RH), così come con la potenza di scarica del plasma, misurata utilizzando le figure di Lissajous. Per studiare i trattamenti diretti al plasma, le spore di *Bacillus subtilis* depositate su membrane monostrato vengono trattate utilizzando una DBD di volume (VDBD) al nanosecondo a pressione atmosferica in aria umida, raggiungendo un'inattivazione completa con riduzioni >5 logaritmi dopo 1 minuto di esposizione al plasma. Le membrane vengono trattate nella scarica del plasma VDBD sul lato a terra e sul lato ad alta tensione. Vengono effettuate sia l'analisi FTIR in-situ che la LIF al NO su questa configurazione, mostrando la presenza di O_3 , N_2O e circa 1 ppm di NO in decadimento temporale tra le scariche del plasma. Per valutare l'impatto del campo elettrico nei trattamenti diretti al plasma, vengono effettuate misurazioni di generazione di seconda armonica indotta dal campo elettrico (EFISH) utilizzando un laser al picosecondo e un laser al nanosecondo. Le misurazioni EFISH al picosecondo rivelano caratteristiche precedentemente non osservate nelle misure EFISH al nanosecondo, compresa un'evoluzione del campo elettri-

co diversa a seconda della posizione nella scarica del plasma. Per comprendere i meccanismi del breakdown del plasma al nanosecondo in aria umida, è stato effettuato un confronto con un modello cinetico semplificato. I risultati forniscono informazioni sulla cinetica degli ioni e degli elettroni, rivelando differenze rispetto ai plasmi di azoto studiati precedentemente e sottolineando l'importanza delle specie elettronegative nella dinamica della scarica di plasma. Infine, vengono effettuati test preliminari per raggiungere standard di sterilizzazione.

Key words: Plasmi a bassa temperatura, plasmi freddi, plasmi non termici, Scarica a barriera dielettrica, Fluorescenza indotta dal laser (LIF), LIF di monossido di azoto, EFISH, FTIR in-situ, Decontaminazione al plasma, Applicazioni biologiche dei plasmi, E. coli, Spore *Bacillus subtilis*

Résumé

Les plasmas à basse température (LTPs) à pression atmosphérique représentent une grande promesse pour des applications de désinfection et de stérilisation. Comparés aux technologies traditionnelles de stérilisation telles que l'autoclave, les LTPs peuvent offrir plusieurs avantages, notamment une consommation d'énergie réduite, une température opérationnelle plus basse, l'absence d'exigences élevées en pression ou en vide, des temps de traitement plus courts et l'absence de composés dangereux persistants. Néanmoins, la compréhension de la physique et de la chimie des LTPs reste incomplète en raison des nombreuses variables en jeu. L'objectif de cette thèse est d'améliorer la compréhension des mécanismes responsables de l'inactivation bactérienne dans les LTPs à pression atmosphérique en réalisant une caractérisation physique, chimique et biologique approfondie. Une attention particulière est accordée à la réalisation de mesures dans des conditions identiques à celles des traitements biologiques, abordant l'influence souvent négligée de la cible biologique sur la décharge plasma. Pour examiner les effets des traitements au plasma indirect sur *E. coli*, une décharge à barrière diélectrique en surface (SDBD) dans l'air, alimentée par un générateur d'impulsions nanosecondes, est utilisée. Les traitements démontrent une inactivation bactérienne allant jusqu'à des réductions de 4 logarithmes après 10 minutes d'exposition au plasma. La spectroscopie FTIR in-situ révèle la présence de O_3 , NO_2 , N_2O et N_2O_5 , tandis que la fluorescence induite par laser (LIF), utilisant un laser picoseconde, est utilisée pour mesurer la cinétique du NO produit dans le plasma devant la surface de la SDBD. Les résultats montrent une corrélation entre la concentration des espèces réactives de l'oxygène et de l'azote (RONS) avec l'humidité relative (HR) et la puissance de décharge plasma, mesurée à l'aide de figures de Lissajous. Pour étudier les traitements directs au plasma, des spores de *Bacillus subtilis* sur des membranes monocouches sont traitées à l'aide d'une décharge de volume nanoseconde (VDBD) à pression atmosphérique dans de l'air humide, atteignant une inactivation complète avec des réductions de plus de 5 logarithmes après 1 minute d'exposition au plasma. Les membranes sont traitées dans la décharge plasma VDBD du côté sol et du côté haute tension. Les analyses FTIR in-situ et NO LIF sont réalisées sur cette configuration, montrant la présence de O_3 , N_2O et environ 1 ppm de NO décroissant temporairement entre les décharges plasma. Pour évaluer l'impact du champ électrique dans les traitements directs au plasma, des mesures de génération d'harmonique de second ordre induite par champ électrique (EFISH) à l'aide d'un laser picoseconde et d'un laser nanoseconde sont effectuées. Les mesures EFISH en pico-

seconde révèlent des caractéristiques précédemment non détectées par les mesures EFISH en nanoseconde, y compris une évolution du champ électrique différente en fonction de la position dans la décharge plasma. Pour comprendre les mécanismes de la rupture du plasma nanoseconde dans l'air humide, une comparaison avec un modèle cinétique simplifié a été réalisée. Les résultats révélant des différences avec les plasmas d'azote précédemment étudiés et soulignant l'importance des espèces électronégatives dans la dynamique de la rupture. Enfin, des tests préliminaires pour atteindre les normes de stérilisation sont réalisés.

Mots clefs : Plasmas à basse température, plasmas froids, plasmas non thermiques, Décharge à barrière diélectrique, Fluorescence induite par laser (LIF), NO LIF (Fluorescence induite par laser du monoxyde d'azote), EFISH, FTIR in-situ, Stérilisation au plasma, Désinfection au plasma, Décontamination au plasma, Applications biologiques des plasmas, E. coli, Spore *Bacillus subtilis*

Contents

Acknowledgements	i
Abstract (English/Italiano/Français)	iii
List of figures	xiii
List of tables	xxv
1 Low-Temperature Plasmas for Bacterial Inactivation	1
1.1 Introduction to low-temperature plasmas	2
1.1.1 Thermal and non-thermal plasmas	3
1.1.2 Townsend mechanism of electric breakdown	5
1.1.3 Dielectric barrier discharges	7
1.1.4 DBD mechanisms and regimes	9
1.1.5 Nanosecond-pulsed plasma discharges	10
1.2 Biological applications of LTPs	11
1.2.1 LTPs bacterial inactivation mechanisms	12
1.2.2 Final considerations on plasma bactericidal factors	17
1.3 Sterilization and disinfection	18
1.3.1 Sterilization methods overview	18
1.3.2 Introduction to microorganisms	20
1.3.3 Gram-positive and Gram-negative bacteria	21
2 Dielectric Barrier Discharges and Experimental Setup	25
2.1 Surface dielectric barrier discharges	26
2.1.1 PCB-fingers SDBD	26
2.1.2 On the humidity issue and reproducibility	27
2.1.3 Perforated-disc SDBD	30
2.2 Volume dielectric barrier discharge	30
2.3 Nanosecond-pulsed high-voltage power supply	32
2.4 Bio-plasma reactor	35
2.5 Gas flow system	37
2.6 DBDs prototypes	39

3	Physical Characterization: Plasma Discharge Power	41
3.1	Plasma discharge power measurements	42
3.2	Introduction to Lissajous figures	43
3.2.1	Plasma discharge power derivation from Lissajous Figures	45
3.2.2	Monitor capacitor selection	46
3.2.3	Almond-shaped Lissajous figures of SDBDs	47
3.2.4	Nanosecond-pulsed Lissajous figures	48
3.3	Experimental setup and data analysis	50
3.4	Plasma discharge power measurements	53
3.4.1	PCB-fingers SDBD power measurements	53
3.4.2	Perforated-disc SDBD power measurements	55
3.4.3	VDBD power measurements	57
3.4.4	Power measurements of Sinhon Electronics stripes SDBD	58
3.5	Conclusions	60
4	Physical Characterization: EFISH	63
4.1	Electric-field induced second harmonic generation	64
4.2	Introduction to EFISH theory	65
4.2.1	EFISH considerations for strongly focused laser beams	66
4.3	Nanosecond-pulsed laser EFISH in the VDBD plasma discharge	70
4.3.1	Ns EFISH experimental setup	72
4.3.2	Analysis of the jitter between the plasma discharge and the laser pulse	74
4.3.3	Diffuse plasma discharge	77
4.3.4	Ns EFISH calibration	78
4.3.5	Ns EFISH results	81
4.4	Picosecond-pulsed laser EFISH in the VDBD plasma discharge	83
4.4.1	Diode pumped high energy picosecond Nd:YAG laser	83
4.4.2	Ps EFISH experimental setup	85
4.4.3	Single-shot measurements method	88
4.4.4	Analysis of the jitter between the plasma discharge and the lase pulse	90
4.4.5	Ps EFISH calibration	91
4.4.6	Ps EFISH results	92
4.4.7	Ps EFISH at different plasma discharge power	99
4.4.8	Ps EFISH with membrane on top of dielectric	100
4.5	Kinetic model comparison	102
4.6	Conclusions	105
5	Biological Characterization: Bacteria Plasma Treatments	109
5.1	Indirect plasma treatments of <i>E. coli</i>	110
5.1.1	<i>E. coli</i> culture management	110
5.1.2	<i>E. coli</i> plasma treatments protocol and counting	110
5.1.3	Indirect plasma treatments of <i>E. coli</i> results	114
5.2	Direct plasma treatments of <i>Bacillus Subtilis</i> Spores	118

CONTENTS

5.2.1	<i>Bacillus Subtilis</i> spores on monolayer membrane preparation	120
5.2.2	<i>Bacillus Subtilis</i> spores on monolayer membrane plasma treatments protocol and counting	121
5.2.3	Direct plasma treatments of <i>Bacillus Subtilis</i> spores results	122
5.3	Preliminary sterilization experiments with biological indicators	128
5.3.1	BT96 biological indicator protocol	128
5.3.2	Plasma treatments of BT96 results	129
5.4	Conclusions	131
6	Chemical Characterization: FTIR Spectroscopy	133
6.1	Introduction to Fourier transform infrared spectroscopy	134
6.1.1	FTIR spectrum absolute calibration	136
6.2	In-situ FTIR spectroscopy experimental setup	138
6.2.1	Calibration of O ₃ , N ₂ O, NO ₂ and HNO ₃	142
6.3	FTIR spectroscopy measurements	144
6.3.1	PCB-fingers SDBD FTIR measurements	145
6.3.2	Perforated-disc SDBD FTIR measurements	149
6.3.3	VDBD FTIR measurements	152
6.4	Conclusions	155
7	Chemical Characterization: Nitric Oxide LIF	157
7.1	Introduction to nitric oxide laser-induced fluorescence	158
7.1.1	Theory of nitric oxide LIF	159
7.2	Nitric oxide LIF experimental setup	162
7.2.1	Triggering system for synchronization	165
7.2.2	ICCD ROI and data analysis for the SDBD setup	166
7.2.3	Experimental setup modifications for the VDBD setup	168
7.3	PCB-fingers SDBD nitric oxide LIF measurements	170
7.3.1	Laser energy and calibration	170
7.3.2	NO LIF results in the SDBD setup	171
7.3.3	NO LIF measurements during the high-voltage pulse	174
7.3.4	Preliminary results obtained with the PMT	175
7.4	VDBD nitric oxide LIF measurements	177
7.4.1	Laser energy and calibration	177
7.4.2	NO LIF results in the VDBD setup	178
7.5	Conclusions	179
8	Summary and Conclusions	181
	Bibliography	214
	Curriculum Vitae	

List of Figures

1.1	Classification of plasmas depending on electron temperature and particle densities (source: [2]).	2
1.2	Illustration of some plasma-based technologies present in the everyday life, and some that are currently under development and might be present in the near future (source: [4]).	3
1.3	Evolution of the plasma temperature (electrons and heavy particles) with the pressure in a mercury plasma arc. T_e , T_i and T_n represent the temperature of the electrons, ions and neutrals, respectively (adapted from [6]).	4
1.4	Schematics of Townsend avalanche in a plane-to-plane electrical discharge (source: [7]).	6
1.5	Paschen curves obtained for helium, neon, argon, hydrogen and nitrogen, using the expression for the breakdown voltage as a function of the parameters A,B that interpolate the first Townsend coefficient (source: [9]).	7
1.6	Basic planar configurations of DBDs: (a) volume DBD (1-symmetric, 2-asymmetric, 3-floated dielectric); (b) surface DBD (1-symmetric, 2-asymmetric 'actuator' design); (c) coplanar discharge. (source: [11]).	8
1.7	Example of (a) a filamentary discharge and (b) a diffuse discharge (source: [16]).	9
1.8	Nanosecond high-voltage pulse with plasma optical emission in arbitrary units, representing the two plasma discharges during the rising-edge and falling-down of the voltage pulse.	10
1.9	Products of low-temperature plasmas.	12
1.10	Illustration of a set of RONS produced in LTPs (adapted from [83]).	15
1.11	UV radiation spectra, with UV-A, UV-C and UV-C band highlighted. A guideline on the bactericidal efficacy of the UV bands is reported (source: [101]).	16
1.12	Time-temperature curves developed for the inactivation of various microorganisms using heat treatment to achieve 3-log (e.g., 99.9%) reduction. Solid lines show the linear fit of the data, and dotted lines show 95% prediction intervals (adapted from [108]). For more details, please refer to Ref. [108].	17
1.13	Schematics of the differences between Gram-positive and Gram-negative bacteria.	21
1.14	Low-temperature electron micrograph of a cluster of <i>E. coli</i> bacteria (source: [124]).	23
1.15	SEM image of <i>Bacillus subtilis</i> spores deposited on a monolayer membrane surface (courtesy of Anna Machkova).	23

2.1	Pictures of the PCB-fingers SDBD (a) idle and (b) operating in air at 5 kV, 400 ns long pulses, 1 kHz repetition frequency.	26
2.2	Pictures of the PCB-fingers SDBD plasma when operating correctly (a) and after ~1 hour of uninterrupted use in high humidity conditions (b).	27
2.3	Photographs of the plasma visible emission after 30 minutes of continuous plasma operation at relative humidities of (a) 36% ambient air; (b) 50% ambient air; (c) 71% and (d) 86% (source: [12]).	28
2.4	(a) A drop of water placed on the virgin FR4 dielectric has a contact angle of ~ 60°, as indicated in the inset. (b) When a drop of water is placed onto the FR4 dielectric after 10 minutes of SDBD plasma operation, it spreads evenly over the FR4 surface between the electrodes, as indicated inside the red curve. A simple contact angle measurement is not possible in these conditions.	29
2.5	(a) Picture of the perforated-disc SDBD idle and (b) operating at 8 kV, 400 ns long pulses, at 1 kHz repetition frequency.	30
2.6	Schematic of the VDBD components.	31
2.7	(a) Picture of the VDBD with the schematics of the inflow and outflow positions and (b) close-up of the plasma while operating at 12 kV, 200 ns long pulses, at 1 kHz repetition frequency.	31
2.8	(a) Picture of the VDBD for the bacteria treatments from top and (b) close-up of the plasma while operating at 12 kV, 200 ns long pulses, at 1 kHz repetition frequency.	32
2.9	Picture of the nanosecond-pulsed high-voltage power supply with visible emergency shut-down button on top.	33
2.10	Block diagram of the electric circuit of the nanosecond-pulsed high-voltage power supply.	33
2.11	Example of a nanosecond pulse waveform generated by the power supply. The optical emission from the plasma is depicted in arbitrary units, with the two peaks corresponding to the two plasma discharges occurring with each pulse.	34
2.12	Front panel of the nanosecond-pulsed high voltage power supply. The labels are referring to (a) current monitor, (b) voltage monitor, (c) TTL triggers for laser synchronization, (d) reference pulse and (e) LAN port to laptop connection.	35
2.13	(a) CAD 3D drawing of the reactor, mounted on a motorized translation stage. (b) Actual reactor positioned on the optical bench, featuring the top lid upon which the PCB-fingers SDBD is mounted.	36
2.14	Picture of the closed bio-plasma reactor with the PCB-fingers SDBD operating inside, at ~5 kV, 400 ns long pulses, at 1 kHz repetition frequency.	36
2.15	(a) Lateral view of the modified reactor positioned within the sample compartment of the FTIR spectrometer. (b) Top view of the modified reactor inside the sample compartment. It is possible to notice the 2 missing flanges, a Petri dish in the middle and the tip of the relative humidity probe on the left-bottom flange.	37
2.16	Schematics of the gas flow system.	38

LIST OF FIGURES

2.17	Picture of the actual gas flow system with mass flow controllers for (a) synthetic air, (b) oxygen, (c) nitrogen, and (d) N ₂ /NO. The crucial component of the gas flow system is the (e) bubbler, where the dry air increase its humidity content by passing through it.	39
2.18	PCB-fingers SDBD prototypes. The only difference between the three of them is the material used for the dielectric: (a) FR4, (b) Kapton and (c) solderresist. . .	39
2.19	Sihon Electronics SDBD prototypes. The only difference between the three of them is the electrode configuration: (a) honeycomb, (b) stripes and (c) mesh. .	40
3.1	Schematic representation of a DBD with one electrode covered by a dielectric. On the right-hand side, current and voltage characteristics are depicted. In practical terms, the plasma within the DBD system exhibits filamentary behavior, consisting of discrete filaments with durations on the order of $< 10^{-7}$ seconds, separated both in space and time. This characterization deviates from the simplified electrical model which assumes continuous current and a constant gap voltage U_b during discharge (source: [136]).	42
3.2	Schematic of the circuit used to generate the Lissajous figure of a DBD using a monitor capacitor.	43
3.3	Ideal Lissajous Figure exhibiting a distinctive parallelogram shape. The 'plasma off' segments are highlighted in red, while the 'plasma on' segments are indicated in green. Directional arrows within the green segments represent the progression of time. Further details regarding the symbols utilized in this figure are elaborated upon in the main text (source: [136]).	44
3.4	Example of characteristic Lissajous figures shape for (a) VDBDs and (b) SDBDs (adapted from [142]).	47
3.5	(a) Graphical representation of the plasma expansion across the available dielectric surface with increasing applied voltage in a SDBD. (b) Resulting Lissajous figure with corresponding capacitance of the system at different timings of the plasma discharge expansion (adapted from [136]).	48
3.6	Example of Lissajous figures of a nanosecond-pulsed actuator (an SDBD with a single electrode), for different gaps between the ground and HV electrode (source: [130]).	49
3.7	Example of polyester film and ceramic capacitors used for the power measurements, with capacitance values, from left to right, of 1 nF, 68 nF and 10 nF. . . .	50
3.8	(a) Picture of the experimental setup used for the power measurements. On the oscilloscope, the Lissajous figure obtained in this specific case is visible. (b) Close up of the voltage probe connections to the monitor capacitor on the ground side of the VDBD.	50
3.9	Example of Lissajous figures obtained from the raw signals and from the filtered signals, for a particular case of the VDBD.	51

3.10 (a) Waveforms of the applied voltage to the PCB-fingers SDBD at 4.5 kV, 400 ns long pulses, 1 kHz repetition frequency, and voltage measured at the monitor capacitor. The plasma optical emission in arbitrary units is also represented to show the position in time of the 2 plasma discharges. (b) Lissajous figure obtained from the waveforms shown in (a). Points 1, 2 and 3 are used to highlight specific key points in the 2 plots.	52
3.11 Sequence of Lissajous figures obtained at increasing applied voltage for the PCB-fingers SDBD (a) and VDBD (b).	53
3.16 Waveforms of the applied voltage on the VDBD and voltage on the monitor capacitor in series to the VDBD for the perforated-disc SDBD powered by the PAW power supply. (a) Signals with the 100 Hz modulation visible and (b) zoom on the 21 kHz frequency waveforms.	56
3.17 Lissajous figures obtained from the whole modulation period of the perforated-disc SDBD powered by the PAW power supply.	57
3.18 Signals of the applied voltage on the VDBD and voltage on the monitor capacitor in series to the VDBD. (a) Signals in absence of plasma, at ~3.8 kV applied voltage, below the breakdown voltage. (b) Signals in the presence of plasma, at ~8 kV applied voltage, above the breakdown voltage. It is possible to note the increased noise in correspondence of the rising edge of the voltage, during ignition of the first plasma discharge.	57
3.19 (a) Example of Lissajous figures of the VDBD at different applied voltages. (b) Computed plasma discharge power from the Lissajous figures at increasing applied voltages.	58
3.20 Comparison of the plasma discharge power, computed from the Lissajous figures at increasing applied voltages, between the the case with the membrane in the middle and without the membrane.	59
3.21 The voltage waveform of the Shinon Electronics stripes SDBD for nominal 8 kV peak-to-peak. The blue curve shows the applied voltage; the orange curve shows the voltage across the monitor capacitor. The waveform distortion is caused by the transient response of the high-voltage amplifier when using high-frequency bursts (adapted from [129]).	59
3.22 (a) Example of Lissajous figure of the Shinon Electronics stripes SDBD. (b) Computed plasma discharge power from the Lissajous figures at increasing nominal applied voltages (source: [129]).	60
4.1 Example of second harmonic generation by non-linear crystal and separations of wavelength through prism.	65
4.2 Scheme of second harmonic generation.	66
4.3 The impact of the electrode length, represented as $2L$, on the peak-normalized EFISH signal within the plane-wave approximation, as described by Equation 4.4, is illustrated for a wave mismatch of $\Delta k = -0.5 \text{ cm}^{-1}$ (source: [163]).	67

LIST OF FIGURES

4.4	Schematics of focusing point parameters. The gaussian beam width $\omega(z)$ as a function of the axial distance z is shown, as well as the beam waist ω_0 , the confocal parameter b , the Rayleigh range z_R and the angular spread Θ	68
4.5	Simplified schematic of the interaction length L_{int} in the case of the VDBD. . .	69
4.6	The effect of electrode length ($2L$) on $\frac{A'}{z_R}$, which corresponds to the EFISH signal, is graphed here in logarithmic scale for three distinct values of z_R (source: [163]).	70
4.7	Schematic of the VDBD components.	71
4.8	Scheme of the laser beam direction, denoted with the z-axis, with respect to the plasma discharge.	71
4.9	Experimental setup schematics of the nanosecond EFISH measurements (source: [145]).	72
4.10	Schematics of the ns EFISH measurements triggering system.	73
4.11	Typical voltage (black), current (red) and SPS(0,0) band emission taken through the monochromator using the PMT (source: [145]).	75
4.12	Current jitter, of the first (B) and second (C) current spikes, corresponding to the plasma discharges, with respect to the rising edge of the high voltage pulse (source: [145]).	76
4.13	Jitter of the laser pulse with respect to the HV rising edge. (A) Averaged waveforms created by taking the simple average of 6000 individual waveforms (blue line) and the averaged waveform corrected for jitter (red line). (B) The distribution of peak positions over time and the corresponding normal distribution, displaying a FWHM of 3.4 ns (source: [145]).	77
4.14	(A) Compilation of individual plasma emission images captured during the discharge pulse, employing a camera gate duration of 50 ns, in both humid and dry air. (B) Kinetic images obtained using a fixed gate duration of 3 ns during the emission of the 1st and 2nd discharge pulses in humid air. The gate position corresponds to the point highlighted in the PMT (red) and ICCD (blue) intensities plot (source: [145]).	78
4.15	Normalized square root of the PMT signal (green), obtained under constant electric field conditions, superimposed with the photodiode signal (blue). Both signals are the result of an average of 256 laser shots. Additionally, the ratio of these signals is presented (grey). The labeled section of the graph indicates the time interval within which the time-accurate EFISH data can be observed (red). The gas pressure is $p = 760$ torr and the laser pulse energy is 9 mJ. The constant applied voltage (yellow) is also reported (source: [145]).	79
4.16	The calibration of EFISH signals is accomplished by employing either a voltage pulse (A) or a constant voltage (B). The corresponding calibration factors A obtained from these calibration methods are presented in the figures (source: [145]).	80

4.17 Time-resolved measurements within the discharge gap at three distinct vertical positions, as indicated in the upper section of the figure. The figure provides a view of the following data: EFISH signal (black dots), raw EFISH signal (brown dots), Laplacian electric field (blue), and current data (red) (source: [145]). . . . 82

4.18 Picture of the EKSPLA Diode Pumped High Energy Picosecond Nd:YAG Laser on the optical bench [169]. 83

4.19 Typical energies of the PL2231-50 by EKSPLA, at maximum amplification, with respect to the emission wavelength [169]. 84

4.20 Experimental setup schematics of the ps EFISH measurements. The differences with the ns EFISH experimental setup are labeled in red. 85

4.21 Spatial filter based on a pinhole adjustment setup. The Gaussian beam is narrowly focused in a pinhole of appropriate dimensions to clean the fringes of the Gaussian beam (source: [170]). 86

4.22 (a) Input Gaussian beam with side fringes. (b) Cleaned Gaussian beam after passing through the pinhole (source: [170]). 86

4.23 (a) Pinhole adjustment system. (b) Motorized high-load vertical translation stage. 87

4.24 Schematics of the ps EFISH measurements triggering system. 88

4.25 (a) Waveforms acquired in a single-shot measurement: PMT and photodiode signals in volts, and applied voltage and current, reported in arbitrary units. (b) Zoom in of the photodiode and PMT signals, corresponding to the 1st and 2nd harmonic signals. 89

4.26 (a) PDF of the time jitter of the plasma discharge with respect to the voltage pulse. Distribution of the delay between the rising-edge of the voltage pulse waveform and the rising-edge of the plasma discharge, averaged into 200 ps bins. (b) PDF of the maximum of the first current peak, binned in 0.1 A. 90

4.27 (a) Ps EFISH signal in arbitrary units at increasing applied electric field in the air gap of the VDBD. The measurements are taken at a fixed position in time at the flat top of the nanosecond pulse waveform where the electric field is constant, nominally at 200 ns (see (b)). (b) Ps EFISH signal evolution over the duration of the nanosecond voltage pulse at 8 kV, expressed in kV/cm obtained from Equation 4.9 within the air gap of the VDBD. 91

4.28 Position of the laser beam passing inside the gap of the VDBD. The scheme shows the three distinct positions used for the EFISH measurements: Center, HV and Ground. The diagram also highlights that the beam width at the edge of the VDBD electrode measures approximately 270 μm 92

4.29 Calibrated ps EFISH raw measurements in the Center position during the whole nanosecond voltage waveform. Applied electric field and current are also reported. The points of inversion of the electric field are highlighted. 93

4.30 Calibrated ps EFISH corrected for the negative values of the electric field before and after the plasma discharges. The measurements are taken in the Center position during the entire ns-voltage waveform. Applied electric field and current are also reported. The dips after the two plasma discharges are highlighted. . . 94

LIST OF FIGURES

4.31	Calibrated ps EFISH measurements in the three different positions, namely Ground, Center and HV, within the gap of the VDBD. The applied electric field and the current are also reported.	95
4.32	Calibrated ps EFISH measurements raw (black) and grouped and averaged in 1 ns long bins (red), at the Center position during the whole nanosecond voltage waveform. Applied electric field and current are also reported.	95
4.33	Calibrated ps EFISH measurements grouped and averaged in 1 ns long bins, at the Center, Ground and HV, positions during the whole nanosecond voltage waveform. Applied reduced electric field and current are also reported.	96
4.34	Calibrated ps EFISH measurements in the Ground position. (a) Zoom on the first plasma discharge of the single-shot EFISH measurements. (b) Zoom on the first plasma discharge of the binned EFISH measurements. The red circles highlight the information lost from the single-shot to the binned measurements.	97
4.35	Picture of the VDBD, with visible plasma generation in between the electrode and the dielectric (indicated by the red arrow).	97
4.36	Calibrated ps EFISH measurements of the "faulty" VDBD system, grouped and averaged in 1 ns long bins, at the Center, Ground and HV, positions during the whole nanosecond voltage waveform. The applied electric field and current values are also provided. Notably, the misalignment of the laser is evident in (b), particularly in the HV and Ground positions (for additional information, please refer to the main text).	98
4.37	Calibrated ps EFISH measurements averaged in 1 ns long bins, at three different plasma discharge powers, namely ~ 1.8 W, ~ 2.2 W and ~ 2.4 W. The applied electric field and the current are reported for reference, however, they are not the same intensity for the three different dataset.	100
4.38	(a) ICCD image of the first plasma discharge without the membrane in the VDBD gap. (b) ICCD image of the first plasma discharge with the membrane placed on top of the dielectric surface in the VDBD gap. Both images are acquired with a gate time of 30 ns, for 10 on-ccd accumulations.	101
4.39	Calibrated ps EFISH measurements averaged in 1 ns long bins, taken in the Center position in the VDBD gap, with and without a membrane placed on top of the dielectric, on the grounded side. The applied electric field and the current are also reported for reference.	101
4.40	Ns EFISH measurements (represented by black dots) with the model predictions in the gap centerline. The variables of interest shown in the plot are the electric field ($E(x/d = 0.5)$), the applied electric field (U/d^*), the plasma discharge current (I), and the densities of electrons (n_e), positive ions (n_+), and negative ions (n_-). The applied voltage waveform is fitted to the experimental data (source: [145]).	103
4.41	Schematics of the ions and electrons kinetic differences in a ns plasma discharge in air or nitrogen at atmospheric pressure.	104

5.1 Schematics of the *E. coli* plasma treatment protocol, from storage to CFU counting. For details, please refer to the main text. 111

5.2 Example of Petri dishes with bacteria colonies growing on the surface, after plasma treatments. The Petri dishes are disposed according to the duration of the plasma treatment on the vertical axis and the dilution level on the horizontal axis. 112

5.4 Single measurement of the log reduction of *E. coli* CFU/mL at increasing plasma treatment times. Bacteria treatments were performed with no flow at a distance of 1 cm from the plasma surface. 114

5.6 PCB-fingers SDBD after being damaged by humidity, showing a patchy, non-uniform plasma ignition over the surface. 115

5.7 Schematic of the experimental setup for the bacteria plasma treatments with the PCB-fingers SDBD. 116

5.8 Log reduction of *E. coli* CFU/mL depending on the duration of plasma exposure. The mean and standard deviation of the log reduction for the triplicate are represented. Different lowercase letters indicate significant differences ($p \leq 0.05$).117

5.9 Image of the diffused VDBD plasma discharge with a membrane placed in the gap. 118

5.10 ICCD image of the first plasma discharge (a) without the membrane in the VDBD gap and (b) with a full membrane placed on top of the dielectric surface. All images are acquired with a gate time of 30 ns, for 100 on-ccd accumulations. . . 118

5.12 Schematics of the *Bacillus subtilis* plasma treatment protocol, from storage to CFU counting. For details, please refer to the main text. 120

5.15 Log reduction of *Bacillus Subtilis* spores CFU/mL depending on the duration of plasma exposure. The mean and standard deviation of the log reduction for the triplicate are represented. 123

5.16 Example of treated full membranes of *Bacillus Subtilis* spores CFU/mL, directly plated on an agar Petri dish, depending on the duration of plasma exposure. The region inactivated by the plasma is highlighted in red, showing the bacteria surviving on the side of the membrane, where the plasma does not reach. . . . 123

5.18 ICCD image of the first plasma discharge (a) without the membrane in the VDBD gap and (b) with a quarter of a membrane placed on top of the dielectric surface. All images are acquired with a gate time of 30 ns, for 100 on-ccd accumulations. 124

5.19 Log reduction of *Bacillus Subtilis* spores CFU/mL depending on the duration of plasma exposure. The mean and standard deviation of the log reduction for the triplicates are represented. The red data refers to the HV position, while the black data refers to the Ground position. Note that the errorbars of the data at 180 s are too small to appear on the plot. 125

5.20 Picture of membrane after plasma treatments. The surface modification is clearly visible as "wrinkles" on the membrane. 126

LIST OF FIGURES

5.21	VDBD adapted for <i>Bacillus Subtilis</i> spores plasma treatments on membrane placed at the Center position. The nylon strings used to keep the membrane in place are visible.	127
5.22	Log reduction of <i>Bacillus Subtilis</i> spores CFU/mL depending on the duration of plasma exposure. The blue data represent the treatments performed with the membrane in the Center position. The HV and Ground position are also plotted for reference.	127
5.23	BT96 biological indicator used for the sterilizations experiments.	129
5.25	BT96 BI used for the sterilization experiments after 48 hours. The yellow vials corresponds to unsuccessful treatments, while the purple ones are obtained after successful treatments.	130
6.4	Example of a FTIR spectrum, featuring annotations indicating the corresponding molecule for each distinctive absorbance peak.	137
6.7	FTIR absorbance spectra example of a sequence of acquisition with plasma operating. The significant peak at 1352 cm^{-1} , increasing with time, is KNO_3 forming on the surface of the KBr windows.	140
6.9	FTIR spectra of specific molecules expressed in arbitrary units, namely O_3 , NO, NO_2 , N_2O , N_2O_5 , HNO_3 , CO_2 and H_2O	141
6.12	Schematics of the in-situ FTIR experimental setup of the PCB-fingers SDBD measurements.	145
6.13	FTIR spectra, represented in arbitrary units, recorded during a 10-minute operation of the PCB-fingers SDBD under three distinct flow configurations: 0% RH, 13% RH, and 23% RH. Distinct colors represent the consecutive spectral acquisitions throughout the entire 10-minute data collection, illustrating the buildup of the detected species.	146
6.14	FTIR spectra obtained for the 0% RH flow setup of the PCB-fingers SDBD at 0 s, 108 s, 208 s and 308 s from the initiation of the plasma discharge.	146
6.16	Absorbance FTIR spectra of 1 ppm of NO (top) and 10 ppm of NO (center), and absorption spectra of NO and H_2O (bottom) for reference. Nitric oxide is injected into the bio-plasma reactor using the same configuration as the PCB-fingers SDBD setup for the FTIR measurements. The absorption spectrum of NO is barely identifiable at a concentration of 10 ppm, and completely indistinguishable at a concentration of 1 ppm. This is mainly caused by the low signal intensity, while the water absorption peaks would prevent an accurate absolute calibration.	148
6.17	Schematics of the in-situ FTIR experimental setup of the perforated-disc SDBD measurements.	149

6.18 FTIR spectra, represented in arbitrary units, collected during a 10-minute operation of the perforated-disc SDBD under the static configuration and the ~ 70% RH flow configuration. Distinct colors represent the consecutive spectral acquisitions throughout the entire 10-minute data collection, illustrating the buildup of the detected species.	150
6.19 FTIR spectra acquired for the static configuration of the perforated-disc SDBD at different time points, specifically at 0 s, 108 s, 208 s, and 308 s from the initiation of the plasma discharge.	150
6.21 Schematics of the in-situ FTIR experimental setup of the VDBD measurements.	152
6.22 FTIR spectra, represented in arbitrary units, collected during a 10-minute operation of the VDBD under the three different flow configurations: static, ~ 70% RH flow without pump, and ~ 70% RH flow with pump. Distinct colors represent the consecutive spectral acquisitions throughout the entire 10-minute data collection, illustrating the buildup of the detected species. Please note the different scale between the static case and the two flow cases.	153
6.23 FTIR spectra acquired for the static configuration of the VDBD at different time points, specifically at 0 s, 108 s, 208 s, and 308 s from the initiation of the plasma discharge.	153
6.24 10-minutes evolution of the absolute concentration of O ₃ , N ₂ O and HNO ₃ in ppm obtained from the FTIR absorption spectra in the static configuration of the VDBD setup.	154
7.1 Basic representation of a LIF experiment. The laser beam, with intensity $I_L\nu$, excites the absorber molecules $N_{absorber}$ among the background gas N_{gas} molecules. The fluorescence $I_F(\nu_F)$ is then collected through collection lenses by the photo detector, while the scattered light $I_S(\nu)$ is filtered.	158
7.2 The diagram illustrates the various processes involved in the laser excitation of a molecular system, including radiative processes such as absorption, stimulated emission, and fluorescence, as well as non-radiative processes like collisional quenching. Additionally, elastic scattering is also shown as part of the excitation process. These processes occur within the electronic, vibrational, and rotational levels of the molecular system.	159
7.4 Schematics of the experimental setup used for the nitric oxide LIF measurements.	162
7.8 Schematics of the ps-laser LIF measurements triggering system.	166
7.11 Example of a time-resolved data set of the LIF signal, showing the fluorescence decay timing and the exponential fit used to infer the quenching rate Q	168
7.13 ICCD image of the plasma discharge, acquired with a 30 ns long gate. The ROI selected for the data acquisition in the VDBD is highlighted in red.	170
7.17 NO concentration in ppm over a 2D 4x4 mm area, perpendicular to the DBD surface, at 0% RH (a), 13% RH (b), and 23% RH (c), 500 μ s after the voltage pulse. Please note the different scales of the color bars for the three plots. A schematic of the SDBD is reported to show the position of the plasma discharge in pink.	173

LIST OF FIGURES

7.19 NO concentration during the high-voltage pulse at 4.7 kV, 400 ns long pulses, and 1 kHz repetition frequency at 0% RH, 13% RH, and 23% RH. The optical emission of the plasma is also reported for reference. 175

7.20 Example of the PMT signal acquired during plasma operation (red curve), the PMT signal acquired in the absence of the plasma discharge (blue curve), and the background-subtracted LIF signal (black curve), used for the analysis of the NO concentration. The laser pulse position (in yellow) is reported as a reference. 176

7.21 NO concentration in arbitrary units over a 2D 4x4 mm area, perpendicular to the DBD surface, at 0% RH (a), 1% RH (b) and 10% RH (c). These measurements are taken using a PMT in place of the ICCD, and despite not being calibrated, they show the same pattern found in the measurements obtained with the ICCD. Please note the different scales of the color bars for the three plots. A schematic of the SDBD is reported to show the position of the plasma discharge in pink. . 176

7.23 NO concentration in between plasma discharges at 11.6 kV, 200 ns long pulses and 1 kHz repetition frequency. 178

List of Tables

2.1	Nanosecond pulse parameters range	34
4.1	Picosecond laser parameters	84
6.1	FTIR parameters	141
6.2	HITRAN parameters	142
6.3	Wavenumber range	143
7.1	ICCD parameters	163
7.2	Flow rates for SDBD NO calibration measurements	171
7.3	Flow rates for VDBD NO calibration measurements	178

1 Low-Temperature Plasmas for Bacterial Inactivation

This chapter provides an overview of low-temperature plasmas (LTPs) in the context of biological applications, specifically emphasizing their uses in disinfection and sterilization. The numerous benefits of LTPs compared to traditional sterilizing methods render them a highly promising alternative to the energy-intensive autoclaving approach, which continues to be extensively used. They may serve as a viable substitute for harmful gases in the sterilization of heat-resistant materials. Additionally, their simplicity facilitates construction and operation. This chapter also emphasizes the necessity of conducting a thorough physical, chemical, and biological analysis of plasma treatments to have a complete understanding of the mechanisms involved in the inactivation of bacteria.

The low-temperature plasma properties are introduced in Section 1.1, reviewing details about the ignition mechanisms and most common source configuration, with specific attention to dielectric barrier discharges. The achievable regimes under atmospheric pressure conditions are thoroughly described, along with a comprehensive analysis of the plasma properties when employing different waveforms.

Section 1.2 is dedicated to the discussion of the current status of research about the applications of LTPs in the field of biology. The most significant findings in the fields of plasma medicine, agriculture, food processing, and disinfection and sterilization are showcased. The following section provides a list of the plasma products that exert an impact on biological targets, specifically emphasizing their efficacy in sterilizing microorganisms.

The final section provides a comprehensive examination of sterilization and disinfection, specifically focusing on conventional sterilization procedures that are presently employed. It includes a detailed listing and description of these methods. The benefits of plasma sterilization and its potential as an alternative to current approaches is discussed. The final section of the chapter provides a concise overview of the microorganisms employed in this thesis to evaluate the sterilization efficacy of plasma treatments.

1.1 Introduction to low-temperature plasmas

Plasma, also referred to as the fourth state of matter, is a gas that is partially or completely ionized. Chemist Irving Langmuir was the first to define it in the 1920s. Plasmas constitute approximately 99.9% of the observable cosmos, primarily manifesting as nebulae and stars. However, they may also be observed in nature on Earth in the form of auroras and lightning [1].

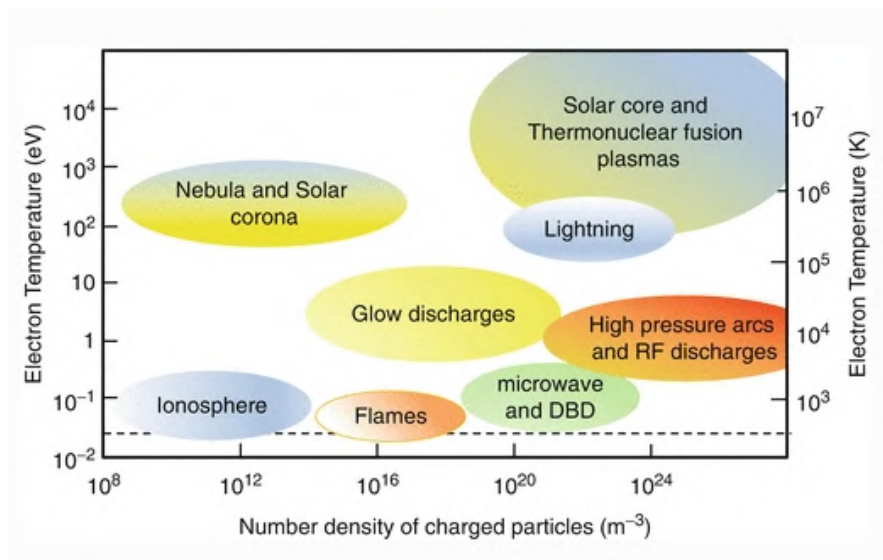
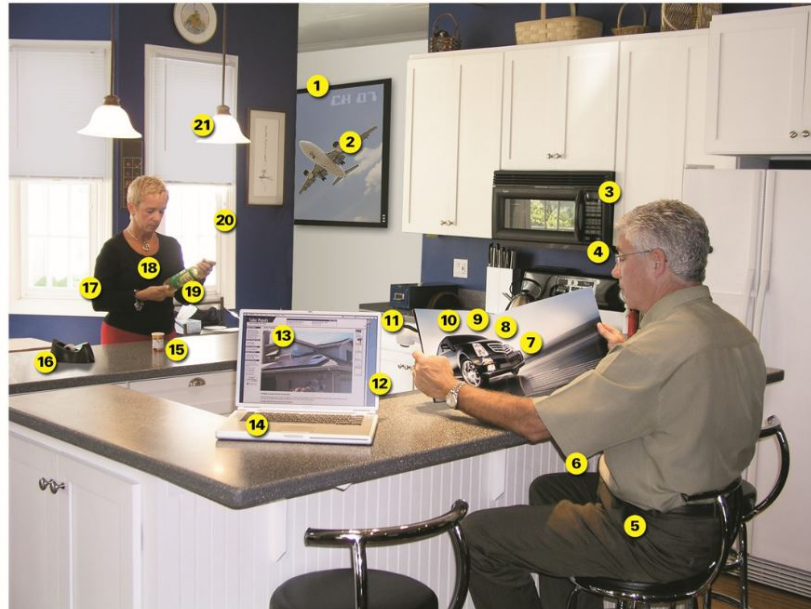


Figure 1.1: Classification of plasmas depending on electron temperature and particle densities (source: [2]).

Plasmas are present in several phenomena, which can be differentiated based on the charge density and temperature, as depicted in Figure 1.1. The temperature and density range of existence of plasma phenomena is broad and the properties of the plasma exhibit large variations in relation to these factors. Plasma possesses features that render it indispensable in several industrial operations, apart from its application in thermonuclear fusion research, as shown in Figure 1.2. The interaction of plasma with electromagnetic fields is harnessed in various modern technical devices such as plasma televisions or plasma etching [3]. In recent decades, there has been a significant growth and increasing recognition of an emerging field of study, namely plasma applied to biology. The interplay between plasma and live organisms is producing encouraging outcomes and presenting several unexplored opportunities. The plasmas utilized in this domain are referred to as low-temperature plasmas, alternatively known as cold, non-equilibrium, or non-thermal plasmas. The primary characteristic of this plasma, as indicated by its several names, is its low gas temperature, which can reach levels as low as that of ambient temperature. Consequently, it presents numerous benefits in the realm of biology, as the cells or other biological entity are not harmed by the temperature of the plasma, yet the plasma still exerts an impact through other byproducts it produces. Prior to delving into the biological uses of LTPs, it is necessary to provide an in-depth description

of the primary attributes of these plasmas and elucidate how they are able to maintain a temperature equal to that of the surrounding environment.



- | | | |
|--|--|---|
| 01—Plasma TV | 09—Plasma-aided combustion | 16—Plasma-treated polymers |
| 02—Plasma-coated jet turbine blades | 10—Plasma muffler | 17—Plasma-treated textiles |
| 03—Plasma-manufactured LEDs in panel | 11—Plasma ozone water purification | 18—Plasma-treated heart stent |
| 04—Diamondlike plasma CVD eyeglass coating | 12—Plasma-deposited LCD screen | 19—Plasma-deposited diffusion barriers for containers |
| 05—Plasma ion-implanted artificial hip | 13—Plasma-deposited silicon for solar cells | 20—Plasma-sputtered window glazing |
| 06—Plasma laser-cut cloth | 14—Plasma-processed microelectronics | 21—Compact fluorescent plasma lamp |
| 07—Plasma HID headlamps | 15—Plasma-sterilization in pharmaceutical production | |
| 08—Plasma-produced H ₂ in fuel cell | | |

Figure 1.2: Illustration of some plasma-based technologies present in the everyday life, and some that are currently under development and might be present in the near future (source: [4]).

1.1.1 Thermal and non-thermal plasmas

Plasma formation typically involves providing a sufficient amount of energy, through various methods, to a neutral gas to ionize it. Electrons transfer this energy to neutral particles through collisions. If electrons possess enough energy, they undergo inelastic collisions, resulting in the ionization of neutral species and the formation of excited species and ions. Alternatively, inelastic collisions take place, where electrons impart kinetic energy to the other species, while keeping the majority of the energy, caused by the wide difference in mass between the particles. When the collision frequency is sufficiently high and the plasma is sustained for sufficiently long time, the ions, electrons, and neutral species in the plasma achieve thermodynamic equilibrium through elastic collisions, resulting in all species reaching the same temperature. Plasmas in which the temperatures of electrons and heavier particles, such as ions and neutrals, are the same are referred to as thermal plasmas. Nevertheless, the temperatures required to

generate thermal plasmas are extremely elevated. The plasma temperature in an arc discharge is approximately 10^4 K and in a fusion reactor it can reach up to 10^8 K. These are typical thermal plasmas where the electron density falls within the range of 10^{21} - 10^{26} m^{-3} [5]. If the collision frequency is low, or if the plasma is not sustained for enough time, the temperature of the electrons significantly deviates from that of the heavier particles. It is not feasible to determine a common temperature in this scenario, necessitating the individual treatment of each species. Non-thermal plasmas, also known as non-equilibrium plasmas, are characterized by the fact that the species involved do not achieve thermodynamic equilibrium. In these plasmas, the electron temperature significantly exceeds the temperature of the heavy particles. Within a glow discharge, the electron temperature tends to be around 10^4 K, but the temperature of heavier particles spans from 300 K to 1000 K. Furthermore, the electron density of non-thermal plasmas is typically lower than that of thermal plasmas, and usually falls below 10^{19} m^{-3} [5].

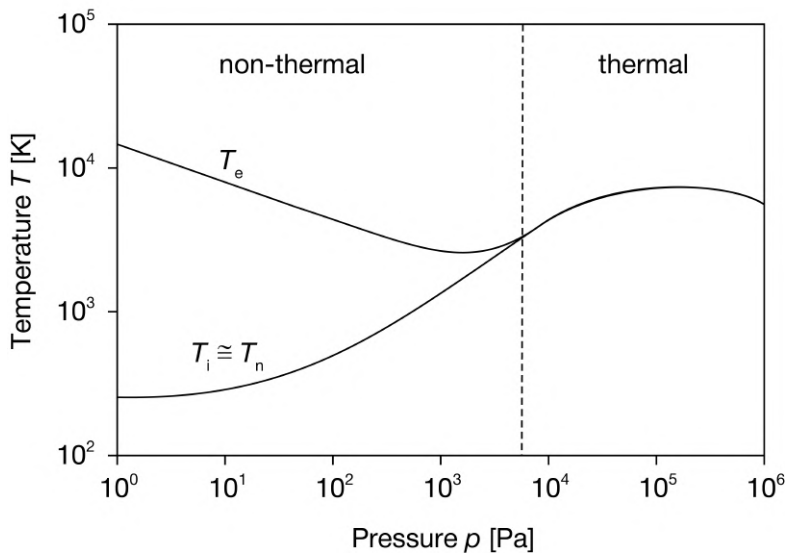


Figure 1.3: Evolution of the plasma temperature (electrons and heavy particles) with the pressure in a mercury plasma arc. T_e , T_i and T_n represent the temperature of the electrons, ions and neutrals, respectively (adapted from [6]).

As depicted in Figure 1.3, non-thermal plasmas are typically observed at low pressure (below 10^4 Pa) due to the fact that the collision frequency is dependent on the density of the gas, which is directly influenced by the pressure. As the pressure increases, the frequency of collisions also increases. They promote both chemical reactions in the plasma (through inelastic collisions) and the increase in temperature of the heavy particles (via elastic collisions). This difference between T_e and T_h (which refers to heavier particles like neutrals T_n and ions T_i) is reduced, resulting in the plasma state approaching thermal equilibrium. Nonetheless, it is feasible to produce non-thermal plasma even under atmospheric pressure conditions. The input power significantly affects the condition of the plasma. In general, a high power leads to the formation of thermal plasmas, such as arc plasmas. On the other hand, non-thermal plasmas are more likely to occur when there is either a low power or a pulsed power source.

In this scenario, the brief length of the pulse prevents the establishment of the equilibrium state [5]. In contrast to thermal plasmas, non-thermal plasmas exhibit a high-energy plasma chemistry due to the elevated electron temperature ($T_e \sim 10^4$ K). Additionally, they have a low gas temperature ($T_n \sim 300$ K) due to the short duration of the pulses, which prevents the system from reaching equilibrium. Therefore, the terms "low-temperature" or "cold" plasmas are used as an alternative name. Henceforth, we shall designate this category as low-temperature plasmas.

In recent years, there has been a growing interest in atmospheric pressure low-temperature plasmas, particularly those generated in air, due to their numerous potential applications and advantages. Unlike low pressure plasmas, these plasmas do not necessitate vacuum chambers, hazardous gasses, or challenging-to-handle gases. They are also quick and simple to construct and employ. The primary means of generating LTPs typically include electrical discharges. However, before delving into a detailed description of these plasma sources, it is necessary to examine the fundamental principles behind plasma ignition in LTP, which is the subject of next section.

1.1.2 Townsend mechanism of electric breakdown

The fundamental concept of electrical discharges involves the application of a high voltage across a gap filled with gas. For simplicity, we will consider a parallel planar electrodes configuration as the one illustrated in Figure 1.4. When the voltage exceeds the "breakdown" voltage, which depends on the pressure, gas gap and composition, the electrons gain enough energy to ionize the neutral particles in the gas.

This initiates a cascade event known as the Townsend avalanche, resulting in the generation of plasma [8]. The initial electrons are created through ionization by cosmic rays. When a voltage is applied across two electrodes, the free electrons are accelerated by the electric field E , thereby acquiring energy as they move towards the anode. The particles undergo exclusively elastic collisions with the gas until they acquire sufficient energy to ionize the neutral species of the gas through inelastic collisions. The electrons produced during this process undergo identical dynamics, resulting in an exponentially increasing cascade, as depicted in Figure 1.4. This cascade is characterized by the first Townsend coefficient α , which quantifies the number of newly generated electrons per unit length:

$$\alpha = pA \exp\left(-\frac{B}{E/p}\right), \quad (1.1)$$

where A and B are constants dependent on the gas and p represents the pressure. Conversely, cations migrate towards the cathode, producing additional electrons by collisions with the surface of the electrode and possibly through photoionization. The Townsend breakdown mechanism refers to the process by which a self-sustained discharge in a gap is ignited.

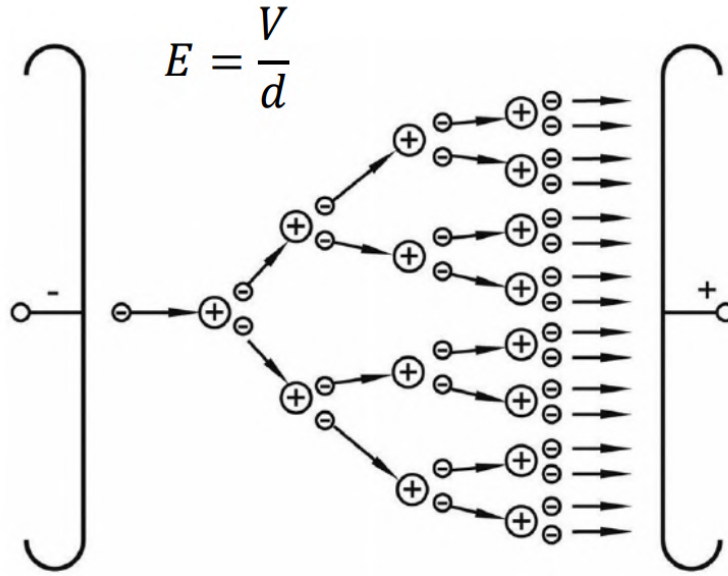


Figure 1.4: Schematics of Townsend avalanche in a plane-to-plane electrical discharge (source: [7]).

The second Townsend coefficient γ considers the contribution of these additional produced electrons, from the collisions of the ions on the surface of the cathode. The requirement for plasma ignition, which guarantees an increase in the number of electrons, can be described as follows:

$$\gamma(e^{\alpha d} - 1) \geq 1, \quad (1.2)$$

where d is the length of the gas gap. By combining Equations 1.1 and 1.2, it is possible to obtain the so-called Paschen's law, reported for some gases and air in Figure 1.5, which defines the breakdown voltage as the lowest voltage required to induce electrical conductivity in an insulator:

$$V_b = \frac{B \cdot p d}{\log\left(\frac{A \cdot p d}{\log(1 + 1/\gamma)}\right)}. \quad (1.3)$$

Paschen's law states that the breakdown voltage is dependent on the dimensions of the gas gap, denoted as d , and the pressure, denoted as p . The relationship can be graphed for several gases using experimental gas constants, as depicted in Figure 1.5. Every curve has a minimum breakdown voltage, for a specific $p \cdot d$ value. Due to this factor, igniting plasma in atmospheric pressure is more challenging, although it can still be achieved by either increasing the voltage or reducing the gap distance. In air the value to reach breakdown is approximately ~ 3 kV/cm.

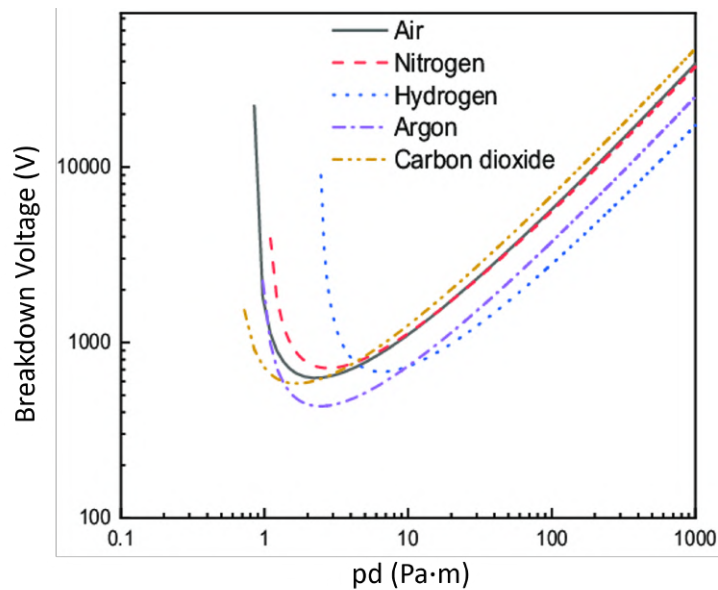


Figure 1.5: Paschen curves obtained for helium, neon, argon, hydrogen and nitrogen, using the expression for the breakdown voltage as a function of the parameters A,B that interpolate the first Townsend coefficient (source: [9]).

1.1.3 Dielectric barrier discharges

There are various configurations of electrical discharges, but the most common in biological applications is known as dielectric barrier discharge (DBD) [10]. A DBD is a plasma source consisting of two electrodes that are separated by a dielectric component, as illustrated in Figure 1.6. The dielectric material serves as an insulator or barrier, which is why the source is named as such. The dielectric barrier functions as a quencher for the charges, inhibiting the creation of direct electrical channels and so preventing the occurrence of electric arcs. The creation of an arc not only leads to device damage, but also hinders the generation of low-temperature plasma discharge. Various configurations of DBDs exist, including plasma jets, floating-electrode DBDs, surface and volume DBDs, multi-hollow DBDs, and plasma actuators. A comprehensive categorization of these variants may be found in [11]. We will specifically emphasize planar DBDs, also known as plane-to-plane DBDs, as these are the devices used in our study. The geometry of planar DBDs is characterized by flat and parallel electrodes and dielectrics surface. They can be classified into volume and surface DBDs based on the region where the plasma is generated, as depicted in Figure 1.6. In volume DBDs (VDBDs), the two flat electrodes are separated by a gas gap, and at least one of the electrode surfaces is coated with a dielectric material. The arrangement including a floating dielectric, as depicted in Figure 1.6(a₃), is uncommon. The plasma is formed within the gas volume located between the two electrodes, hence the term "volume DBD". Widening the gap width leads to an increase in the breakdown voltage gap and a decrease in the stability of the plasma. The gap distances frequently used are typically less than 1 cm, whereas the voltage breakdown

occurs within the range of 5-20 kV.

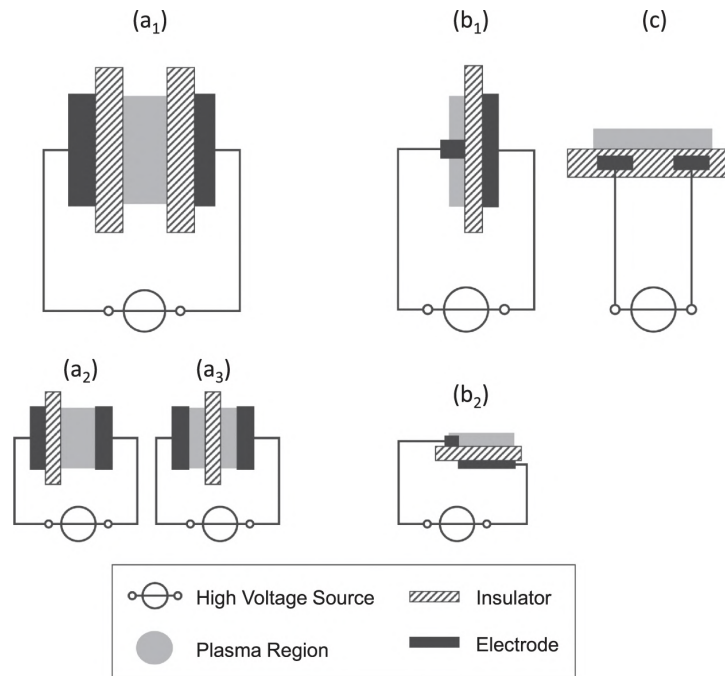


Figure 1.6: Basic planar configurations of DBDs: (a) volume DBD (1-symmetric, 2-asymmetric, 3-floated dielectric); (b) surface DBD (1-symmetric, 2-asymmetric 'actuator' design); (c) coplanar discharge. (source: [11]).

In surface DBDs (SDBDs), however, the two electrodes are positioned next to each other and are only separated by the dielectric barrier. The plasma is generated at the edges of the electrodes, where the electric field is more intense. Due to the typical preference for generating plasma on only one face of the SDBD, one of the electrodes is either fully covered by the dielectric or it is larger than the electrode on the opposite side. This effectively prevents plasma ignition on one side. Hence, the electrode employed for initiating the plasma often possesses a mesh or grid-like structure to maximize the area for plasma generation. In these devices, the breakdown voltage and the power needed to initiate the plasma are typically lower compared to VDBDs, due to the significantly shorter distance between the electrodes. The minimum breakdown voltage is significantly lower than the breakdown voltage in VDBDs, since the path of the electric field lines through air is shorter. DBDs are constructed using a variety of materials. Stainless steel or copper are commonly preferred for the electrodes, whereas alumina is recognized as one of the most used dielectric materials. Quartz and FR4 (flame-retardant 4) are also frequently used as dielectric barrier materials due to their high resistance to heat. Nevertheless, the utilization of FR4 can lead to complications related to humidity [12].

1.1.4 DBD mechanisms and regimes

Without attempting to be exhaustive, this section provides a brief overview of the mechanisms and regimes of DBD plasmas. For a comprehensive explanation, kindly consult Ref. [13, 14]. The initiation of plasma ignition in electrical discharges is facilitated by the Townsend mechanism. This occurs when the voltage is higher than the breakdown voltage, as determined by Paschen's law [15]. During the second phase, a phenomenon known as streamer generation typically occurs, resulting in the creation of robust conductive channels that connect the two electrodes [13]. Following this phase, an electric arc formation typically follows, but the dielectric material employed in the DBDs restricts the flow of direct current, allowing only displacement currents to pass. The dielectric acts as a quencher, preventing the transition of an electric arc by accumulating charges on the surface of the barrier. The electric field produced by the accumulating charges intensifies until it counterbalances the external field, causing the streamer to cease. The complete sequence, encompassing the development of an avalanche and the subsequent termination of the discharge, is referred to as microdischarge. The density of these microdischarges depends on the frequency and voltage of the power source. Furthermore, as a result of the charge accumulation, they are evenly distributed across the surface of the DBD.

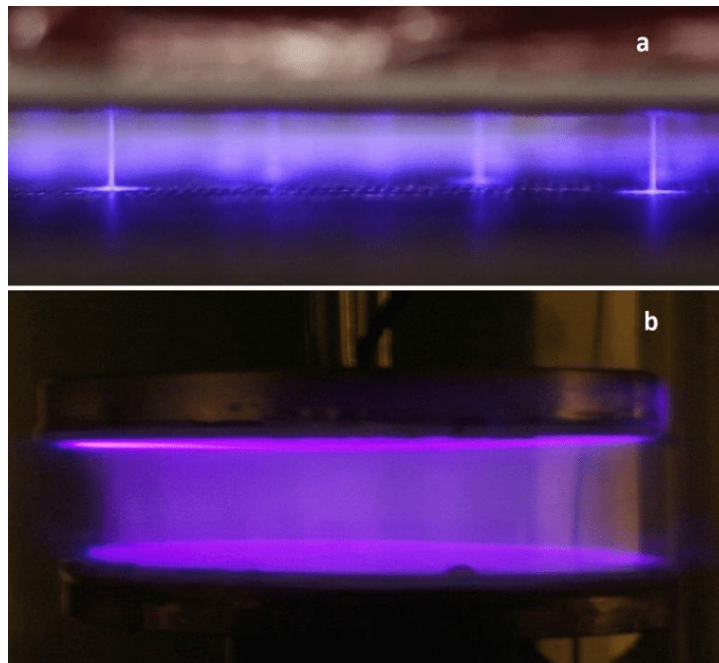


Figure 1.7: Example of (a) a filamentary discharge and (b) a diffuse discharge (source: [16]).

This plasma regime observed in DBDs is referred to as "filamentary" mode, which is clearly apparent without the use of any instruments, as depicted in Figure 1.7(a). The occurrence of microdischarges in AC driven DBDs is attributed to the phenomenon known as "memory effect", wherein the microdischarges consistently appear in the same locations with a change in the polarity of the electric field. Alternatively, it is possible, under specific circumstances, to

inhibit these strong conductive channels, resulting in a uniform and evenly distributed plasma [11, 14]. This plasma regime, known as "diffuse" mode is shown in Figure 1.7(b). Diffuse plasma discharges are most often observed in low pressure plasma, whereas atmospheric pressure plasma often operates in filamentary mode. Nevertheless, it has been demonstrated that atmospheric pressure diffused discharges can be attained by manipulating certain parameters such as electrode structure, dielectric configuration, gas type, and waveform characteristics [17, 18].

1.1.5 Nanosecond-pulsed plasma discharges

This section presents the advantages of using nanosecond-pulse waveforms to power DBDs in the context of biological applications of LTPs. DBDs are often powered by sinusoidal voltage sources, although there are various alternatives that can impact the performance of the DBD. The most attractive option is to take advantage of a monopolar nanosecond pulsed voltage source. It has already been demonstrated to be more effective for several reasons. Firstly, it exhibits higher power efficiency due to the occurrence of two plasma discharges for each pulse, with the second discharge being spontaneous, as shown in Figure 1.8.

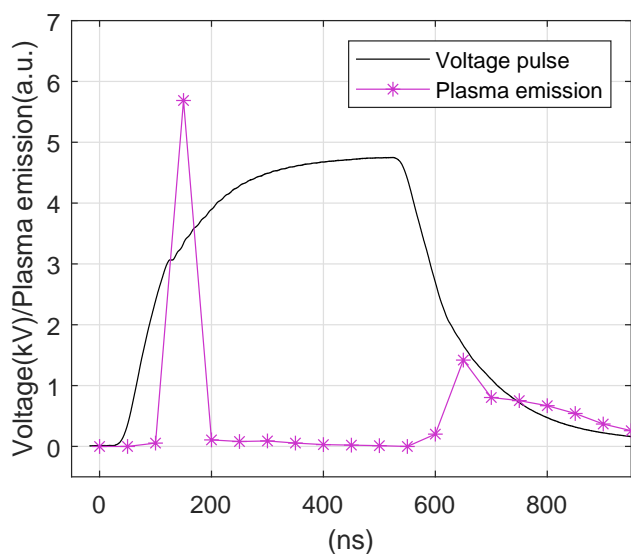


Figure 1.8: Nanosecond high-voltage pulse with plasma optical emission in arbitrary units, representing the two plasma discharges during the rising-edge and falling-down of the voltage pulse.

The first discharge is triggered by the increasing voltage of the pulse and terminated by the electric field produced by the accumulation of charges in the dielectric barriers [19]. Following the extinguishing of the discharge, the charges remain stable on the barriers until the voltage decreases and the electrons are released into the gas, causing a subsequent "spontaneous" discharge [20]. Two plasma discharges take place for every pulse, and the second discharge

operates without requiring any additional power input from the source. Various studies have shown evidence for the higher power efficiency of nanosecond pulsed waveforms compared to sinusoidal waveforms [21, 13]. In addition, the rapid increase in voltage during nanosecond pulses amplifies the generation of high-energy electrons, leading to an increased production of reactive species [22, 21]. Studies have shown that nanosecond pulses result in greater amounts of atomic oxygen and ozone compared to sinusoidal waveforms, when the power input is kept constant. In addition, generating diffused plasma discharges with nanosecond pulses has been proven in multiple works [23, 24], being aware that voltage and pressure affect the regime of the plasma discharge [25]. The relaxation intervals between subsequent pulses enable the reactive species generated in the preceding cycle to evenly spread out throughout the entire region of the DBD. The rapid increase in voltage then initiates many simultaneous discharges across the entire gap filled with gas [26]. In addition, the absence of a voltage reverse results in the absence of a local "memory effect" caused by the accumulation of charges on the same locations of the dielectric surface, preventing the microdischarges to occur in the same specific areas [27].

1.2 Biological applications of LTPs

Biological applications are becoming increasingly prominent in the realm of LTP. Due to the combination of high-energy chemistry caused by high-energy electrons and a low-temperature substrate determined by the low energy of the heavy particles, LTPs have proven to be highly effective in several biological applications, ranging from biomedical and food applications to plasma agriculture. Plasma agriculture involves applying low-temperature plasma to seeds and plants to enhance their germination, ability to withstand stress, and antimicrobial properties [28, 29, 30, 31]. LTPs have been extensively investigated in the context of the food processing industry, namely for the purposes of decontamination and preservation [32, 33, 34, 35]. Biomedical applications encompass the use of LTP in medical contexts, such as plasma medicine, disinfection, and sterilization, including therapy of cells and tissues [36, 37, 38]. LTP treatments have demonstrated success in wound healing by accelerating wound closure and facilitating re-epithelialization [39, 40]. It also effectively regulates blood coagulation rates with minimal adverse effects [41], promoting accelerated healing [42, 43]. In addition, LTP has also found applications in dentistry [44]. They have also been investigated for cancer therapies [45, 46, 47] and solid tumor therapies [48], drug resistance in cancer [49] and the selectivity of plasma in cancer cells [50].

Regarding decontamination, LTPs have been extensively investigated in numerous studies. These investigations have explored the use of plasma jets, where the plasma is directed to a specific area through a gas flow, as well as VDBD and SDBD, which involve generating plasma within a volume or over a surface, respectively. The treatment can be defined either as direct or indirect based on the device arrangement and the relative position of the biological target with respect to the plasma. If the target is in direct physical contact with the plasma, the treatment is classified as "direct". Conversely, if the target is not in direct contact with the

plasma but is sufficiently close for by-products of the plasma, such as RONS, to reach it, then the treatment is referred to as "indirect". Plasma jets and VDBDs are commonly employed for direct plasma treatments, while SDBDs are used for indirect plasma treatments. While direct plasma treatments are generally faster [51, 52], indirect plasma therapies have also been demonstrated to be effective and have the advantage of easier implementation [53, 54, 55, 35, 56]. The efficacy of LTP treatments has been proven not only on bacteria [57, 58, 59, 54, 60], but also on spores [61, 62, 63], fungi [64, 55], viruses [65, 66] and bio-films [51, 67, 56].

1.2.1 LTPs bacterial inactivation mechanisms

Although LTPs have proven effective in bacterial inactivation and have shown success in deactivating various types of spores, fungi, and viruses, the specific mechanisms behind these interactions remain a subject of ongoing discussion.

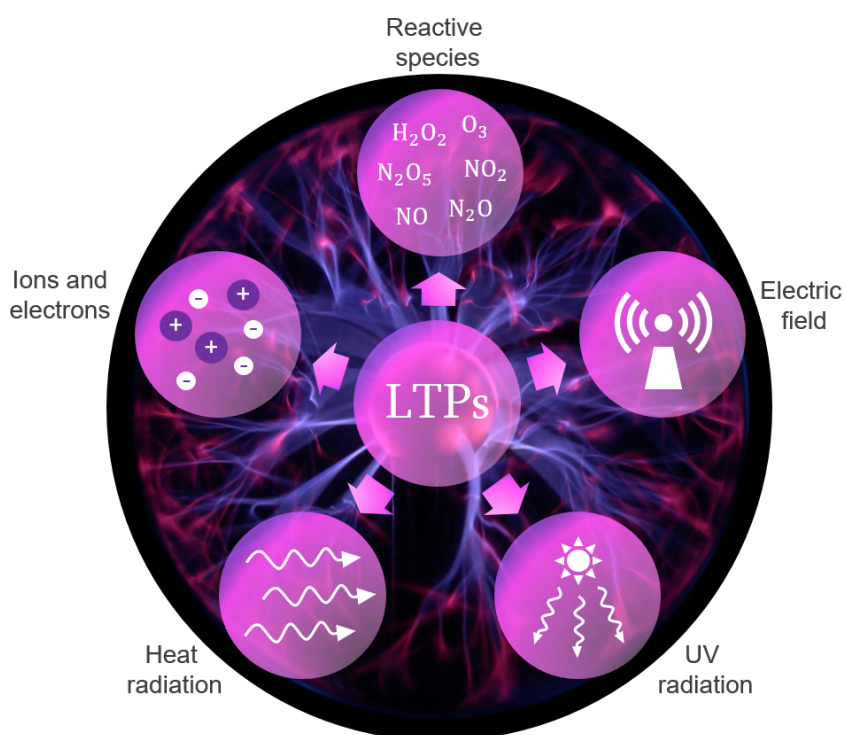


Figure 1.9: Products of low-temperature plasmas.

LTPs generate ions, electrons, reactive species, UV radiation, heat, and electric fields, as depicted in Figure 1.9. Therefore, it is challenging to identify the specific elements that have a significant impact on microorganisms. Typically, it is widely acknowledged that a combination of these mechanisms is considered to be the reason for the inactivation of bacteria by LTPs. Nevertheless, numerous studies concur on the importance of reactive species, particularly in air plasmas, where newly formed molecules aggressively target the biological target. Given that this thesis specifically examines the atmospheric pressure LTP in

air, our attention will be on the reactive oxygen and nitrogen species (RONS) that are generated in this scenario. Depending on the arrangement of the DBD and the mode of administering the plasma treatments, whether by direct or indirect exposure, certain parameters hold greater significance than others. Let us examine the role of each of the characteristics mentioned above in further depth.

Charged particles

Since plasma is a partially ionized gas, electrons and ions are crucial to the way plasma affects the inactivation of microorganisms. Charged particles have an impact only in direct plasma treatments, where the biological target is either located within the plasma or in direct contact with it. Indeed, ions and electrons exist solely during the plasma discharge and promptly recombine thereafter. Consequently, their lifespan is insufficient to reach a distant target, such as in indirect plasma treatments. The effect of charged particles on bacteria is twofold: one is through the bombardment of ions and electrons, and the other is through the presence of electric fields caused by the accumulation of charges on the cell membrane. The first process breaches the membrane of microorganisms through the mechanical collision of particles with the membrane, potentially leading to the inactivation of the microorganism [68, 69]. The second one elucidates the effect of electric fields on the membranes of bacteria. Research has demonstrated that the buildup of charges on the surface of microorganisms can create powerful localized electric fields on the cell wall, which plays a significant part in the process of inactivating bacteria [70]. If the electrostatic forces surpass the tensile strength of the membrane of the microorganism, they can result in the rupture of the outer membrane [70, 71].

Electric fields

Just like the accumulation of charge on the bacteria membrane, the electric field generated in the plasma can greatly affect the biological target. Nevertheless, this aspect of LTPs is frequently overlooked and underestimated as it is not considered to have a role in the bacterial inactivation process by LTP. Electroporation is a recognized phenomenon wherein a cell's membrane becomes permeable to molecules that would typically be unable to enter, as a result of exposure to a high-intensity electric field. The permeability of the cell membrane is attributed to the creation of minuscule and transient pores, facilitating the passage of molecules. Electroporation is a reversible phenomenon, and the pores will eventually shut, thereby restoring the membrane's original permeability. Nevertheless, the imbalance in the concentration of ions within the bacteria can result in the expansion and subsequent rupture of the membrane, ultimately inactivating them [72]. The magnitude of the electric field necessary for the deactivation of microorganisms is dependent upon various factors. Research has shown that in order to decrease the *E. coli* population in tap water by ten times, electric fields of 100 kV/cm were required for 60 ns pulses, whereas 70 kV/cm was sufficient in nutrient broth [73]. The precise impact of the electric field in direct LTP bacteria treatments remains

poorly understood, mostly due to its frequent neglect and the inherent difficulty in quantifying the local electric field within a plasma discharge. Not surprisingly, the effect of electric field is only relevant in direct plasma treatments, since they do not extend over the plasma with a significant intensity.

Reactive oxygen and nitrogen species

The consensus throughout the community is that reactive oxygen and nitrogen species (RONS) play an essential part in atmospheric pressure LTP treatments [74, 75]. This is particularly true for indirect plasma treatments, as the only plasma byproducts that reach the biological target are RONS, together with ultraviolet (UV) radiation. The discussion of UV radiation will be presented in the following section. The impact of RONS on microorganisms stems from their capacity to provoke severe oxidative and/or nitrosative stress on the bacteria, ultimately leading to the disruption of the cell membrane, or to the normal functions of the cell [1, 76, 77, 78, 40]. The plasma generates various reactive species in the air that are of interest for their antimicrobial properties, as illustrated in Figure 1.10. These include atomic oxygen (O), ozone (O₃), hydroxyl radicals (OH), hydrogen peroxide (H₂O₂), the anion superoxide (O₂⁻), nitric oxide (NO), nitrogen dioxide (NO₂), and nitric acid (HNO₃), to name the most relevant. Certain species, such as O₂⁻, exhibit high reactivity and rapidly recombine, while others, like O₃, are rather stable. The reactive species can be classified as short-lived or long-lived according to the lifetime of the molecule [79, 80]. Highly reactive molecules such as OH, O₂⁻, O etc. are referred to as short-lived species, while more stable molecules such as NO, O₃, NO₂, etc. are classified as long-lived species. Short-living species are more relevant in direct plasma treatment, and being highly reactive can have a disruptive effect on the microorganisms. For example, atomic oxygen leads to significant etching of bacteria [81] and undergo further reactions, resulting in the formation of the hydroxyl radical OH, which is yet another anti-microbial molecule [82]. This radical is extremely reactive and capable of crossing membranes to cause damage to the DNA present within the cell.

Ozone, instead, is a key long-lived antibacterial molecule among the RONS produced by LTPs, as evidenced by several studies [84, 85, 86]. The bactericidal effect of ozone originates from the perturbation of the cellular respiration mechanism. The antimicrobial properties of ozone have been thoroughly investigated for various purposes, such as treating both dry and wet surfaces [87, 88], decontaminating food [86], and inactivating bacterial biofilms [67]. Prior studies have demonstrated a correlation between ozone and the ability to kill bacteria, indicating that ozone is a key reactive molecule generated by LTPs in comparable setups and it plays a critical role in inactivating bacteria [89]. Nevertheless, it is important to highlight that the process of bacterial inactivation during plasma treatments is also greatly influenced by the presence of NO_x (nitrogen oxides) products, as demonstrated in previous studies [90]. These molecules, such as NO₂, N₂O, HNO₃ and N₂O₅ can have a crucial impact on the basic functions of microorganisms [91, 92, 93]. Nitric oxide (NO) is also a crucial molecule in this context, serving not only as a bactericidal agent but also as a precursor to

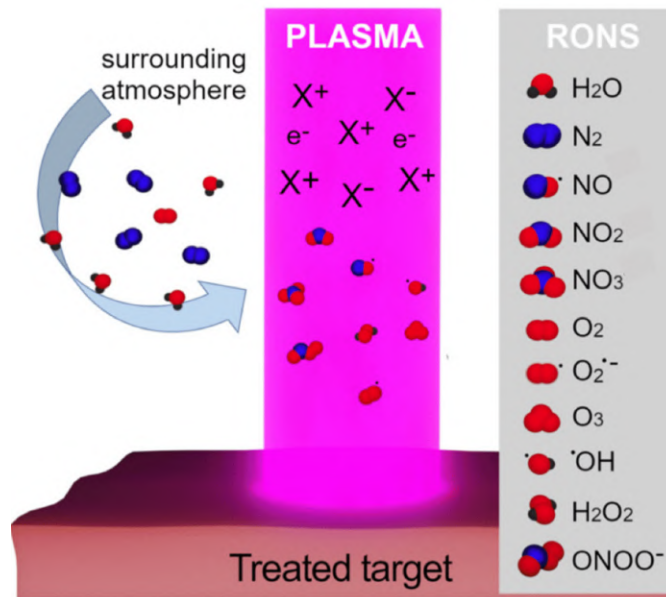


Figure 1.10: Illustration of a set of RONS produced in LTPs (adapted from [83]).

additional NO_x molecules [94, 95, 96]. While simulations indicate that the concentration of NO is minimal in the region adjacent to the plasma, there is a lack of experimental evidence on the concentration and kinetics of NO in SDBD and VDBD setups. Prior investigations on NO in SDBD plasmas have predominantly focused on spatially and temporally averaged measurements, which do not supply data on the concentration at precise distances from the plasma source or at specific time intervals between discharges [97, 98]. Hence, the present comprehension of RONS generated by SDBDs and VDBDs is insufficient, specifically regarding the impact of crucial factors such as power, applied voltage, relative humidity, and proximity to the plasma.

UV radiation

UV radiation is a recognized sterilizing agent that is extensively used for decontamination purposes [99, 100, 101]. The basic explanation for its efficacy is its ability to induce DNA damage, which prevents the replication of microbes. UV photons are generated by plasma, primarily influenced by the gas composition and, secondarily, by other factors such as power and pressure. The effectiveness of UV light in inactivating microorganisms is highly dependent on the wavelength of the radiation. Photons with shorter wavelengths possess greater energy, which is essential for the disruption of chemical bonds, while exhibiting reduced penetration capability. Conversely, photons with longer wavelengths have lower energy but greater penetration power. UV radiation can be categorized into UV-A, UV-B, and UV-C based on their respective wavelengths, as illustrated in Figure 1.11. The UV-C range (100 to 280 nm) is widely accepted as the most effective spectrum for UV inactivation [102, 101, 103]. Specifically, it was discovered that the most effective wavelengths for inactivating *Bacillus subtilis* spores are

between 220 and 270 nm, as well as between 125 and 170 nm [104]. The gap between 170 nm and 220 nm stems from the protein-based outer layer of spores, which effectively absorbs UV radiation within this wavelength range, so preventing it from reaching the cell interior and DNA. This discovery was made by simulating the outer layer of spores using the absorption coefficient of the albumin protein [105]. The high efficacy of inactivation in the 125 nm to 170 nm range can be attributed to the similarity in absorption between albumin and DNA.

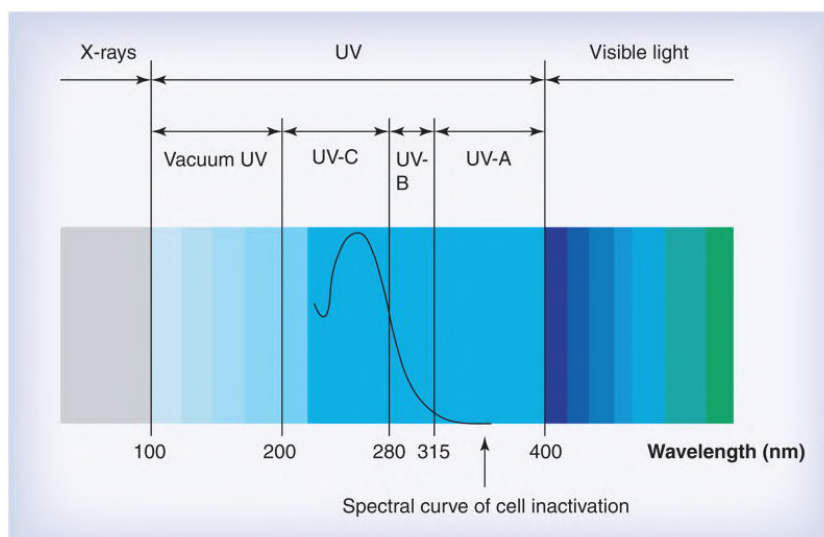


Figure 1.11: UV radiation spectra, with UV-A, UV-C and UV-C band highlighted. A guideline on the bactericidal efficacy of the UV bands is reported (source: [101]).

This can be explained by a favorable combination of high energy and enough penetration depth, or by the inactivation caused by the breakdown of the membrane. While UV-C photons can be effectively emitted at low pressure by excited NO molecules in the NO_γ band (about 200 to 285 nm), the same efficacy is not observed at atmospheric pressure. Although the use of a gas mixture consisting of N_2 and O_2 makes it challenging to generate a significant quantity of UV-C photons [106], UV radiation is not considered a primary factor in the inactivation of bacteria during atmospheric pressure LTP treatments [75].

Heat

Heat is one of the main factors in currently employed sterilization processes like autoclaves. Nevertheless, the majority of low-temperature plasma discharges operate at room temperature. Depending on the DBD arrangement and operating conditions, they can achieve higher temperatures, however typically the temperature remains below 70°C . The inactivation temperature of microorganisms varies across different species and can span from 40°C to $> 130^\circ\text{C}$ [107, 108], as shown in Figure 1.12. The typical temperatures involved in DBD plasma are insufficient to effectively inactivate all types of bacteria, thereby rendering it negligible in terms of its involvement in bacterial inactivation [75]. Nevertheless, it is crucial to consider

that increased temperature can amplify the impact of other mechanisms, such as the generation of reactive species like nitric oxide, whose production is strictly related to temperature. Conversely, the use of low temperature in plasma treatments is advantageous for sterilizing heat-sensitive materials, which are currently treated with harmful gasses such as ethylene oxide or formaldehyde [109]. Additionally, in the context of medical therapies, maintaining a high temperature can potentially cause harm to the tissue or biological target, rather than solely producing beneficial outcomes.

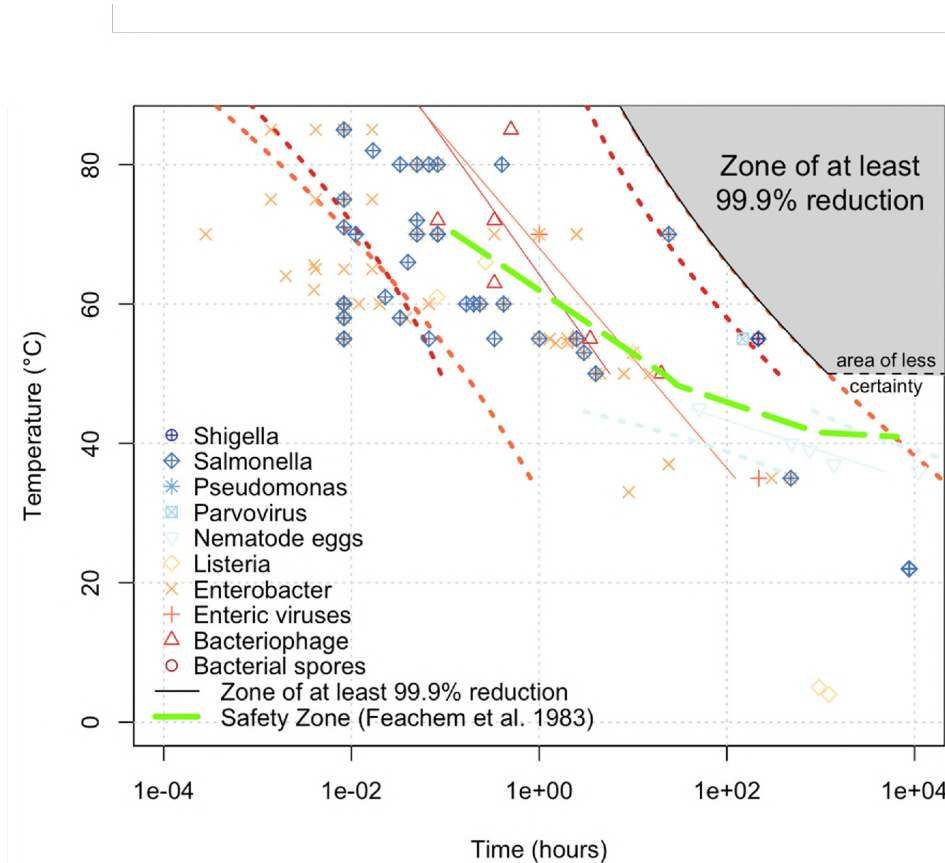


Figure 1.12: Time-temperature curves developed for the inactivation of various microorganisms using heat treatment to achieve 3-log (e.g., 99.9%) reduction. Solid lines show the linear fit of the data, and dotted lines show 95% prediction intervals (adapted from [108]). For more details, please refer to Ref. [108].

1.2.2 Final considerations on plasma bactericidal factors

The contribution of several mechanisms in atmospheric pressure plasma for the inactivation of bacteria is still a subject of debate [106, 110]. It appears that RONS play a significant part in treatments performed by LTPs in air at atmospheric pressure [75], as described in both direct and indirect treatments. However, in direct plasma treatments, the importance of RONS may differ. Overall, the effectiveness of plasma as an inactivation agent is derived

from the combined effects of RONS, UV light, electric fields, and charged particles. However, the challenge of accurately determining which of these products plays a more critical role arises from the wide range of configurations and the failure to consider all the parameters that influence plasma properties. These parameters include power, frequency, gas composition, flow rate, humidity, exposure distance, treatment time, initial concentration of microorganism suspension, and the characteristics of the growth media and target microorganisms [111]. To have a complete understanding of the mechanisms involved in low-temperature plasma treatments, it is necessary to conduct a thorough physical, chemical, and biological characterization. It is important to clarify that in this context, "biological characterization" refers to evaluating the efficacy of the plasma setup under investigation on the biological target, by carefully characterizing the properties of the target and the protocols used for the evaluation.

1.3 Sterilization and disinfection

The potential to achieve sterilizing levels through low-pressure and atmospheric pressure LTPs has been extensively examined and analyzed, taking into account the disinfection efficacy of LTP in bacterial inactivation [112, 113, 114, 115]. The term sterilization is occasionally misused and can lead to confusion. As per the International Standard ISO 11139 [116], sterilization is "a validated process used to render products free from viable microorganisms". In reality, to completely free a product from microorganisms and to provide evidence of it is not practical. Hence, the World Health Organization (WHO) has established a specific reduction value to provide a measurable criterion for defining a sterilized product: "However, sterilization is never absolute; by definition, it reduces the number of microorganisms by a factor of more than 10^6 (more than 99.9999% of the microorganisms are killed)" [117]. If this condition is not met and the decrease is less than 10^6 , the appropriate terminology to employ is decontamination or disinfection, which refer to the reduction of microbiological contamination to a level that is considered safe according to the World Health Organization (WHO) [117].

1.3.1 Sterilization methods overview

Various methods can be employed to achieve sterilization. Each of them has benefits and drawbacks, as well as different areas of use. The process of sterilizing in laboratory settings differs from that in hospitals, and it also differs from pharmaceutical sterilization. Every industry and application possess distinct and specific requirements. A brief overview of the currently used sterilization methods is presented.

Autoclaves

Autoclaves are essential in sterilizing facilities, where they are used to reprocess utensils, reagents, and waste materials. They play a crucial role in research in the life sciences and are also vital in hospitals. They use pressurized steam at around 121°C to inactivate microbes.

The duration of the cycle can vary considerably, while the minimum duration required for sterilization is 20 minutes, excluding the time required for temperature buildup and subsequent drying. They operate continuously throughout the day to fulfill the requirements of the research laboratories and hospitals. Regrettably, an average autoclave not only consumes up to several hundred liters of water during a single sterilization cycle, resulting in a significant environmental impact, but it also consumes significant amounts of energy in the process [118]. In addition, items that are sensitive to humidity and temperature cannot be sterilized via autoclaving. Alternative techniques are occasionally employed or designated for specific needs. Flaming and dry heat, like autoclaving, employ high temperatures to inactivate the microorganisms but are either less efficient than autoclaving, or can cause damage to the object.

Chemicals

Currently, chemical sterilization is the more practical option for thermo-sensitive materials. The predominant gases employed are ethylene oxide and formaldehyde, however, their efficacy is dependent on the humidity in the environment. This approach precludes the sterilization of water-sensitive materials. Moreover, these compounds pose a significant risk not only to microbes but also to humans. Ethylene oxide (EtO) is a transparent and toxic gas that targets the cellular proteins and nucleic acids of microorganisms. Formaldehyde is categorized as a carcinogenic substance that can induce respiratory and skin irritation when exposed to. The toxicity of these gases poses a challenge for their extensive employment.

Radiation

Radiation is a highly effective procedure for sterilization. Microorganisms experience significant DNA or RNA damage as a result of exposure to high-energy radiation. Gamma rays are ideal for this purpose because of their high energy and strong penetrating capabilities resulting from their short wavelength. Gamma rays are a form of electromagnetic radiation that is naturally emitted during the decay of an atomic nucleus. Exclusively, Cobalt-60 is recommended for the purpose of sterilizing processing [119]. The radiation emitted by Cobalt-60 is sufficiently strong to exterminate bacteria, however lacks the necessary energy to induce radioactivity in the treated items. Primarily, it is employed for the sterilization of manufactured medical products such as needles and human tissue grafts. However, handling and controlling is extremely hazardous due to the presence of radioactive risks.

Ozone

An emerging technique involves the utilization of ozone. It has been demonstrated to be an effective sterilizer against a wide range of microbes, including the highly resistant *Geobacillus stearothermophilus*, which is commonly used as a benchmark bacterium for biological indi-

cators. Ozone is a promising low-temperature sterilization technology, however it requires lengthy treatment durations to achieve effectiveness. Ozone functions by generating a highly oxidizing environment that is detrimental to microbes.

Hydrogen peroxide

The use of H₂O₂ is more widespread, with commercially accessible systems such as Sterrad being referred to as gas plasma sterilizers due to the ionization of H₂O₂ vapor as part of the sterilization process. Nevertheless, doubts exist regarding the impact of plasma in this system, as the effectiveness of this method is primarily attributed to H₂O₂. The expression "plasma sterilizer" is inaccurately employed because its cycles involve a chemical phase, when vapors with proven sterilizing attributes are used. On the other hand, it can be referred to as a "real" plasma sterilizer, a system where plasma is the single agent responsible for inactivating microorganisms, excluding any purely chemical processes [115][120].

Advantages of LTP-based sterilization

Compared to autoclaving, sterilizing techniques based on LTPs provide many advantages such as reduced energy consumption, lower temperature demands, absence of high pressure or vacuum needs, shorter treatment durations, and the absence of persistent hazardous compounds. Due to these benefits, LTP sterilization provides an efficient alternative for sterilizing thermo-sensitive and water-sensitive materials that are currently unsuitable for autoclave sterilization. While LTPs show potential for new sterilization methods and companies are developing LTP sterilization systems globally, it is crucial to have a thorough understanding of the physical, chemical, and biological aspects before implementing and expanding this technology commercially.

1.3.2 Introduction to microorganisms

As previously discussed, sterilization is only achieved when all microorganisms are rendered non-viable, with viable referring to cells that are metabolically or physiologically functional [121]. Microorganisms are defined as "any microbiological entity, cellular or non-cellular, capable of replication or of transferring genetic material" [117]. Microorganisms encompass both unicellular and certain multicellular organisms. The organisms encompassed by this classification include bacteria, fungi, algae, and protists. Spores are a significant form of these microorganisms. They are reproductive structures produced, as part of their life cycle, adapted for dispersal and survival in harsh conditions. Spores are more resistant forms of microorganisms and for this reason used to assess the efficacy of sterilization methods. More precisely, bacteria spores, but also bacteria not in spore form, are the microorganisms of choice in research for decontamination and sterilization studies for practical reasons. Bacteria are abundant and diverse, with numerous species available for study. This diversity

allows researchers to assess the effectiveness of sterilization methods against a wide range of microorganisms. They are relatively easy to handle and cultivate in laboratory settings. They can be grown quickly, and their growth and response to sterilization processes can be readily observed.

Commonly, studies of sterilization techniques employ standardized bacterial strains, such as *Escherichia coli*, *Bacillus subtilis*, or *Geobacillus stearothermophilus*. Specifically, *Bacillus subtilis* and *Geobacillus stearothermophilus* spores exhibit a high level of resistance to different sterilization procedures, which makes them ideal for evaluating the efficacy of sterilization processes. In laboratory settings, bacteria are often considered to be less hazardous than some fungi, hence posing fewer threats to researchers. The protocols for containing bacteria are well-established and generally simple. In addition, bacteria exhibit greater resilience compared to numerous fungi, particularly bacterial spores. Their durability makes them an ideal model to evaluate the efficacy of sterilization techniques, which must be able to eradicate extremely resistant germs. Although bacteria are frequently employed, there are certain cases where alternative microorganisms, such as fungi, can be used for specific research or validation purposes [65, 55]. The selection depends on the research objectives and the particular criteria of the sterilizing procedure under examination. One example is the use of *Geobacillus stearothermophilus* spores to evaluate the efficiency of steam sterilization methods, as they are highly thermo-resistant bacteria.

1.3.3 Gram-positive and Gram-negative bacteria

The membrane of microorganisms is crucial for decontamination purposes as most sterilization techniques rely on rupturing and disrupting the outer membrane to render them inactive. The Gram-staining technique distinguishes bacteria by identifying peptidoglycan, a compound consisting of glycan and peptides that is present in bacterial cell walls. Gram-negative bacteria possess a multi-layered membrane, with peptidoglycan being the sole constituent, as depicted in Figure 1.13.

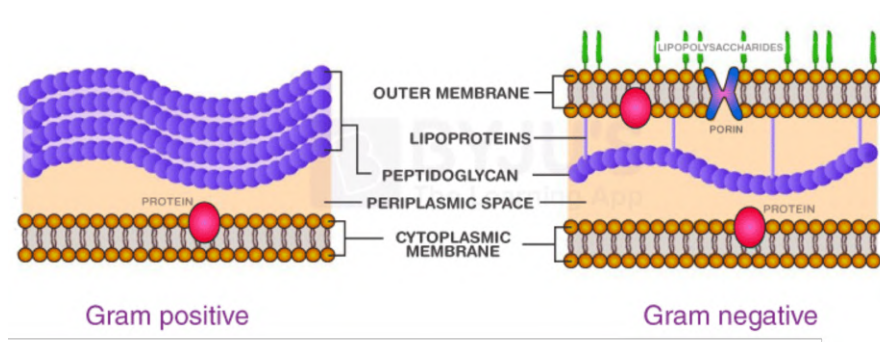


Figure 1.13: Schematics of the differences between Gram-positive and Gram-negative bacteria.

Gram-positive bacteria possess a single, thicker layer of peptidoglycan in their cell wall. Gram-positive bacteria typically exhibit greater resistance to physical assaults as a result of their

sturdier membrane structure. However, different types of bacteria might exhibit varying degrees of resistance to various sterilizing procedures. Bacteria are often rendered inactive at temperatures exceeding 55°C, whereas spores are capable of surviving at temperatures as high as 100°C, the reason why autoclaves operate at temperatures of around 121°C or higher. Similar patterns of behavior have been observed in relation to both UV radiation and chemicals. Spores exhibit greater resistance to plasma treatments, necessitating a longer duration for their inactivation. Nevertheless, conflicting findings have emerged about the difference in resistance to plasma treatments between Gram-positive and Gram-negative bacteria [122, 123]. Considering the distinctions between Gram-positive and Gram-negative bacteria, three specific bacteria have been chosen for examination in this study: *Escherichia coli*, *Bacillus subtilis* spores, and *Geobacillus stearothermophilus* spores.

***Escherichia coli* overview**

Escherichia coli, shown in Figure 1.14, is a bacterium that has a rod-like structure and is classified as Gram-negative. Additionally, it is responsible for the nomenclature of coliform bacteria, which are characterized as rod-shaped, Gram-negative, non-spore producing bacteria capable of lactose fermentation at specific temperatures. The typical size of each bacterium is about 1 – 3 µm in length. It is frequently present in the large intestine of endothermic animals, and the majority of the strains are benign and crucial for maintaining optimal digestive well-being. Nevertheless, certain serotypes possess harmful properties. They secrete toxins and have the potential to induce foodborne illness. *E. coli* is a highly researched organism in the fields of molecular biology and genetics due to its short duplication period (~ 20 minutes), which enables fast growth and convenient cultivation in laboratory environments. It is a widely studied and well-understood bacterium, serving as a model organism in microbiological research.

***Bacillus subtilis* spores overview**

Bacillus subtilis is a bacterium with a rod-shaped structure that is frequently present in soil and belongs to the Gram-positive group. The organism is widely used as a model in microbiology and has been extensively researched for multiple purposes, notably due to its capacity to produce resilient spores. The diameter of the bacterium usually falls between the range of 0.5 to 1 µm, while its length is normally between 2 and 5 µm. *Bacillus subtilis* has the ability to undergo sporulation, a process that is initiated by the absence of nutrients or other stressful conditions, resulting in the formation of spores. The process entails the conversion of the vegetative cell into a spore by a sequence of morphological alterations, finally resulting in the creation of a quiescent, exceedingly resilient spore. The organism is protected by multiple layers, namely the exosporium, spore coat, cortex, and inner membrane. The spore coat, specifically, enhances its resilience by offering extra protection against different environmental stresses. They have exceptional resistance to heat, desiccation, radiation, and chemical disinfectants. The spores possess a remarkable ability to endure adverse environments and



Figure 1.14: Low-temperature electron micrograph of a cluster of *E. coli* bacteria (source: [124]).

maintain their viability for prolonged durations. Their capacity to endure and withstand adverse circumstances renders them extremely significant in the examination of sterilizing procedures. *Bacillus subtilis* spores, along with *Geobacillus stearothermophilus*, are commonly employed as biological indicators in laboratories to assess the efficacy of autoclaving and other sterilizing techniques.



Figure 1.15: SEM image of *Bacillus subtilis* spores deposited on a monolayer membrane surface (courtesy of Anna Machkova).

***Geobacillus stearothermophilus* spores overview**

Geobacillus stearothermophilus is a bacterium that thrives in high temperatures environment. This organism is classified as Gram-positive and has the ability to produce spores, which enhance its ability to survive in harsh environments. Thermophiles are living beings that flourish in surroundings with high temperatures. *G. stearothermophilus* is commonly found in hot springs, compost heaps, and other places with increased temperatures. The bacterium is often elongated and has a rod-like shape, with dimensions that usually fall within the range from 2 to 5 μm in length. The spores of *G. stearothermophilus* are frequently employed as biological indicators to verify the efficiency of autoclaves and other sterilization techniques, guaranteeing their ability to eradicate extremely resilient spores.

2 Dielectric Barrier Discharges and Experimental Setup

In this chapter, we delve into the various aspects of the dielectric barrier discharges (DBDs) and experimental setup used for the work of this thesis. It outlines the design considerations, operational robustness, and components of different DBD configurations used in the experiments. Here's a brief summary of the key points covered in this chapter:

Section 2.1 discusses the surface dielectric barrier discharge (SDBDs) used for this work. The PCB-fingers SDBD is the first SDBD configuration designed for indirect bacteria treatments and laser-based diagnostics. However, humidity caused material deterioration and plasma disruption in this particular device, preventing correct operation. The perforated-disc SDBD is introduced as a solution to address material deterioration and reproducibility concerns encountered with the PCB-fingers SDBD.

In Section 2.2 we describe the volume dielectric barrier discharge (VDBD) configuration, focusing on its design, electrode geometry, and dielectric materials. This setup is specifically designed to explore the effects of direct plasma treatments and offers precise control over experimental parameters.

We then discuss the details of the custom-made nanosecond-pulsed high-voltage power supply used to power the plasma sources in Section 2.3. The range of the system and the typical waveform produced by the power supply.

Section 2.4 highlights the design and features of the sealed stainless steel cylindrical reactor used in this work. The reactor is versatile and can accommodate various applications, including bacterial treatments and spectroscopy diagnostics like LIF and FTIR. Sapphire windows and flanges are added to facilitate experiments, and adaptations are made for compatibility with FTIR measurements.

Finally, Section 2.5 explains how the gas flow system is crucial for maintaining precise control over the gas composition within the reactor. The components and the method used to produce precise relative humidity levels are presented.

2.1 Surface dielectric barrier discharges

As previously indicated in Section 1.1.3, surface dielectric barrier discharges (SDBDs) are typically planar devices designed to generate plasma uniformly on a surface. When the device is thoughtfully designed, it ensures homogeneous plasma distribution. This characteristic makes SDBDs particularly well-suited for indirect plasma treatments of biological specimens. Within the scope of this study, two distinct SDBD configurations were employed. The first configuration, identified as the PCB-fingers SDBD, served as the initial prototype for conducting indirect bacteria treatments and implementing laser-induced fluorescence diagnostics. However, the device exhibited sub-optimal performance in humid conditions, prompting us to explore alternative designs. This exploration culminated in the development of the perforated-disc SDBD, our second configuration. This new design incorporates distinct dielectric material and electrode configuration, rendering it a more robust and durable device suitable for prolonged plasma operation, especially in high humidity environments.

2.1.1 PCB-fingers SDBD

The PCB-fingers SDBD, illustrated in Figure 2.1, is constructed using a printed circuit board (PCB) with a disc-shaped structure measuring 74 mm in diameter, designed to comfortably fit within a standard 90 mm diameter Petri dish for biological treatments.

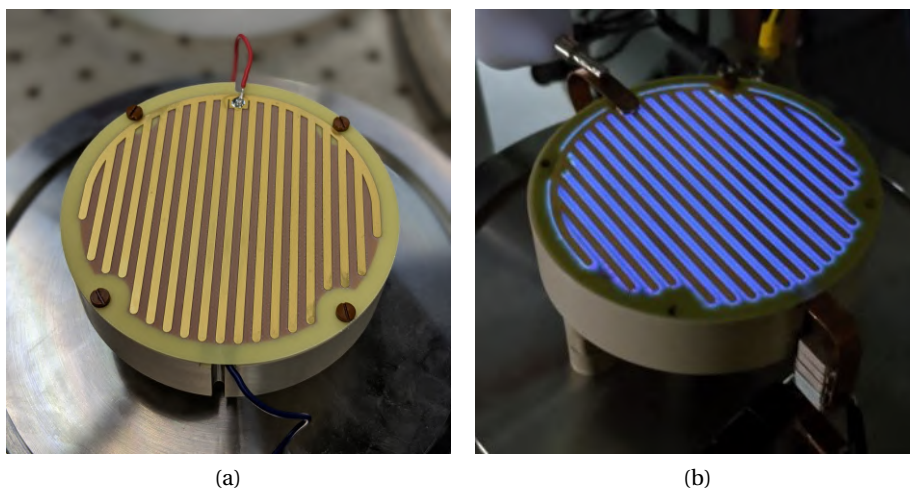


Figure 2.1: Pictures of the PCB-fingers SDBD (a) idle and (b) operating in air at 5 kV, 400 ns long pulses, 1 kHz repetition frequency.

The dielectric material utilized for the DBD is a 0.3 mm-thick FR4 glass fiber plate with no specific cleaning procedure. Both the high-voltage and grounded electrodes are fabricated from 0.1 mm-thick copper plating, treated with an electroless nickel immersion gold (ENIG) coating. This treatment involves nickel plating to facilitate soldering and a gold film coating to safeguard the copper electrodes from oxidation and corrosion. The high-voltage electrode is

configured as a connected array of flat fingers, each measuring 2 mm in width and spaced 2 mm apart. On the reverse side, the ground electrode is a round plate. The multi-finger design of the high-voltage electrode ensures the generation of a homogeneous plasma distribution over the entire surface. This feature enhances the uniformity and reproducibility of plasma treatments by covering the entire area of the Petri dish surface. Additionally, the symmetrical arrangement of the electrode fingers makes it well-suited for line-integrated diagnostics along the electrode direction, such as laser-induced fluorescence (LIF). The flatness of the electrode allows the laser beam to approach the plasma surface as closely as possible.

2.1.2 On the humidity issue and reproducibility

The selection of FR4 as the dielectric material was driven by several factors, including its capacity to endure high voltages and its excellent resistance to both heating and damage caused by electric arcs. In addition, the PCB-fingers SDBD is a commercially available product that, while easily procurable, presents challenges in terms of laboratory reproduction.

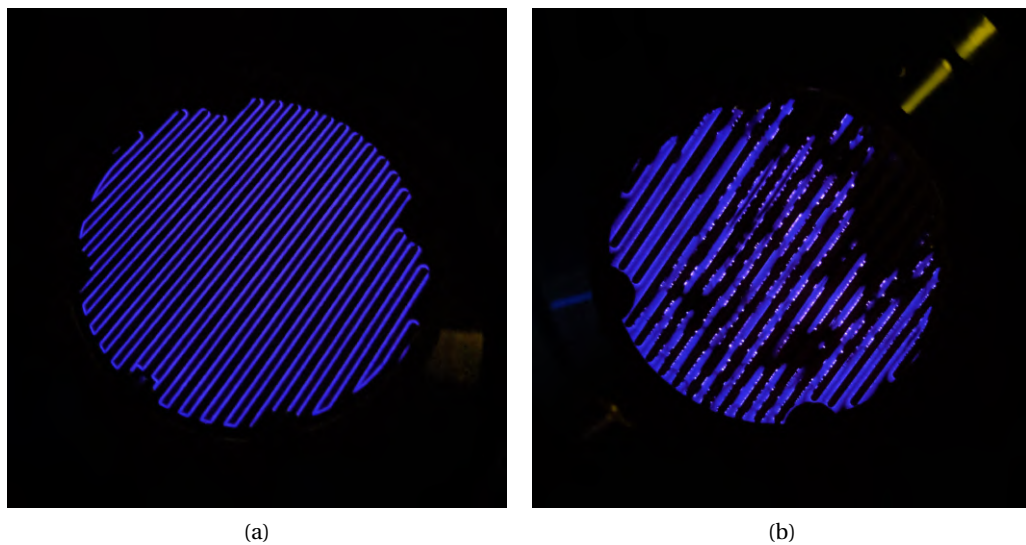


Figure 2.2: Pictures of the PCB-fingers SDBD plasma when operating correctly (a) and after ~ 1 hour of uninterrupted use in high humidity conditions (b).

However, as our work progressed, we encountered challenges related to the reproducibility of plasma treatments, described in detail in Section 5.1, stemming from issues with the DBD device itself. Subsequently, we identified a connection between these problems and an empirical observation: a gradual reduction in plasma brightness over time, as depicted in Figure 2.2, and the formation of a white oxidation layer around the edges of the metallic electrode. These effects were further investigated, and it was found that the SDBD was aging over time with prolonged use. It seemed to be mainly attributed to humidity, where the damage was either reversible or irreversible, depending on the experimental conditions. The effects of increasing humidity are shown in Figure 2.3 where exposure to 50% or more relative

humidity (RH) resulted in dimmer plasma with a patchy and non-uniform distribution of lights over the DBD surface.

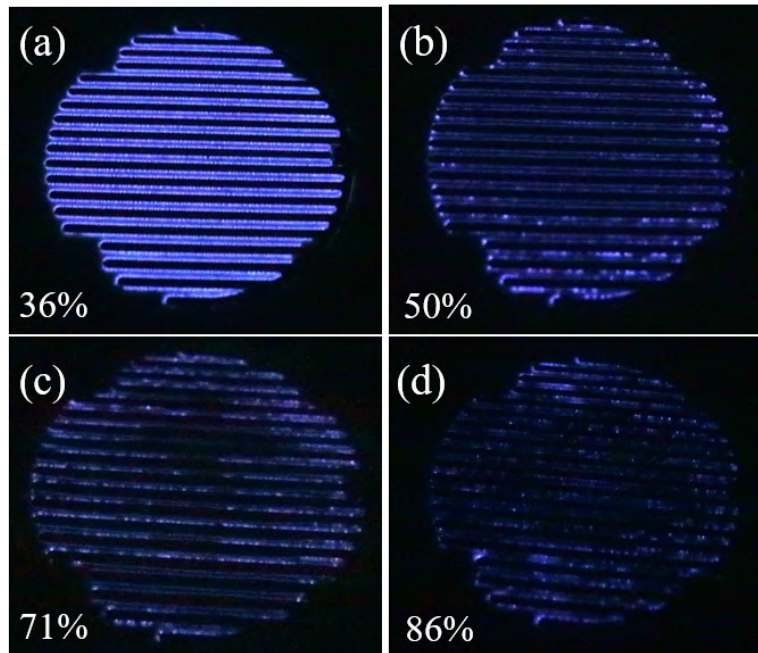


Figure 2.3: Photographs of the plasma visible emission after 30 minutes of continuous plasma operation at relative humidities of (a) 36% ambient air; (b) 50% ambient air; (c) 71% and (d) 86% (source: [12]).

The reduced performance in a humid environment can be attributed to both irreversible damage to the DBD caused by continuous plasma operation in high humidity conditions and reversible degradation of plasma performance. In our specific case, it's worth noting that FR4, which serves as the dielectric material, is inherently hygroscopic [125][126]. Moreover, the plasma surface activation further enhances the adsorption of moisture, exacerbating the effects of humidity on the system. The uncleaned, virgin FR4 exhibits only a mild hydrophilic nature. However, within a matter of minutes following exposure to SDBD plasma, the FR4 surface undergoes a significant modification, becoming highly hydrophilic. This change is observable when a water droplet is placed on the surface, spreading uniformly and covering the entire space between the electrodes, as illustrated in Figure 2.4, with a contact angle too small to be accurately measured.

In addition to the irreversible damage to the dielectric and electrodes due to continuous plasma operation, another reversible consequence of working in high humidity conditions is the formation of a thin water film atop the DBD's surface, preventing proper plasma ignition. Due to the involvement of humidity and the release of water content by biological targets in many applications of SDBDs, we have undertaken the task of designing and constructing a new SDBD to specifically tackle these challenges. There are several potential solutions to this issue, which vary depending on the specific requirements of the setup. Opting for better-performing

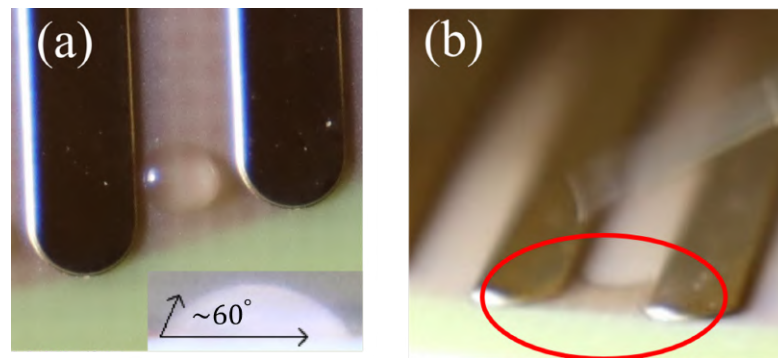


Figure 2.4: (a) A drop of water placed on the virgin FR4 dielectric has a contact angle of $\sim 60^\circ$, as indicated in the inset. (b) When a drop of water is placed onto the FR4 dielectric after 10 minutes of SDBD plasma operation, it spreads evenly over the FR4 surface between the electrodes, as indicated inside the red curve. A simple contact angle measurement is not possible in these conditions.

materials in high-humidity circumstances is the very first choice. Alumina, specifically, is a dielectric material that appears to be very resistant to humidity. Stainless steel is a highly durable material for the electrodes that exhibits greater resistance to plasma etching. The second countermeasure involves raising the temperature of the electrodes and dielectric by increasing the power supplied to the SDBD. In general, the most efficient approach in any situation is a hybrid dielectric barrier discharge (HDBD), achieved by elevating the patterned electrode above the dielectric surface. This would prevent the formation of a thin layer of water from negatively impacting the plasma ignition and enhance overall performance in high humidity conditions [12]. Within the context of this thesis, changing the materials and electrode arrangement and increasing the power delivered to the SDBD, proved to be enough to enhance the performance for the chosen experiments. The outcome of our efforts is the perforated-disc SDBD, a device characterized by a more 3-dimensional configuration and the utilization of different materials [12]. This design was specifically engineered to ensure operational robustness in high-humidity environments. The design of the perforated-disc SDBD is detailed in the next section.

Concerning the use of the PCB-fingers SDBD, we implemented two key measures to ensure the reliable operation of the SDBD and, consequently, the precise execution of experiments. Firstly, we restricted the operation of the PCB-fingers SDBD to environments characterized by low relative humidity (RH), specifically those with RH levels below 30%. Additionally, given that we possessed more than 100 identical copies of the PCB-fingers SDBD, we adopted a practice of periodic replacement after a certain duration of operation. This replacement was prompted by any evidence of electrode oxidation or surface degradation. These measures were put in place to uphold the dependable performance of the PCB-fingers SDBD and guarantee the reproducibility of the experiments.

2.1.3 Perforated-disc SDBD

The perforated-disc SDBD was specifically engineered to address the material deterioration concerns outlined in Section 2.1.2, which affected the PCB-fingers SDBD. In this new configuration, the high-voltage electrode is constructed from a flat stainless steel mesh with a 1 mm thickness. This mesh features electro-chemically perforated 2 mm square apertures, separated by 0.4 mm-wide steel strips. We utilize a 1 mm-thick alumina disc (Al_2O_3 99.6% purity) with an 81 mm diameter as a dielectric spacer.

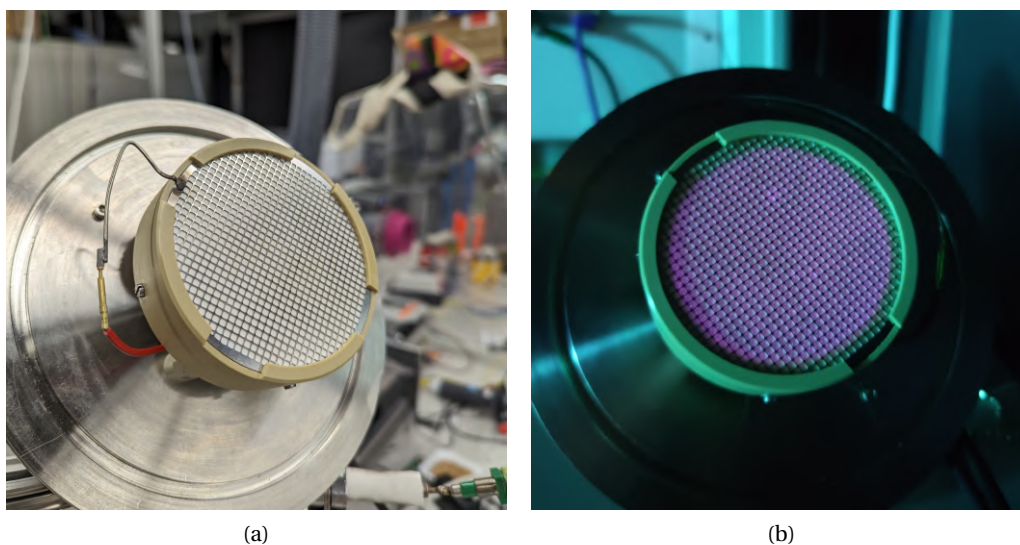


Figure 2.5: (a) Picture of the perforated-disc SDBD idle and (b) operating at 8 kV, 400 ns long pulses, at 1 kHz repetition frequency.

The perforated-disc SDBD has demonstrated superior resilience and efficiency in high-humidity environments [12]. Consequently, it has been employed as the plasma source for a plasma-activated water (PAW) reactor within the Bio-plasma lab at the SPC. The significance of this more robust device lies in its consistent performance over extended periods of time. Such stability is fundamental for enhancing the reproducibility of experiments conducted in the laboratory. The selection of materials and electrode layout alone is inadequate to ensure optimal performance in high-humidity environments. Therefore, in experimental setups where the relative humidity is greater than 70% RH, a power supply with increased power output is employed for the plasma discharge.

2.2 Volume dielectric barrier discharge

To explore the effects of direct plasma treatments, we designed and built a volume dielectric barrier discharge (VDBD). The configuration features a plate-to-plate round electrode geometry. The electrodes are circular stainless steel brass plates 20 mm in diameter. Each electrode is covered by a CoorsTek 99.5% alumina (Al_2O_3) ceramic plate 0.668 mm thick, used

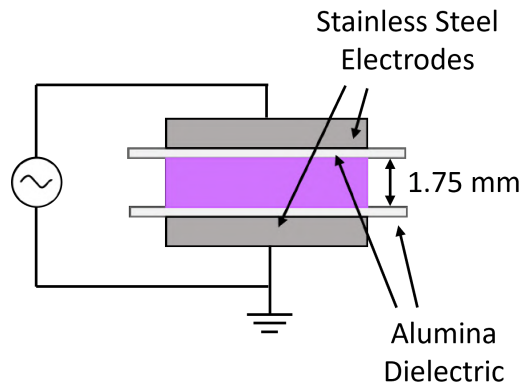


Figure 2.6: Schematic of the VDBD components.

as a dielectric barrier. The gaps between the electrodes and the ceramic plates are filled with a silicone adhesive (Model/Make) in the prototype used for the nanosecond-laser EFISH measurements, while for other prototypes we avoided any adhesive, and the electrodes are simply pushed against the alumina plates.

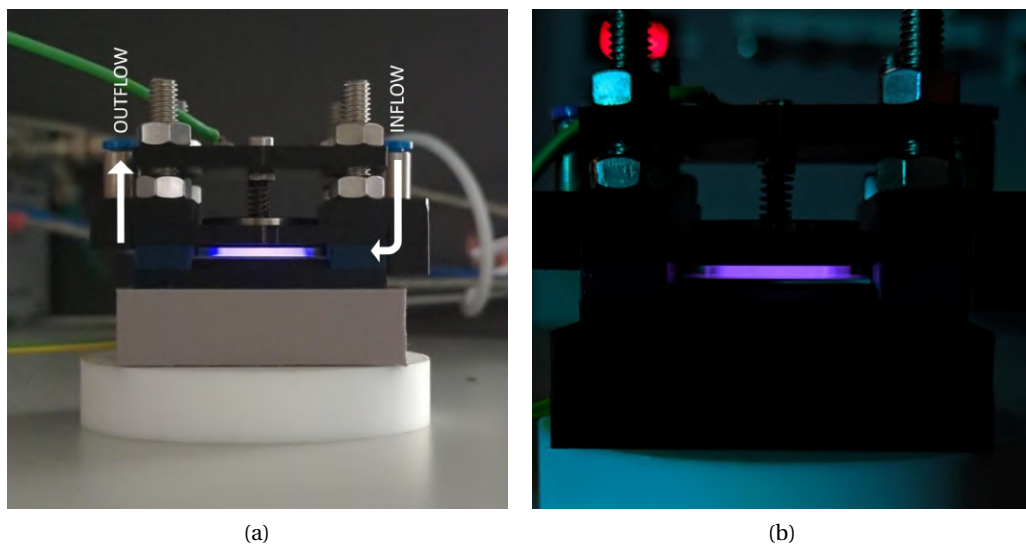


Figure 2.7: (a) Picture of the VDBD with the schematics of the inflow and outflow positions and (b) close-up of the plasma while operating at 12 kV, 200 ns long pulses, at 1 kHz repetition frequency.

The discharge gap, i.e., the distance between the ceramic plates, is 1.75 mm, with an uncertainty of $\sim 50 \mu\text{m}$ associated with the 3D printing precision. A 3D-printed structure is designed and built to keep the electrodes and dielectrics in place and to allow a gas flow to be injected very close to the plasma region, whose position is shown in Figure 2.7.

In addition, we developed an adapted version of the VDBD design, shown in Figure 2.8 using

3D-printed components specifically for conducting bacteria treatments.

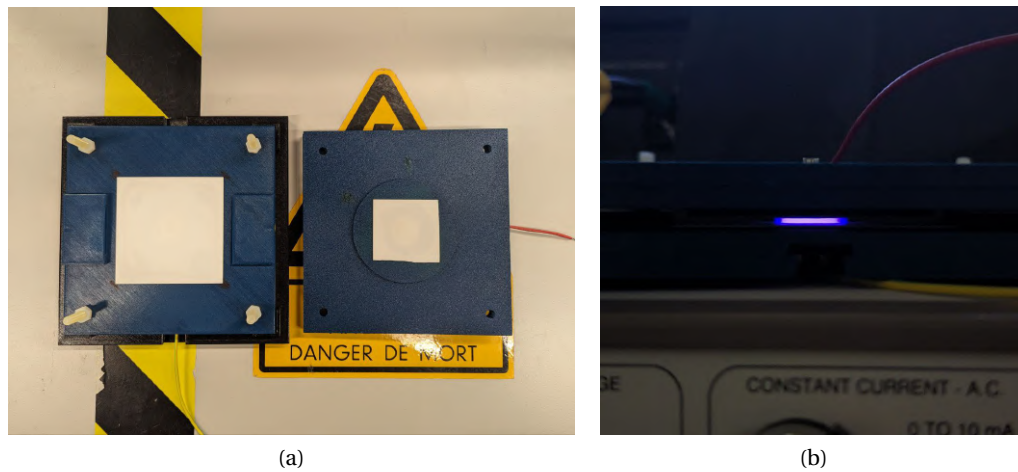


Figure 2.8: (a) Picture of the VDBD for the bacteria treatments from top and (b) close-up of the plasma while operating at 12 kV, 200 ns long pulses, at 1 kHz repetition frequency.

The fundamental parameters of this adapted VDBD are consistent with those used for all other measurements, including the use of the same materials, maintaining an identical air gap of 1.75 mm, utilizing electrodes with a diameter of 2 cm, and maintaining the same distance between the flow and the plasma discharge. However, for practical reasons, we opted for a larger dielectric plate to facilitate the placement of bacterial membranes. Additionally, we made design improvements to simplify the device's assembly and disassembly process, ensuring efficient access to the plasma discharge area while maintaining overall functionality.

2.3 Nanosecond-pulsed high-voltage power supply

The DBDs are powered by a custom-made nanosecond-pulsed high-voltage power supply, which was developed entirely at the Swiss Plasma Center (SPC) using off-the-shelf components. The underlying operational principle involves the switching of a DC power supply's output, buffered by capacitors, through the use of a specialized high-voltage switch. This power supply system can be divided into three main components, as represented in Figure 2.10: control, high-voltage, and switching. The control system is powered by a compactRIO (National Instruments cRIO-9063 [127]), an embedded controller for advanced control and monitoring applications. It is responsible for generating the pulse that triggers the high-voltage switch and provides synchronization signals for external devices. The cRIO-9063 controller features an FPGA (field-programmable gate array), a real-time processor running a Linux operating system (OS), and embedded user interface capability. Leveraging its FPGA capacities, the cRIO is capable of generating pulses as short as 50 ns. Furthermore, the cRIO controls the high-voltage power supply (Gp 250 146 10 CLD), capable of delivering voltages up to 25 kV, albeit at a current limit of 14 A. To allow the generation of current peaks, two high-voltage

capacitors have been integrated into the power supply's output. The core component of the system, a MOSFET push-pull switch from Behlke (HTS 241-20-GSM), plays a pivotal role in switching the voltage on and off with precise timing, as dictated by the cRIO. The repetition frequency of the pulses ranges from 100 Hz to 2 kHz.



Figure 2.9: Picture of the nanosecond-pulsed high-voltage power supply with visible emergency shut-down button on top.

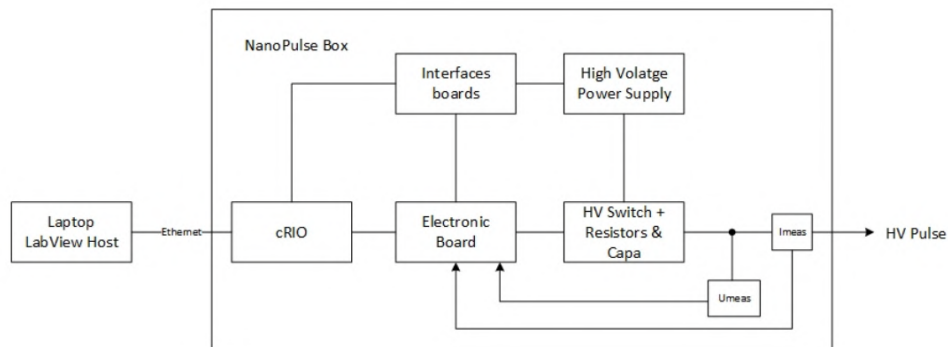


Figure 2.10: Block diagram of the electric circuit of the nanosecond-pulsed high-voltage power supply.

The maximum pulse length is limited by the chosen repetition frequency, and the rise time of the pulse is approximately ~ 50 ns. A summary of the range of the parameters of the nanosecond high-voltage pulses is presented in Table 2.1. For the full electrical schematics of the nanosecond-pulsed high-voltage power supply, please refer to the Appendix.

Table 2.1: Parameters range of the nanosecond high-voltage pulses.

	min	max
Voltage	-	25 kV
Pulse Length	50 ns	Limited by Pulse Frequency
Pulse Frequency	100 Hz	2000 Hz
Current Peak	-	14 mA

An example of a typical waveform generated by the nanosecond-pulsed high-voltage power supply is shown in Figure 2.11. The plasma discharges are shown as plasma emission in arbitrary units in correspondence of the rising edge and falling edge of the voltage pulse.

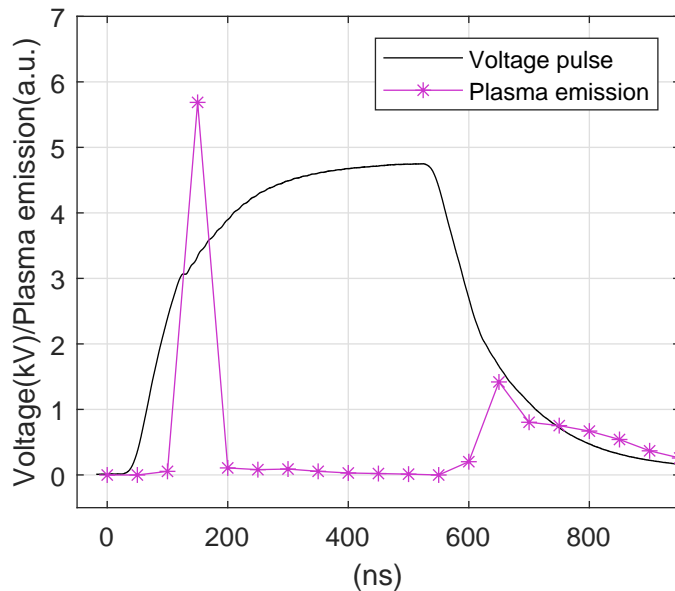


Figure 2.11: Example of a nanosecond pulse waveform generated by the power supply. The optical emission from the plasma is depicted in arbitrary units, with the two peaks corresponding to the two plasma discharges occurring with each pulse.

The power supply also serves as the master trigger for laser diagnostic experiments, generating three TTL (Transistor-Transistor Logic) trigger signals that can be utilized for external triggering of the laser. The time delay between these three TTL signals can be adjusted to control the energy of the laser pulse. This feature is applicable to the nanosecond-pulsed laser employed to the experiments conducted in Bari. On the other hand, the picosecond-pulsed laser used at SPC requires only a single trigger, with internal energy control. It's worth noting that the frequency of these triggers can be independently adjusted from the frequency of the nanosecond pulses to match the specific frequency requirements of the laser, 20 Hz for the ns-laser and 50 Hz for the ps-laser.

The front panel of the power supply, as depicted in Figure 2.12, includes six BNC output

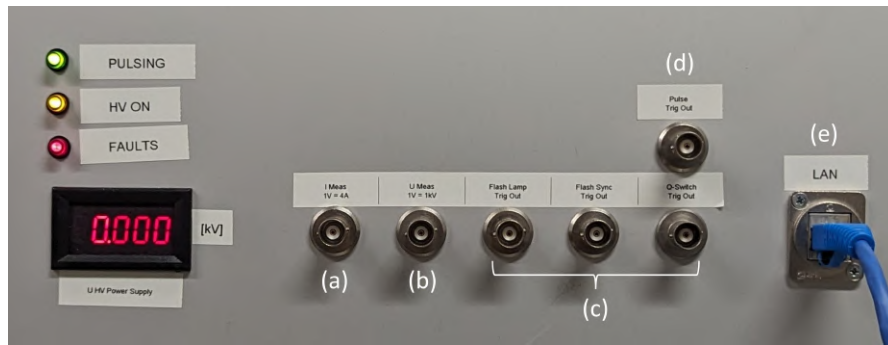


Figure 2.12: Front panel of the nanosecond-pulsed high voltage power supply. The labels are referring to (a) current monitor, (b) voltage monitor, (c) TTL triggers for laser synchronization, (d) reference pulse and (e) LAN port to laptop connection.

connectors. Two of these connectors are utilized for monitoring voltage and current, with measurements carried out internally using a Rogowski coil and a high voltage probe. The remaining four connectors are designated for various functions: three of them are TTL trigger outputs employed for laser synchronization, while the fourth serves as a reference pulse used to control trigger delays. Additionally, the power supply is equipped with an emergency shutdown button for safety purposes. The power supply is connected to a laptop via an Ethernet cable, and it is controlled through a LabVIEW interface. This user interface comprises two main panels: one panel allows the user to control the waveform parameters, including voltage, pulse length, and frequency, while the second panel enables the user to adjust the frequency and timing delays of the TTL trigger signals. Notably, the frequency of the trigger signals is adjusted as a ratio of the voltage pulse frequency.

2.4 Bio-plasma reactor

A sealed stainless steel cylindrical reactor was custom-manufactured by the mechanical workshop at SPC. The primary aim behind this reactor's design was to provide precise control over the environment surrounding the plasma discharge, while also allowing convenient access to the plasma itself. This reactor has been thoughtfully and purposefully designed to accommodate various applications, including bacterial treatments as well as diagnostics like LIF and FTIR spectroscopy. Both the CAD design and the physical realization of the reactor used in this study are depicted in Figure 2.13. The internal diameter of the reactor is 15 cm, resulting in an approximate volume of 2 liters. The reactor is equipped with eight lateral flanges that are symmetrically positioned to facilitate access to the plasma chamber.

For the LIF measurements, sapphire windows have been positioned at 90-degree angles. These windows allow the laser beam to enter and permit the fluorescence to exit the reactor, all while maintaining a sealed environment. Among the reactor's eight flanges, one is dedicated to measuring relative humidity and temperature through the use of a relative humidity probe (Vaisala HUMICAP HM42 [128]), while the other two flanges serve as gas inflow and outflow

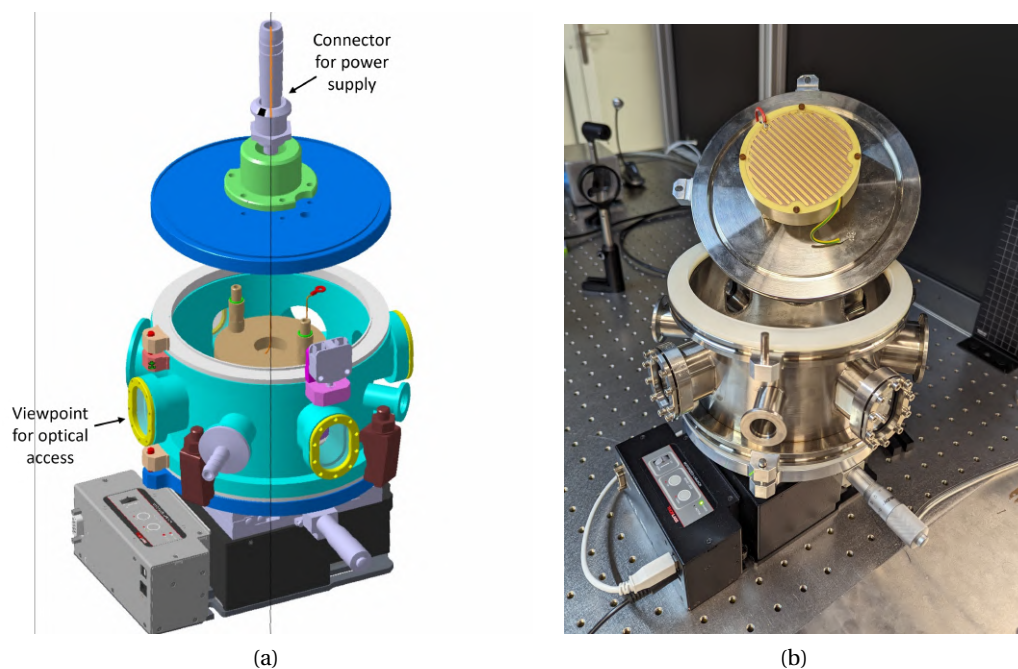


Figure 2.13: (a) CAD 3D drawing of the reactor, mounted on a motorized translation stage. (b) Actual reactor positioned on the optical bench, featuring the top lid upon which the PCB-fingers SDBD is mounted.

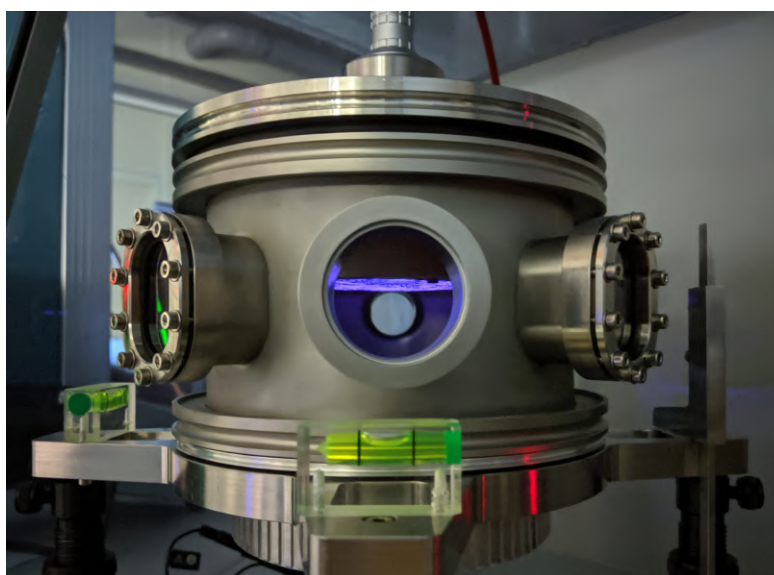


Figure 2.14: Picture of the closed bio-plasma reactor with the PCB-fingers SDBD operating inside, at ~ 5 kV, 400 ns long pulses, at 1 kHz repetition frequency.

ports. The SDBD is fixed to the top lid of the reactor thanks to a PEEK (Polyether Ether Ketone) support, as illustrated in Figure 2.13b. This top lid is additionally equipped with a high-voltage connector to power the DBDs with the nanosecond-pulsed power supply. When the reactor is

closed, the SDBD operates with the plasma surface directed downwards, as shown in Figure 2.14. Between the main body of the reactor and both the bottom and top lids, a nylon o-ring is employed to ensure an effective seal. The choice of a nylon o-ring over a standard rubber o-ring was made due to its superior resistance to deformation, which improves the position accuracy of the LIF measurements.

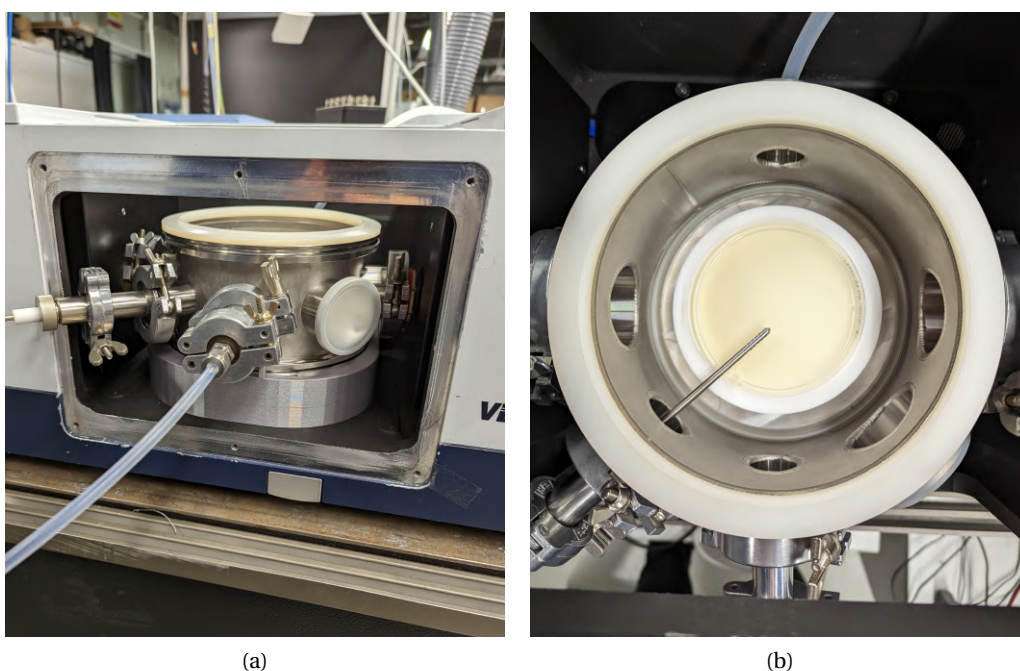


Figure 2.15: (a) Lateral view of the modified reactor positioned within the sample compartment of the FTIR spectrometer. (b) Top view of the modified reactor inside the sample compartment. It is possible to notice the 2 missing flanges, a Petri dish in the middle and the tip of the relative humidity probe on the left-bottom flange.

Various versions of the bio-plasma reactor have been designed and developed to satisfy specific experimental requirements. Notably, a modified version of the reactor, shown in Figure 2.15, has been created specifically for FTIR measurements to facilitate the passage of the whole infrared beam through the reactor. To accommodate these changes, two opposite round flanges have been expanded to accommodate the installation of appropriate windows. Additionally, the number of flanges on the reactor has been reduced, as the sample compartments of the FTIR spectrometer do not allow access on one side, as depicted in Figure 2.15. These adjustments were made to optimize the reactor's compatibility with FTIR experiments.

2.5 Gas flow system

As emphasized in Section 2.1.2, relative humidity significantly impacts both the proper operation of plasma sources and the reproducibility of experiments. Therefore, it is imperative to

consistently monitor and control RH levels throughout experiments to establish correlations between observed variations and fluctuations in relative humidity. This practice is crucial for conducting accurate experiments.

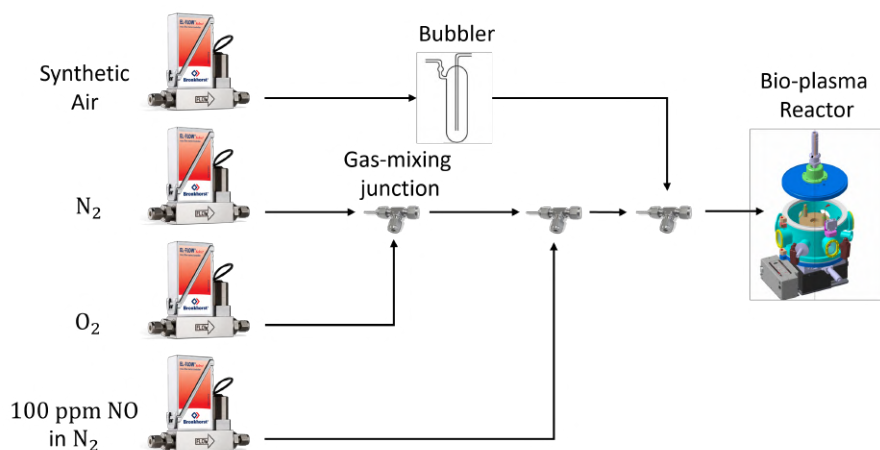


Figure 2.16: Schematics of the gas flow system.

To maintain precise control over the gas composition within the reactor, a gas flow system has been incorporated, as depicted in Figure 2.16.

The gas flow is meticulously regulated through the use of three Bronkhorst mass flow controllers: one for pure nitrogen (N₂), one for pure oxygen (O₂), and one for dry synthetic air (80%/20% N₂/O₂). The mass flow controllers feature an accuracy of 1% of their maximum flow rate, which amounts to 30 sccm for the N₂ mass flow controller (with a maximum flow of 3000 sccm), and 10 sccm for both the O₂ and dry synthetic air mass flow controllers (with a maximum flow of 1000 sccm). Highly accurate flow measurements with minimal uncertainties are crucial for maintaining precise and reliable flow conditions across diverse experimental configurations. To introduce humidity into the synthetic air, a specialized approach is adopted. Dry synthetic air is injected into a bubbler filled with deionized water, as shown in Figure 2.17. This process results in the generation of saturated humid synthetic air, which is carefully controlled to maintain a consistent level of humidity in the gas mixture. To optimize the mixing of gases with differing flow rates, dedicated Bronkhorst gas-mixing junctions are employed. This method ensures the precise and reliable evaluation of relative humidity changes within the gas mixture. On occasion, an additional Bronkhorst mass flow controller is utilized to introduce nitric oxide (NO) into the gas mixture used for calibrating the laser-induced fluorescence measurements. The nitric oxide is contained within a N₂ bottle at a concentration of 100 ppm (parts per million). Consequently, the mass flow controller is configured for nitrogen gas, as it serves as the carrier gas for the introduction of nitric oxide into the mixture.

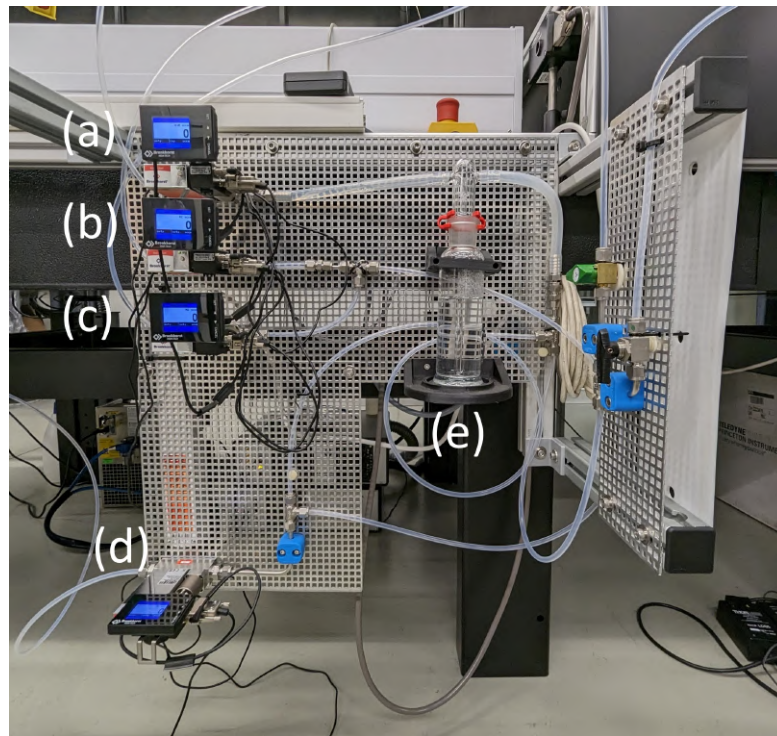


Figure 2.17: Picture of the actual gas flow system with mass flow controllers for (a) synthetic air, (b) oxygen, (c) nitrogen, and (d) N_2/NO . The crucial component of the gas flow system is the (e) bubbler, where the dry air increase its humidity content by passing through it.

2.6 DBDs prototypes

Besides the SDBD and VDBD described in Section 2.1 and 2.2, other DBDs were used during this project. Some of them are part of the process to improve the operational parameters of the device and overcome the humidity issue, others were used for other projects in the Bio-Lab.

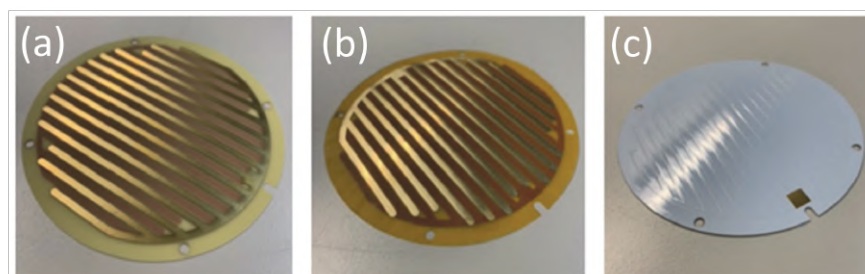


Figure 2.18: PCB-fingers SDBD prototypes. The only difference between the three of them is the material used for the dielectric: (a) FR4, (b) Kapton and (c) solderresist.

The PCB-fingers SDBD was produced in series, together with other two prototypes. The configuration of the electrodes is identical, while the dielectric material is different. The second prototype (Figure 2.18(b)) uses Kapton, while the third prototype (Figure 2.18(c)) uses

solderresist.

Another set of commercially available SDBDs was purchased and used, specifically for plasma treatments of seeds [129]. The DBDs are Sihon Electronics devices with different electrode configurations: mesh (Figure 2.19(a)), stripes (Figure 2.19(b)), and honeycomb (Figure 2.19(c)). The materials used for these DBDs are alumina for the dielectric and stainless steel for the electrodes. The dimensions of these rectangular-shaped SDBDs are $9 \times 4 \text{ cm}^2$.

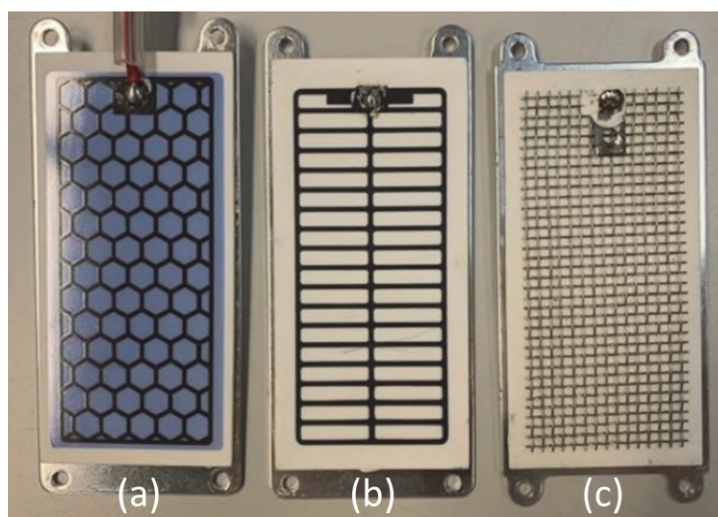


Figure 2.19: Sihon Electronics SDBD prototypes. The only difference between the three of them is the electrode configuration: (a) honeycomb, (b) stripes and (c) mesh.

3 Physical Characterization: Plasma Discharge Power

This chapter delves into the measurements of the power dissipated in the plasma generated by the DBDs used in this thesis. Physical characterization of the low-temperature plasma discharge, particularly in the context of bacteria treatments, is of paramount importance. In this case, physical characterization primarily entails electrical characterization because the two most crucial physical parameters in low-temperature plasma discharges for biological applications are the power of the plasma discharge and the electric field generated within the plasma. To quantify these parameters, the Lissajous figures method, described in this chapter, and the electric field-induced second harmonic (EFISH) generation technique, presented in Chapter 4, have been employed. These measurements highlight the significance of considering the impact of the biological target on the plasma discharge. Therefore, characterizing real-life scenarios rather than ideal ones is of paramount importance.

In Section 3.1, a concise overview of the techniques employed to quantify the power of an electrical system is presented. The discussion revolves around the factors to consider while attempting to quantify the power dissipated in the plasma as opposed to the power dissipated in the circuit itself.

Next, in Section 3.2, we present an overview of the Lissajous figures technique for measuring power dissipation in plasma discharges. We explain the underlying theory, discuss different types of Lissajous figures, and highlight the difficulties associated with these measurements, particularly when working with nanosecond-pulsed powered DBDs.

In the following sections, we will discuss the experimental setup used for measuring Lissajous figures (Section 3.3), and show the power measurements of the DBDs used in this thesis, as well as other DBDs utilized in the Bio-lab (Section 3.4). Finally, a brief summary highlighting the results of this chapter is presented.

3.1 Plasma discharge power measurements

One of the paramount factors to consider in the context of biological applications of LTPs, and plasmas in general, is the power dissipated in the plasma, or plasma discharge power. A common approach for electrical power measurement involves the use of the voltage-current product $P(t) = V(t) \cdot I(t)$ [57, 130], otherwise called the shunt resistor method or V-I method, to obtain the average power dissipated in a circuit:

$$\bar{P} = \frac{1}{T} \int_0^T V(t)I(t)dt, \quad (3.1)$$

with T being the period of the voltage waveform. However, when dealing with plasma, the complexity of the system increases, necessitating the consideration of various factors if one wishes to employ this method effectively. First and foremost, it is essential to account for the rapid nature of plasma microdischarges. While it is possible to achieve spatially uniform discharges in DBDs under specific conditions [131, 132, 133, 134], filamentary discharges are more common under typical circumstances [135]. These filaments are inherently self-limiting since they charge the dielectric surface and locally neutralize the gap voltage, leading to their extinction within typically 10^{-7} seconds.

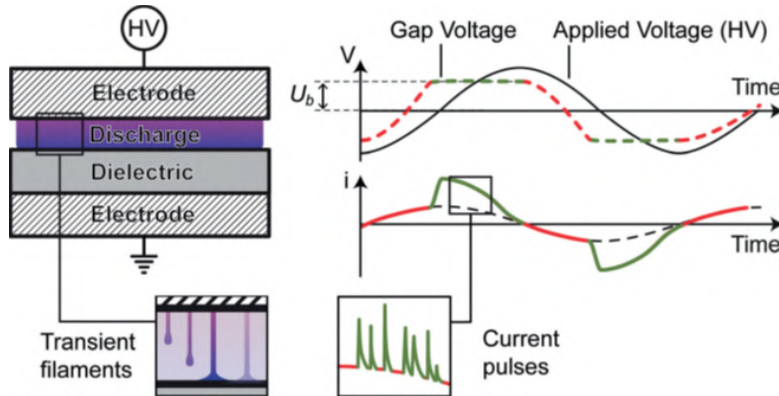


Figure 3.1: Schematic representation of a DBD with one electrode covered by a dielectric. On the right-hand side, current and voltage characteristics are depicted. In practical terms, the plasma within the DBD system exhibits filamentary behavior, consisting of discrete filaments with durations on the order of $< 10^{-7}$ seconds, separated both in space and time. This characterization deviates from the simplified electrical model which assumes continuous current and a constant gap voltage U_b during discharge (source: [136]).

Not only are the filaments randomly spatially distributed over the surface, they also manifest over a broad time frame. For instance, in the case of a DBD driven by a sinusoidal external voltage at a frequency of 100 kHz, filaments ignite over approximately $\sim 3 \mu\text{s}$ during each half-cycle, at various phases of the external voltage waveform [137]. Consequently, when measuring the current during plasma discharge, one must employ a current probe and oscilloscope capable of time-resolving the microdischarges spikes, as shown in Figure 3.1. The accuracy of

the shunt resistor method may be compromised due to the low signal-to-noise ratios of the oscilloscopes used, coupled with the wide dynamic range of the current spikes [138]. Another challenge arises from the fact that the current during the plasma ON phase comprises both capacitive current and plasma-generated current. Therefore, it is imperative to subtract the capacitive current component to obtain only the power dissipated in the plasma. Ideally, the capacitive current can be measured in isolation when the plasma is in the OFF state. Nevertheless, it can be challenging to measure the capacitive current under precisely the same conditions, including voltage, air gap, and gas composition, as during the plasma ON phase.

Despite these challenges, in particular setups and with appropriate precautions, the V-I method proves to be as effective as another, more reliable technique, like Q-V plots, otherwise called Lissajous figures [139]. This method, developed in 1943 by Manley for ozone generators, is still widely accepted in research and technology. Nonetheless, discrepancies have emerged between measurements obtained through these two methods, particularly in the case of nanosecond-pulsed single-electrode SDBDs, or actuators [130]. For this reason, and considering the reliability of the Lissajous figures method, we chose to compute the plasma discharge power of our DBDs using this technique, which is detailed below.

3.2 Introduction to Lissajous figures

A Lissajous figure is a graphical representation of the charge-voltage (Q-V) relationship, which is constructed by plotting the voltage, $V(t)$, across the electrodes of the DBD against the corresponding accumulated charge $Q(t)$ on a monitoring capacitor placed in series with the DBD on the ground side of the circuit, as represented in Figure 3.2.

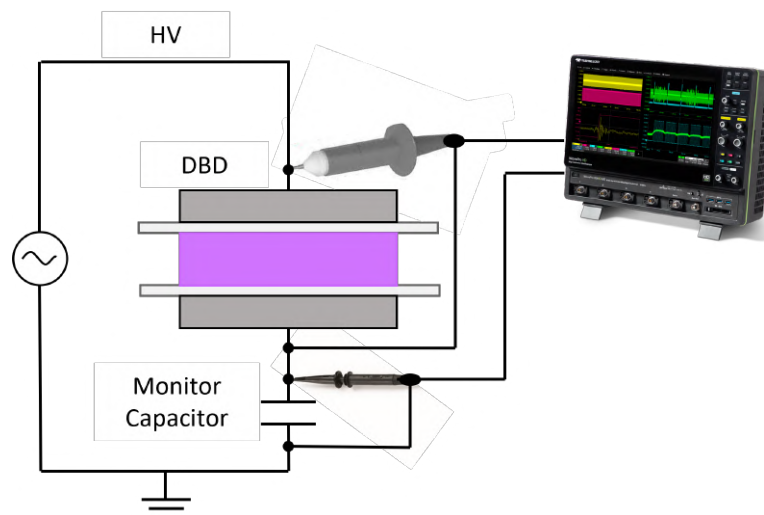


Figure 3.2: Schematic of the circuit used to generate the Lissajous figure of a DBD using a monitor capacitor.

To ensure accurate measurements, it is recommended to use a calibrated high voltage probe,

typically with a 1000:1 attenuation ratio, and connect it as closely as possible to the electrodes. Simultaneously, the voltage on the monitoring capacitor with capacitance C_m , placed between the DBD and the ground, is measured using a standard oscilloscope probe with a 10:1 attenuation ratio. The instantaneous voltage, $V_m(t)$, across the capacitor can be converted into the instantaneous charge, $Q(t)$, on the monitor capacitor by applying the relationship described in Equation 3.2.

$$Q(t) = C_m V_m(t) \quad (3.2)$$

An ideal Lissajous figure is characterized by a parallelogram shape, as schematically depicted in Figure 3.3. Depending on the DBD and waveform, deviations from this ideal shape can occur. However, the fundamental principles of analysis remain consistent across all types of Lissajous figures.

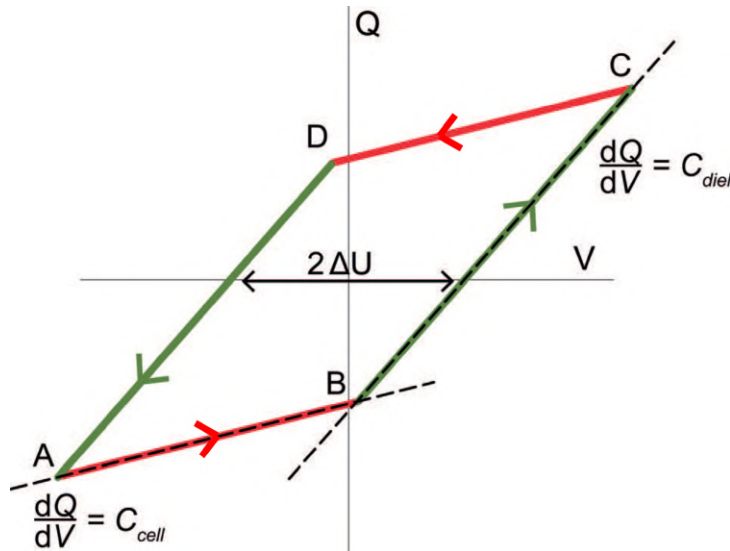


Figure 3.3: Ideal Lissajous Figure exhibiting a distinctive parallelogram shape. The 'plasma off' segments are highlighted in red, while the 'plasma on' segments are indicated in green. Directional arrows within the green segments represent the progression of time. Further details regarding the symbols utilized in this figure are elaborated upon in the main text (source: [136]).

The simplest case involves parallelogram-shaped Lissajous figures, where the different phases of the plasma discharge cycle are clearly distinguishable through various line segments, such as AB, BC, CD, and DA in Figure 3.3. This shape is usually obtained from a parallel plate VDBD powered by an AC sinusoidal voltage. There are two "plasma off" phases (AB and CD in Figure 3.3) and two "plasma on" phases (BC and DA in Figure 3.3). During the "plasma off" or capacitive phase, the DBD behaves as if it consists of two capacitors connected in series. These capacitances stem from the dielectric layer, denoted as C_{diel} , and the gap containing the discharge gas, known as C_{gap} . Both of these elements can store electric charge, whether

it's from an applied voltage or charges accumulated due to a plasma discharge. To obtain the overall capacitance of the "DBD cell," denoted as C_{cell} , considering these two components (C_{diel} and C_{gap}), Kirchoff's laws are applied, resulting in the following relationship:

$$\frac{1}{C_{cell}} = \frac{1}{C_{diel}} + \frac{1}{C_{gap}}. \quad (3.3)$$

The capacitances C_{cell} and C_{diel} can be determined from the characteristics of an ideal Lissajous figure. Since $C = dQ/dV$, the slopes of the lines AB, BC, CD, and DA in Figure 3.3 correspond to constant capacitance values.

For lines AB and CD in the Lissajous figure, which represent the capacitive phase (i.e., when the plasma is off), the slope corresponds to C_{cell} . In the absence of a plasma in the gap, the only path for current flow is through the capacitive elements C_{diel} and C_{gap} . Conversely, the slopes of lines BC and DA, corresponding to the discharging phase (i.e., when the plasma is on), are typically identified as C_{diel} [139]. This is often explained qualitatively as the microdischarges "bridging the gap", effectively nullifying the C_{gap} term so that $C_{cell} = C_{diel}$ in Equation 3.3. However, this perspective suggests that the voltage drop across the gas gap, represented as U_{gap} , immediately decreases to zero as soon as even a single microdischarge ignites anywhere in the gap. In the case of parallelogram-shaped Lissajous figures, the process of extracting discharge properties is relatively straightforward. However, for other shapes resulting from different waveforms and DBD configurations, the derivation of discharge properties becomes more cumbersome. In the context of this thesis, the Lissajous figure method was exclusively employed to measure the power dissipated in the plasma discharge.

3.2.1 Plasma discharge power derivation from Lissajous Figures

A widely adopted application of Lissajous figures is the determination of active power dissipated in the discharge, which is achieved by calculating the area enclosed by the hysteresis loop [138]. While some literature provides equations for power calculation based on the geometric characteristics of the Lissajous figure, assuming an ideal parallelogram shape [139, 140], it's important to note that depending on the waveform and DBD configuration, this ideal behavior can easily change. To provide a comprehensive understanding, we will establish the relationship between area and average power, applicable to Lissajous figures of any shape. By differentiating Equation 3.2 with respect to time, the current passing through the monitor capacitor, denoted as $i_m(t)$, is given by:

$$i_m(t) = C_m \frac{dV_m(t)}{dt} = i(t), \quad (3.4)$$

where $i(t)$ is the current flowing in the DBD. The final equality arises from the principle of current continuity within the series circuit comprising the DBD and the monitor capacitor, as

illustrated in Figure 3.2. Subsequently, the instantaneous power, denoted as $P(t)$, within the DBD, can be expressed as:

$$P(t) = V(t)i(t) = V(t) \cdot C_m \frac{dV_m(t)}{dt}. \quad (3.5)$$

The time-averaged power, denoted as \bar{P} , can be computed by integrating Equation 3.5 with respect to time and substituting the charge relationship given in Equation 3.2:

$$\bar{P} = \frac{1}{T} \int_0^T V(t) \cdot C_m \frac{dV_m(t)}{dt} dt = \frac{1}{T} \int_0^T V(t) \cdot C_m dV_m(t) = \frac{1}{T} \oint_0^T V(t) dQ(t). \quad (3.6)$$

This expression demonstrates that the average power dissipated over a complete discharge cycle is determined by the area enclosed by the Lissajous figure, multiplied by the frequency of the discharge cycle $f = 1/T$. When employing numerical techniques to evaluate this integral, it is crucial to ensure that the integration of the acquired data is carried out over precise multiples of the discharge time T . Failing to do so would result in the reactive power in the capacitive portions of the circuit not averaging out to zero.

3.2.2 Monitor capacitor selection

To effectively apply the Lissajous figures method, it's crucial to choose a suitable monitor capacitor. The selection of the monitor capacitor depends on the capacitance of the DBD, C_{cell} . The capacitance of the monitor capacitor C_m should significantly exceed the capacitance of the DBD, meaning $C_m \gg C_{cell}$. As a general guideline, a ratio of $C_m : C_{cell}$ ranging from 100:1 to 10,000:1 is typically suitable [136]. As long as $C_m \gg C_{cell}$, nearly all the voltage applied to the DBD and monitor capacitor falls across the DBD. This setup also prevents the monitor capacitor from being exposed to high voltages. Nevertheless, Equation 3.3 reveals that if C_m is excessively large compared to C_{cell} , the voltage across the monitor capacitor's amplitude will become very small. This can result in a low signal-to-noise ratio, which may pose problems, especially when the oscilloscope has a minimum range of 20 mV full scale or if the noise level is elevated. When dealing with potential noise caused by microdischarges or fast-rising voltage pulses, such as in nanosecond-pulsed waveforms, it's advisable to select a smaller capacitor. This choice can help enhance the signal-to-noise ratio, making it easier to discern and accurately measure the relevant signals. In summary, choosing an appropriate capacitance value requires careful consideration of the trade-off between achieving a favorable signal-to-noise ratio and minimizing the impact of the monitor capacitor on the electrical circuit. While the selection of a relatively low voltage capacitor (in the range of 100–250 V) is often motivated by robustness, adjusting the capacitor size in response to specific noise characteristics and signal requirements can significantly improve the accuracy and reliability of the measurements in such challenging conditions.

In terms of capacitor type, class 1 ceramic capacitors are preferable due to their relatively low parasitic capacitance, providing greater accuracy and stability when used in resonant circuits, which both DBD systems and measurement circuits represent. Whenever possible, measuring the capacitance of the monitor capacitor and the assembled monitoring circuit with an LCR meter is recommended, as measured values may deviate from those provided by the manufacturer. The monitoring circuit can introduce additional capacitance, introducing further inaccuracies in determining the absolute value of $Q(t)$. An alternative to using a monitor capacitor is to measure the voltage across a shunt resistor or an inductive Rogowski coil in place of a monitor capacitor, as already mentioned in Section 3.1. This method relies on the direct measurement of current $i(t)$ from the DBD to ground, eliminating the need to integrate current on a capacitor. Time-integration of $i(t)$ can then be used in post-processing to obtain $Q(t)$. However, this approach, especially in the presence of fast-rising currents in the sub-nanosecond range associated with filamentary discharges, demands a high bandwidth measurement system and a high sampling rate to avoid measurement errors. The advantage of integrating on a capacitor is that it ensures no charge moving through the DBD is missed, even with a low bandwidth (and sampling rate) of the probe plus oscilloscope, enabling more accurate power measurements.

3.2.3 Almond-shaped Lissajous figures of SDBDs

While parallelogram ideal Lissajous figures are typically measured in plate-to-plate VDBDs, almond-shaped Lissajous figures, are commonly observed in SDBDs, particularly when high dielectric constant materials are used [141, 142]. The striking difference between the two configuration is illustrated in Figure 3.4.

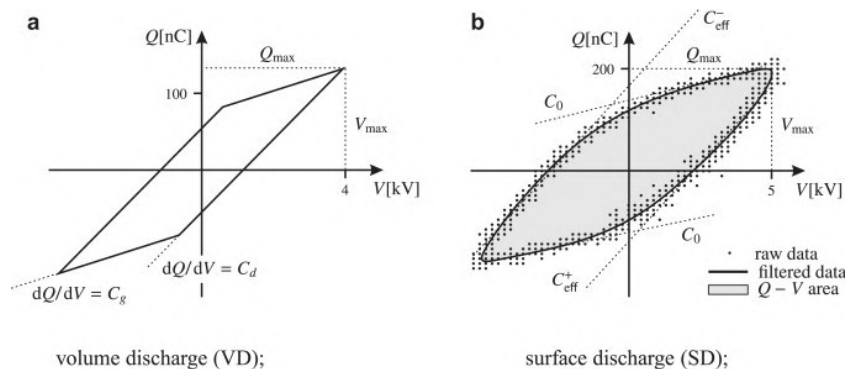


Figure 3.4: Example of characteristic Lissajous figures shape for (a) VDBDs and (b) SDBDs (adapted from [142]).

In a plane-parallel VDBD configuration with uniformly spaced gas gaps, the ignition voltage for the plasma, known as the burning voltage, or breakdown voltage, U_b , remains relatively constant during the discharging phase, leading to straight lines in the Lissajous figures. However, in discharges with non-uniform gap widths like SDBDs, plasma can ignite across a wide range of gap voltages, as the breakdown criterion varies. This allows the plasma to expand

across the available dielectric area during the discharge phase, as shown in Figure 3.5.

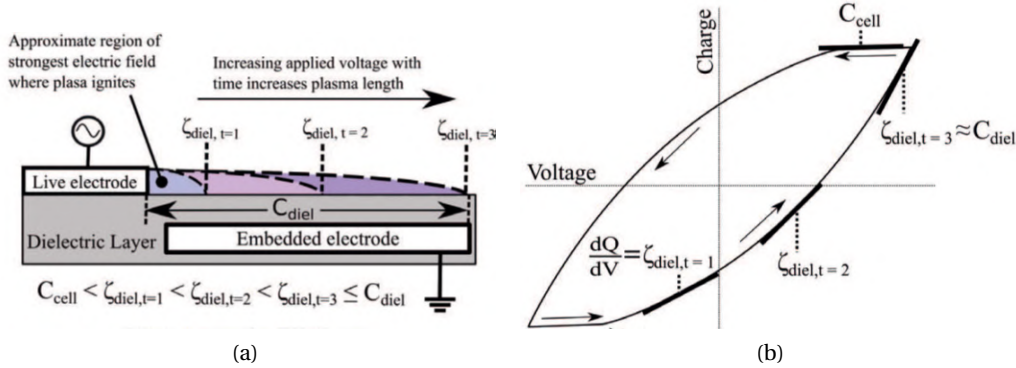


Figure 3.5: (a) Graphical representation of the plasma expansion across the available dielectric surface with increasing applied voltage in a SDBD. (b) Resulting Lissajous figure with corresponding capacitance of the system at different timings of the plasma discharge expansion (adapted from [136]).

In plasma actuators and SDBDs in general, as shown in Figure 3.5, the electric field is initially strongest at the minimum distance between the two electrodes. As the applied voltage increases during the AC cycle, discharging begins at the point with the highest electric field strength (where the breakdown criterion is met first) and gradually spreads across the electrode's surface as the breakdown criterion is met for wider gaps. During this plasma expansion, the fraction of the surface area that actively participates in the discharge increases resulting in a larger gap capacitance C_{gap} and dielectric capacitance C_{diel} . This leads to an effective capacitance during discharging, denoted as $\zeta_{diel,t}$, which grows over a half-cycle, as seen in Figure 3.5. Once the dielectric area charged by the plasma reaches its maximum, the Lissajous figure's line gradient becomes steepest. However, once the applied voltage $V(t)$ reaches its maximum, no further discharging can occur because electric field strengths start to decrease everywhere in the gas gap, and no more breakdown criteria are met. This results in the sharp apex at the maximum and minimum voltage points on the Lissajous figure.

3.2.4 Nanosecond-pulsed Lissajous figures

The rapid rise time characteristic of nanosecond-pulsed plasma discharges presents significant challenges when using Lissajous figures to measure the plasma discharge power. This swift rise time substantially amplifies the impact of stray capacitance within the circuit. The stray capacitance primarily arises within the cable loops connecting the voltage probes to both the monitor capacitor and the DBD. This undesired capacitance contributes to elevated noise levels in the voltage measurements applied to the DBD, with the effect being particularly notable in the voltage readings acquired from the monitor capacitor. To mitigate the noise resulting from stray capacitances, the most effective approach is to minimize cable length, particularly in areas where circuit loops may form. This necessitates the use of the shortest

possible cables between the DBD and the monitor capacitor, as well as between the monitor capacitor and the ground. Additionally, it is advisable to connect the voltage probe as close as possible to the capacitor to minimize the creation of large loops. Furthermore, considering that the signal amplitude across the monitor capacitor is determined by its capacitance, as elaborated in Section 3.2.2, it is advisable to opt for a smaller capacitor. This choice can serve to enhance the signal's amplitude, subsequently improving the signal-to-noise ratio. These precautions should suffice to enhance the signal quality, allowing for post-processing through techniques such as smoothing or filtering to further refine and clean the signal.

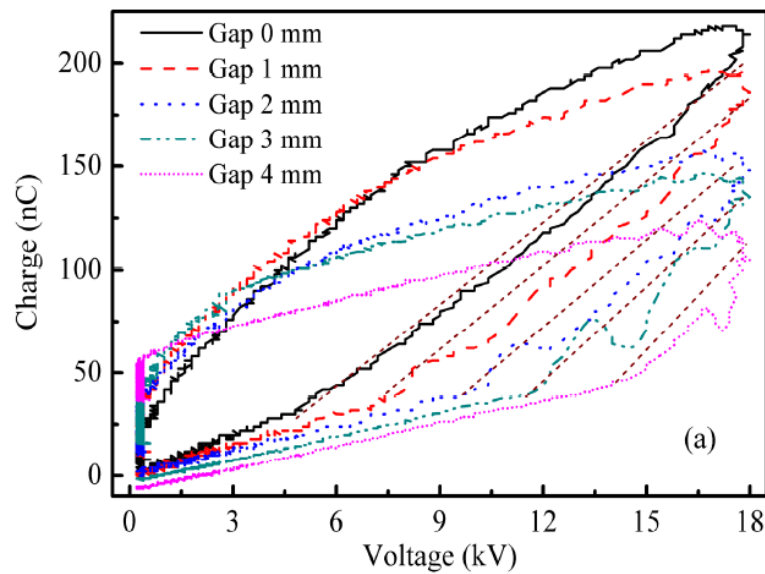


Figure 3.6: Example of Lissajous figures of a nanosecond-pulsed actuator (an SDBD with a single electrode), for different gaps between the ground and HV electrode (source: [130]).

A secondary issue pertains to the synchronization of signals, specifically, of the charge, $Q(t)$, and voltage on the DBD, $V(t)$. Given that the timescale of the HV pulse in nanosecond-pulsed plasma discharges is significantly shorter than that of lower frequencies AC-powered discharges, even a minor discrepancy of the order of few nanoseconds between these signals can introduce substantial errors in the power estimate. To address this concern, it is imperative to calculate and account for the time delay between the probes during power measurements. It is important to note that in most cases, accurately determining the probes delay between each other remains uncertain, introducing potential inaccuracies in signal synchronization. Therefore, it is crucial to acknowledge the possibility of synchronization errors when using this method for nanosecond-pulsed DBDs. Even after implementing the precautions mentioned above, it is essential to recognize that the results may still exhibit noise. Consequently, extracting discharge properties from the Lissajous figures should be approached with caution, as discussed in [143].

3.3 Experimental setup and data analysis

In this work, the power of each DBD utilized was determined using Lissajous figures. The experimental setup employed for these measurements did not change, with the exception of the monitor capacitor used to gauge the charge transferred within the DBD. As discussed in Section 3.2.2, selecting the appropriate value of the capacitance for the monitor capacitor is crucial to achieve an optimal signal-to-noise ratio, while minimizing alterations to the circuit. Consequently, depending on the capacitance of the DBD being utilized, a corresponding capacitor was chosen. We used exclusively polyester capacitors or ceramic capacitors like the ones shown in Figure 3.7.

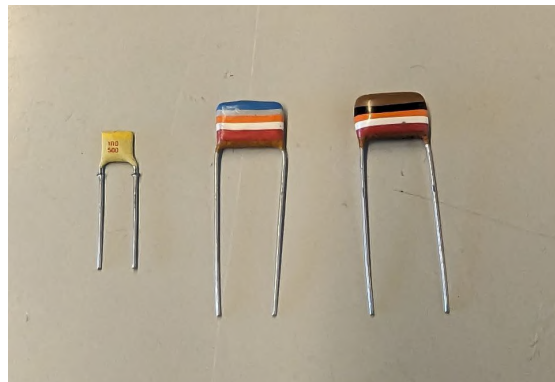


Figure 3.7: Example of polyester film and ceramic capacitors used for the power measurements, with capacitance values, from left to right, of 1 nF, 68 nF and 10 nF.

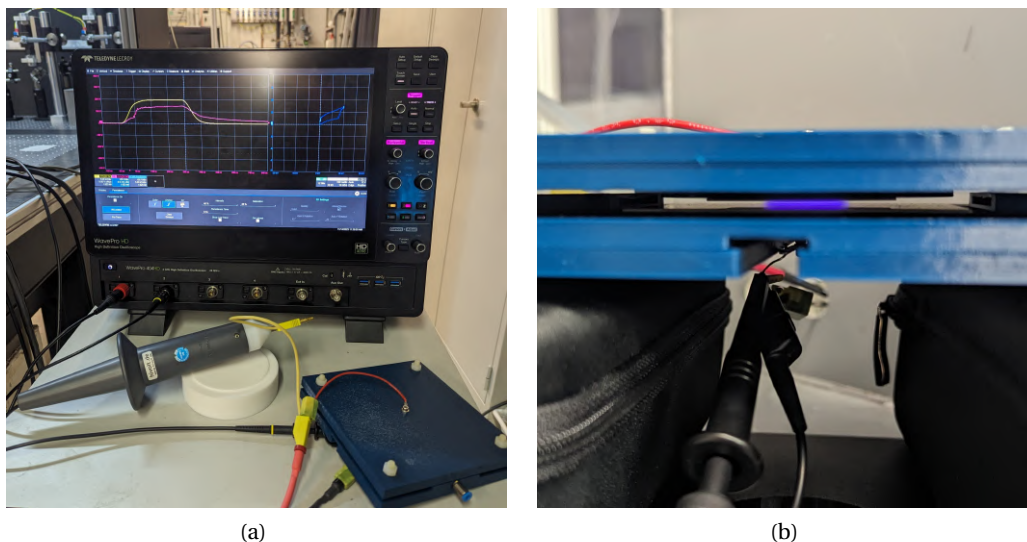


Figure 3.8: (a) Picture of the experimental setup used for the power measurements. On the oscilloscope, the Lissajous figure obtained in this specific case is visible. (b) Close up of the voltage probe connections to the monitor capacitor on the ground side of the VDBD.

The same circuit depicted in Figure 3.2 was employed, with the sole distinction being the grounding of the high-voltage probe used to measure the voltage across the DBD. This grounding necessitated a post-processing step to obtain the voltage across the DBD, involving the subtraction of the voltage reading on the capacitor.

$$V_{DBD}(t) = V_{HV\,probe}(t) - V_m(t) \quad (3.7)$$

The voltage on the monitor capacitor, connected as close as possible to the DBD, as shown in Figure 3.8b, is measured using a standard 10:1 voltage probe (Tektronix TPP0201), while the voltage on the SDBD is measured using a high voltage probe (PMK PHV 4002-3). The signals are acquired by a Teledyne Lecroy oscilloscope (Lecroy HDO WavePro 404HD), as shown in Figure 3.8a. To enhance signal stability, the oscilloscope averages the signals over 500 cycles, and additional post-processing involves signal smoothing and filtering. An example of the Lissajous figure obtained from the raw and smoothed signals is shown in Figure 3.9.

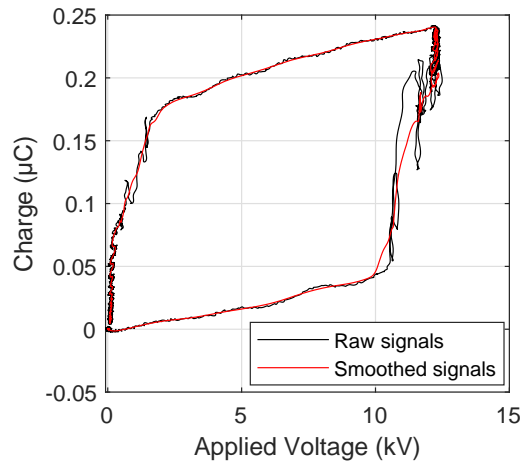


Figure 3.9: Example of Lissajous figures obtained from the raw signals and from the filtered signals, for a particular case of the VDBD.

Subsequently, the signals are synchronized by adjusting for the measured delay between them. The delay has been measured by using two voltage probes with the same cable length to simultaneously measure the same waveform in the same position of the electrical circuit. Power measurements are then conducted with a 2-3 nanosecond shift between the signals, employing Equation 3.6, which, when discretized, takes the form:

$$\bar{P} = f \cdot \sum_i V_i \cdot (Q_{i+1} - Q_i), \quad (3.8)$$

where f is the frequency of the pulses, Q_i the charge obtained from the voltage on the monitor capacitor by $Q_i = C_m V_m$ and V_i the voltage on the DBD. This methodology is applied

consistently throughout the experimental measurements.

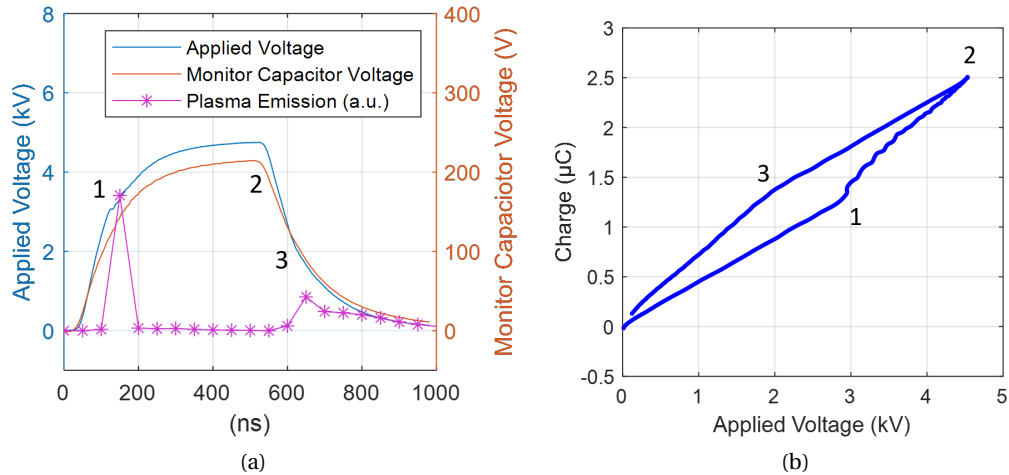


Figure 3.10: (a) Waveforms of the applied voltage to the PCB-fingers SDBD at 4.5 kV, 400 ns long pulses, 1 kHz repetition frequency, and voltage measured at the monitor capacitor. The plasma optical emission in arbitrary units is also represented to show the position in time of the 2 plasma discharges. (b) Lissajous figure obtained from the waveforms shown in (a). Points 1, 2 and 3 are used to highlight specific key points in the 2 plots.

A representative Lissajous figure obtained for an SDBD powered by the nanosecond-pulsed power supply is illustrated in Figure 3.10b. Specifically, this example features the PCB-fingers SDBD driven by a 4.5 kV, 400 ns long high voltage pulse at a 1 kHz repetition frequency. Figure 3.10a displays both the applied voltage and the voltage across the monitor capacitor, used to generate the Lissajous figure, along with the plasma optical emission presented in arbitrary units for temporal identification of the two plasma discharges. In Figure 3.10, point 1 signifies the initiation of the plasma discharge, evident in the Lissajous figure by the change in slope. Point 2 corresponds to the voltage peak at the end of the plateau and the maximum point of the Lissajous figure, while point 3 marks the start of the second plasma discharge, also discernible in the Lissajous figure through a change in slope.

The position of the plasma discharges relative to the waveform remains consistent across all nanosecond-pulsed powered DBDs. However, what varies is the shape of the Lissajous figure depending on the specific DBD. Figure 3.11 provides an example of the successive Lissajous figures obtained by increasing the applied voltage to the PCB-fingers SDBD and the VDBD. As anticipated, elevating the applied voltage results in larger Lissajous figures, indicating an increased power dissipation in the plasma discharge. Despite the distinct shapes of the Lissajous figures for the two different DBDs, the same key points identified in Figure 3.10 remain valid, even for the VDBD and across different applied voltages.

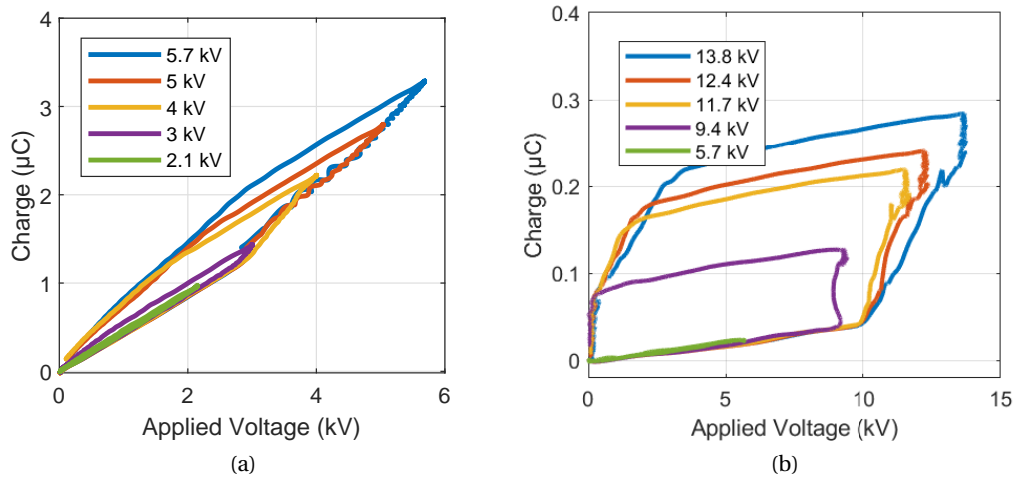


Figure 3.11: Sequence of Lissajous figures obtained at increasing applied voltage for the PCB-fingers SDBD (a) and VDBD (b).

3.4 Plasma discharge power measurements

In this section, the results obtained by measuring the plasma discharge power through Lissajous figures are presented. Several DBDs have been analyzed, but only the power measurements of the ones that are relevant to the topic of this thesis will be presented.

3.4.1 PCB-fingers SDBD power measurements

In Figure 3.12, the signals of the applied voltage and the voltage across the monitor capacitor are shown. The capacitor used for the PCB-fingers power measurements has a capacitance of 11.7 nF. It is important to note the noise increase when the plasma is ignited, as evident from the difference between the plot at lower voltages when the plasma is off and higher voltages when the plasma is on. The noise is also more significant at the moment of the first plasma discharge, during the rising edge of the voltage waveform.

This noise generates the ripples on the Lissajous figures obtained for the PCB-fingers SDBD, shown in Figure 3.13. The measurements are performed at 1 kHz repetition frequency. The power of the PCB-fingers SDBD exhibits a plateau rapidly after the breakdown voltage before increasing again. This behavior is not well understood, but it might be linked to a saturation effect right after the breakdown voltage. Due to the extremely thin FR4 thickness, plasma discharges can be easily ignited at more favorable locations. Subsequently, when the plasma covers the entire surface, raising the voltage does not appear to enhance either the density or the extent of the plasma. Consequently, the power of the plasma discharge remains unchanged. Given that this behavior is exclusively witnessed with the PCB-fingers SDBD, it is likely attributable to the materials and geometry of the SDBD. Another possible explanation could be

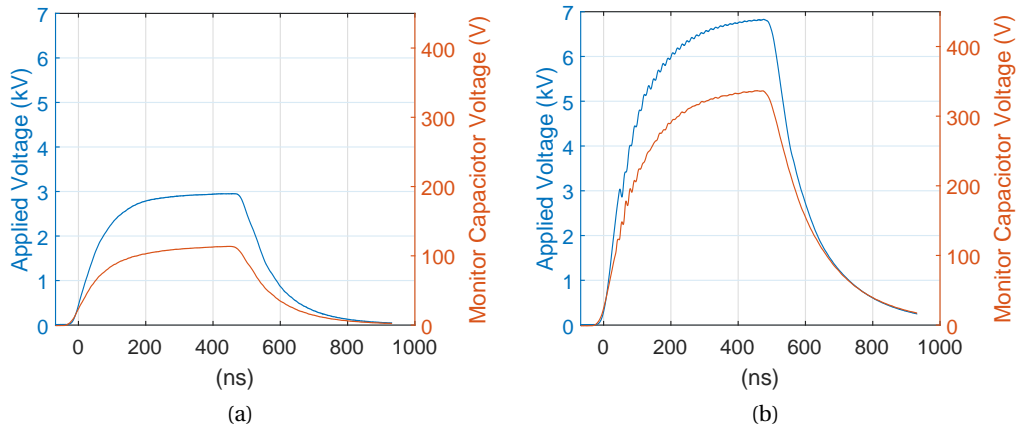


Figure 3.12: Signals of the applied voltage on the PCB-fingers SDBD and voltage on the monitor capacitor in series to the SDBD. (a) Signals in the absence of plasma, at the applied voltage of 3 kV, below the breakdown voltage. (b) Signals in the presence of plasma, at ~ 7 kV applied voltage, above the breakdown voltage. It is possible to note the increased noise in correspondence with the rising edge of the voltage, during ignition of the first plasma discharge.

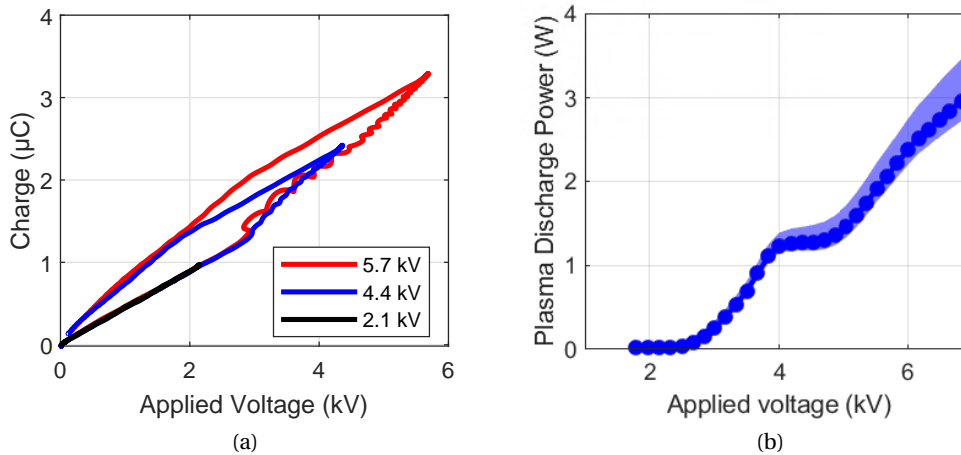


Figure 3.13: (a) Example of Lissajous figures of the PCB-fingers SDBD at different applied voltages. (b) Computed plasma discharge power from the Lissajous figures at increasing applied voltages.

attributed to a coupling mismatch between the power supply and the plasma discharge, when plasma starts to ignite, but it appears to be less likely to occur. In any case, the power level remains significantly low, at less than 5 watts. This is primarily attributed to the use of the nanosecond-pulsed power supply that generates very brief plasma discharges. Consequently, for a substantial portion of each cycle, plasma is absent, resulting in a consistently low average power over the course of a full cycle.

3.4.2 Perforated-disc SDBD power measurements

The capacitor used for the power measurements of the perforated-disc SDBD has a capacitance of 15 nF. The applied voltage and monitor capacitor signal are reported in Figure 3.14. The Lissajous figures obtained for the perforated-disc SDBD, at 1 kHz repetition frequency, are shown in Figure 3.15. The plasma discharge power for the perforated-disc is slightly larger than the PCB-fingers one, probably due to the larger surface of plasma and thickness of the electrode, which increase the total volume of plasma generated in this configuration. As mentioned earlier, this SDBD does not exhibit the power saturation plateau observed in the PCB-fingers SDBD. The breakdown voltage is higher due to a larger dielectric thickness and the use of a different dielectric material.

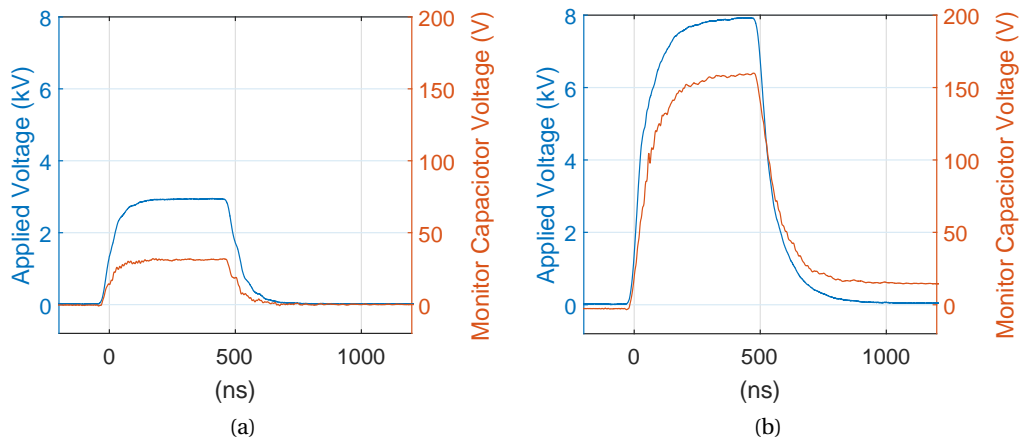


Figure 3.14: Signals of the applied voltage on the perforated-disc SDBD and voltage on the monitor capacitor in series to the SDBD. (a) Signals in absence of plasma, at ~3 kV applied voltage, below the breakdown voltage. (b) Signals in the presence of plasma, at ~8 kV applied voltage, above the breakdown voltage. It is possible to note the increased noise in correspondence of the rising edge of the voltage, during ignition of the first plasma discharge.

Perforated-disc SDBD power measurements with PAW power supply

The Perforated-disc SDBD was also employed with an alternative power source in the context of the sterilization experiments detailed in Section 5.3 and for the operation of the plasma-activated water (PAW) reactor utilized at the Bio-Lab at the SPC. This power source is hereafter referred to as the "PAW power supply". It has been adapted from a commercially available ozone generator and produces a sinusoidal waveform with a peak-to-peak voltage of 8.8 kV and a frequency of 21 kHz. This waveform is modulated at a frequency of 100 Hz, as depicted in Figure 3.16, which also illustrates the voltage across the monitor capacitor.

Due to the varying energy per pulse with each cycle of the 21 kHz waveform, it became necessary to employ a different methodology for quantifying the power dissipated within

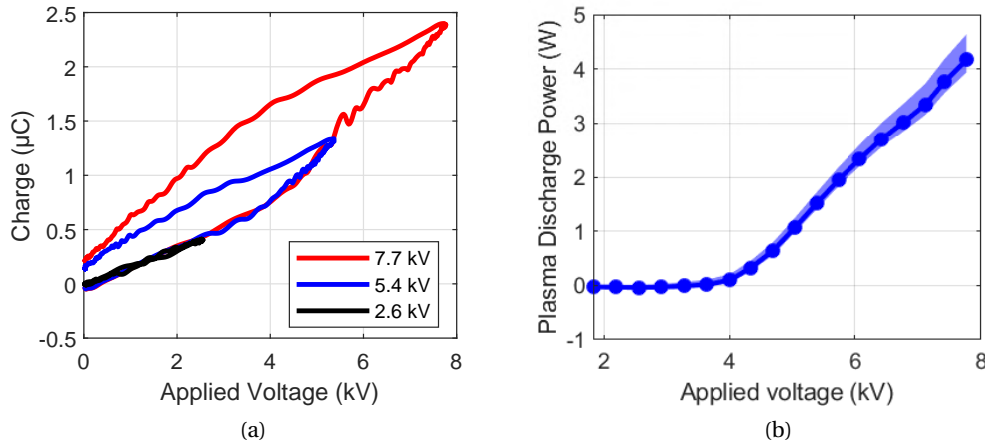


Figure 3.15: (a) Example of Lissajous figures of the Perforated-disc SDBD at different applied voltages. (b) Computed plasma discharge power from the Lissajous figures at increasing applied voltages.

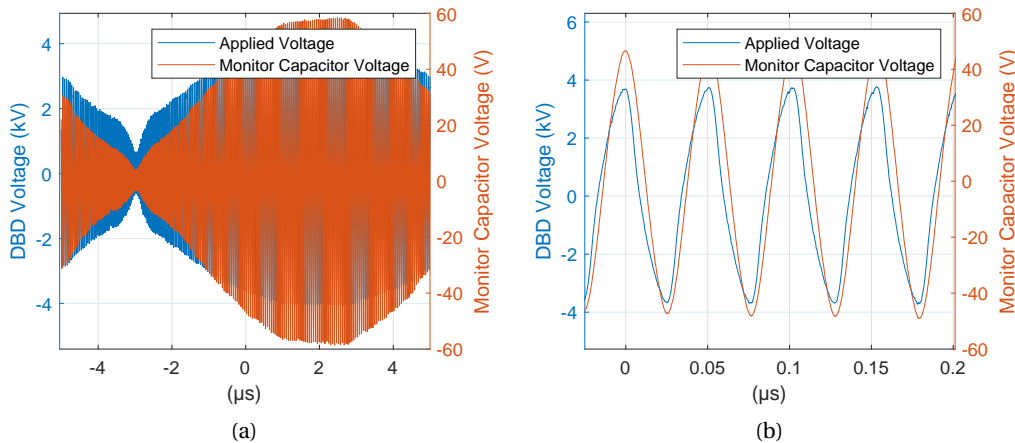


Figure 3.16: Waveforms of the applied voltage on the VDBD and voltage on the monitor capacitor in series to the VDBD for the perforated-disc SDBD powered by the PAW power supply. (a) Signals with the 100 Hz modulation visible and (b) zoom on the 21 kHz frequency waveforms.

the plasma discharge. As a result, Lissajous figures were generated to encompass an entire period of the 100 Hz modulation, as depicted in Figure 3.17. The energy within this entire time interval was calculated using Equation 3.8 and subsequently multiplied by the modulation frequency of 100 Hz. The measured power dissipated in the plasma discharge in this setup was measured to be ~ 39 W.

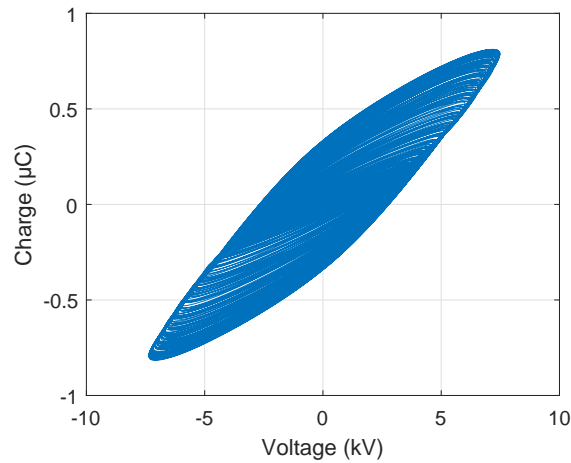


Figure 3.17: Lissajous figures obtained from the whole modulation period of the perforated-disc SDBD powered by the PAW power supply.

3.4.3 VDBD power measurements

In the following section we describe the plasma discharge power measurements performed on the VDBD, presented in Section 2.2.

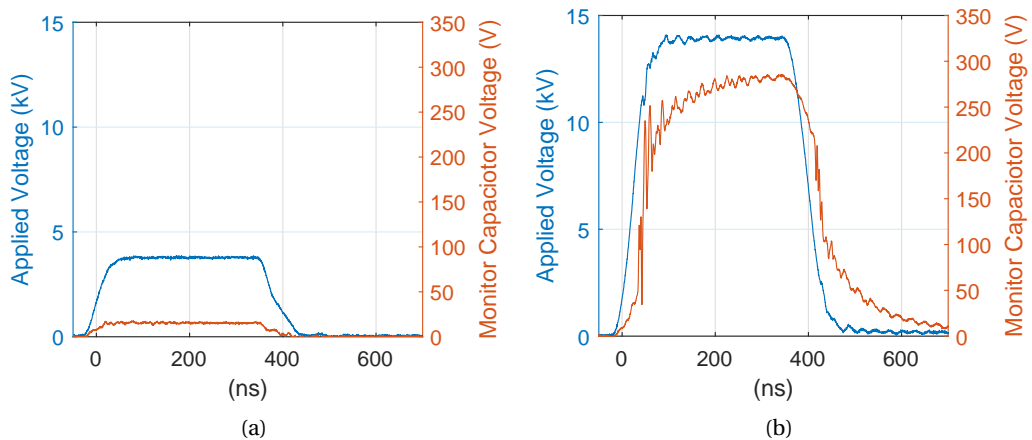


Figure 3.18: Signals of the applied voltage on the VDBD and voltage on the monitor capacitor in series to the VDBD. (a) Signals in absence of plasma, at ~ 3.8 kV applied voltage, below the breakdown voltage. (b) Signals in the presence of plasma, at ~ 8 kV applied voltage, above the breakdown voltage. It is possible to note the increased noise in correspondence of the rising edge of the voltage, during ignition of the first plasma discharge.

The waveforms of the applied voltage and monitor capacitor, reported in Figure 3.18, show the noise generated during the plasma discharge is much higher with respect to the SDBD case. This is caused by the more abrupt plasma discharge ignition, since differently from the SDBDs, it does not have the time to diffuse over a surface, but occupies the whole volume

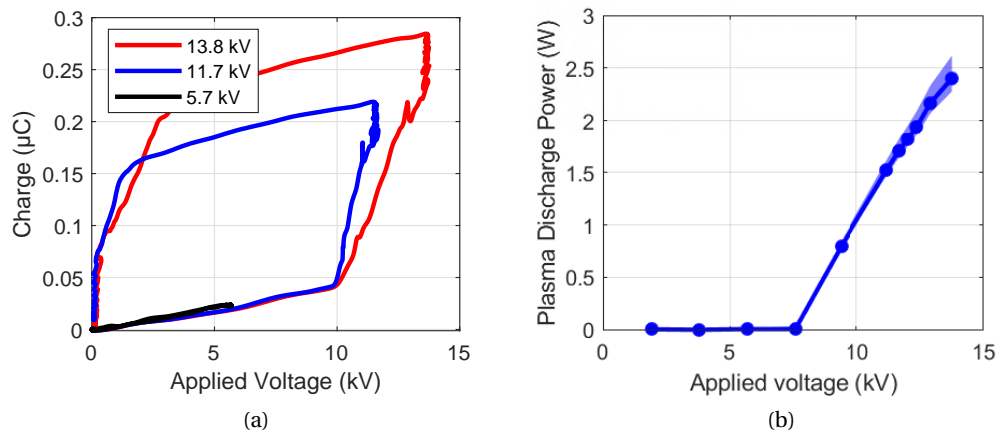


Figure 3.19: (a) Example of Lissajous figures of the VDBD at different applied voltages. (b) Computed plasma discharge power from the Lissajous figures at increasing applied voltages.

in the DBD gap simultaneously. The Lissajous figures obtained for the VDBD are shown in Figure 3.19. The ceramic capacitor used has a capacitance of 1 nF. The power dissipated in the VDBD plasma is still in the same range of the SDBDs because of the nanosecond-pulsed power supply, and the fact that the surface is much smaller than the SDBDs, despite the volume of the generated plasma.

VDBD power measurements with membrane in the gap

To simulate the bacterial treatments carried out using the VDBD and to assess whether there were any variations in the plasma discharge power when a membrane was positioned on top of the dielectric, we conducted power measurements. This investigation aimed to replicate a real-case scenario, and as part of this study, we quantified the power dissipated in the discharge when the membrane was placed over the dielectric.

The results are illustrated in Figure 3.20. In the graph, the plasma discharge power is depicted in blue for the measurements conducted without the membrane and in red for the measurements taken with the membrane in place. The plot clearly demonstrates a difference between the two scenarios, underscoring the notion that inserting a full membrane in the middle of the VDBD could lead to subtle alterations in the plasma characteristics. As a result, if not taken into account the real-case scenario, the measurements taken in the ideal-case may not accurately represent the plasma parameters during the bacterial treatments.

3.4.4 Power measurements of Sinhon Electronics stripes SDBD

As mentioned in Section 2.6, other SDBDs were used for other projects in the Bio-Lab. The power of these plasma sources was measured in the framework of this thesis. The Shinon

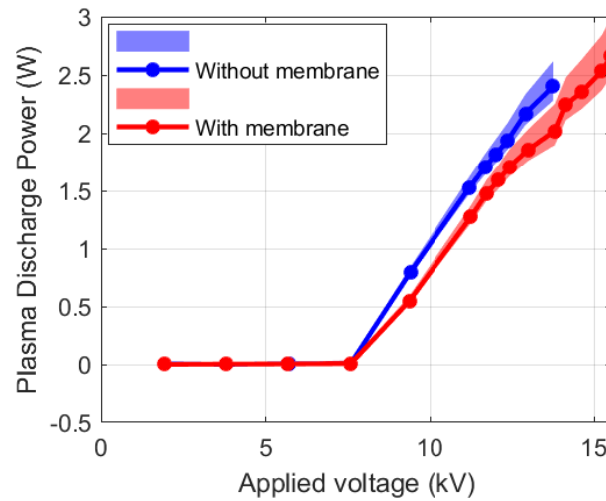


Figure 3.20: Comparison of the plasma discharge power, computed from the Lissajous figures at increasing applied voltages, between the the case with the membrane in the middle and without the membrane.

Electronics stripes SDBD was used for plasma treatments of seeds [129]. The SDBD was powered by an AC voltage waveform, nominally a sine wave, 8 kV peak-to-peak at 10 kHz. To avoid overheating the substrate and seeds with continuous wave (cw) power, the AC supply was power modulated at 500 Hz with a duty cycle of 10%, similar to the technique used in [30]. This corresponds to a burst of two AC cycles per power modulation period as shown in Figure 3.21. The waveform is consistent and reproducible over time, although it is distorted by the high-voltage amplifier. The capacitor used has a capacitance of 68 nF.

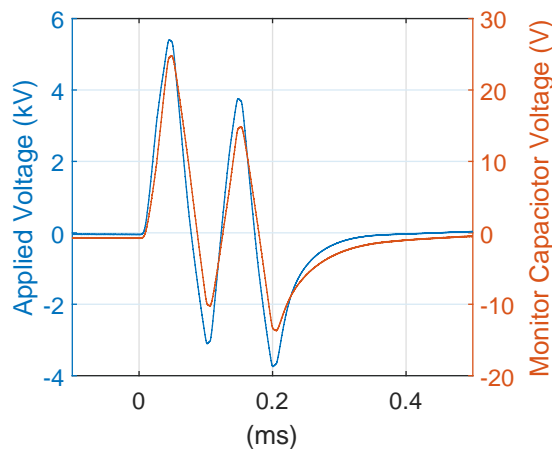


Figure 3.21: The voltage waveform of the Shinon Electronics stripes SDBD for nominal 8 kV peak-to-peak. The blue curve shows the applied voltage; the orange curve shows the voltage across the monitor capacitor. The waveform distortion is caused by the transient response of the high-voltage amplifier when using high-frequency bursts (adapted from [129]).

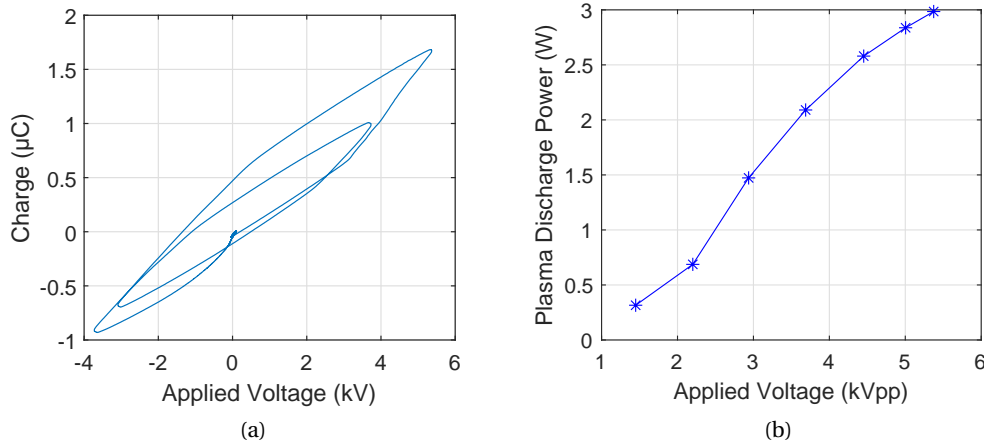


Figure 3.22: (a) Example of Lissajous figure of the Shinon Electronics stripes SDBD. (b) Computed plasma discharge power from the Lissajous figures at increasing nominal applied voltages (source: [129]).

Since the 2 cycles are not identical due to the transient distortion by the high-voltage amplifier, the resulting Lissajous figure shown in Figure 3.22a is not conventional. The locus is not a parallelogram because the waveform is not a continuous sinusoidal wave, but a burst whose voltage converges to 0 every 2 cycles. This produces the discontinuity at the origin visible in the figure. Nonetheless, the area within the locus of the voltage vs. charge contour for each cycle represents the energy per cycle dissipated in the plasma. Accounting for the 500 Hz modulation frequency of the burst, the time-averaged dissipated power for different voltages is shown in Figure 3.22b.

3.5 Conclusions

The plasma discharge power, a critical parameter to monitor in low-temperature plasmas, has been quantified for all the DBDs used in this thesis. The measurements were conducted using a reliable and widely accepted method in the DBD literature called Lissajous figures. The challenges faced in implementing this technique for nanosecond plasma discharges were successfully overcome by meticulously addressing the experimental setup, specifically the cables, capacitor, and probes, as well as by carefully evaluating the signal delay throughout the analysis. This enabled us to measure the power dissipated in the discharge, depending on the applied voltages. The nanosecond pulsed generator offers the advantage of operating at low power, while still exhibiting excellent efficacy in terms of bacterial inactivation, as demonstrated in Chapter 5. The power of the plasma discharge generated by the PCB-fingers SDBD, perforated-disc SDBD, and VDBD, powered by the nanosecond generator, was measured to reach a maximum of 3 W. This low power provides us with insights into the primary molecules that are generated, based on the surface power density of the plasma [144, 90].

Additional information regarding these considerations is presented in Chapter 6. To characterize the power used for the sterilization experiments outlined in Section 5.3, the power of the perforated-disc SDBD plasma discharge powered by the PAW power supply was also measured. The results indicate that the power dissipated in the plasma reaches around 40 W in this particular configuration. Finally, the power characterization of another SDBD prototype used for seeds treatment is reported [129].

4 Physical Characterization: EFISH

This chapter presents electric field measurements inside the plasma discharge generated in the VDBD by electric field induced second harmonic (EFISH) generation. This advanced laser technique measures the electric field locally with high space and time resolution, providing insights on the charged particle dynamics during the plasma discharge. This is not only important to investigate the effect of electric fields on biological treatments but also to understand the basic physics of atmospheric pressure LTP in air.

In Section 4.1, we introduce the EFISH method for measuring electric fields in the plasma, highlighting its advantages over alternative techniques. The basic theory and precautions for strongly focused lasers are presented.

Section 4.3 details the data campaign conducted at CNR in Bari in collaboration with Dr. Paolo F. Ambrico. The results consist of nanosecond laser EFISH measurements of the electric field generated in the plane-to-plane configuration of the VDBD. We comprehensively describe the experimental setup, the analysis of the data, and the results. The culmination of this work carried out in Bari has been published in Ref. [145].

Section 4.4, showcases the EFISH measurements carried out at the Bio-lab at the SPC, using the same VDBD setup but with significant improvements. We explain how the use of a picosecond laser, a spatial filter, and a vertical motor enhanced the quality and resolution of the measurements. We provide a detailed description of the experimental setup and present the final results, revealing certain features that were not visible in the nanosecond EFISH measurements. Additionally, we present picosecond EFISH results at various plasma discharge powers and with a membrane in the VDBD gap to study the setup used for the bacteria treatments [146].

Then, Section 4.5 introduces a kinetic model developed to improve our understanding of the behavior of charged particles in the plasma discharge. The essential parameters and primary conclusions derived from comparing the model predictions with the EFISH experimental data are presented. Lastly, a summary of the conclusions of this chapter is provided.

4.1 Electric-field induced second harmonic generation

In Section 1.2, we discussed the fundamental role of the electric field generated within a plasma in the context of biological plasma treatments. This is particularly relevant when the biological target is situated within the plasma or in direct contact with it. Surprisingly, the electric field aspect of plasma treatments often receives less attention compared to the focus on reactive oxygen and nitrogen species (RONS), and the chemical reactions induced within the plasma. However, it's essential to recognize that the electric field wields a significant influence on biological targets and can potentially cause damage to cell membranes through a phenomenon called "electroporation" [73, 72]. Therefore, precise measurements of the spatial distribution and temporal evolution of the electric field generated by the plasma are of paramount importance, especially in the context of direct plasma treatments.

A widely employed method for electric field measurement is the use of a calibrated capacitive probe [147, 148]. While this approach offers high temporal resolution (approximately 1 ns), it comes with a relatively low spatial resolution (about 1 cm). More recently, the development and deployment of electro-optic probes have allowed for improved spatial resolution (approximately 1 mm) of electric field measurements in atmospheric pressure plasma jets [149]. However, it's worth noting that the presence of the probe can perturb the plasma, particularly in conditions where surface charge accumulation might occur on the probe housing. Consequently, there is a pressing need for the development of non-intrusive diagnostics that provide field vector information, possess high spatio-temporal resolution, and are essential for a quantitative understanding of ionization kinetics, charge transport, species generation within the plasma, and wave propagation.

Another technique for electric field measurement in nitrogen or air plasmas relies on optical emission spectroscopy (OES). The intensity ratio of spectral bands within the first negative system of N_2^+ (FNS, $B^2\Sigma_u^+ \rightarrow \chi^2\Sigma_g^+$) and the second positive system of N_2 (SPS, $C^3\Pi_u \rightarrow B^3\Pi_g$) is widely acknowledged as a spectroscopic signature for quantifying the reduced electric field strength in air-like discharges [150, 151, 25, 152]. Typically, this ratio is calculated from the intensities of the FNS(0,0) band and SPS(0,0) band. Due to the significantly different excitation thresholds for direct electron-impact ionization and excitation of the respective upper radiative states, the FNS(0,0)/SPS(0,0) intensity ratio exhibits high sensitivity to the reduced electric field strength E/N , where E represents the electric field magnitude and N denotes the gas number density [153]. However, this method is constrained by the optical emission of the plasma and cannot be used when the plasma discharge fade out. It is an indirect measurement, and as such, it relies on certain assumptions on the electron energy distribution function (EEDF) and on the availability of reliable data for the excitation cross sections and quenching rate coefficients, which may not hold in all experimental setups.

In contrast, electric-field-induced second harmonic (EFISH) generation offers several advantages over other techniques. Picosecond (ps) and femtosecond (fs) lasers can achieve sub-nanosecond time resolution, and similar time resolution can be attained using nanosec-

ond (ns) lasers. Spatial resolution is determined by the width of the laser beam, allowing for sub-millimeter spatial resolution by using focusing lenses. Nonetheless, it's imperative to be cautious when dealing with the focusing of Gaussian-shaped laser beams, as we will elaborate on in the following sections. EFISH stands out as a non-invasive and direct measurement technique, characterized by ease of calibration and the absence of constraints related to the gas employed in the plasma discharge. Of particular significance, it can provide accurate measurements of the electric field throughout the entire voltage waveform, including the phase when the plasma is "off." Consequently, electric field measurements in plasmas, facilitated by EFISH with ultrashort pulsed lasers [154, 155], have gained increasing prominence. This technique finds application in a diverse range of plasma environments, including ionization wave plasmas in air, nitrogen, hydrogen, and hydrocarbon flames, as well as argon and helium plasma jets [154, 156, 157, 158]. Before delving into the specifics of the experimental setup used in this thesis to perform EFISH measurements, I will give a brief introduction to electric-field second harmonic generation and offer some insights into the theory underpinning EFISH.

4.2 Introduction to EFISH theory

Second-harmonic generation (SHG) represents the most fundamental form of wave-wave non-linear interaction observed in a wide range of systems, spanning optical, radio, atmospheric, and magnetohydrodynamic systems [159]. SHG was initially discovered as a nonlinear optical phenomenon, where two photons of the same frequency interact within a nonlinear material, giving rise to a new photon with double the energy of the initial photons (equivalently, twice the frequency and half the wavelength). Importantly, this process preserves the coherence of the excitation [160]. SHG constitutes a particular case of sum-frequency generation, involving the combination of two photons, and is part of the broader category of harmonic generation phenomena.

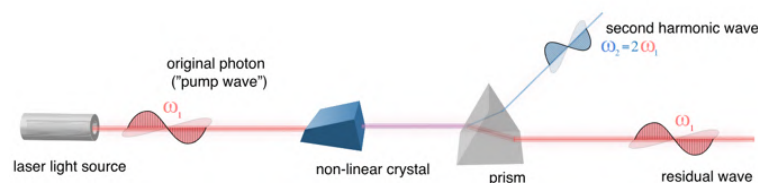


Figure 4.1: Example of second harmonic generation by non-linear crystal and separations of wavelength through prism.

The second-order nonlinear susceptibility of a medium describes its propensity to induce SHG, and this susceptibility arises from inherent asymmetries within the system. In a centrosymmetric system, the occurrence of second harmonic generation is deemed impossible. Nevertheless, in the presence of an external electric field, this symmetry can be broken, enabling the molecules to emit light at the second harmonic frequency. This technique was initially explored during the 1960s and 1970s and has subsequently been predominantly employed for the measurement of the hyperpolarizabilities of various species.

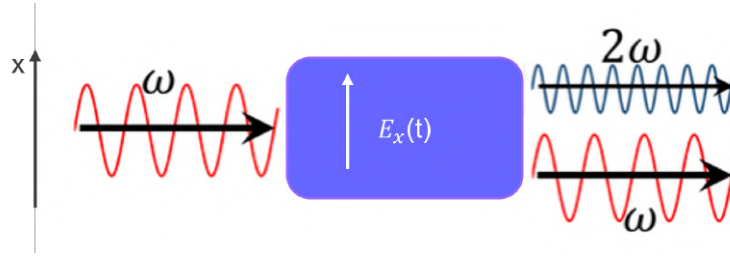


Figure 4.2: Scheme of second harmonic generation.

Electric field-induced second harmonic generation is described as a third-order nonlinear process, entailing the interplay between the incident light field and the external electric field, as characterized by the following expression [155, 161]:

$$P_i^{(2\omega)} = \frac{3}{2} N \chi_{i,j,k,l}^{(3)}(-2\omega, 0, \omega, \omega) E_j^F E_k^{(\omega)} E_l^{(\omega)}, \quad (4.1)$$

where $P_i^{(2\omega)}$ represents the induced polarization at the second harmonic frequency 2ω , while $E_{k,l}^{(\omega)}$ denotes the electric fields of the incident laser beam, and are the same for the second harmonic generation. E_j^F is the dipole-inducing electric field targeted for measurement, and N corresponds to the number density of the gas. The third-order nonlinear susceptibility tensor, denoted as $\chi_{i,j,k,l}^{(3)}$, depends on the molecular dipole moments and the orientations of the fields involved. The subscripts are indicative of the polarizations of the respective fields. It is worth noting that the intensity of the second harmonic signal is directly proportional to the square of the induced polarization, yielding the following relationship:

$$I^{(2\omega)} = A \cdot (E_{ext})^2 (I_{pump})^2, \quad (4.2)$$

where $I^{(2\omega)}$ stands for the intensity of the induced second harmonic signal, A represents a calibration constant acquired through measurement, E_{ext} denotes the external electric field targeted for measurement, and I_{pump} corresponds to the intensity of the pump laser beam, as outlined in [162].

4.2.1 EFISH considerations for strongly focused laser beams

The majority of the topics discussed in this section have been previously explored and elaborated upon in [163]. For the sake of consistency, the nomenclature and figures will be retained as Reference [163]. Equation 4.2 has already been adjusted to account for the constant terms in both the calibration measurement and the actual measurement. To comprehend the underlying physics of this diagnostic technique, it is advantageous to take a step back and consider the principles of laser wave physics while also being mindful of certain precautions necessary for accurate EFISH measurements. In the context of the plane-wave approximation and under

the assumption of a uniform external electric field E_{ext} , the intensity of the second harmonic signal, denoted as $I^{(2\omega)}$, can be expressed as follows:

$$I^{(2\omega)} \propto \left[\chi_{i,j,k,l}^{(3)} \cdot N \cdot (E_{ext})_j \cdot E_k^{(\omega)} E_l^{(\omega)} \right]^2 \cdot \left| \int_{-L}^L \exp(i \cdot \Delta k z) dz \right|^2 \quad (4.3)$$

$$= \left[\chi_{i,j,k,l}^{(3)} \cdot N \cdot (E_{ext})_j \cdot E_k^{(\omega)} E_l^{(\omega)} \cdot \frac{2 \sin(\Delta k \cdot L)}{\Delta k} \right]^2, \quad (4.4)$$

where Δk corresponds to the wave mismatch, representing the difference between the wave vectors of the fundamental and second harmonic waves. The parameter $2L$, which is equal to the electrode length, effectively establishes the interaction length L_{int} , the region where E_{ext} and $E^{(\omega)}$ overlap. Furthermore, z denotes the axis along which the beam propagates.

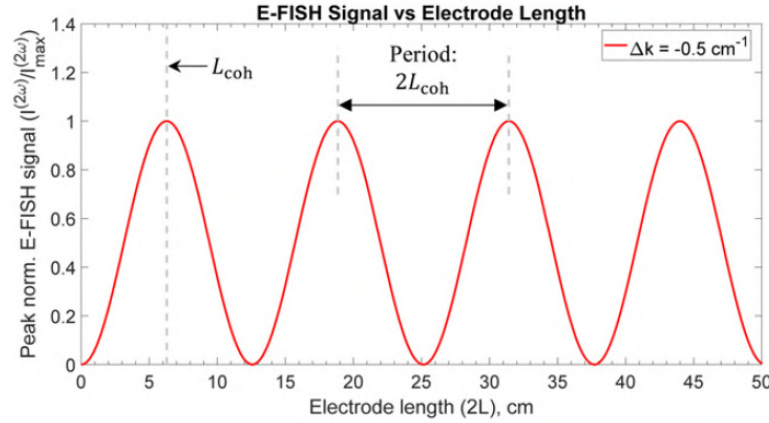


Figure 4.3: The impact of the electrode length, represented as $2L$, on the peak-normalized EFISH signal within the plane-wave approximation, as described by Equation 4.4, is illustrated for a wave mismatch of $\Delta k = -0.5 \text{ cm}^{-1}$ (source: [163]).

Equation 4.4 holds when the conversion efficiency of the second harmonic signal is extremely weak, and the depletion of the probe beam can be safely assumed to be negligible, resulting in $I^{(\omega)}$ remaining constant throughout the interaction length. Additionally, this equation implicitly assumes a centrosymmetric medium, which means that in the absence of an external electric field (E_{ext}), there will be no second harmonic generation from lower-order processes. This assumption can be verified experimentally or enforced by selecting an appropriate gas composition. Furthermore, it's important to note that in a gas or plasma, the wave vector mismatch, Δk , which is effectively proportional to the difference in the refractive indices at the fundamental ($n^{(\omega)}$) and second harmonic ($n^{(2\omega)}$) frequencies, is necessarily negative. This is indicated by $\Delta k = [2k^{(\omega)} - k^{(2\omega)}] \propto [n^{(\omega)} - n^{(2\omega)}] < 0$. The wave vector mismatch $\Delta k = -0.5 \text{ cm}^{-1}$ corresponds to fundamental and second harmonic wavelengths of 1064 nm and 532 nm, respectively, in air. These values are based on the refractive indices calculated under standard conditions of room temperature and pressure, as indicated in Reference [164]. The

effect of electrode length on the EFISH signal in the plane-wave approximation is illustrated in Figure 4.3 for $\Delta k = -0.5 \text{ cm}^{-1}$ [165]. Analogous to SHG from non-centrosymmetric media, constructive interference between the fundamental and second harmonic waves leads to an increase in signal with electrode length up to $L_{coh} = \frac{\pi}{|\Delta k|} = 6.28 \text{ cm}$, beyond which they begin to destructively interfere, causing the power in the second harmonic to flow back into the fundamental. The sine-squared term in Equation 4.4 ensures that this interaction repeats itself with a period equal to $2L_{coh} = \frac{2\pi}{|\Delta k|} = 12.56 \text{ cm}$. Therefore, in the plane-wave approximation, the EFISH signal reaches a maximum for electrode lengths that are multiples of $(2p + 1) \cdot L_{coh}$, where p is a positive integer. In earlier studies involving EFISH as an electric field diagnostic, the interaction length, denoted as L_{int} , has frequently been defined as the confocal parameter, which is equivalent to twice the Rayleigh range ($2z_R$) of the laser beam (i.e., $L_{int} = 2z_R$). In the field of optics the Rayleigh length or Rayleigh range (z_R) refers to the distance along the propagation direction of a beam from its waist to the point where the cross-sectional area is doubled, as depicted in Figure 4.4. The Rayleigh length is mathematically defined as $z_R = \frac{\pi \omega_0^2}{\lambda}$, where ω_0 represents the beam waist and λ denotes the wavelength. A related parameter is the confocal parameter b , which is precisely twice the Rayleigh length. The Rayleigh length holds particular significance when modeling beams as Gaussian beams.

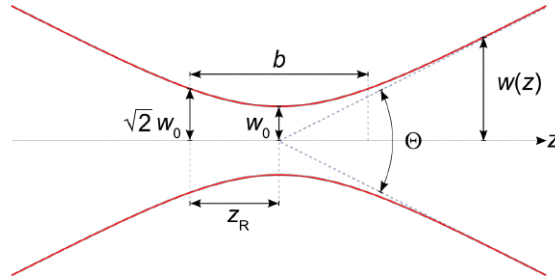


Figure 4.4: Schematics of focusing point parameters. The gaussian beam width $\omega(z)$ as a function of the axial distance z is shown, as well as the beam waist ω_0 , the confocal parameter b , the Rayleigh range z_R and the angular spread Θ .

To explore the impact of a focused Gaussian beam on the EFISH signal, the second harmonic EFISH power has been redefined and derived in [163]. The resulting equation is as follows:

$$P^{(2\omega)} \propto \left[\chi_{i,j,k,l}^{(3)} \cdot N \cdot E_{ext} \cdot P_0^{(\omega)} \right]^2 \cdot \left(\frac{1}{z_R} \right) \cdot \left| \int_{-L}^L \frac{\exp(i \cdot \Delta k z)}{\left[1 + i \cdot \left(\frac{z}{z_R} \right) \right]} dz \right|^2. \quad (4.5)$$

The terms within the square brackets can be considered as constants, and the dependency of the EFISH power on the length of the external field profile is contained solely within the following expression:

$$P^{(2\omega)} \propto \left(\frac{\Lambda'}{z_R} \right), \quad \text{where} \quad \Lambda' = \left| \int_{-L}^L \frac{\exp(i \cdot \Delta k z)}{\left[1 + i \cdot \left(\frac{z}{z_R} \right) \right]} dz \right|^2 \quad (4.6)$$

In Equation 4.5, the term $\left(\frac{1}{z_R} \right)$ takes into account the intensity variation caused by the focusing of the beam, while maintaining a constant input power, $P_0^{(\omega)}$. It is essential to note that the term in the integral in the above expression differs from the plane-wave approximation (as seen in Equation 4.3) due to the inclusion of the factor $\left[1 + i \cdot \left(\frac{z}{z_R} \right) \right]$ in the denominator. As discussed in [161], this factor can be expanded into a more detailed but more elucidating form: $\frac{\exp[-i \cdot \text{atan}\left(\frac{z}{z_R}\right)]}{\sqrt{1 + \left(\frac{z}{z_R}\right)^2}}$, where the numerator contains an expression corresponding to the Gouy phase shift, denoted as $\phi_g(z) = +\text{atan}\left(\frac{z}{z_R}\right)$ [166]. The denominator is linked to the evolution of the Gaussian beam width along the z -axis. A notable observation is that the integral within the modulus of Equation 4.6 tends toward zero as the electrode length L approaches infinity. However, Λ' does not diverge as long as L is finite. From the standpoint of the EFISH diagnostic, this suggests that the measured signal explicitly depends on the spatial evolution of the external field in addition to other parameters, such as the magnitude of the external field E_{ext} , wave vector mismatch (Δk), and the choice of z_R .

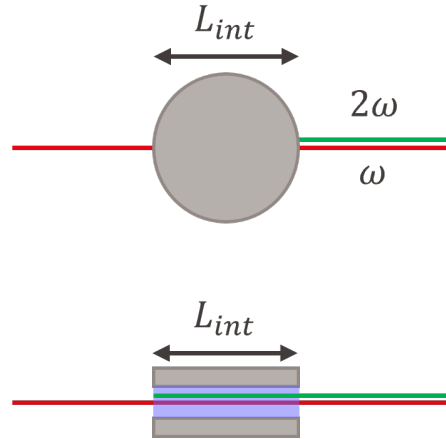


Figure 4.5: Simplified schematic of the interaction length L_{int} in the case of the VDBD.

Crucially, this observation contradicts the original notion of designating the confocal parameter as the interaction length, denoted as L_{int} . Instead, it implies that L_{int} should be considered as the entire length of the external field profile, as illustrated in Figure 4.5 for the VDBD case. This redefines the interpretation of the interaction length in the context of the EFISH diagnostic.

Figure 4.6 illustrates Λ' as a function of electrode length ($2L$) for three specific values of the Rayleigh range, namely $z_R = 0.847$ mm, 3.39 mm, and 9.41 mm. These z_R values correspond to approximations for three commonly used focal length lenses with focal lengths of $f = 15$ cm, 30 cm, and 50 cm, respectively. These approximations are based on an initial unfocused beam

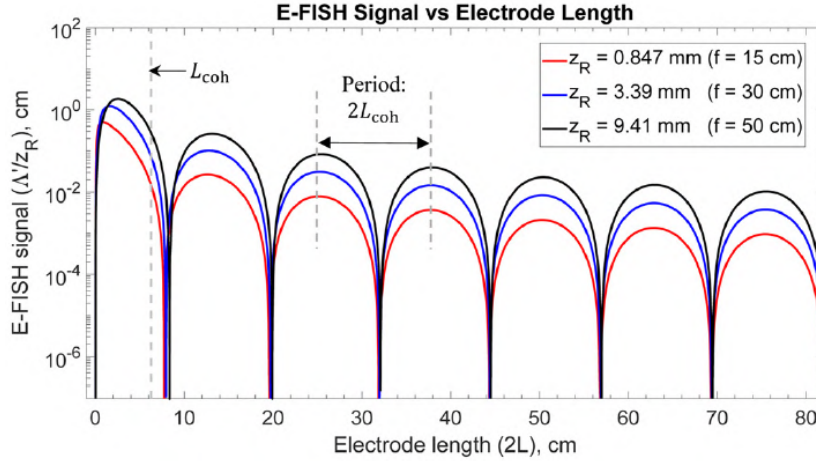


Figure 4.6: The effect of electrode length ($2L$) on $\frac{A'}{z_R}$, which corresponds to the EFISH signal, is graphed here in logarithmic scale for three distinct values of z_R (source: [163]).

waist of 3 mm and a probe laser wavelength of 1064 nm. The graph provides an overview of how A' changes with variations in electrode length for these different lens focal lengths and Rayleigh ranges. The plot clearly depicts an exponentially decreasing EFISH signal, modulated with a period corresponding to the coherence length L_{coh} . An additional critical discovery from [163] is the inability to resolve the EFISH signal along the beam propagation direction. The spatial evolution of the signal is influenced by both the spatial development of the laser intensity (which is effectively addressed in the modified plane wave approximation) and the total phase mismatch, which encompasses an added contribution from the Gouy phase shift. Because both the length and shape of the electric field profile have a marked impact on EFISH signal generation, failing to consider this contribution can result in incorrect interpretations of the signal, ultimately leading to an inaccurate measurement of the electric field. This highlights the importance of accounting for the spatial dependencies inherent in EFISH signal generation for accurate electric field measurements.

4.3 Nanosecond-pulsed laser EFISH in the VDBD plasma discharge

Measurements of EFISH on the VDBD described in Section 2.2 were conducted in two different setups employing two different laser systems. Figure 4.7 provides a reminder of the VDBD schematics.

In this section, the EFISH measurements performed in collaboration with Dr. Paolo F. Ambrico at the CNR, Istituto per la Scienza e Tecnologia dei Plasmi, Sede di Bari, will be described [145]. While EFISH measurements are typically carried out using femtosecond (fs) and picosecond (ps) lasers, it has been possible to perform steady-state electric field measurements in ambient air with nanosecond (ns) pulse duration lasers for more than four decades [167]. The main limitation of using readily available ns pulse duration Nd:YAG lasers for EFISH diagnostics

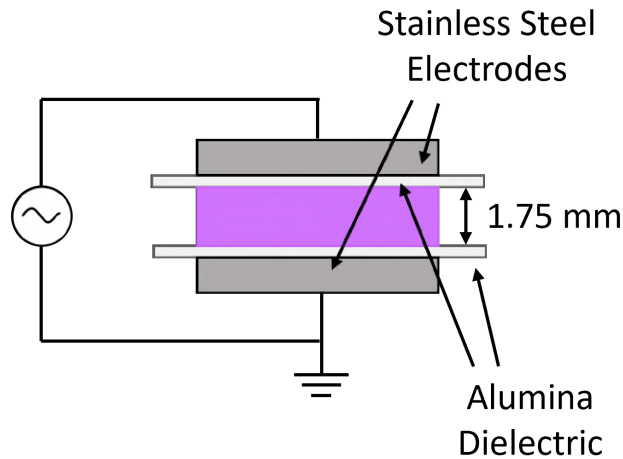


Figure 4.7: Schematic of the VDBD components.

is their temporal resolution, which is typically around 10 ns. This timeframe often exceeds the required duration for critical processes such as breakdown development, plasma self-shielding, and ionization wave propagation in high-pressure pulsed plasmas. To enhance temporal resolution and track electric field variations throughout the ns laser pulse duration, we adopted an approach detailed in [168]. This approach allows a temporal resolution limited solely by the response time of the detector and oscilloscope. In our experiments, we monitor the evolution of the electric field in a nanosecond discharge operating at a repetition rate of 1 kHz in synthetic humid air. The choice of gas mixture allowed us to obtain a more diffused plasma and more accurate time resolution measurements by reducing the jitter between the plasma discharge and the voltage waveform. To address the issues described in Section 4.2.1, we took various precautions on the design of the VDBD, already described in Section 2.2. Firstly, we chose the length of the VDBD electrodes to be shorter than the coherence length in air, $L_{coh} = 6.28$ cm. The diameter of the electrodes is $L = 2$ cm, which ultimately corresponds to L_{int} as it is the length of the plasma discharge. This choice increased the intensity of the EFISH signal.

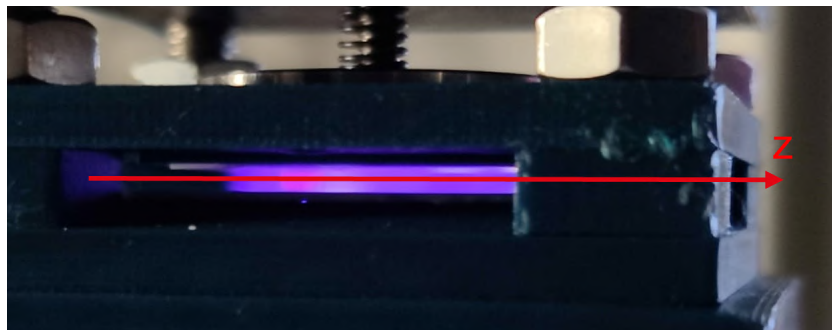


Figure 4.8: Scheme of the laser beam direction, denoted with the z -axis, with respect to the plasma discharge.

Additionally, considering the parallel plate geometry of the VDBD, it is reasonable to assume that the electric field remains constant along the laser beam direction, i.e., $\frac{\partial E}{\partial z} = 0$, as depicted in Figure 4.8. This assumption holds under the condition that the plasma is diffused rather than filamentary, as elucidated in Section 4.3.2.

4.3.1 Ns EFISH experimental setup

The schematic of the experimental setup used for generating ns EFISH measurements is presented in Figure 4.9. In summary, the fundamental 1064 nm output from a ns pulse Nd:YAG laser pump (Opotek Opolette 355 LD, pulse duration of 7 ns full width at half maximum (FWHM), pulse repetition rate up to 20 Hz, with a "flat top" beam profile) is directed between the two parallel plane circular electrodes of the VDBD described in Section 2.2. The polarization plane of the laser beam can be adjusted using a zero-order half-wave plate (Thorlabs WPH05ME-1064) in a rotation mount (Thorlabs RSP1/M). The laser beam is focused between the electrodes by a 50 cm focal length lens. The polarization plane of the laser beam can be adjusted using a zero-order half-wave plate (Thorlabs WPH05ME-1064) in a rotation mount (Thorlabs RSP1/M). The laser beam is focused between the electrodes by a 50 cm focal length lens.

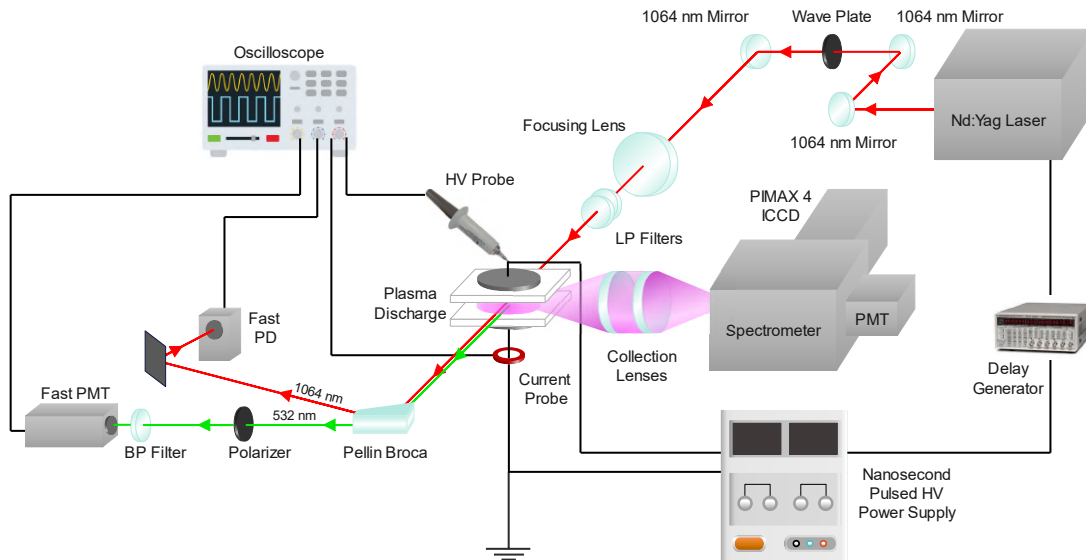


Figure 4.9: Experimental setup schematics of the nanosecond EFISH measurements (source: [145]).

The stray second harmonic signal generated within the focusing lens is blocked using an 850 nm long-pass (LP) filter (Thorlabs FGL850M). After passing through the electrodes, the laser beam contains the second harmonic signal at 532 nm, generated by the electric field between the electrodes, alongside the 1064 nm pump beam. The second harmonic beam is separated from the remaining pump beam using a Pellin Broca prism (Thorlabs ADBU-10) and is detected by a photomultiplier tube (Hamamatsu Fast PMT, model H10721-20, with a nominal rise time of 0.57 ns), as depicted in Figure 4.9. A thin film polarizer (Thorlabs PWISE050-A) in a rotation mount is positioned before the PMT to isolate the vertically polarized EFISH signal, generated by the vertical electric field component between the electrodes. A

narrow band-pass (BP) filter (Thorlabs FL532-10, 1" Laser Line Filter, $CWL = 532 \pm 2$ nm, $FWHM = 10 \pm 2$ nm) placed in front of the PMT blocks stray light and reflections from the pump laser beam. The PMT gain is adjusted to ensure linearity over the entire range of the measured electric field. A reflection of the 1064 nm beam, controlled by an iris diaphragm, is detected by a photodiode (AlphaLas Fast Photodiode UPD-200-UP, with a nominal rise time of ~ 175 ps) to monitor the time-resolved laser pulse intensity. The laser pulse energy remains stable within a 5% variation. The alignment of the optical system is achieved using the second harmonic generated by the optical parametric oscillator (OPO), which is subsequently removed.

The VDBD used for the measurements is described in detail in Section 2.2. The electrodes are held in a 3D-printed plastic electrode assembly mounted on a vertical translation stage, allowing for the adjustment of the relative position of the laser beam in the discharge gap. The process gas used is synthetic air (Rivoira, 5.0), flowing at 2 slm (or 2000 sccm) through an MKS flowmeter controlled by an MKS PR-4000. The gas can flow directly into the chamber or pass through a 500cc glass bubbler to produce humid air. Under normal laboratory conditions (21°C and atmospheric pressure), the relative humidity (RH) of the humid air is approximately 75%. The VDBD is powered by the nanosecond-pulsed high-voltage power supply described in Section 2.3. The pulse duration is 200 ns, and the voltage rise/fall time is 50 ns. It operates at a pulse repetition rate of 1 kHz. The discharge was initiated in a synthetic humid air environment with an applied voltage of ~ 11.5 kV.

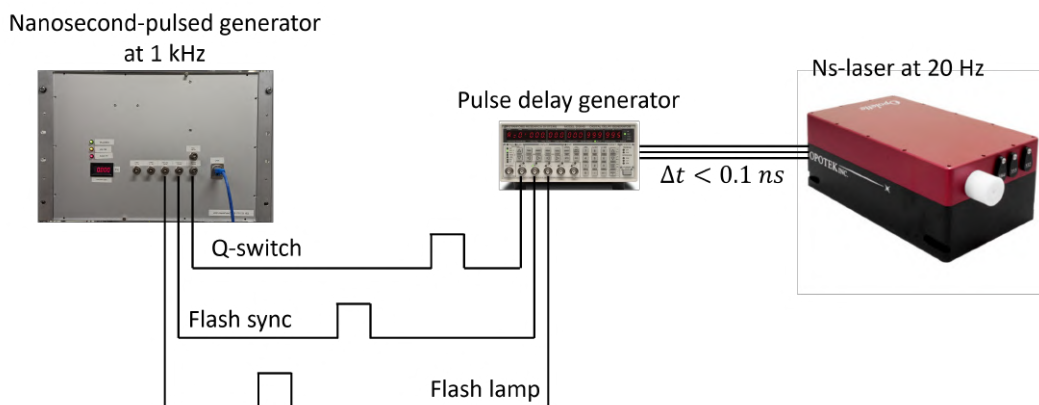


Figure 4.10: Schematics of the ns EFISH measurements triggering system.

The triggering system described in Section 1.1.5 was used to synchronize the ns-laser with the plasma discharge. A schematic of the specific triggering system used for the ns EFISH measurements is shown in Figure 4.10. The flash lamp, flash sync, and Q-switch of the laser are synchronized with the nanosecond pulse generator by means of the internal cards within the pulse generator itself, as well as an external delay generator (HP8112 A Pulse generator) to finely adjust the laser pulse delay with increments of 0.1 ns. It is important to note that the pulse frequency of the laser is 20 Hz, which is different from the repetition frequency of the plasma discharge. To capture the time-varying electric field in the discharge over a period longer than the laser pulse duration, the time delay of the laser pulse relative to the

high-voltage pulse is adjusted. This time delay can be varied by several hundred nanoseconds without affecting the laser pulse energy. The pulse voltage waveform is monitored by the high-voltage pulse generator's internal electronics using an integrated high-voltage probe (Hivolt model PHV4002-3), with a maximum voltage of 40 kV and a bandwidth of 100 MHz. The voltage is measured at the high-voltage electrode using a Tektronix P6015A probe with a maximum voltage up to 40 kV peak, a bandwidth of 75 MHz, and a rise time of 4.7 ns. The current is measured using a Magnelab CT-c1.0 Rogowski coil current monitor with a rise time of 0.7 ns, positioned on the ground electrode. The voltage waveform, photodiode signal, and PMT signal are recorded using a Keysight Infiniivision MSOX 6004 A Mixed Signal Oscilloscope with a 1 GHz bandwidth and a 20 Gsample/s rate.

The plasma light was also monitored to perform optical emission spectroscopy (OES). It was collected by two 30 cm focal length UV-grade quartz lenses, which projected a 1:1 image of the discharge gap onto the entrance slit of a monochromator. The imaged area is constrained by the entrance slit and can extend up to 3 mm in length and 5 mm in height. This light is then dispersed spectrally using a 30 cm spectrometer (Acton Spectra Pro 2300) equipped with a multiple-grating turret featuring 300/600/1200 grooves per millimeter, optimized at 300 nm. The resulting spectrum is recorded with a Princeton Instruments PI-MAX4 1024i CCD camera, which utilizes a 1024 x 1024 pixel sensor (pixel size: 12.8 μm , active area: 13.1 \times 13.1 mm²). One CCD image captured a spectral range of approximately 144/65/30 nm respectively, for the three different gratings. The emission spectra intensities recorded by the ICCD detector were corrected for both spectral and intensity distortions through calibration using halogen lamps. For broadband plasma imaging, the same UV-grade optical setup was utilized, along with a UV-grade objective to magnify the image and a dove prism to rotate the 2 cm \times 1.75 cm discharge image from horizontal to vertical. This ensured alignment with the monochromator's entrance. The ICCD gate duration was adjusted from 3 ns to 120 ns.

4.3.2 Analysis of the jitter between the plasma discharge and the laser pulse

An investigation of the jitters between the plasma discharges and the laser pulse has been conducted to ensure accurate synchronization. Figure 4.11 presents typical waveforms of voltage, current, and PMT output for a single discharge event. The plasma discharge typically initiates with a delay of approximately 90 ns after the onset of the high voltage pulse, as indicated by the second trace, showing the current pulse. Two distinct current peaks are discernible: one at the rising edge of the high-voltage pulse and a second one at the falling edge of the voltage pulse. The typical amplitude of the current pulse at the pulse's onset is approximately 6 A, while it measures around 2 A at the pulse's termination. For a single discharge event, we measured a full-width-at-half-maximum (FWHM) of approximately 15 ns for both current peaks. In addition to tracking the current waveform, the PMT signal records the SPS (0,2) band captured by the monochromator, providing a means to visualize the formation of the plasma discharge.

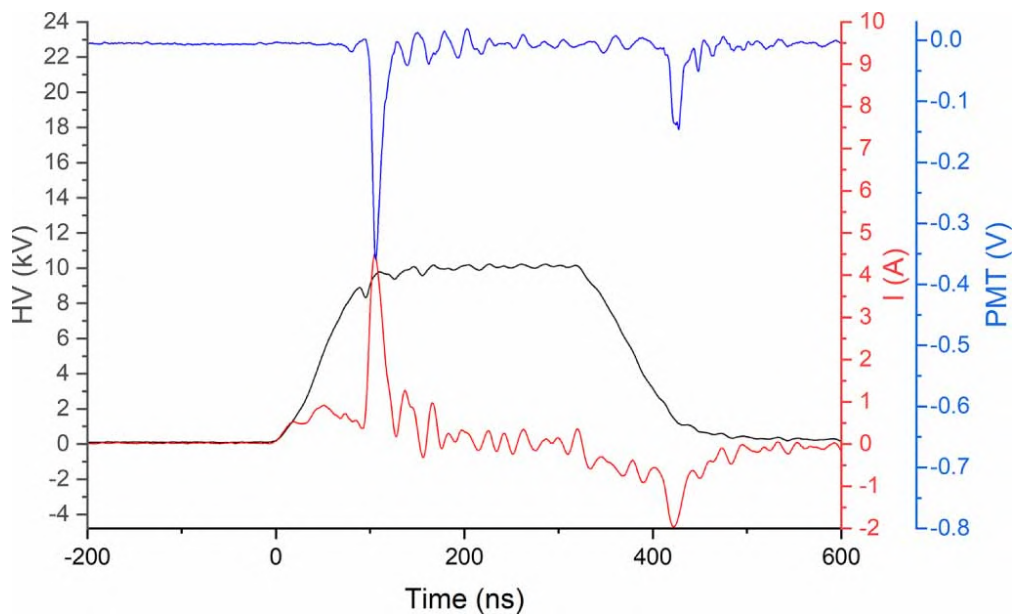


Figure 4.11: Typical voltage (black), current (red) and SPS(0,0) band emission taken through the monochromator using the PMT (source: [145]).

In the present discharge setup, we achieved a reduced overall jitter of the cathode- and anode-directed current, at the onset and switch-off of the HV pulse, with respect to the rising edge of the HV pulse. Figure 4.12 illustrates the distribution of the measured jitter, fitted with a normal distribution. The jitter is determined by tracking the maximum of the current peaks across 3500 single shots, which is more than ten times the typical number of shots used for the EFISH measurements. The FWHM of the normal distribution is approximately 1.7 ns for the first current peak (1) and 0.9 ns for the second current peak (2). The reduced jitter of the second peak can be attributed to a more stabilized condition compared to the discharge onset. Additionally, events with larger jitter or no current signals were not detected when a pre-warm-up procedure (involving a run of 500 shots) was conducted before the measurements. The measured jitter values provide sufficient precision for timing all measurements and recording sequences for statistically averaged imaging and spectroscopic measurements, as well as for current-voltage characteristics.

Another important aspect to consider is the jitter between the laser output pulse and the voltage pulse. We estimated this jitter by synchronizing the acquisition with the HV pulse. Figure 4.13 illustrates the results, interpolated with a normal distribution with an estimated FWHM of 3 ns. This observed jitter can be attributed to the trigger electronic chain used for conducting these measurements. To assess the potential impact of electronics jitter on time-averaged signals in EFISH measurements, we also evaluated the jitter distribution in the laser trigger chain. We acquired several thousand individual fundamental laser shots by employing a fast photodiode to trigger the oscilloscope in synchronization with the HV rising edge, similar to the current measurements. The outcomes are depicted in Figure 4.13.

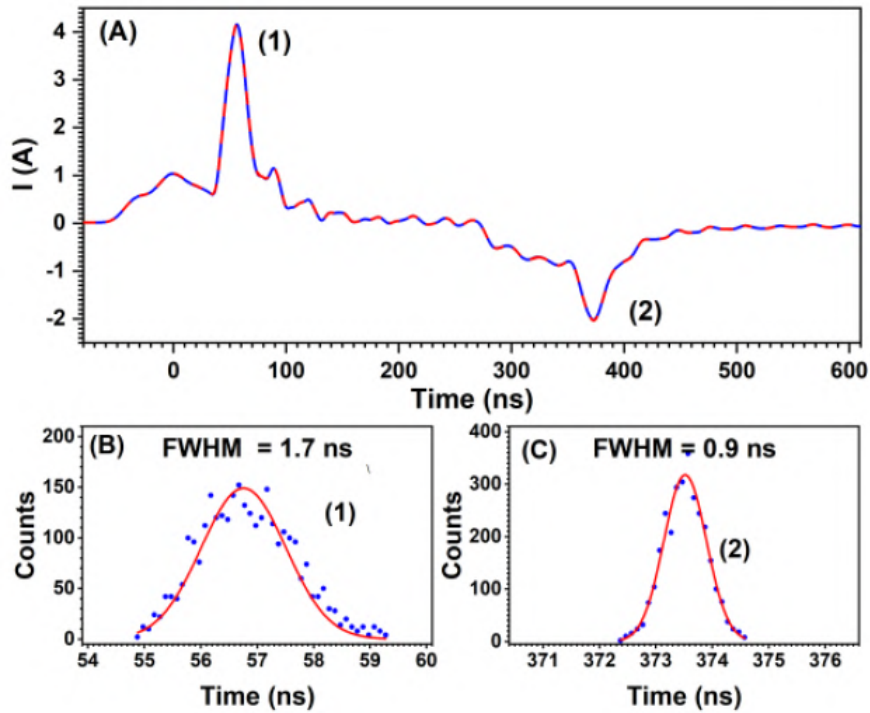


Figure 4.12: Current jitter, of the first (B) and second (C) current spikes, corresponding to the plasma discharges, with respect to the rising edge of the high voltage pulse (source: [145]).

In panel (A) of Figure 4.13, we present both the time-averaged laser pulse shot (averaged over 6,000 acquisitions) and the jitter-corrected data obtained from the same dataset. The jitter-corrected signals completely preserve the multimodal fine structure of the laser pulse, whereas the simple averaged signal smooths out this fine structure. It is essential to note that despite the normal distribution of the jitter delays having an FWHM of 3 ns, we do not observe the laser jitter's effect on the measured signal. This is because we trigger the acquisition using the fast photodiode rather than the HV pulse rising edge.

Indeed, the measured jitter implies that the current electronic chain operates with a response time faster than 4 ns, and any observed jitter will predominantly result from the external laser trigger electronics, although the fundamental shape of the signal will be preserved. However, this level of precision aligns well with the temporal dynamics of the processes we intend to investigate, of the order of ~ 1 ns. If we seek to enhance the time resolution further, it would necessitate a more resource-intensive approach. This approach would involve collecting statistically significant sets of single-shot voltage, current, PMT, and photodiode signals, followed by post-processing through techniques like time binning to correct for the observed time jitter. This methodology has been employed for the picosecond-pulsed laser EFISH measurements discussed in Section 4.4.

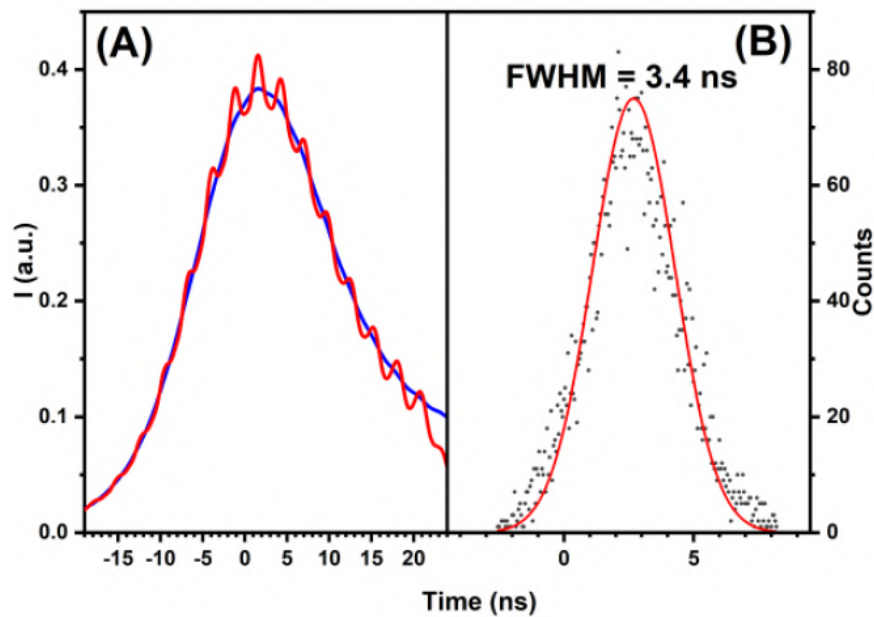


Figure 4.13: Jitter of the laser pulse with respect to the HV rising edge. (A) Averaged waveforms created by taking the simple average of 6000 individual waveforms (blue line) and the averaged waveform corrected for jitter (red line). (B) The distribution of peak positions over time and the corresponding normal distribution, displaying a FWHM of 3.4 ns (source: [145]).

4.3.3 Diffuse plasma discharge

Figure 4.14(A) displays a single-shot image of the broadband plasma emission taken during the discharge pulse, employing a camera gate duration of 50 ns. The images were captured under conditions of both humid air, achieved by passing air through the bubbler, and dry air. Notably, the plasma in humid air exhibits a diffused behavior, with emission filling the entire discharge gap, with no isolated filaments that are apparent in the case of dry air. The transition from filamentary to diffuse plasma, by introducing water vapor in the gas mixture is not yet well understood, and under investigation. Employing a complete kinetic model could potentially provide a solution to this investigation. The diffuse nature of the discharge in synthetic humid air is further affirmed by single-shot images from an ICCD kinetic series, recorded with a camera gate of 3 ns, shown in Figure 4.14(B). A comparison between the single-shot PMT signals and the full vertical binning emission intensities reveals a high degree of agreement. This finding leads us to conclude that the jitter of the current with respect to the HV rising edge has negligible effects on the images, and consequently, on the spectra acquired by the ICCD.

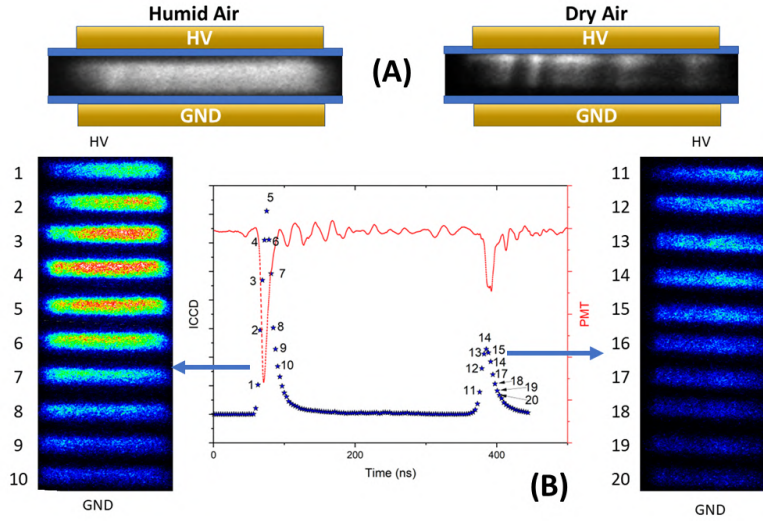


Figure 4.14: (A) Compilation of individual plasma emission images captured during the discharge pulse, employing a camera gate duration of 50 ns, in both humid and dry air. (B) Kinetic images obtained using a fixed gate duration of 3 ns during the emission of the 1st and 2nd discharge pulses in humid air. The gate position corresponds to the point highlighted in the PMT (red) and ICCD (blue) intensities plot (source: [145]).

4.3.4 Ns EFISH calibration

The electric field is determined from the time-resolved PMT and photodiode waveforms, $I^{(2\omega)}(t)$ and $I^{(\omega)}(t)$, respectively, through the following equation:

$$E_{ext}(t) = A \frac{\sqrt{I^{(2\omega)}}}{I^{(\omega)}}, \quad (4.7)$$

where A is the calibration constant that accounts for all constant quantities between the calibration measurements and the plasma discharge measurements, as described in Section 4.2. To determine the stray phase shift between the PMT (second harmonic) and photodiode (pump laser) signals, we rely on the measurement of the steady-state Laplacian electric field. The term Laplacian electric field denotes a steady electric field that can be defined as:

$$E = \frac{\Delta U}{d}, \quad (4.8)$$

where ΔU represents a constant voltage drop, and d represents the effective gap distance. This is the electric field generated between two electrodes with a voltage drop, and it is achieved in the VDBD below voltage breakdown, meaning the VDBD acts as a capacitor and the electric field follows Equation 4.8. During these measurements, the ratio of the square root of the PMT waveform to the photodiode waveform should remain constant since the electric field is

constant, as elaborated in [168].

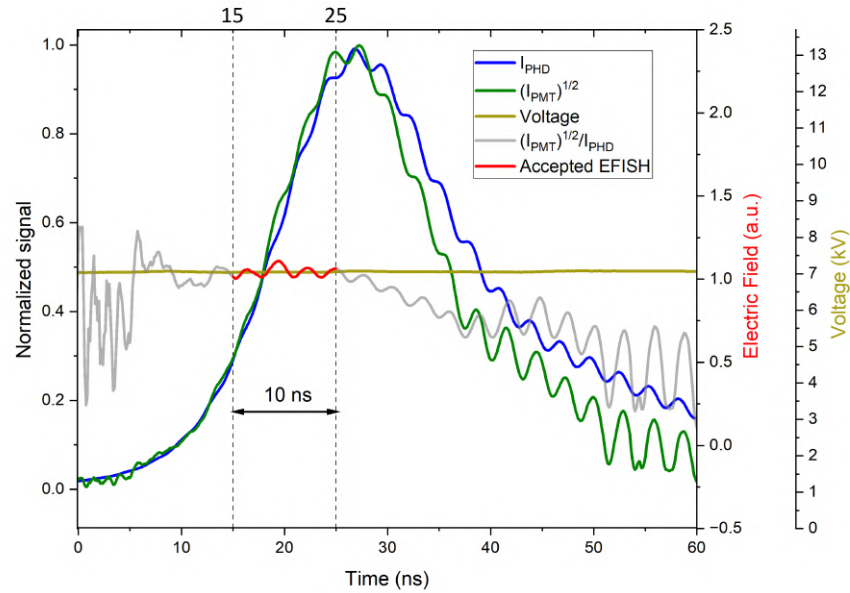


Figure 4.15: Normalized square root of the PMT signal (green), obtained under constant electric field conditions, superimposed with the photodiode signal (blue). Both signals are the result of an average of 256 laser shots. Additionally, the ratio of these signals is presented (grey). The labeled section of the graph indicates the time interval within which the time-accurate EFISH data can be observed (red). The gas pressure is $p = 760$ torr and the laser pulse energy is 9 mJ. The constant applied voltage (yellow) is also reported (source: [145]).

Figure 4.15 presents a comparison between the normalized and averaged square root of the PMT (EFISH signal) and photodiode waveforms, recorded over 256 laser shots. These measurements were conducted in air at atmospheric pressure, under the influence of a constant Laplacian electric field, and with a laser pulse energy of 9 mJ. To preserve the waveform's fine details, the triggering was performed at the fast photodiode's rising edge. During a significant portion of the laser pulse's duration, the observed ratio between the two waveforms, which is directly proportional to the electric field (as indicated by Equation 4.7), remained constant for nearly 10 ns. This result suggests the feasibility of measuring the temporal variation of the electric field during the laser pulse, denoted as $E_{ext}(t)$. For calibration, the Laplacian electric field was determined by applying a constant voltage and a sub-breakdown voltage pulse to the electrodes. Figure 4.16 illustrates the temporal calibration of the EFISH data using a Laplacian electric field pulse lasting approximately 400 ns. The electric field was generated by a sub-breakdown high-voltage pulse with a maximum peak voltage of 7 kV at a pressure of 1 atmosphere, and it was measured using the Tektronix P6015 (75 MHz) high voltage probe.

The EFISH-measured electric field waveforms, displayed in Figure 4.16, were obtained by

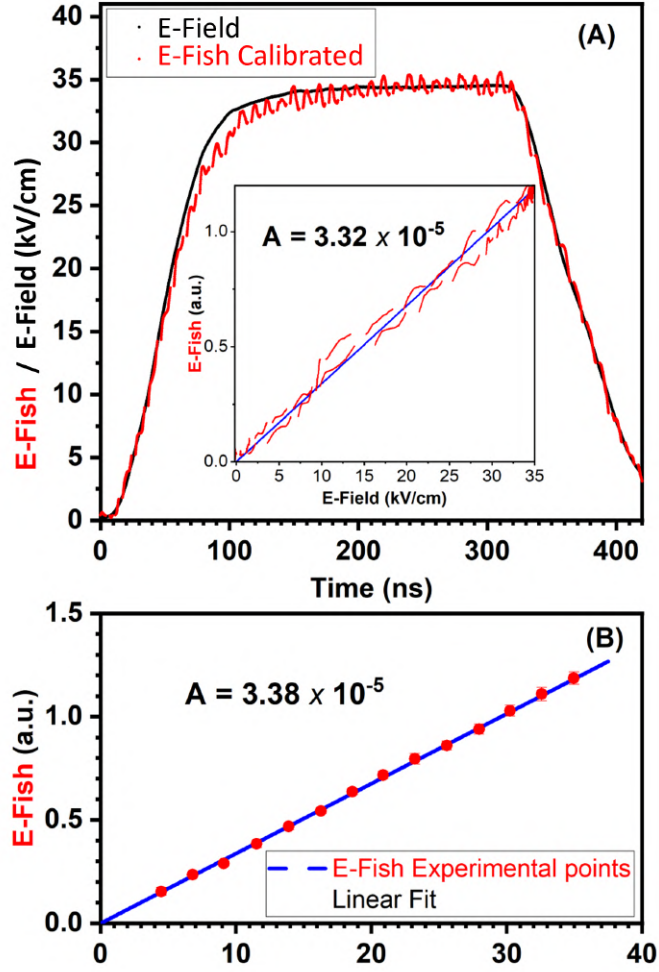


Figure 4.16: The calibration of EFISH signals is accomplished by employing either a voltage pulse (A) or a constant voltage (B). The corresponding calibration factors A obtained from these calibration methods are presented in the figures (source: [145]).

modifying the delay time between the high-voltage pulse and the laser pulse, resulting in more than 50 data sets with up to 10 ns of data utilized in each interval, as displayed in Figure 4.15. The individual data sets with partially overlapping intervals were merged to create the final data sets. In Figure 4.16, the EFISH signal is plotted against the applied electric field in the gap, computed using the following equation:

$$E_{\text{app}}(t) = \frac{U_{\text{app}}(t)}{d^*}, \quad (4.9)$$

where $U_{\text{app}}(t)$ represents the applied voltage, and d^* represents the effective gap distance, which accounts for the voltage drop due to the dielectric surfaces. Specifically, $d^* = d + 2l/\epsilon_r$,

where d equals 1.75 mm for the air gap, l is 0.66 mm for the thickness of each dielectric layer, and $\epsilon_r=9.8$ is the relative dielectric constant of the alumina layer. The comparison reveals that the electric field waveform, inferred from EFISH measurements, closely matches the applied voltage waveform during the voltage waveform rising phase. This observation underscores the temporal accuracy of the composite EFISH data. A calibration curve is then generated by examining the complete EFISH raw data set versus $E_{\text{app}}(t)$, resulting in a calibration constant of $A = 3.32 \times 10^{-5}$. To validate the accuracy of this calibration, an alternative approach was employed, involving a constant HV value and the measured EFISH mean value. The calibration curve derived from this method is presented in Figure 4.16(B). The calibration constant, in this case, is $A = 3.38 \times 10^{-5}$, which is in close agreement with the value obtained using the HV voltage pulse.

4.3.5 Ns EFISH results

The EFISH measurements were conducted during the plasma discharge at three distinct spatial positions, as depicted in the upper section of Figure 4.17. The chosen positions correspond to the maximum distance in the VDBD that the laser beam could traverse without significantly reducing its energy upon exiting. We can assume that, in positions (A) and (C), the laser merely grazes the dielectric barriers, the electric field observed is a spatially integrated representation of the field experienced by the entire volume of the laser beam. At the VDBD entrance, the beam's waist is estimated to be approximately 800 μm . Thus, position (A) represents the point nearest to the high-voltage electrode, (B) corresponds to the midpoint within the gap, and (C) is the closest position to the ground (GND) electrode. The delay time between the high-voltage pulse and the laser pulse was adjusted by 70 increments, with variations ranging from 5 ns on the rising and falling edges to 10-20 ns during the plateau. Figure 4.17 displays EFISH data obtained during the discharge operation, alongside the effective electric field derived from the applied voltage waveforms and the discharge current. On both the rising and falling edges of the HV pulse, the EFISH signal experiences a sign reversal, attributable to the accumulation of residual surface charge on the dielectric material. Since EFISH measurements record the electric field's absolute value, the sign reversal appears as a "dip" in the raw data, reaching the background noise level, with a zero field value at the point of reversal. This necessitates manual adjustment of the field's sign reversal to align with the applied voltage values.

The resulting EFISH measurements, presented in Figure 4.17, exhibit a strong agreement between the electric field as determined from the voltage measurements and the applied voltage waveform, until the point of breakdown, across all three positions. Following the initiation of breakdown, there is a relatively swift decrease in the electric field in all positions, a trend also reflected in the current measurements. However, after the breakdown commences, the electric field, in all cases, never reaches zero. Instead, there is an observed gradual increase in the field, continuing until approximately 300 ns.

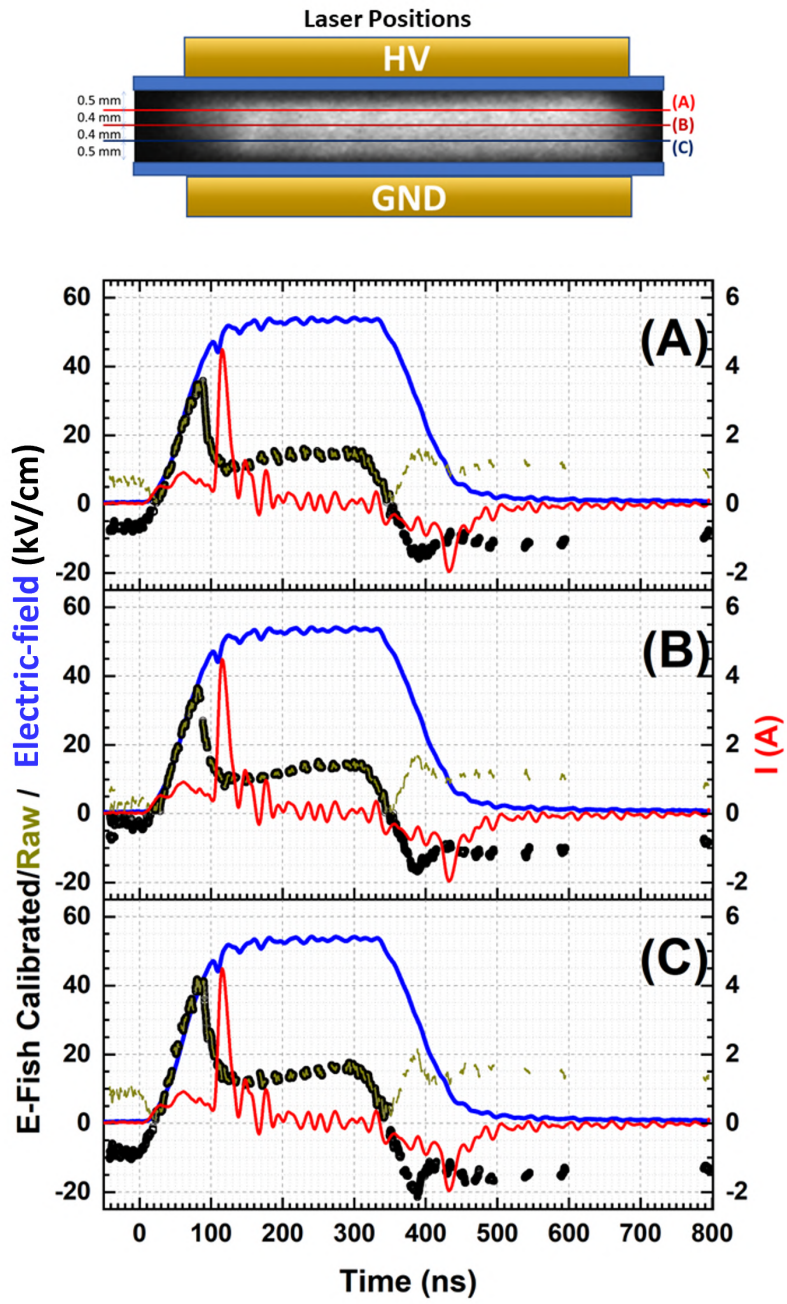


Figure 4.17: Time-resolved measurements within the discharge gap at three distinct vertical positions, as indicated in the upper section of the figure. The figure provides a view of the following data: EFISH signal (black dots), raw EFISH signal (brown dots), Laplacian electric field (blue), and current data (red) (source: [145]).

4.4 Picosecond-pulsed laser EFISH in the VDBD plasma discharge

To validate the ns EFISH measurements conducted in Bari and enhance their spatial and temporal accuracy, we replicated the same experimental setup at the Bio-Lab in the SPC. The primary objectives of these measurements are twofold: firstly, to replicate the results obtained in Bari, thereby confirming the reliability of the method employed to achieve a time resolution shorter than the laser pulse duration. Secondly, we aimed at optimizing the focusing of the laser beam to approach the dielectric surface more closely, investigating potential variations in the electric field evolution as we get closer to the dielectric surface. Accomplishing this necessitated specific modifications to the experimental setup, accounting for differences between the lasers used in the two setups and the need to focus the laser beam into a narrower beam waist over an extended distance equal to the length of the electrodes. The considerations regarding the consequences of focusing the laser beam in the ns EFISH measurements are also valid for the picosecond-pulsed laser EFISH measurements, hence the precautions taken are still valid.

4.4.1 Diode pumped high energy picosecond Nd:YAG laser

For these measurements, a picosecond laser, specifically the PL2231-50 by EKSPLA [169] shown in Figure 4.18, was utilized.

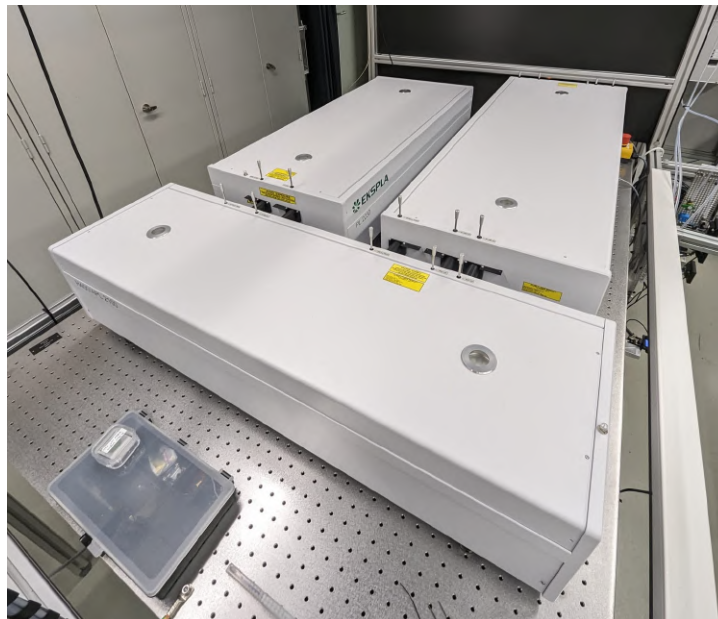


Figure 4.18: Picture of the EKSPLA Diode Pumped High Energy Picosecond Nd:YAG Laser on the optical bench [169].

This laser system consists of a diode-pumped solid-state (DPSS) master oscillator, housed within a sealed monolithic block. It generates high repetition rate pulse trains at 87 MHz, with individual pulse energies in the range of several nJ. To amplify these pulses, diode-pumped

amplifiers were employed, allowing for output energies of up to 30 mJ. The regenerative amplifier, with an impressive amplification factor nearing 10^6 , precedes a multipass power amplifier. This power amplifier is optimized for efficiently extracting stored energy from the Nd:YAG rod, while preserving a nearly Gaussian beam profile and minimizing wavefront distortion. The output pulse energy can be finely adjusted in steps of approximately 1%, while maintaining pulse-to-pulse energy stability at less than 0.5% rms at 1064 nm. The generation of second, third, and fourth harmonics is facilitated through angle-tuned KD*P and KDP crystals, which are housed in thermally stabilized ovens. Harmonic separators are employed to ensure that each harmonic maintains high spectral purity and is directed to distinct output ports. Continuous monitoring of the output pulse energy is facilitated by built-in energy monitors. Information from these energy monitors can be observed on a remote keypad or displayed on a PC monitor. Furthermore, the laser system provides triggering pulses for synchronizing with associated equipment. The key parameters of the laser system are summarized in Table 4.1. In Figure 4.19 the typical energy, at maximum amplification, of the laser beam as a function of wavelength is presented.

Table 4.1: Main parameters of the picosecond-pulsed laser.

Wavelength range	192-2300 nm
Pulse energy stability (StdDev)	~ 1%
Pulse duration	~28 ps
Pulse frequency	50 Hz
Polarization	Vertical
Beam profile	Gaussian
Beam divergence	< 0.7 mrad
Beam diameter	~4 mm

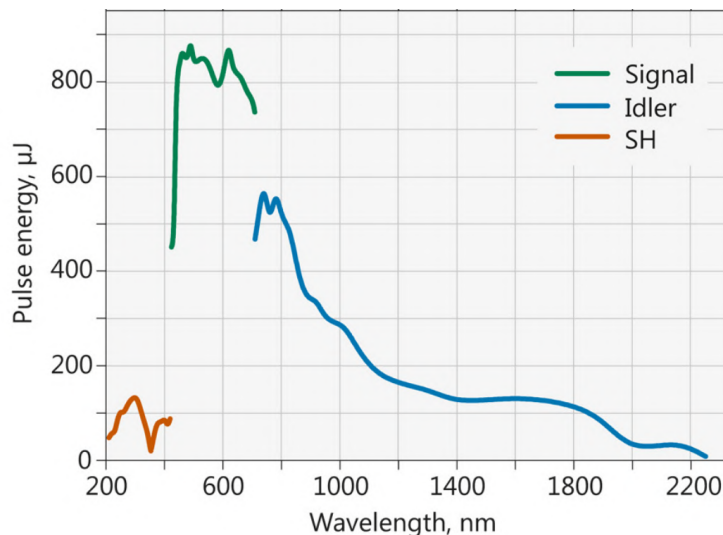


Figure 4.19: Typical energies of the PL2231-50 by EKSPLA, at maximum amplification, with respect to the emission wavelength [169].

4.4.2 Ps EFISH experimental setup

The schematic of the experimental apparatus applied in the ps EFISH generation diagnostics is depicted in Figure 4.20.

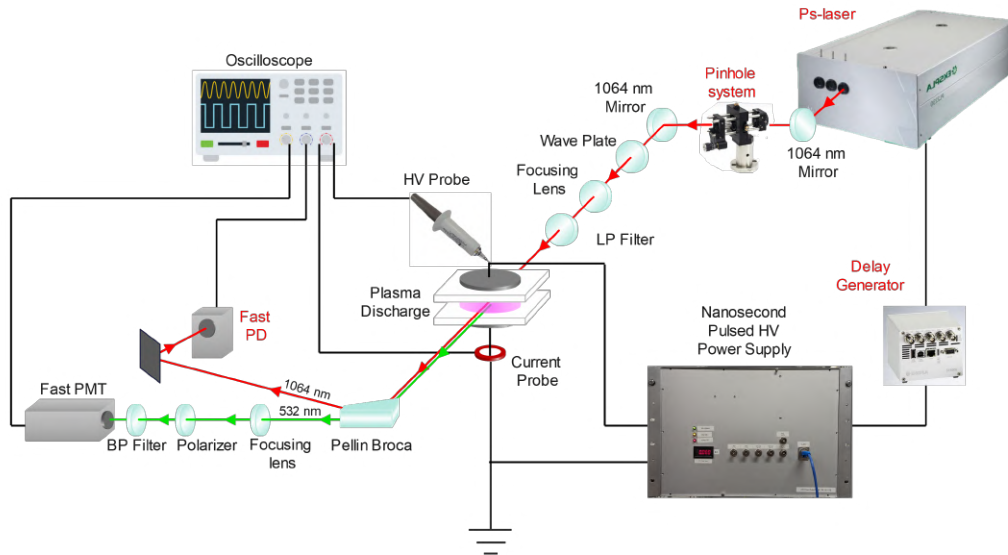


Figure 4.20: Experimental setup schematics of the ps EFISH measurements. The differences with the ns EFISH experimental setup are labeled in red.

The experimental setup employed for the ps EFISH measurements closely mirrors the one used in Bari, with the exception of a few adjustments needed to use a laser with a different triggering system and certain enhancements designed to refine the spatial resolution of the measurements. The main difference involves the integration of a spatial filter, implemented through a pinhole system, highlighted in red in Figure 4.20. The schematics of this process are illustrated in Figure 4.21.

The Gaussian beam of a laser may often exhibit spatially varying intensity irregularities, which cause noise at the edge of the beam, as depicted in Figure 4.22a. To selectively isolate the clean portion of the beam while blocking the "noise" fringes, a pinhole can be precisely centered on the central Gaussian spot. This process is visually illustrated in Figure 4.22. This adjustment yields an improved Gaussian beam quality and a more compact beam diameter. Consequently, it enables the laser to achieve enhanced spatial resolution and approach the surface of the dielectric without clipping on the side of the VDBD. For these measurements, we employed a stainless steel pinhole with a diameter of $75\ \mu\text{m}$ (Thorlabs P75K), and 25 mm N-BK7 aspheric lenses, $f = 50\ \text{mm}$ (Thorlabs AL2550-C) to focus the beam into the pinhole, installed on an

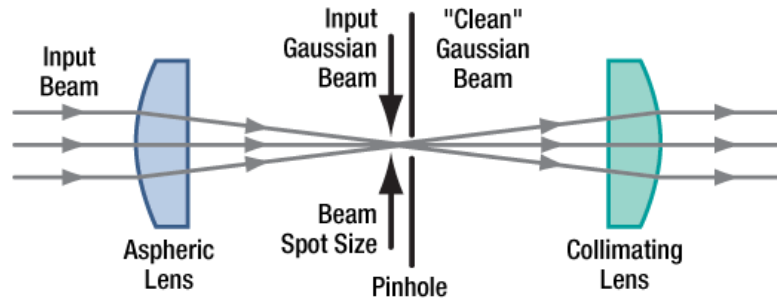


Figure 4.21: Spatial filter based on a pinhole adjustment setup. The Gaussian beam is narrowly focused in a pinhole of appropriate dimensions to clean the fringes of the Gaussian beam (source: [170]).

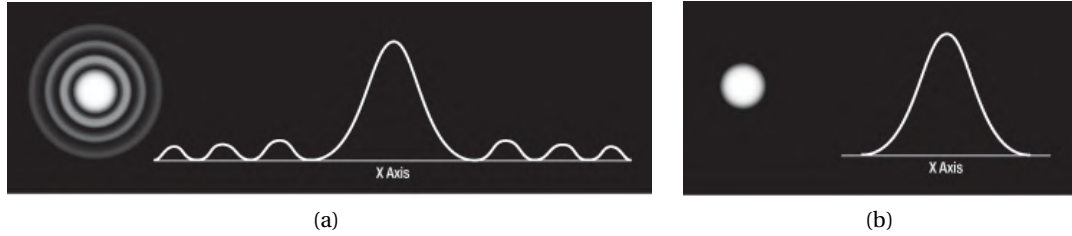


Figure 4.22: (a) Input Gaussian beam with side fringes. (b) Cleaned Gaussian beam after passing through the pinhole (source: [170]).

adequate system shown in Figure 4.23a. The diameter of the pinhole was chosen taking into account the diameter of the focused point D according to:

$$D = \frac{f \cdot \lambda \cdot M^2}{\phi}, \quad (4.10)$$

where f is the focal length of the aspheric lens, λ is the wavelength of the beam, M is the laser beam quality factor, and ϕ is the radius of the laser beam at the aspheric lens [170]. Given the parameters $f = 50$ mm, $\lambda = 1064$ nm, $M = 2.5$, and $\phi = 3$ mm in this setup, we can calculate the beam diameter D as approximately $44 \mu\text{m}$. To ensure effective performance, the pinhole should be selected to be roughly 30% larger than D , as a safety rule [170], which led us to choose a pinhole with a diameter of $75 \mu\text{m}$. It is essential to avoid a pinhole that is too small, as this could result in clipping the laser beam at the edges of the pinhole, diminishing the quality of the signal.

The fundamental 1064 nm output generated by the picosecond laser (as described in Section 4.4.1) is directed to the spatial filter using Nd:YAG dual-order laser mirrors (Thorlabs NB1-K13), accommodating both the fundamental (1064 nm) and the 2nd harmonic (532 nm), for alignment purposes. Upon traversing the spatial filter, the cleaned laser beam is directed between the two parallel plane circular electrodes of the VDBD, described in detail in Section

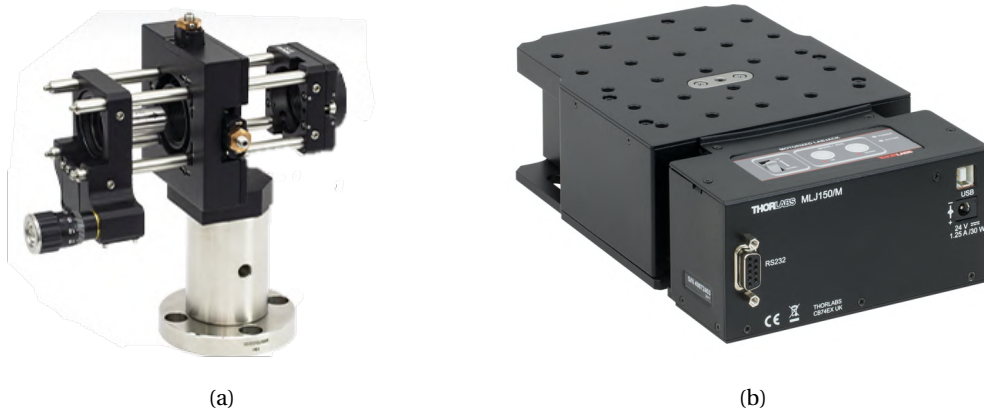


Figure 4.23: (a) Pinhole adjustment system. (b) Motorized high-load vertical translation stage.

2.2. The polarization plane of the laser is initially vertical (as indicated in Table 4.1). However, for fine adjustments and to correct minimal errors, a polymer zero-order half-wave plate (Thorlabs WPH10E-1064) is employed, fixed in a rotation mount. Stray second harmonic signals generated within the focusing lens and residual signals stemming from the laser optical parametric generator (OPG) are effectively blocked using an 850 nm long-pass (LP) filter (Thorlabs FGL850M). A 50 cm focal length lens is utilized to focus the laser beam between the electrodes, as depicted in Figure 4.20. The VDBD is situated on a motorized high-load vertical translation stage (Thorlabs MLJ150/M), shown in Figure 4.23b, allowing for precise control of the laser beam vertical position within the plasma discharge with an accuracy of $<30\ \mu\text{m}$.

Following its passage between the electrodes, the laser beam contains both the second harmonic signal at 532 nm, generated by the electric field between the electrodes, and the 1064 nm pump beam. The second harmonic beam is separated from the remaining pump beam using a Pellin Broca prism (Thorlabs ADBU-10), refocused, and then detected by a photomultiplier tube (Hamamatsu Fast PMT, model H10721-20, nominal rise time of 0.57 ns). To isolate the vertically polarized EFISH signal, which arises from the vertical electric field component between the electrodes, a thin film polarizer (Thorlabs PWISE050-A) on a rotation mount is positioned before the PMT. To eliminate stray light and reflections of the fundamental harmonic, a narrow band-pass (BP) filter (Thorlabs FL532-10, $\text{CWL} = 532 \pm 2\ \text{nm}$, $\text{FWHM} = 10 \pm 2\ \text{nm}$) is placed in front of the PMT. The PMT gain, set at 0.6 V, is chosen to ensure linearity across the entire range of the measured electric field. The PMT was originally powered by a power supply provided by the same manufacturer (Hamamatsu). This power generator, however, was susceptible to picking up significant electronic noise generated by the laser components. Despite several attempts to reduce this noise by shielding the power supply, the cables, and the PMT, these efforts proved ineffective. Hence, we opted to replace the power supply with batteries, all encased in a Faraday cage. This solution was the only one proven to be successful. A photodiode (Thorlabs DET10A2) is used to detect a reflection of the 1064 nm beam, which is controlled by an iris diaphragm. This serves to monitor the time-resolved laser pulse intensity,

which remains stable within a 1% margin. The alignment of the optical system was initially attempted with the aid of a collimated laser-diode-pumped diode-pumped solid-state (DPSS) laser module at 532 nm (Thorlabs CPS532-C2), for safety reasons. This technique, frequently used in the alignment process of an optical configuration, proved to be ineffective due to the significant impact caused by the tiniest variation in the laser beam characteristics, such as beam width, energy, and so on. Consequently, the alignment was ultimately carried out using the ps-laser beam. The process gas is synthetic air, flowing at 1000 sccm through a Bronkhorst mass flow controller into a 500 cc glass bubbler filled with deionized water to produce humid air. The voltage waveform is monitored by the nanosecond-pulsed power supply internal electronics using an integrated high-voltage probe (Hivolt model PHV4002-3), with a maximum voltage of 40 kV and a bandwidth of 100 MHz. Simultaneously, it is measured at the high voltage electrode using a high voltage probe (PMK PHV 4002-3, 1000:1 attenuation). The current delivered during the discharge is measured by a Rogowski coil current monitor situated on the ground electrode. The voltage waveform, current, photodiode (PD) signal, and PMT signal are all captured by a Teledyne Lecroy oscilloscope (Lecroy HDO WavePro 404HD), boasting a 4 GHz bandwidth and a sampling rate of 20 Gsample/s.

4.4.3 Single-shot measurements method

In contrast to the ns EFISH measurements, where synchronization was governed by the time response of the instruments, a similar approach was unfeasible in the case of the ps EFISH measurements. This was primarily due to an unavoidable jitter introduced when the picosecond laser is externally triggered. As described in Section 4.4.1, the ps-laser operates with a master oscillator, generating pulse trains at a frequency of 87 MHz. This inherent pulse train frequency leads to an approximately 11 ns jitter when externally triggering the laser. While this issue could be solved by using the laser itself as the master trigger, the nanosecond-pulsed power supply lacked the capability to accept external triggers.

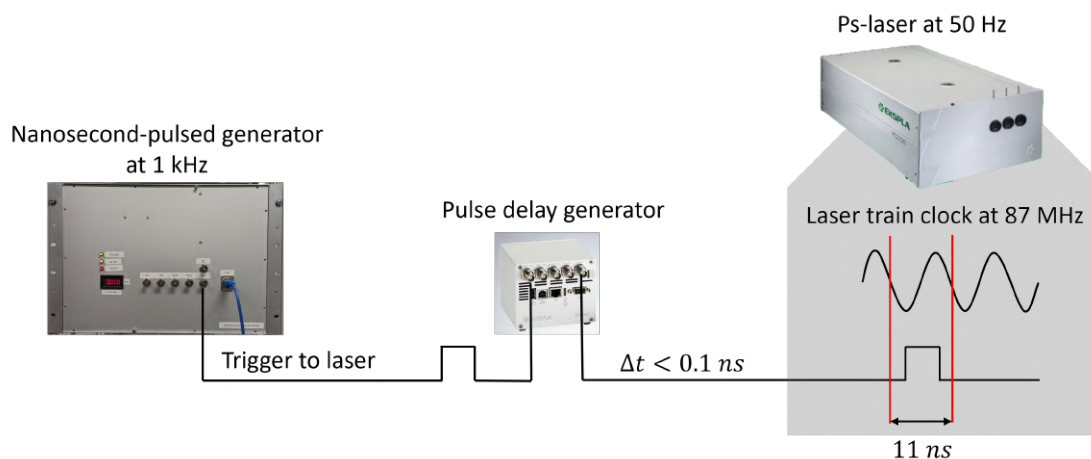


Figure 4.24: Schematics of the ps EFISH measurements triggering system.

Moreover, the endeavor to scale up the ps-laser 50 Hz frequency to the 1 kHz plasma discharge frequency while keeping the signal jitter under 1 ns proved to be a far more difficult challenge than originally anticipated.

We adopted an approach akin to that used in Ref. [148] and Ref. [171]. We retained the nanosecond-pulsed power supply as the master trigger, with the laser externally triggered by it, as depicted in Figure 4.24 and we conducted the measurements as single-shot acquisitions to counter the jitter arising from the passive generation of the laser pulse trains. This approach allowed us to calculate the delay between the laser pulse and the voltage waveform in post-processing for each individual measurement, providing a time position with an accuracy of < 1 ns. Given that the nanosecond-pulsed power supply trigger system had a minimum time-step of 50 ns, we employed a pulse delay generator (Eksma SY4000-OEM) to achieve time-steps as short as 0.1 ns. In contrast to the ns EFISH measurements, the ps-laser pulse duration is much shorter (~ 28 ps) than the response time of the PMT and photodiode.

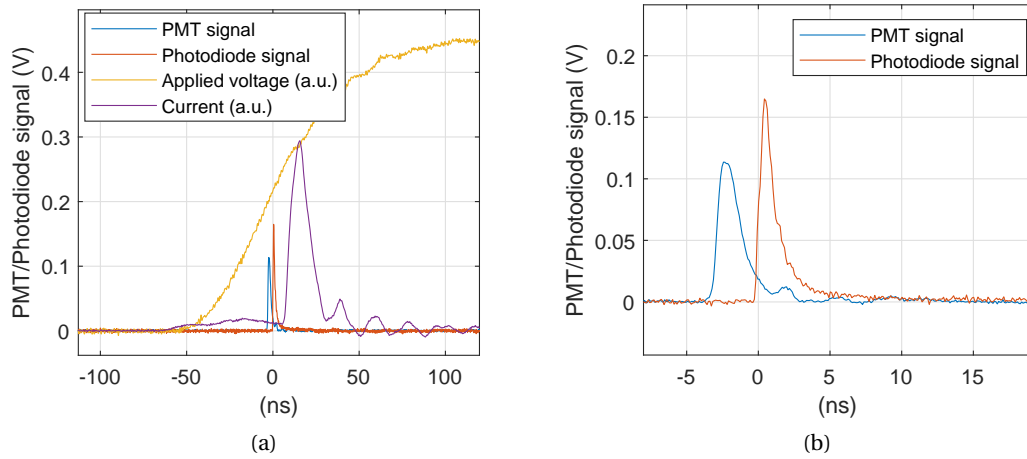


Figure 4.25: (a) Waveforms acquired in a single-shot measurement: PMT and photodiode signals in volts, and applied voltage and current, reported in arbitrary units. (b) Zoom in of the photodiode and PMT signals, corresponding to the 1st and 2nd harmonic signals.

Consequently, the signals captured by these detectors lack temporal information concerning the electric field evolution during the laser pulse. Given this substantial discrepancy between the event duration and the response time of the detectors, the electric field can be considered constant during the time span of the laser pulse. Consequently, the electric field can be obtained from the EFISH signal generated by a single shot through integration of the PMT and photodiode signals, as outlined below:

$$E_{ext}(t) = A \frac{\int \sqrt{I^{(2\omega)}(t)} dt}{\int I^{(\omega)}(t) dt}. \quad (4.11)$$

The PMT and photodiode signals, which correspond to the $I^{(2\omega)}(t)$ and $I^{(\omega)}(t)$ signals, are displayed in Figure 4.25 for a single-shot acquisition, together with the applied voltage and current that were used to time-synchronize the measurement in post-processing.

4.4.4 Analysis of the jitter between the plasma discharge and the laser pulse

In theory, the time resolution is primarily determined by the laser pulse duration and the bandwidth of the data acquisition system. Since each measurement corresponds to a single laser pulse event, it offers a high potential for time resolution. However, the uncertainty introduced by the jitter of the plasma discharge relative to the voltage pulse affects the overall time accuracy of the measurements. Despite this limitation, the technique enables monitoring of the electric field dynamics much faster than the synchronization uncertainty caused by the plasma discharge jitter, since each measurement captures a snapshot of the electric field with a duration of approximately ~ 28 ps, the laser pulse duration. The delay between the rising edge of the voltage pulse waveform and the rising edge of the plasma discharge current has been calculated for each individual shot and used to compute the probability distribution function (PDF), with a resolution of 200 ps, as illustrated in Figure 4.26a. The dataset corresponds to the Ground position for a total of 3732 laser shots. The FWHM of the PDF computed from the data is 1.2 ns.

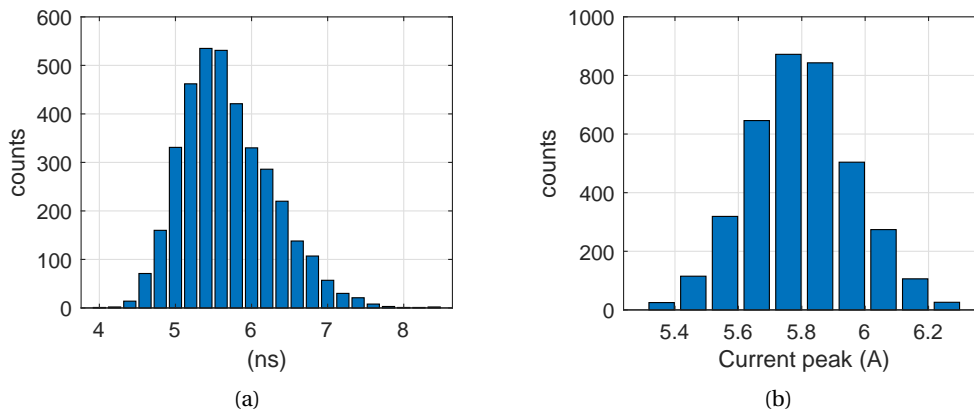


Figure 4.26: (a) PDF of the time jitter of the plasma discharge with respect to the voltage pulse. Distribution of the delay between the rising-edge of the voltage pulse waveform and the rising-edge of the plasma discharge, averaged into 200 ps bins. (b) PDF of the maximum of the first current peak, binned in 0.1 A.

Since the dynamics of the electric field are predominantly influenced by the plasma discharge, a solution to reduce the time inaccuracies caused by the jitter between the plasma discharge and the voltage pulse is to use the rising edge of the current peak as a reference point for signal synchronization in place of the rising edge of the voltage pulse. Indeed, the current peak marks the development of the plasma discharge. Therefore, it seems logical to designate the initiation of the current spike as the starting point for time synchronization. However, it is important

to note that the plasma discharge current exhibits slight variations with each repetition. Consequently, an additional source of uncertainty stems from the inherent instability of the plasma discharge, which can alter the electric field following the discharge. This is shown in Figure 4.26b, where for each individual shot, we have computed the maximum of the first current spike and then obtained the PDF with a resolution of 0.1 A, using the dataset associated with the Ground position. The FWHM of the PDF extracted from this dataset is measured to be 0.3 A. The measurements have been synchronized based on the current rising edge. Nevertheless, no notable enhancement in the results was observed. Consequently, all subsequent results are presented with a delay relative to the rising edge of the voltage pulse.

4.4.5 Ps EFISH calibration

The calibration process for the ps EFISH measurements is performed by applying a Laplacian electric field to the electrodes, similar to the approach utilized for the ns EFISH measurements, as extensively described in Section 4.3.4. The EFISH signal is acquired during the flat top of the nanosecond pulse waveform, where the electric field is constant, at increasing applied voltages below the plasma breakdown voltage. The computation of the electric field applied to the air gap relies on the material properties and dimensions of the VDBD system, assuming a Laplacian electric field and employing Equation 4.9. The laser energy used throughout the measurements is ~ 0.3 mJ.

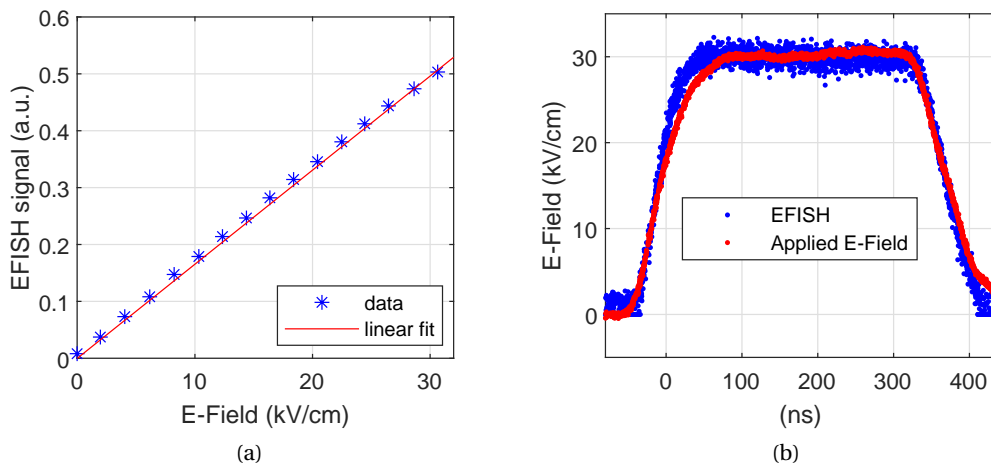


Figure 4.27: (a) Ps EFISH signal in arbitrary units at increasing applied electric field in the air gap of the VDBD. The measurements are taken at a fixed position in time at the flat top of the nanosecond pulse waveform where the electric field is constant, nominally at 200 ns (see (b)). (b) Ps EFISH signal evolution over the duration of the nanosecond voltage pulse at 8 kV, expressed in kV/cm obtained from Equation 4.9 within the air gap of the VDBD.

Subsequently, a calibration curve is constructed by performing a linear fit of the EFISH data against the electric field applied to the gap, as depicted in Figure 4.27a. This analysis yields a

calibration constant of approximately $A \approx 60.5$. To assess the accuracy of this calibration, the temporal evolution of the EFISH signal during the nanosecond pulse waveform at a voltage below the plasma breakdown voltage, specifically 8 kV, has been measured. The resulting data has been calibrated using the constant A obtained from the calibration curve and then compared to the applied electric field. In Figure 4.27b, the calibrated EFISH raw data, presented without any averaging or binning, for each individual shot, totaling approximately 3000 measurements, is plotted alongside the applied electric field. Indeed, the electric field waveform deduced from the EFISH measurements closely matches the applied voltage waveform, underscoring the reliability of the calibration constant and affirming the temporal accuracy of the composite EFISH data.

4.4.6 Ps EFISH results

The ps EFISH measurements were performed at three distinct vertical positions within the air gap of the VDBD. Thanks to the spatial filtering achieved by adjusting the pinhole and utilizing a vertically motorized translation stage, we managed to achieve a beam width of approximately $270 \mu\text{m}$ at the edge of the electrode, as depicted in Figure 4.28.

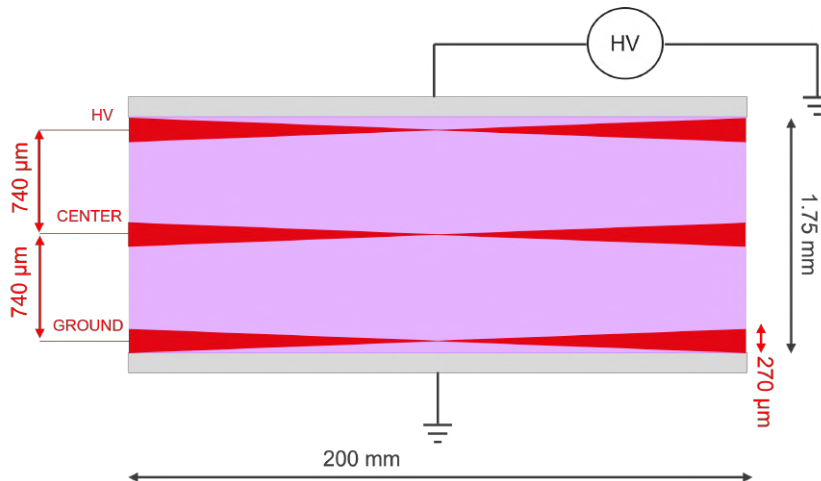


Figure 4.28: Position of the laser beam passing inside the gap of the VDBD. The scheme shows the three distinct positions used for the EFISH measurements: Center, HV and Ground. The diagram also highlights that the beam width at the edge of the VDBD electrode measures approximately $270 \mu\text{m}$.

This represents a substantial enhancement compared to the $800 \mu\text{m}$ spatial resolution achieved in the ns EFISH measurements. The three positions investigated were: in the center of the VDBD gap, referred to as Center, and positions near the high-voltage and grounded electrodes, denoted as HV and Ground, respectively. The voltage of the ns pulse delivered to the VDBD was set at 11.6 kV, corresponding to a $\sim 1.7 \text{ W}$ of power dissipated into the plasma, according to the result in Section 3.4.3. Figure 4.29 shows a representative dataset of ps EFISH measurements obtained during the voltage pulse at the Center position within the gap.

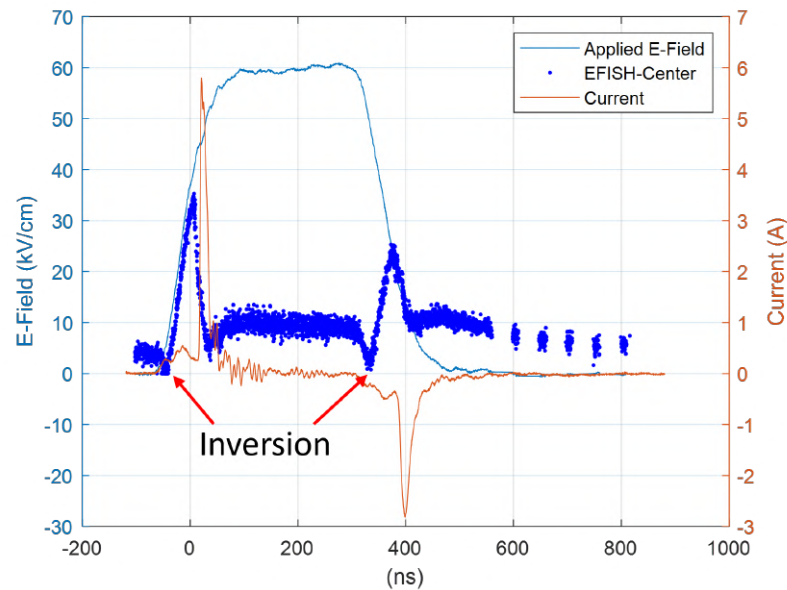


Figure 4.29: Calibrated ps EFISH raw measurements in the Center position during the whole nanosecond voltage waveform. Applied electric field and current are also reported. The points of inversion of the electric field are highlighted.

It is important to note that the calibrated EFISH measurements are all individual single-shot measurements, and the delay is computed for each of these single shots. Additionally, it is necessary to invert the EFISH signal at two specific discontinuity points. This inversion is required when the electric field switches from negative to positive values and vice versa. The PMT signal is always positive, regardless of whether the vertically polarized second harmonic is pointing upward or downward. Hence, following the verse of the current spikes, the EFISH data is inverted to negative values before the rising edge of the voltage pulse and after the falling edge of the voltage pulse, as presented in Figure 4.30. Notably, the electric field is observed to be negative both before and after the plasma discharge, mirroring the same behavior as that found in the ns EFISH measurements, as elucidated in Section 4.3.4. Specifically, we can see the dips in correspondence of the two plasma discharges and the residual electric field before and after the voltage pulse, caused by the accumulated charge on the dielectric surface. Furthermore, the electric field remains constant at roughly 10 kV/cm instead of dropping to zero in the interval between the two plasma discharges.

While these results are consistent with the ns EFISH measurements, it is important to acknowledge some variations in the experimental setup that could influence the electric field values and the dynamics of ions and electrons during the plasma discharge. Firstly, the flow rate of humid air is set at 1000 sccm, which is lower than the rate used in the ns EFISH measurements, set at 2000 sccm. This choice was forced by the maximum flow rate (1000 sccm) achievable by the mass flow controller for humid air employed in the ps EFISH measurements. Secondly, minor discrepancies in the dimensions of the air gap could arise due to the 3D printing accu-

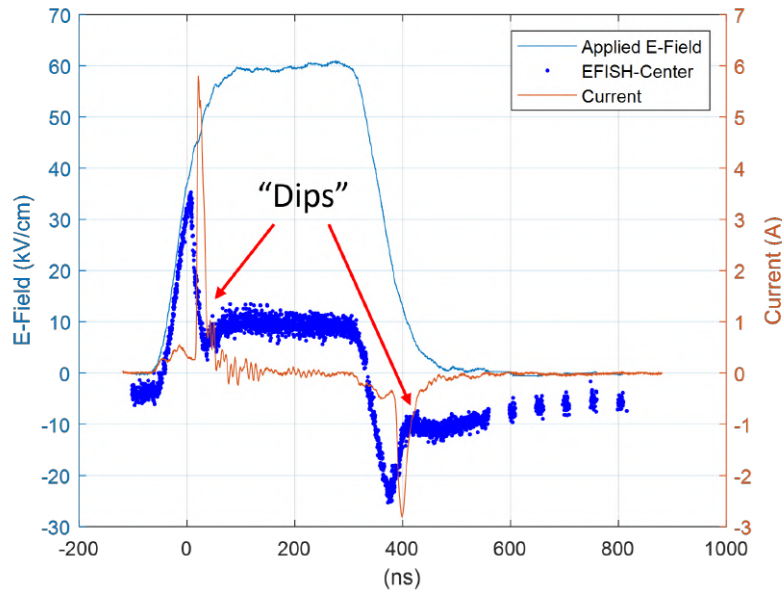


Figure 4.30: Calibrated ps EFISH corrected for the negative values of the electric field before and after the plasma discharges. The measurements are taken in the Center position during the entire ns-voltage waveform. Applied electric field and current are also reported. The dips after the two plasma discharges are highlighted.

racy of the components. Finally, distinct methods were employed to acquire and analyze the data, with the key difference being that the ns EFISH measurements are averaged, while the ps EFISH measurements are single-shot. This allows for the resolution of some electric field features that may be too rapid for the ns EFISH setup to capture.

Figure 4.31 displays the ps EFISH measurements for the three laser positions, presented collectively. In addition to the resemblances with the ns EFISH measurements, distinctions become evident within the different datasets. While in the ns EFISH measurements, there is relatively little variation observed among the three distinct positions, in the ps EFISH measurements, noticeable differences emerge. Specifically, the electric field attains larger values just before the first plasma discharge in the Ground position. Additionally, a more prominent surge in the electric field is noticeable for a few shots. This behavior aligns with the "overshoot" phenomenon previously observed in [171]. Another distinctive feature is the more pronounced "dip" in the electric field during and right after the first plasma discharge in the Center and HV positions, while the Ground position exhibits a secondary, smaller peak. Conversely, during the second plasma discharge, a similar pattern emerges but in the opposite position, specifically the HV position instead of the Ground. Just before the second plasma discharge, there is an upsurge in the electric field in proximity to the HV position. The dip in the electric field is more pronounced in the Ground and Center signals, while the HV signal experiences a quicker recovery of the electric field immediately after the plasma discharge.

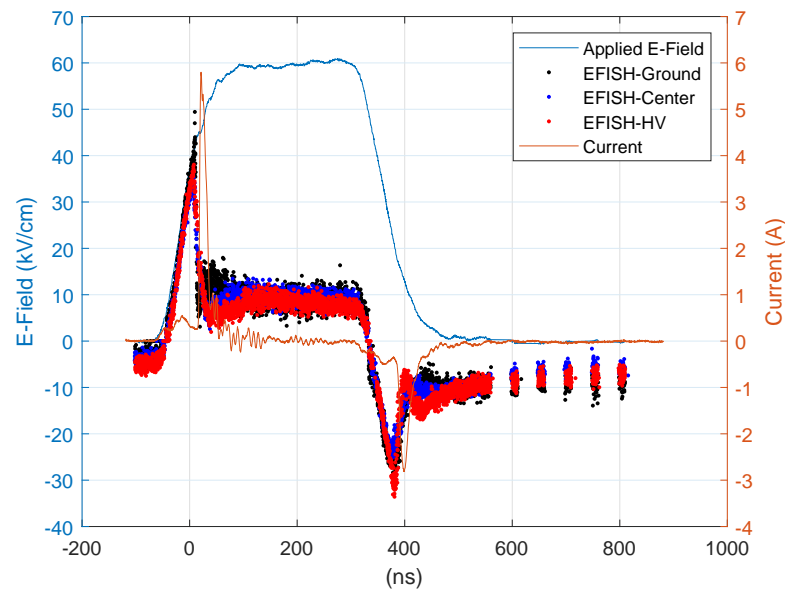


Figure 4.31: Calibrated ps EFISH measurements in the three different positions, namely Ground, Center and HV, within the gap of the VDBD. The applied electric field and the current are also reported.

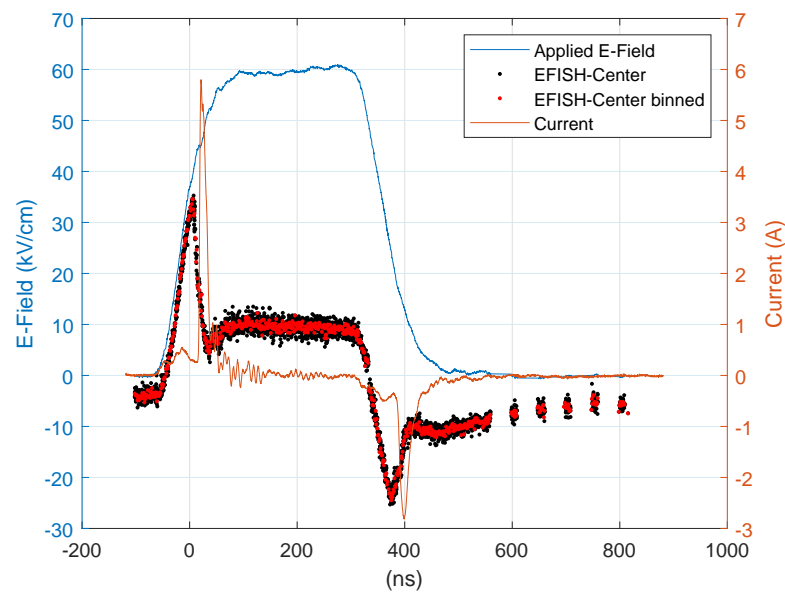


Figure 4.32: Calibrated ps EFISH measurements raw (black) and grouped and averaged in 1 ns long bins (red), at the Center position during the whole nanosecond voltage waveform. Applied electric field and current are also reported.

For clarity, the measurements are binned and averaged into 1 ns time intervals. Although it is feasible to select a bin length as short as 100 ps, it is important to consider the measurement

accuracy, which is determined by the jitter of the plasma discharge with respect to the voltage waveform. Therefore, reducing the time resolution by creating smaller bins would not yield significant benefits. In fact, it would render the measurements nearly identical to the raw data due to insufficient data for meaningful averaging within each bin. An illustration of the outcome of applying 1 ns binning to the raw EFISH data is presented in Figure 4.32 for the Center position.

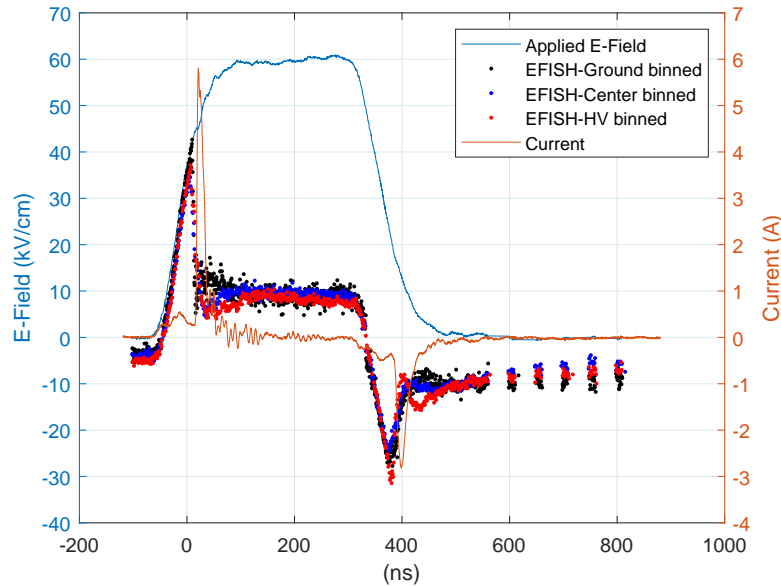


Figure 4.33: Calibrated ps EFISH measurements grouped and averaged in 1 ns long bins, at the Center, Ground and HV, positions during the whole nanosecond voltage waveform. Applied reduced electric field and current are also reported.

When the entire datasets for the three positions are grouped into 1 ns bins and presented collectively, the previously mentioned features become even more pronounced. This is clearly illustrated in Figure 4.33. It is more evident how, after the first plasma discharge, there is a clear "dip" of the electric field close to the HV electrode. In the Center position is less pronounced, and in the Ground position there is no dip anymore, and the electric field presents a smaller second peak instead. The same behavior is present during the second plasma discharge, but in inverted positions.

Binning the data, while enhancing visualization, causes a loss of information. It prevents the detection of electric field features shorter than the bin time length. This limitation is unfortunate, considering that each single measurement represents the electric field measurement over the span of ~ 28 ps, the duration of the laser pulse. The inherent jitter between the plasma discharge and the voltage waveform hinders precise time alignment for each measurement. However, this should not lead to the conclusion that all measurements must be averaged within a 1 ns time window. This issue becomes evident when examining the EFISH measurements in the Ground position, particularly when zooming in on the first plasma discharge,

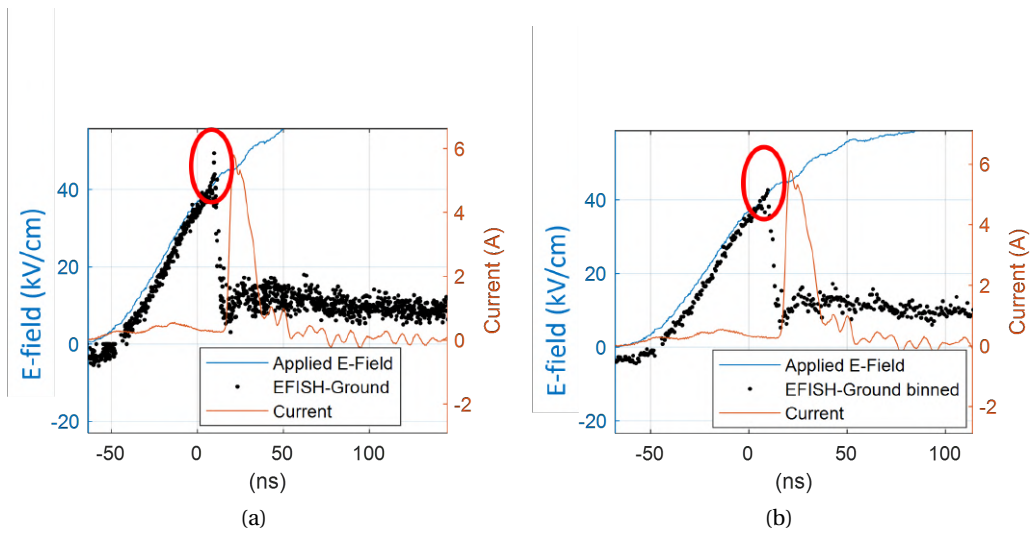


Figure 4.34: Calibrated ps EFISH measurements in the Ground position. (a) Zoom on the first plasma discharge of the single-shot EFISH measurements. (b) Zoom on the first plasma discharge of the binned EFISH measurements. The red circles highlight the information lost from the single-shot to the binned measurements.

as illustrated in Figure 4.34. Here, it becomes apparent how two individual measurements detected a rapid increase in electric field. Such events can occur within a very short time frame, and when the data is binned, these discrete traces vanish into the average with the rest of the measurements.

VDBD and laser alignment issues

The dataset depicted in Figure 4.33 represents the final collection of measurements, following the resolution of certain minor issues. In the process of achieving these final results, we conducted repeated measurements after re-aligning the laser and reassembling the VDBD components. During this iterative process, we discovered that even minor adjustments to the setup could yield notably divergent outcomes. Our initial observation pinpointed an issue associated with the VDBD components utilized to secure the electrodes in position.

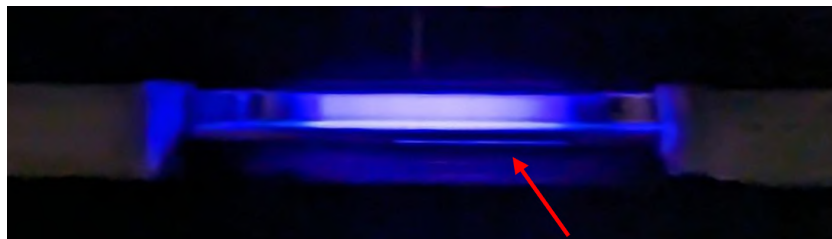


Figure 4.35: Picture of the VDBD, with visible plasma generation in between the electrode and the dielectric (indicated by the red arrow).

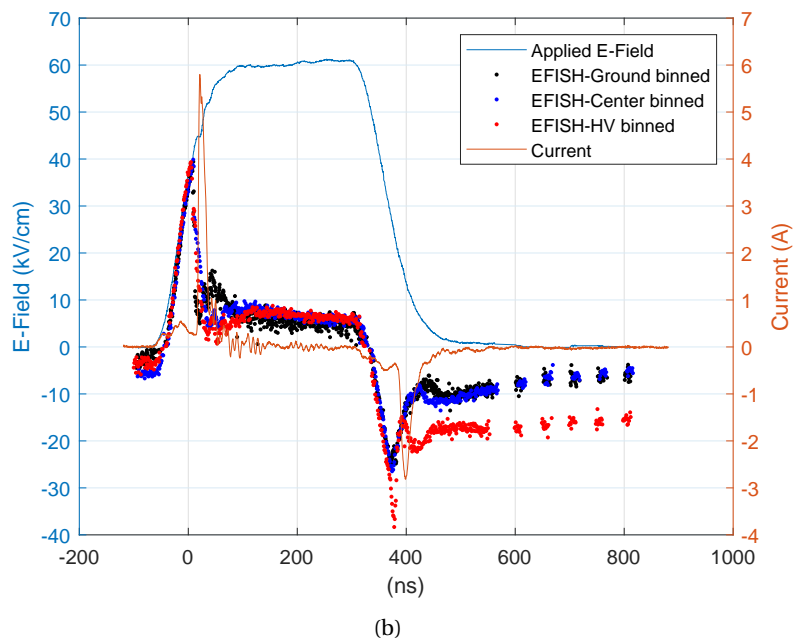
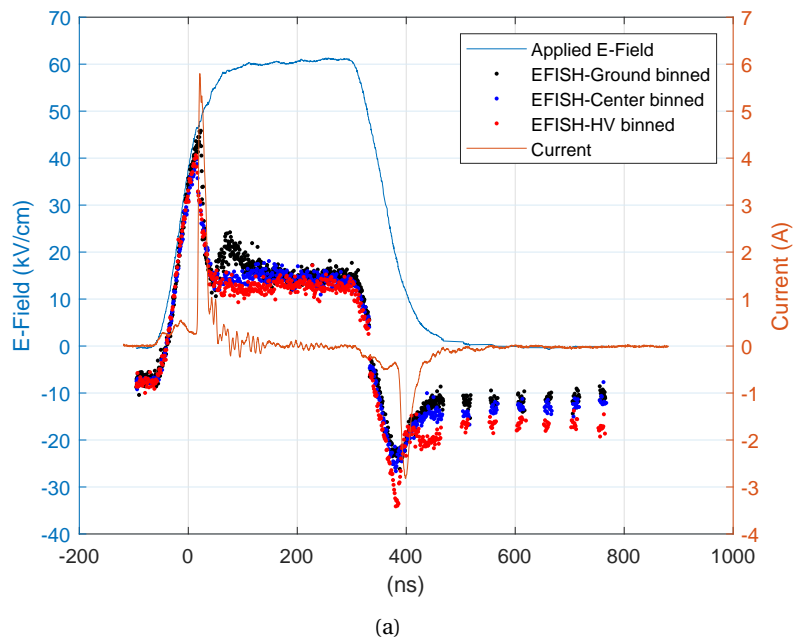


Figure 4.36: Calibrated ps EFISH measurements of the "faulty" VDBD system, grouped and averaged in 1 ns long bins, at the Center, Ground and HV, positions during the whole nanosecond voltage waveform. The applied electric field and current values are also provided. Notably, the misalignment of the laser is evident in (b), particularly in the HV and Ground positions (for additional information, please refer to the main text).

As we refrained from using any adhesive or resin to secure the ground electrode to the dielectric, improper mounting could lead to the unintended formation of a small gap between the electrode and the dielectric material, providing an opportunity for plasma ignition. This particular issue with the VDBD setup was identified while capturing images of the VDBD plasma, as exemplified in Figure 4.35. Consequently, this effect can introduce variations in the electric field during the plasma discharge, particularly noticeable in the plateau region, as depicted in Figures 4.36a and 4.36b. An additional concern pertains to the precision of laser alignment within the VDBD gap. Micro variations in system dimensions due to factors such as thermal expansion, adjustments in the vertical translation motor, and laser beam output can induce substantial errors in the laser beam position within the air gap of the VDBD. This issue is evident in Figure 4.36b, where the laser positions are notably shifted toward the HV electrode. In particular, when in the Ground position, the laser beam was not sufficiently close to the dielectric to capture the surge in the electric field just before the first plasma discharge. Conversely, in the HV position, where the electric field is significantly higher during and after the second plasma discharge, the laser was excessively close. This suggests that the laser might have been partially blocked on the side of the VDBD, as further proximity was unattainable in relation to the measurements displayed in Figure 4.31. Intriguingly, the measurements appear to maintain consistency and validity, reproducing the main features described for Figure 4.31, as each individual measurement factors in the energy of the pump beam. Nevertheless, this technique necessitates additional scrutiny for validation, as it offers the potential to approach the dielectric surface more closely without requiring enhanced focusing. To mitigate these issues, the VDBD was reconstructed with the ground electrode firmly pressed against the dielectric, and laser alignment was continuously monitored throughout the entire duration of the experiments.

4.4.7 Ps EFISH at different plasma discharge power

To further explore the dynamics of the electric field produced by the plasma discharge of this plane-to-plane geometry VDBD, another set of ps EFISH measurements was performed at different plasma discharge powers. The measurements were all taken at the Center position at increasing voltages, namely 12, 12.9 and 13.7 kV. These applied voltages correspond to a plasma discharge power of ~ 1.8 W, ~ 2.2 W and ~ 2.4 W, as computed in Section 3.4.3. The applied electric field and the current are included for reference in the figures. It's worth noting that these parameters exhibit variations in intensity among the three different datasets.

The ps EFISH measurements are displayed in Figure 4.37. Since there is no relevant difference, in this case, between the raw data and the binned data, only the last one is presented. Interestingly, as the applied voltage and, consequently, the power dissipated in the plasma increase, the temporal evolution of the electric field remains relatively consistent. However, there is a notable increase in electric field during the plasma discharges. This is observed both during the plateau and after the second plasma discharge, suggesting that the ions and electrons inside the plasma are unable to shield the external electric field beyond a certain

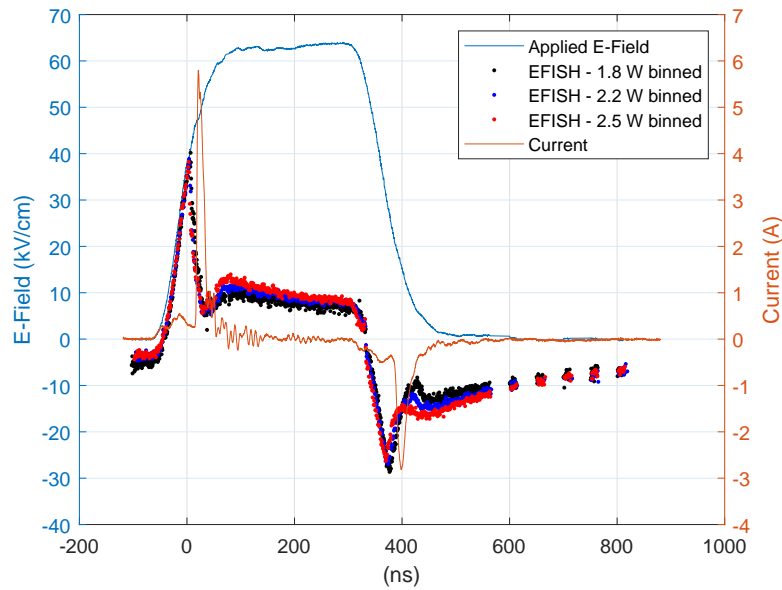


Figure 4.37: Calibrated ps EFISH measurements averaged in 1 ns long bins, at three different plasma discharge powers, namely ~ 1.8 W, ~ 2.2 W and ~ 2.4 W. The applied electric field and the current are reported for reference, however, they are not the same intensity for the three different dataset.

point. Increasing the power does not significantly boost the ionization degree of the plasma, at least not to a sufficient extent, causing the electric field within the plasma to rise with the applied voltage. The electric field at the first peak remains constant because it is determined by the breakdown voltage, which is independent of the voltage applied to the gap. However, the electric field at the second peak appears to decrease slightly with increasing power. This decline is likely due to the second plasma discharge's dependence on charge dynamics and accumulation from the first plasma discharge to the plateau.

4.4.8 Ps EFISH with membrane on top of dielectric

The VDBD was used to perform direct plasma treatments of bacteria by employing membranes placed on the dielectric in the VDBD gap (see Section 5.2). These treatments were conducted to evaluate the impact of the electric field on the bacteria by correlating the EFISH measurements performed in the Ground and HV positions with the bacterial treatments. Firstly, an ICCD image of the first plasma discharge has been acquired to control if the membrane placed in the VDBD gap would change the plasma from diffuse to filamentary, preventing the coupling of the EFISH measurements to the bacteria treatments. The results, presented in Figure 4.38, show the plasma remains diffuse regardless of the presence of the membrane in the VDBD gap. However, the size of the plasma discharge is reduced, likely due to an edge effect induced by the membrane, which is larger compared to the electrode's diameter (2.5 cm).

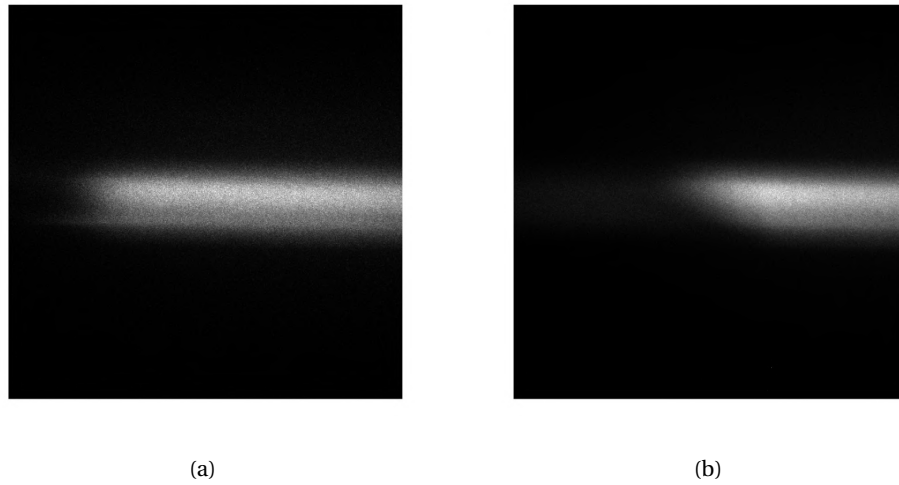


Figure 4.38: (a) ICCD image of the first plasma discharge without the membrane in the VDBD gap. (b) ICCD image of the first plasma discharge with the membrane placed on top of the dielectric surface in the VDBD gap. Both images are acquired with a gate time of 30 ns, for 10 on-ccd accumulations.

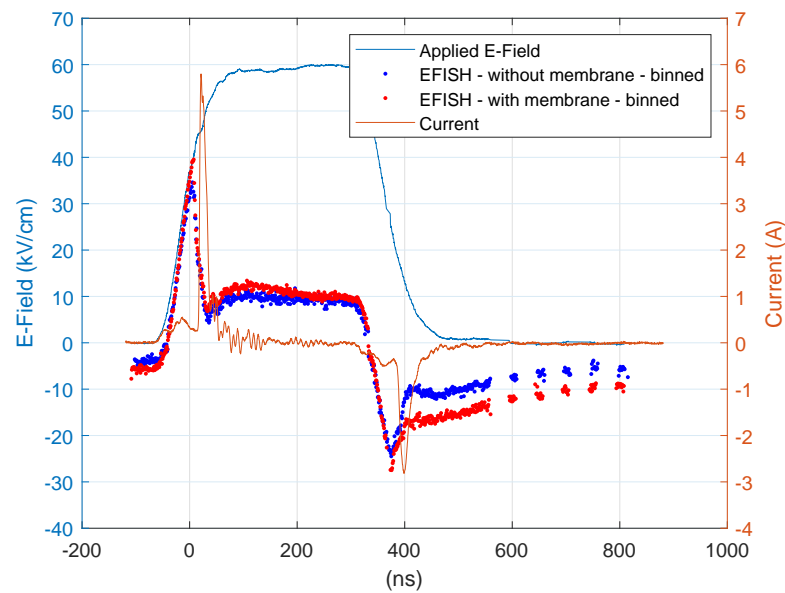


Figure 4.39: Calibrated ps EFISH measurements averaged in 1 ns long bins, taken in the Center position in the VDBD gap, with and without a membrane placed on top of the dielectric, on the grounded side. The applied electric field and the current are also reported for reference.

The validity of the ps EFISH measurements is unlikely to be affected by this effect, as the calibration is also conducted using the membrane in the VDBD gap. To confirm that the presence of the membrane did not exert a significant influence on the plasma or the dynamics

of the electric field within the plasma discharge, we conducted ps EFISH measurements on the same exact setup in the Center position, with a membrane positioned on the surface of the dielectric on the ground side of the VDBD. The results presented in Figure 4.39 exhibit remarkable consistency, with the exception of a larger electric field immediately following the second plasma discharge. This discrepancy could be attributed to the membrane, which may introduce a dielectric effect, leading to a delayed dissipation of charges after the plasma discharge. These findings highlight the existence of subtle variations between the ideal-case diagnostic measurement and real-case application scenarios, as already found out in Section 3.4.3. Such considerations should receive heightened attention within the community engaged in biological plasma applications, as the presence of biological targets often introduces alterations to system properties and, consequently, plasma behavior.

4.5 Kinetic model comparison

A one-dimensional kinetic model was employed to investigate the behavior of the plasma discharge. The kinetic model, developed by Dr. Igor Adamovich and Xin Yang, is based on the model employed in Ref. [171]. The kinetic model was developed to be compared with the ns EFISH results. To access the specific information and variables utilized in constructing the model, please consult Ref. [145]. In this section, the key parameters and the main results, compared to the experimental data obtained by EFISH measurements, are presented.

In summary, the model integrates the one-dimensional equations that describe the number densities of electrons, positive ions, and negative ions in the fluid approximation. These equations are combined with the Poisson equation, which governs the electric potential. The model takes into account the plasma shielding resulting from the buildup of charge on the dielectric surfaces next to the electrodes. The rates of electron impact ionization and dissociative attachment to O_2 , $O_2 + e \rightarrow O + O^- + e$, in humid air (3% water vapor) are calculated using Bolsig+ and the rates of the three-body attachment rate to O_2 , $O_2 + e + M \rightarrow O_2^- + M$, with $M = O_2, H_2O, \text{ and } N_2$, are taken from [172]. The initial electric field in the gap, associated with the accumulation of surface charge from the preceding pulse, $E = 2.5 \text{ kV/cm}$, is derived from the experimental data.

Figure 4.40 displays the model predictions alongside the measured electric field in the center position of the ns EFISH measurements. The applied electric field in the gap, used in the model calculation, is also shown, and it is obtained by fitting the measured applied voltage using Equation 4.8. As depicted in Figure 4.40, the increase of the electric field in the gap matches the increase in the applied voltage, as anticipated. Due to the low initial electron and ion densities in the gap, the electric field within the gap remains Laplacian, except for the offset generated by the deposition of charge on the dielectric surfaces during the preceding discharge pulse. Prior to reaching breakdown, when there is a fast rise in the number of electrons and a decrease in the electric field, the electric field shows a significant temporary increase, occurring within a time frame of less than one nanosecond (refer to Figure 4.40). The

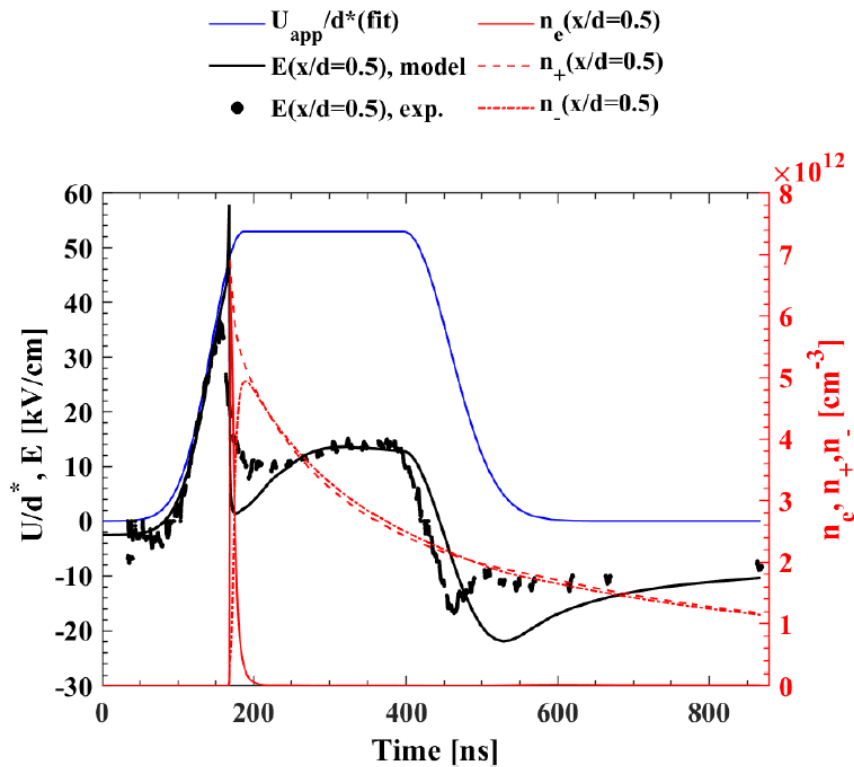


Figure 4.40: ns EFISH measurements (represented by black dots) with the model predictions in the gap centerline. The variables of interest shown in the plot are the electric field ($E(x/d = 0.5)$), the applied electric field (U/d^*), the plasma discharge current (I), and the densities of electrons (n_e), positive ions (n_+), and negative ions (n_-). The applied voltage waveform is fitted to the experimental data (source: [145]).

comparison with the modeling predictions revealed that the overshoot of the electric field, right before the plasma breakdown, is a result of the development of an ionization wave in the plasma [171]. This phenomenon has been observed in previous studies, where electric field measurements were conducted on a diffuse ionization wave in ambient air [165] and on a nanosecond pulse discharge in nitrogen [171] using ps EFISH. Note that the ns EFISH measurements do not detect this overshoot. This could be attributed to the limited time resolution of the ns EFISH diagnostic as well as the sub-ns jitter of the breakdown moment pulse-to-pulse. However, the ps EFISH measurements in the center of the plasma discharge gap, despite the improved time resolution, are in agreement with the ns EFISH results and do not detect any increase in the electric field at the start of the plasma discharge. Interestingly, the overshoot is observed in the Ground position, where an increase in electric field happens right before the plasma discharge breakdown. The reason for the absence of overshoot in the Center and HV positions remains unclear, as the ionization wave is anticipated to traverse the full space between the two electrodes. Increasing the number of single-shot data could potentially improve the statistical significance, hence facilitating the understanding of the lack

of overshoot in these positions. The kinetic model also predicts a sharp decrease in the electric field caused by the breakdown of the plasma discharge, followed by a rapid recovery. This "dip" is observed in the ns EFISH data, but it is less pronounced, whereas the ps EFISH results exhibit better agreement with the model predictions. Additionally, similarly to the overshoot case, the ps EFISH measurements reveal that the electric field dip is more prominent near the high-voltage dielectric surface of the VDBD, proving once again that there are differences in the electric field intensity depending on the location inside the plasma discharge. During the second plasma discharge, the pattern is inverted, resulting in a larger electric field on the HV side and a lower dip on the ground side.

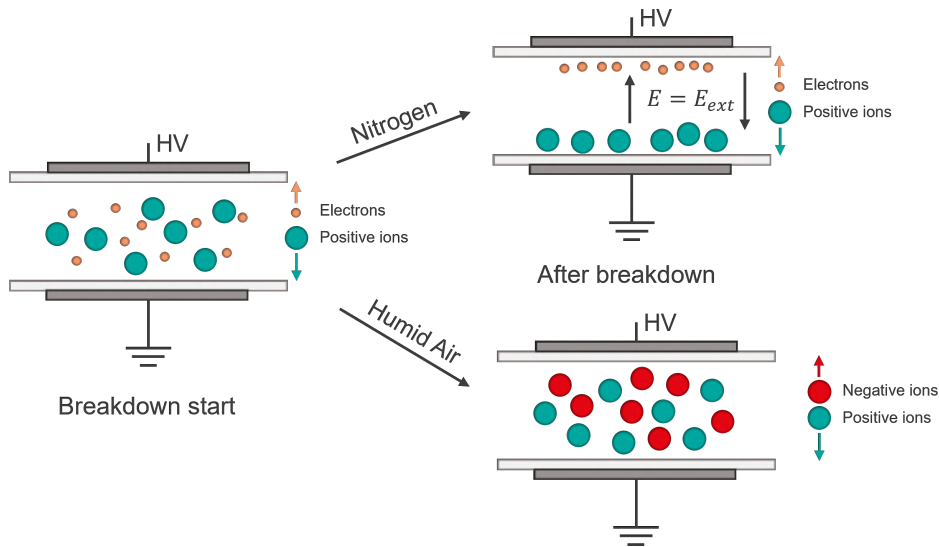


Figure 4.41: Schematics of the ions and electrons kinetic differences in a ns plasma discharge in air or nitrogen at atmospheric pressure.

Previous works in nitrogen show that following plasma breakup, the electric field drops to zero [171]. This is explained by the self-shielding caused by the migration of the charged particles to the anode and cathode. The major difference between the current data and the prior electric field measurements in nitrogen [171] is that the electric field does not decrease to a negligible level after breakdown. Instead, it remains at approximately 30% of the breakdown value, exhibiting a gradually increasing plateau. The difference between the modeling predictions in nitrogen and humid air can be attributed to the quick electron attachment, predominantly through three-body attachment, and a notably accelerated electron-ion recombination in the latter scenario. As illustrated in Figure 4.41, the cause of this behavior is attributed to the presence of electronegative molecules stemming from the chemistry of O_2 and H_2O . When the breakdown occurs in humid air, the plasma consisting of electrons and positive ions quickly transforms into a plasma consisting of negative ions and positive ions. This is observed in the model by the rapid decrease in electron density, which happens within approximately 10 nanoseconds. This significantly limits the movement of the negative charges, resulting in a partial inhibition of the plasma self-shielding caused by charge separation. This

process prevents self-shielding from occurring within a few nanoseconds, as it would in the absence of electronegative species, or negatively charged ions. This leads to a reduced buildup of electrons on the dielectric wall near the anode. Normally, this buildup would provide a polarization field across the entire gap to counterbalance the applied electric field, as observed in the nitrogen plasma [171]. This does not happen in air plasmas since the electron density decrease happens within a few nanoseconds, which significantly slows down the flow of negative charges to the anode and prevents the plasma self-shielding caused by the low mobility of the negative ions, as illustrated in Figure 4.41. Furthermore, the movement of the positively charged ions towards the wall next to the grounded electrode during the remaining duration of the pulse, accelerated by a highly intense field in the cathode sheath, creates the negative space charge in the remaining part of the discharge gap. In an electron-ion plasma, the negative space charge would quickly disperse due to the movement of the extremely mobile electrons. In the ion-ion plasma, the space charges are present for an extended duration, mostly because of the significantly reduced mobility of the negative ions. This phenomenon is accountable for the steady increase of the electric field within the gap subsequent to the initial quick dip triggered by the breakdown.

Additional examination of the modeling predictions reveals that the primary cause for the differences between the model and the experimental findings can be attributed to two factors: the lack of certainty in the number density of water vapor in the moist air, which governs the overall rate of the three-body attachment in the plasma, and the failure to consider the presence of multiple ion species and ion conversion reactions, which impact the overall rate of electron-ion recombination. The modeling predictions indicate that the electric field in the plasma following breakdown is mostly influenced by the rate at which electron density decreases, which is determined by both electron attachment and recombination, with similar contributions from each process. Hence, by comparing the current experimental results with the high-fidelity models that incorporate comprehensive humid air chemistry and a whole range of ion-molecule reactions, we can gain further understanding of plasma dynamics and elucidate any remaining disparities.

Therefore, to address the constraints of the current model, we initiated a collaboration with the Plasma Technology Laboratory (PTL) of University of Bologna. They are currently working on developing a comprehensive model for simulating DBD plasma in air [173, 174]. The initial findings show great promise, but due to ongoing work, they cannot be included in this thesis.

4.6 Conclusions

This chapter presents the measurements of the electric field employing the EFISH diagnostic, during the plasma discharge in the VDBD gap, using first a ns-laser and then a ps-laser. The EFISH measurements provide valuable information not only about the changes in the electric field over time but also, using kinetic modeling, on the behavior and interactions of ions and electrons during the nanosecond plasma discharge. The measurements were performed

in different positions of the VDBD gap to verify the presence of spatial variations within the plasma discharge. The measurements were conducted in the identical settings as the biological treatments outlined in Chapter 5.

The ns EFISH experiments exhibit the capability to achieve a time resolution that is shorter than the duration of the laser pulse. The measurements were taken at three specific locations within the plasma discharge: specifically, at the center and near both the high-voltage and ground dielectric surfaces. The importance of the gas mixture used in the plasma discharge is emphasized by comparing the EFISH data with a kinetic model. The key difference from previous studies on nitrogen lies in the presence of a significant and stable electric field subsequent to the initial plasma discharge. This is explained by the difference in electronegativity of the molecules in the gas, mainly introduced by oxygen and water molecules. When breakdown occurs, electrons quickly convert into negative ions within a nanosecond, which significantly slows down their movement and maintains the distribution of space charge in the gap.

The kinetic model accurately predicts the evolution of the electric field, as observed by the ns EFISH diagnostic. However, some features of the electric field time evolution predicted by the model have not been observed in the ns EFISH measurements. A key aspect missing from the ns EFISH data is an electric field overshoot just before the breakdown of the plasma discharge. The higher spatial and temporal resolution of the ps EFISH data partially overcomes this inconsistency. Nevertheless, the ps EFISH measurements only detect the overshoot in the close vicinity of the dielectric surface on the ground, while it is not observed in the HV position, and, similarly to the ns EFISH data, it is also absent in the center of the gap. Ongoing investigations are being conducted to determine the cause of this behavior, as the kinetic model predicts the presence of this feature in the center of the gap. Another feature to consider is the electric field dip following the breakdown of the plasma discharge. This characteristic is more evident in the ps EFISH data compared to the ns EFISH results, but it is more prominent in close proximity to the high-voltage dielectric surface of the VDBD, with respect to the ground and center locations. During the second plasma discharge, the pattern is inverted, resulting in a higher electric field on the HV side and a more significant dip on the ground side. Although the ns EFISH data shows no noticeable change among the three positions in the plasma discharge, the ps EFISH measurements consistently show changes among the three locations, indicating that the temporal dynamics of the electric field differ depending on the position within the plasma discharge. In addition, the ps EFISH measurements are performed on both the ground and HV sides at a distance of 270 μm from the dielectric surface, which suggests that the changes in the electric field may be more noticeable when the distance from the surface of the dielectric is shorter.

To evaluate the impact on the electric field of biological targets placed within the plasma discharge, a membrane employed for the treatment of *Bacillus subtilis* spores was positioned on the surface of the dielectric. The findings revealed a minor change in the electric field, particularly in the plateau area and following the second plasma discharge. Additionally, there was a discernible change in the electric field peak before plasma ignition, indicating that the

membrane acts as a dielectric, hence increasing the breakdown voltage within the gap. This observation highlights the significance of taking into account the impact of the biological target on the plasma discharge.

In addition to the plasma for sterilization study, the VDBD configuration offers an optimal platform for code validation. Therefore, nitric oxide LIF measurements were performed using the same VDBD configuration as the ps EFISH experiments. Building upon the early findings regarding the electric field and nitric oxide measurements, we started a collaboration with the Plasma Technology Laboratory (PTL) at the University of Bologna, where a comprehensive model for DBD plasma in air is under development. This improved kinetic model addresses the constraints of the kinetic model employed in Ref. [145], hence enabling a deeper understanding of the physics underlying nanosecond plasma discharges in humid air. The preliminary results exhibit great promise, however, they cannot be incorporated into this thesis due to the ongoing research.

In summary, we performed the first measurements of ns and ps EFISH in a nanosecond diffuse plasma discharge generated in humid air using a plane-to-plane VDBD geometry. The experimental findings, compared with a basic kinetic model, provided a new understanding of the fundamental kinetic mechanisms governing the electric field in atmospheric pressure plasmas produced by ns pulse discharges. The results demonstrated the impact of electronegative molecules on the formation of the plasma discharge. The ps EFISH measurements revealed significant variations in the electric field development between the central region of the discharge and the vicinity of the dielectric surfaces, as well as changing the plasma discharge power. Furthermore, these measurements demonstrated the potential impact of biological targets on the behavior of the plasma discharge when positioned within the discharge.

5 Biological Characterization: Bacteria Plasma Treatments

This chapter details the biological characterization of the plasma sources developed at the SPC, introduced in Chapter 2. The primary goal of this thesis is to investigate the bactericidal efficacy of low-temperature plasma treatments in different configurations and to acquire a deeper understanding of the critical factors involved in bacterial inactivation by plasma. The study involves direct and indirect plasma treatments with different microorganisms and protocols. Each plasma treatment method is meticulously designed to correlate plasma treatments with plasma diagnostic data, replicating the same conditions encountered by the biological target.

In Section 5.1, we investigate indirect plasma treatments on *Escherichia coli* employing the PCB-fingers SDBD, powered by the nanosecond-pulsed generator. High humidity from the agar Petri plate causes non-uniform plasma ignition, preventing reproducible results. By introducing airflow and maintaining lower humidity levels, we significantly enhance treatment reproducibility. The 10-minute plasma treatments showed promising 4-log reduction in bacteria CFU/mL. We also examine the effect of nitric oxide (NO) on bacterial inactivation and find that it does not directly affect bacterial populations in this particular setting.

To study direct plasma treatments, we used the same VDBD setup employed for ps EFISH measurements to couple the results. *Bacillus Subtilis* spores deposited on monolayer membranes are treated in different positions in the VDBD gap. This technique presented numerous benefits, including the preservation of the diffuse plasma and the flexibility to position the membrane at various locations within the plasma discharge. The procedure, setup, and results are detailed in Section 5.2.

In the final section, we discuss the first tests for sterilization. The perforated-disc SDBD, powered by the PAW power supply, is used to achieve the first successful sterilization outcomes. We assess the treatments using a biological indicator, specifically the BT96, containing at least $\geq 10^6$ *Geobacillus stearothermophilus* ATCC 7953 spores, placed at various positions inside the reactor. Ultimately, an overview showcasing the outcomes of this chapter is provided.

5.1 Indirect plasma treatments of *E. coli*

The primary focus of this thesis revolves around examining the interaction between plasma and bacteria, and the key factors involved in the inactivation process. This research aims to improve our understanding of low-temperature plasma, offering insights that can be harnessed to optimize plasma sources and improve the decontamination process. The ultimate objective is to develop a device capable of achieving sterilization levels, potentially revolutionizing the sterilization market by offering a more sustainable and efficient solution. To investigate the impact of low-temperature plasma treatments on bacteria, we first conducted indirect plasma treatments on *Escherichia coli*. Our research was carried out in the Bio-plasmas lab, a laboratory equipped with the necessary infrastructure for the safe handling and management of non-pathogenic bacteria (BSL1 - biological safety level). The laboratory includes essential equipment such as laminar flow cabinets, ultra-cold freezers (-80°C), autoclaves, and more. The Bio-plasmas lab stands out as a unique laboratory that accommodates both the biological and physiochemical aspects of our research, allowing for their concurrent investigation.

5.1.1 *E. coli* culture management

The non-pathogenic *Escherichia coli* K-12 strain MG1655 serves as the test subject for evaluating the decontamination effectiveness of indirect plasma treatments within this experimental setup. This particular bacterial strain is widely employed in research, as previously detailed in Section 1.3.2, due to its non-pathogenic nature, potential for rapid replication, and well-documented history as a standard in biological research. Figure 5.1 illustrates the complete procedure employed for the *E. coli* treatments. *E. coli* cell stocks are securely stored and preserved in a solution of Lysogeny Broth (LB) and glycerol (30% v/v) at a temperature of -80°C . From the stock, $100\mu\text{L}$ are inoculated into 10 mL of LB and then incubated at 37°C and 180 rpm for a minimum of 8 hours, to produce the overnight culture. To reactivate the bacterial culture, $10\mu\text{L}$ of the overnight culture is inoculated into 10 mL of fresh LB and incubated at 37°C and 180 rpm. The growth phase of the cells is monitored by measuring the optical density (OD) at 600 nm. The bacteria are treated during the mid-log phase, characterized by optimal environmental conditions for bacterial replication. This phase is typically identified by an OD reading between 0.2 and 0.3, which corresponds to a concentration of approximately 10^6 colony-forming units per milliliter (CFU/mL) [175, 176]. Treating a culture with a concentration of 10^6 CFU/mL enables the assessment of treatment efficacy up to a maximum reduction of 6-logs.

5.1.2 *E. coli* plasma treatments protocol and counting

To facilitate the assessment of various reduction levels at different time points, it is necessary to reduce the cell culture's bacterial density through dilution. This lower bacterial density enables accurate counting following treatments. Consequently, from the initial culture of 10^6 CFU/mL, we produce five serial dilutions, namely from 10^{-1} to 10^{-5} , and plate them on

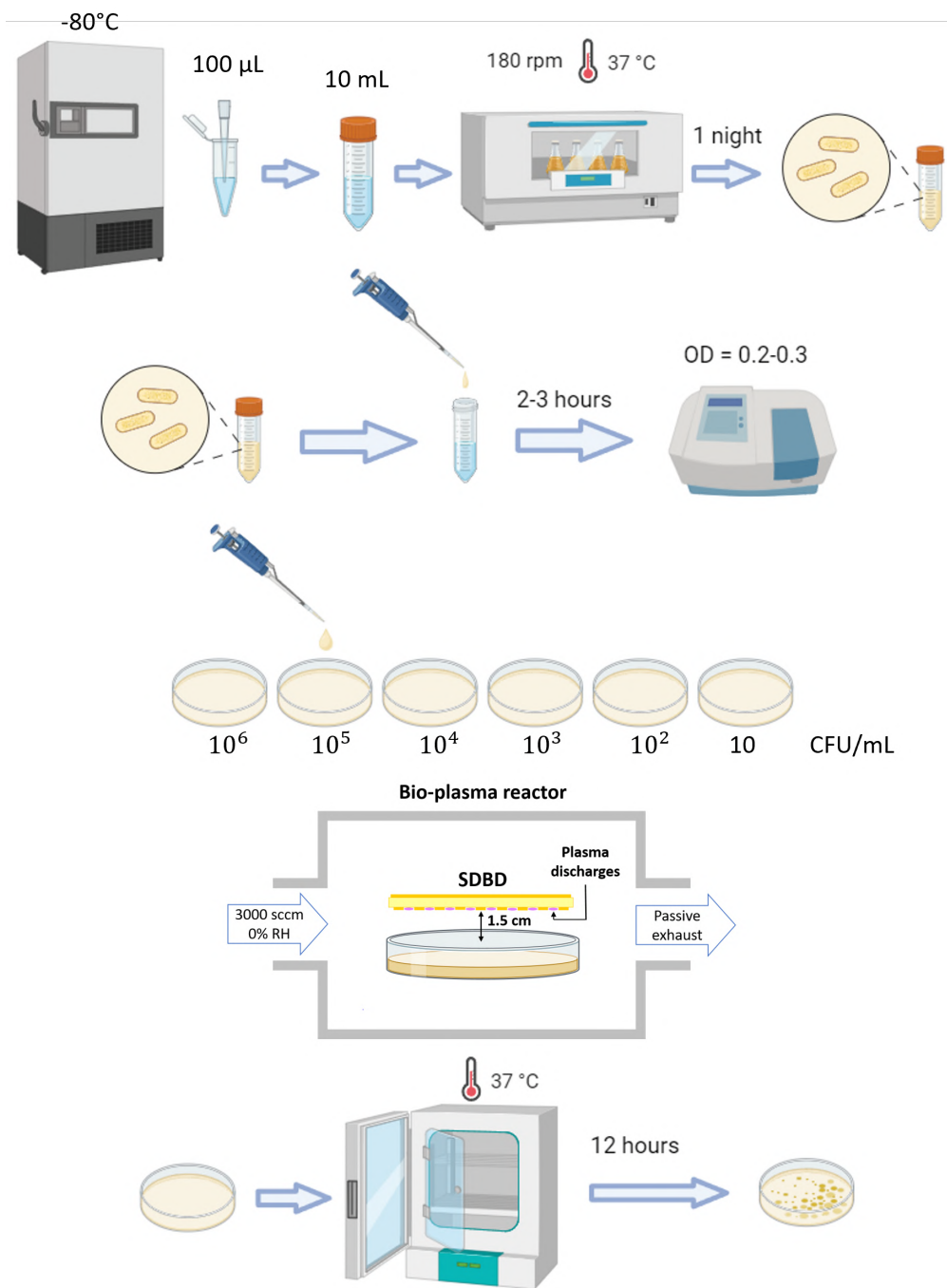


Figure 5.1: Schematics of the *E. coli* plasma treatment protocol, from storage to CFU counting. For details, please refer to the main text.

standard Petri dishes containing LB agar, as shown in Figure 5.1. For each treatment duration, all six concentrations, comprising the five dilutions and the undiluted sample, are subjected to the same plasma treatment protocol. Following plasma treatments, the bacteria cultures

are incubated at 37 °C for 12 hours, during which time each CFU grows colonies of sufficient size for manual counting.

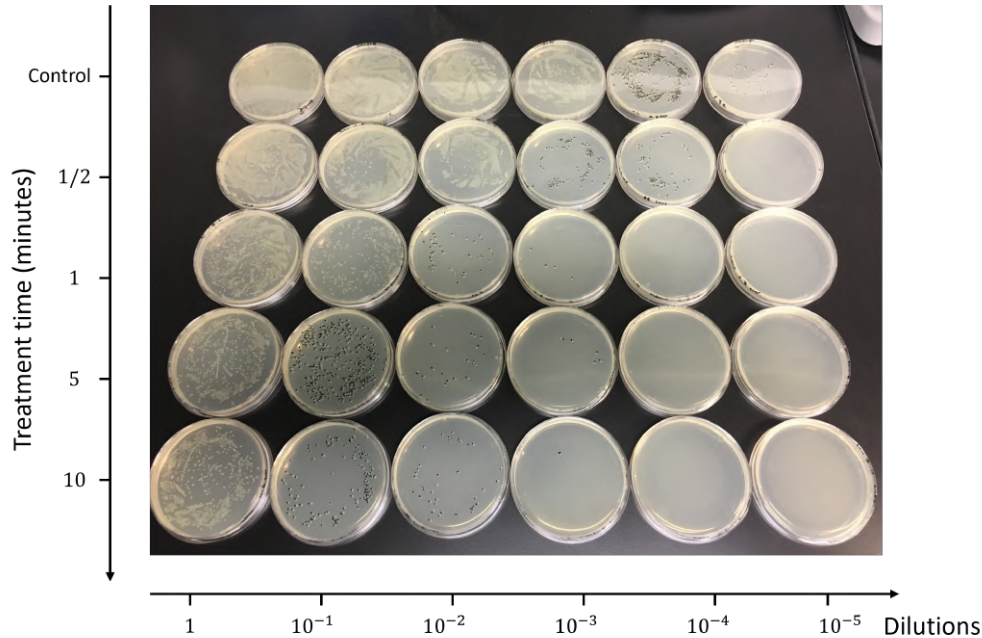


Figure 5.2: Example of Petri dishes with bacteria colonies growing on the surface, after plasma treatments. The Petri dishes are disposed according to the duration of the plasma treatment on the vertical axis and the dilution level on the horizontal axis.

Colony counting is restricted to plates with colony counts falling within the range of 10 to 300. Colonies outside this range are excluded from the count due to their potential lack of accuracy. Subsequently, to determine the total number of colonies N in the initial solution, we employ Equation 5.1. In this equation, $\sum n$ represents the cumulative count of colonies on all the plates that were included in the counting, j_1 stands for the number of counted plates at the lowest dilution level considered, j_2 corresponds to the number of counted plates at the next higher dilution level, and d denotes the reciprocal of the lowest dilution factor [107].

$$N = \frac{\sum n}{j_1 + 0.1j_2} d. \quad (5.1)$$

Owing to the protocol employed in this study, it is important to note that both j_1 and j_2 consistently assume values of either 0 or 1, as only one plate is prepared for each dilution. Among the six dilutions subjected to treatment, only one or two plates are suitable for counting. Therefore, Equation 5.1 can be simplified to:

$$N = \frac{\sum n}{1.1} d \quad \text{or} \quad N = \frac{\sum n}{1} d, \quad (5.2)$$

The number of dilutions counted determines whether we have data from 1 or 2 plates. The results are then graphed using a logarithmic scale, following the established convention in microbiology, defined as follows:

$$R = \log_{10} \left(\frac{N_0}{N_t} \right), \quad (5.3)$$

where N_0 represents the initial bacterial population, which is determined through counting in the control group, and N_t stands for the bacterial population after the plasma treatment, both measured in CFU/mL. We will refer to R as the "log-reduction" value, which quantifies the reduction in CFU/mL on a logarithmic scale following the plasma treatment.

Statistical analysis

For the statistical analysis, the CoStat statistical program [177] was employed. An analysis of variance (ANOVA) was conducted to compare the various treatment times. Significant differences were detected through the Student-Newman-Keuls multiple range test [178, 179], with a confidence level set at $p \leq 0.05$. In the results, distinct lowercase letters, ranging from *a* to *c*, are used to denote significant statistical differences between the data points.

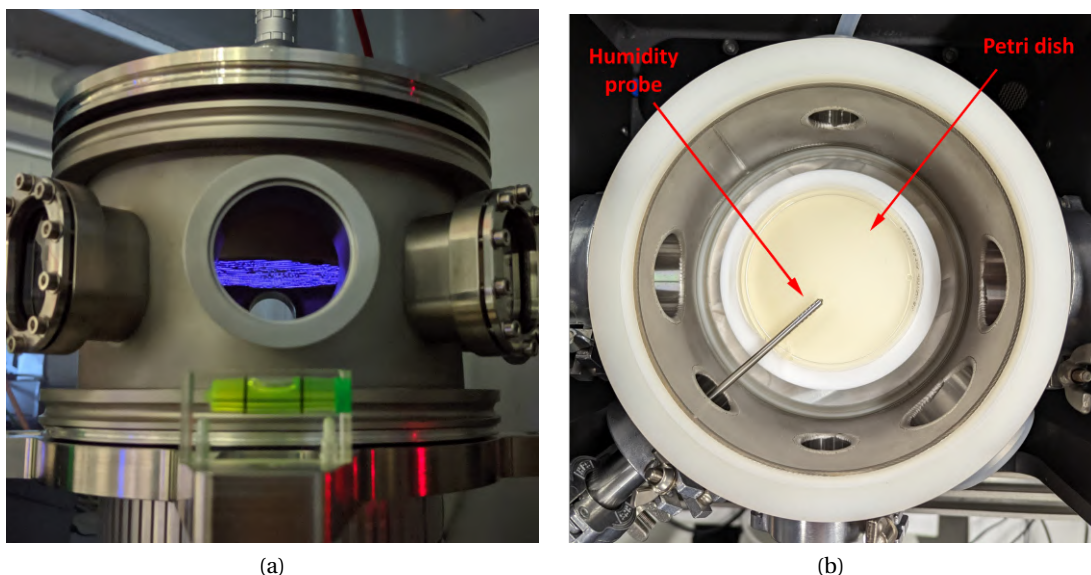


Figure 5.3: (a) The PCB-fingers SDBD in operation inside the reactor. (b) Illustration of the Petri dish placement within the reactor, with the temperature and relative humidity probe initially positioned on top for a test. During the actual bacterial treatments, the probe is relocated to the side of the Petri dish.

5.1.3 Indirect plasma treatments of *E. coli* results

To perform the indirect plasma treatments of *E. coli* we used the PCB-fingers SDBD, described in Section 2.1.1. The SDBD was powered by the nanosecond-pulsed generator using a fixed voltage of 4.7 kV, 400 ns long pulses and 1 kHz frequency, corresponding to ~ 1.3 W, as found in Section 3.4.1.

These values of applied voltage are barely above the breakdown voltage of the SDBD. This choice was driven by the necessity to minimize the temperature increase and prevent potential damage to the SDBD surface caused by prolonged excessive plasma power. Initially, the treatments were conducted in a static environment to facilitate the accumulation of RONS inside the reactor. As illustrated in Figure 5.3, the Petri dishes were positioned so that the agar surface, where the *E. coli* cultures are deposited, was approximately 1 cm away from the surface of the PCB-fingers SDBD, placed upside down inside the bio-plasma reactor. The initial results, as presented in Figure 5.4, were promising. Even with very low power settings, we achieved 4-log reductions after only 10 minutes of plasma exposure. However, when we attempted to perform triplicate experiments and repeat the treatments, we encountered challenges in achieving measurement reproducibility.

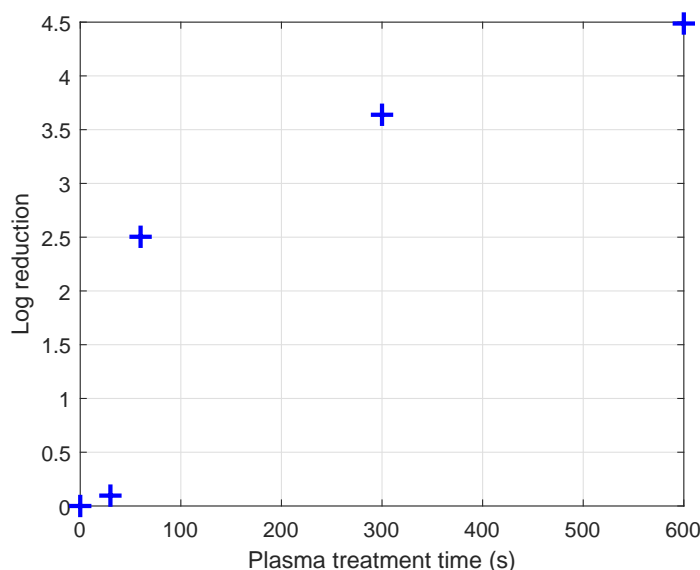


Figure 5.4: Single measurement of the log reduction of *E. coli* CFU/mL at increasing plasma treatment times. Bacteria treatments were performed with no flow at a distance of 1 cm from the plasma surface.

The cultures on the Petri dishes displayed a growth pattern that was consistently identical or similar across different Petri dishes, as illustrated in Figure 5.5. This prompted us to investigate the uniformity of the plasma on the DBD surface. We observed that the plasma exhibited a patchy and partial ignition across the surface, as depicted in Figure 5.6.

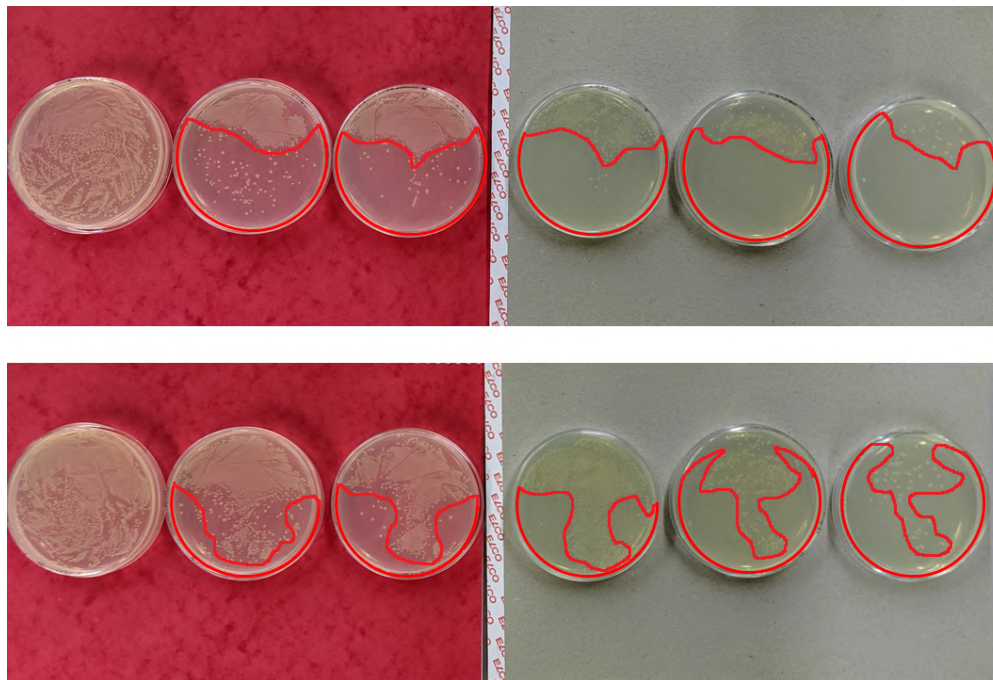


Figure 5.5: Bacteria cultures at 6 different dilutions of *E. coli* after plasma treatments of two different replicates. It is clearly visible a consistent inactivation pattern, highlighted in red, caused by the partial ignition of the plasma over the SDBD surface.

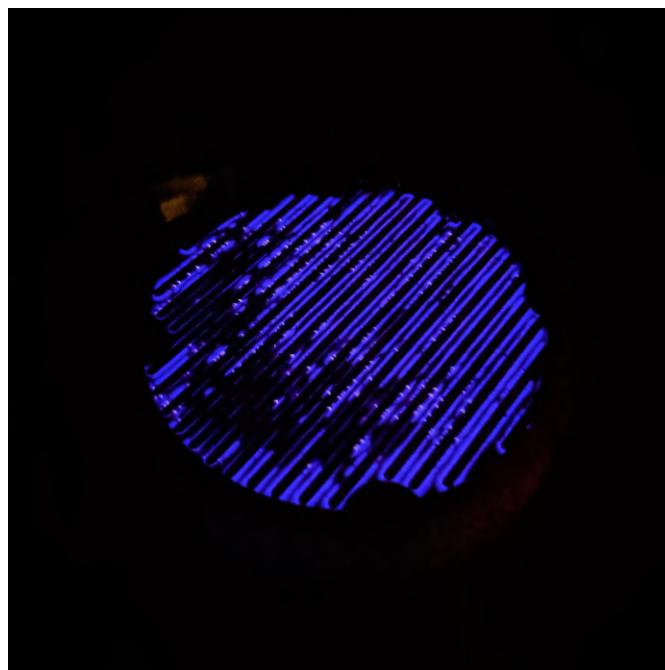


Figure 5.6: PCB-fingers SDBD after being damaged by humidity, showing a patchy, non-uniform plasma ignition over the surface.

This was eventually explained by the damage and/or deterioration caused to the PCB-fingers SDBD by the high humidity inside the reactor. Specifically, in the absence of airflow within the reactor, the moisture released by the agar in the Petri dish accumulated, leading to a relative humidity (RH) level ranging between 75 – 85%. This high humidity adversely affected and damaged the SDBD, as detailed in Section 2.1.2. The unsuccessful results, not only showed that the biological target can drastically change the operation of the plasma, by affecting humidity and gas composition, but also that the plasma treatments, despite being indirect with the bacteria as far as 1 cm from the plasma surface, can exhibit a local effect, as shown from the identical inactivation pattern observed on the Petri dishes in Figure 5.5. Consequently, in response to these findings, we made the decision to introduce airflow into the reactor to prevent such a substantial increase in RH and enhance the reproducibility of the treatments. To maintain the RH at the lowest possible level, we introduced a flow of 3000 sccm of dry synthetic air composed of 80% pure nitrogen and 20% pure oxygen. The system configuration is depicted in Figure 5.7.

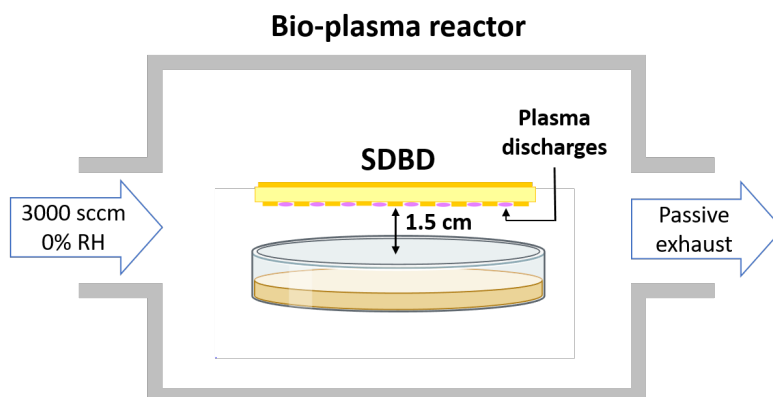


Figure 5.7: Schematic of the experimental setup for the bacteria plasma treatments with the PCB-fingers SDBD.

For simplicity, we will refer to this flow configuration as "0% RH" although the actual relative humidity inside the reactor reached approximately 10-13% RH due to the moisture released by the agar in the Petri dish. Additionally, we adjusted the distance between the agar surface and the DBD surface to 1.5 cm to allow the flow to reach the interior of the Petri dish, as the edges of the dish effectively created a secondary enclosed environment inside the reactor. Given the fragility of the PCB-fingers SDBD, which was sensitive to both moisture content and extended plasma operation, we made the decision to replace the used SDBD with a new one before each replicate of the plasma treatment. Under these conditions, the reproducibility of the treatments significantly improved. These treatments were conducted in triplicate, spanning a duration of 30 seconds to 10 minutes of continuous plasma exposure inside the reactor with the 0% RH flow configuration and using the same pulse settings. The results, in terms of the mean and standard deviation of the CFU/mL log-reduction for these indirect plasma treatments of *E. coli*, are presented in Figure 5.8.

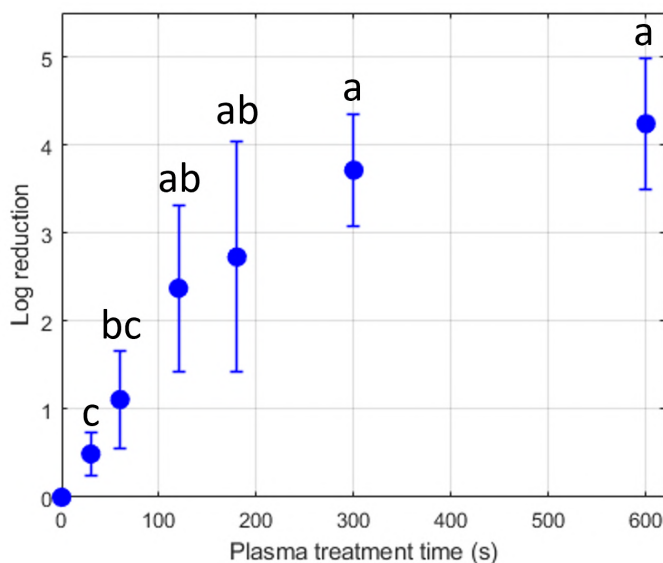


Figure 5.8: Log reduction of *E. coli* CFU/mL depending on the duration of plasma exposure. The mean and standard deviation of the log reduction for the triplicate are represented. Different lowercase letters indicate significant differences ($p \leq 0.05$).

The exposure to plasma for 10 minutes led to a substantial reduction of the bacterial population by 4-logs. Notably, adjustments such as the gas flow, perpendicular to the plasma surface, and the increased distance between the bacteria and the plasma did not significantly impact the disinfection efficacy of the treatments. The lowercase letters in Figure 5.8 signify the statistical significance, which was calculated for $p \leq 0.05$.

In this thesis, one of the primary reactive nitrogen species (RNS) under investigation is nitric oxide (NO), a molecule believed to play a crucial role in bacterial inactivation processes [95, 94]. Through laser-induced fluorescence, we measured the NO density to be lower than 1 ppm in this specific experimental setup, as elaborated on in Section 7.3. To assess the isolated impact of nitric oxide on bacteria, *E. coli* was exposed to a 10-minute treatment with 1 ppm of NO in a 3000 sccm synthetic air flow, employing the same setup used for the plasma treatments. These nitric oxide treatments, performed in triplicate, revealed that exposure to 1 ppm of NO did not result in any discernible effect on the bacterial population. These findings suggest that nitric oxide may not have a direct role in the bacterial inactivation process in this specific setup, especially in the context of non-indirect treatments at low plasma discharge power. However, it's worth noting that NO serves as a primary molecule necessary for the generation of secondary reactive oxygen and nitrogen species (RONS). Some of these secondary RONS, as indicated by the FTIR measurements discussed in Section 6.3.1, are detected in higher concentrations. These include species like N_2O , NO_2 , and O_3 , which might potentially play a more significant role in bacteria decontamination.

5.2 Direct plasma treatments of *Bacillus Subtilis* Spores

To study the effect on bacteria of direct plasma treatments, we employed the VDBD described in Section 2.2. However, we opted for a different approach than the one utilized for the SDBD indirect plasma treatments. When agar substrate is used to treat bacteria with the VDBD, the plasma shifts from diffuse to filamentary, preventing reproducibility and the possibility of reliably coupling the EFISH measurements to the biological treatment. We adopted a method proposed in [180], which involved using polycarbonate membranes loaded with a monolayer of spores. This approach was well-suited to the objectives of our study and offered several advantages for direct plasma treatments. First and foremost, it allowed us to conduct bacteria treatments without significantly altering the properties of the plasma. The membranes were dry and thin, measuring less than 100 μm in thickness, and had minimal impact on the nature of the plasma discharge. While they did have a slight effect on plasma discharge power and the electric field produced by the plasma, the discharge remained diffuse, as shown in Figure 5.9.



Figure 5.9: Image of the diffused VDBD plasma discharge with a membrane placed in the gap.

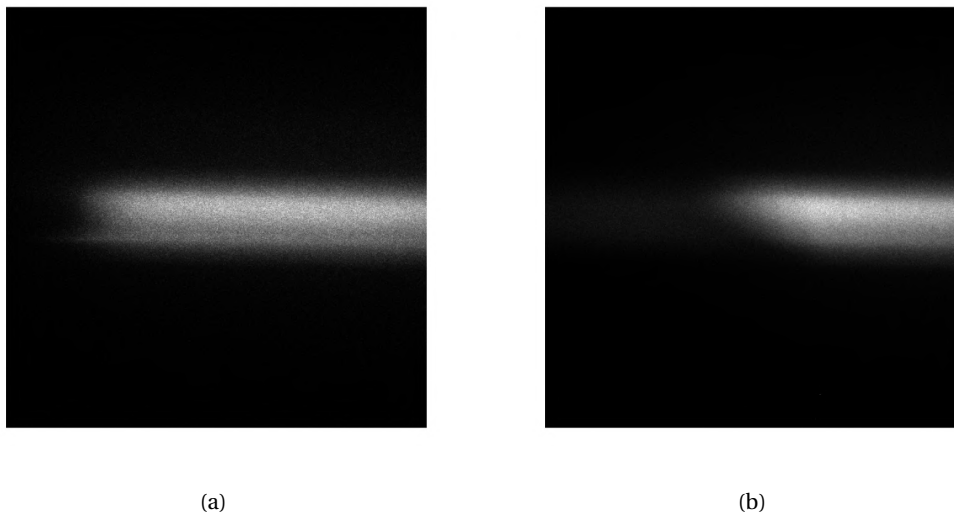


Figure 5.10: ICCD image of the first plasma discharge (a) without the membrane in the VDBD gap and (b) with a full membrane placed on top of the dielectric surface. All images are acquired with a gate time of 30 ns, for 100 on-ccd accumulations.

Additionally, ICCD short-gated images are acquired to confirm that the plasma remains diffuse. In Figure 5.10, the ICCD-acquired image of the first plasma discharge with and without membrane in the VDBD gap is shown. The plasma remains diffused in both cases, however, as previously noted in Section 4.4, the presence of the full membrane leads to a reduction in the size of the plasma discharge. This is likely due to an edge effect caused by the larger membrane compared to the dimensions of the electrodes. As it will be discussed in Section 5.2.3, the effect of the membrane on the plasma is further mitigated by splitting the membrane into four pieces, reducing the surface of the membrane to a smaller region at the center of the plasma discharge. Unlike previous studies [181], we were able to maintain a diffused and consistent plasma during both diagnostic measurements and bacteria treatments, ensuring that our measurements remained consistent with the conditions of the bacteria treatment process. Secondly, spores are known to be more resistant than bacteria, providing an opportunity to assess the efficacy of direct VDBD plasma treatments on more resilient targets. Furthermore, the monolayer deposition of bacteria on the membrane allows for a more reproducible protocol. Figure 5.11 shows the *Bacillus subtilis* spores deposited evenly over the membrane surface. Last but not least, the membranes allowed us to perform plasma treatments in a very thin region of the plasma, either on the high-voltage (HV) side or on the ground side of the dielectric. This configuration enabled us to investigate the impact of the electric field in direct plasma treatments, since the ps EFISH results, detailed in Section 4.4, showed a different electric field evolution close to the dielectric surface between the ground side and the HV side.

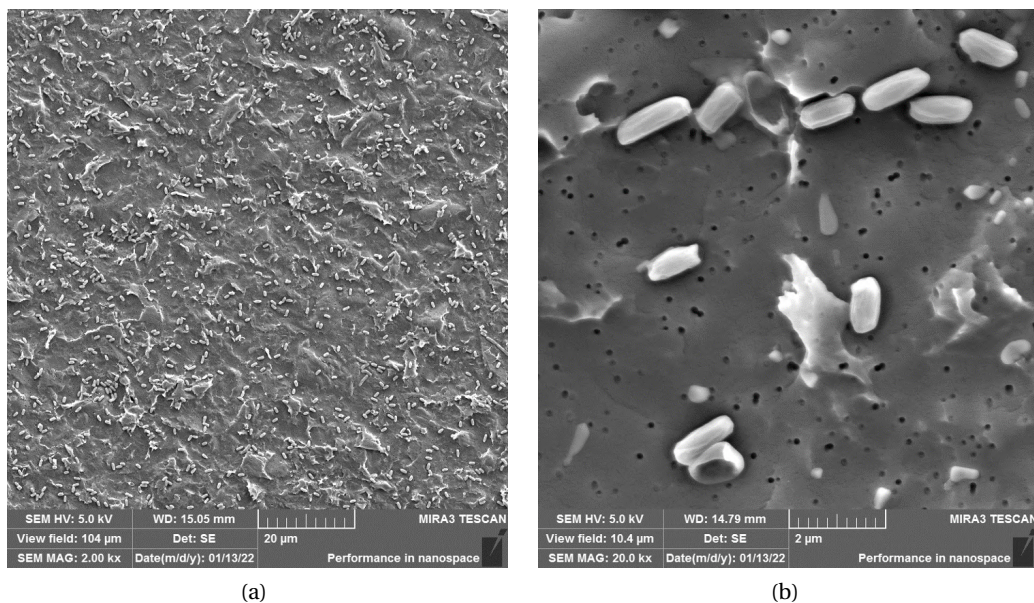


Figure 5.11: (a) SEM image of the surface of the membrane covered by *Bacillus subtilis* spores. (b) A close-up image of the spores (courtesy of Anna Machkova).

5.2.1 *Bacillus Subtilis* spores on monolayer membrane preparation

The protocol to prepare, wash, and count the spores on the membrane is detailed in [180]. *Bacillus subtilis* strain ATCC 6633 spores are selected for the treatments, while the membranes used are nuclepore track-etched membranes with a diameter of 25 mm and pore size of 0.1 μm (WHA110605 Whatman). The membranes are carefully placed into the center of opposite syringe-type reusable membrane filter holders (WHA420200 Whatman). The holder is subsequently autoclaved to ensure sterilization after it is securely closed.

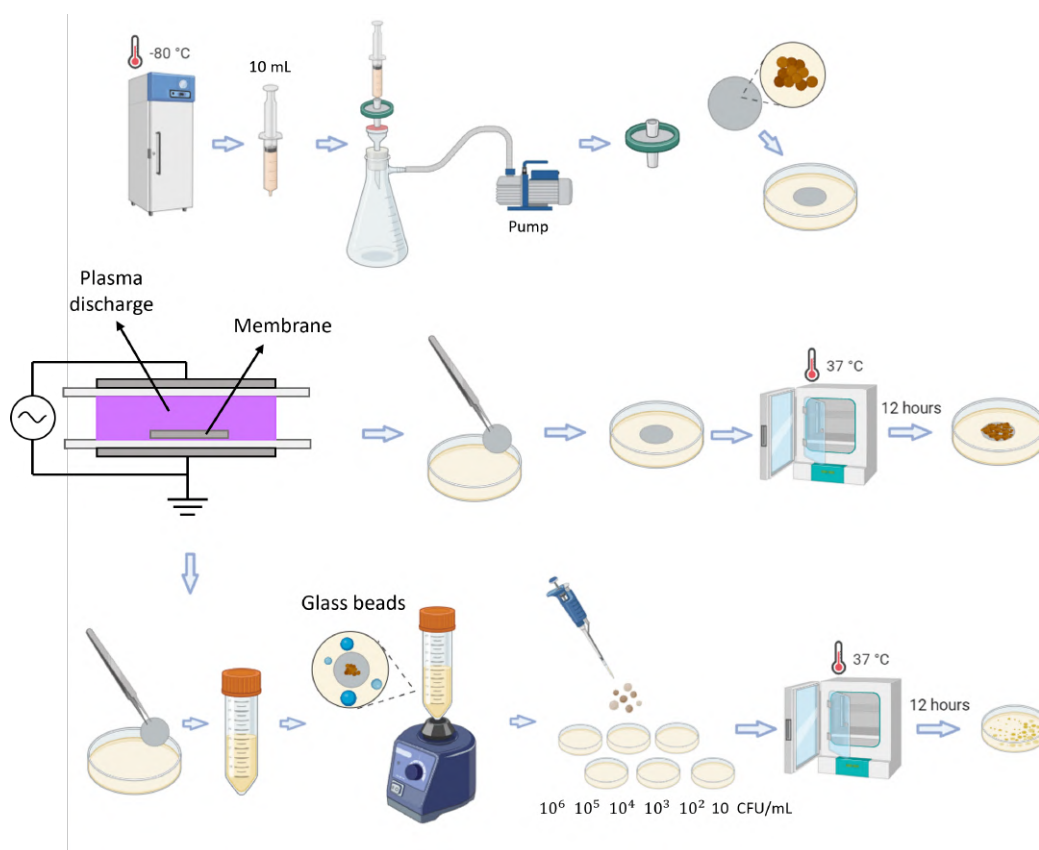


Figure 5.12: Schematics of the *Bacillus subtilis* plasma treatment protocol, from storage to CFU counting. For details, please refer to the main text.

Figure 5.12 depicts the entire protocol used for the spores treatments. A spore suspension is prepared by adding 10 μL of stock suspension of *Bacillus subtilis* spores to 10 mL of Ringer solution, an isotonic solution of electrolytes. A syringe is then filled with the 10 mL of spore suspension. To filter the spores through the membrane, an Erlenmeyer flask is employed. The flask is connected to a pump, and the pressure is monitored using a pressure meter. Subsequently, the flask is sealed by attaching the membrane holder, to which the syringe with spores is connected. This system configuration is depicted in Figure 5.12. Once the pump is activated, the spore suspension is filtered through the membrane holder while maintaining the pressure within the range of 70-80 kPa. After the syringe is emptied, sterile air is circulated

through the system for 5 minutes to ensure uniform membrane coverage. Additionally, a common decimal dilution of the spore suspension is performed to continually monitor its concentration during the preparation of each membrane.

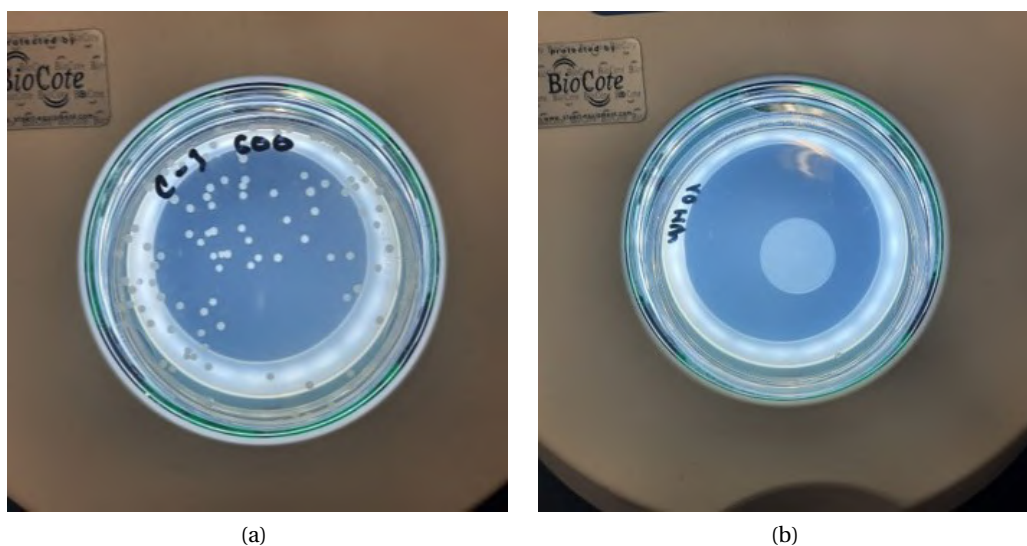


Figure 5.13: (a) Example of washed membrane CFU on petri dish and (b) directly plated membrane as quality control.

Following the filtration process, the membrane is placed on a Petri dish and allowed to air-dry for 20–30 minutes. Once dried, it can be cut into as many parts as required for the selected treatments, making it ready for the plasma treatments. Following this procedure, the spores are deposited on the membrane without piling up and forming a monolayer as clearly shown by the scanning electron microscope (SEM) images of the prepared membrane surface in Figure 5.11.

5.2.2 *Bacillus Subtilis* spores on monolayer membrane plasma treatments protocol and counting

The membrane, whether whole or cut, is then carefully placed on the surface of the dielectric and subjected to the desired treatment duration. Before each treatment, both the dielectric surface and the tweezers are consistently sterilized with ethanol. After the plasma treatments, there are two potential routes for further processing. If quality checking is the immediate objective, the membrane can be directly placed on a Petri dish. In this case, incubating it at 37 °C for 12 hours is sufficient for the CFU to grow and develop on the membrane surface. However, if the membrane is intended for counting purposes, a washing step is necessary. To achieve this, five glass beads are added to a falcon tube, and vortexing is performed to detach the spores from the membrane. Following this step, dilutions are prepared in the same manner as described in Section 5.1. Subsequently, the diluted samples are plated on Petri dishes, which are then incubated for counting purposes.

5.2.3 Direct plasma treatments of *Bacillus Subtilis* spores results

The initial tests were conducted using full membranes, which implies that the plasma discharge did not completely cover the membrane. Furthermore, as discussed in Section 3.4.3 and Section 4.4.8, the presence of a full membrane in the gap slightly impacted the power and electric field in the plasma. Nonetheless, we conducted the direct treatments in triplicates to assess the reproducibility of the treatments. The VDBD was adapted for the membrane treatments, as described in Section 2.2. The nanosecond pulses were configured at 11.6 kV, with 200 ns pulse duration and a 1 kHz repetition frequency. Based on the power measurements discussed in Section 3.4.3, the plasma discharge power for these plasma characteristics is around 1.5–2 W. These treatments were carried out in a static environment, without the presence of a flow, and with the full membrane positioned on top of the dielectric on the ground side, as shown in Figure 5.14a.

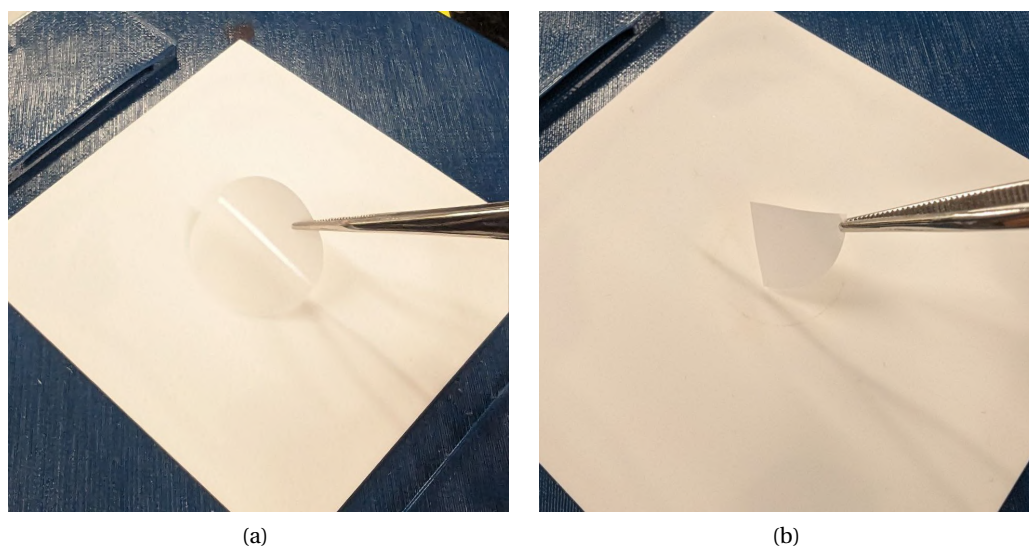


Figure 5.14: (a) Picture of the full membrane being placed on top of the dielectric of the adapted VDBD. (b) Picture of the quarter of the membrane being placed on top of the dielectric.

The results, as shown in Figure 5.15, present the mean and standard deviation of the three replicates. The relatively large standard deviation reflects the notable variations and low reproducibility of these treatments, primarily attributable to the partial coverage of the plasma over the membrane surface, as evident in Figure 5.16.

To enhance the reproducibility of the treatments and minimize the influence of the membrane on the plasma, we divide the membranes into three parts, as illustrated in Figure 5.17a. One half of the membrane was used as a control, while the other half was further divided into two, each corresponding to a quarter of the full membrane. One of the quarters was plasma-treated and subsequently plated to serve as a quality control for evaluating the efficacy of the plasma treatments. The other quarter was subjected to treatment and then washed to obtain quantitative results, as detailed in Section 5.2.2. This quarter of the membrane was

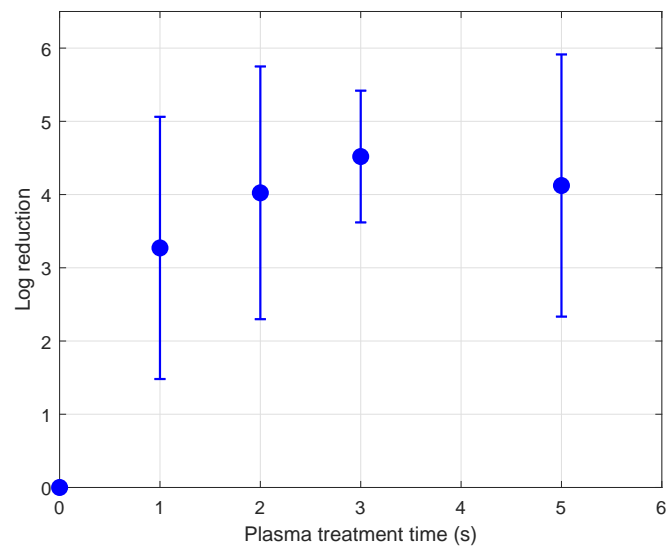


Figure 5.15: Log reduction of *Bacillus Subtilis* spores CFU/mL depending on the duration of plasma exposure. The mean and standard deviation of the log reduction for the triplicate are represented.

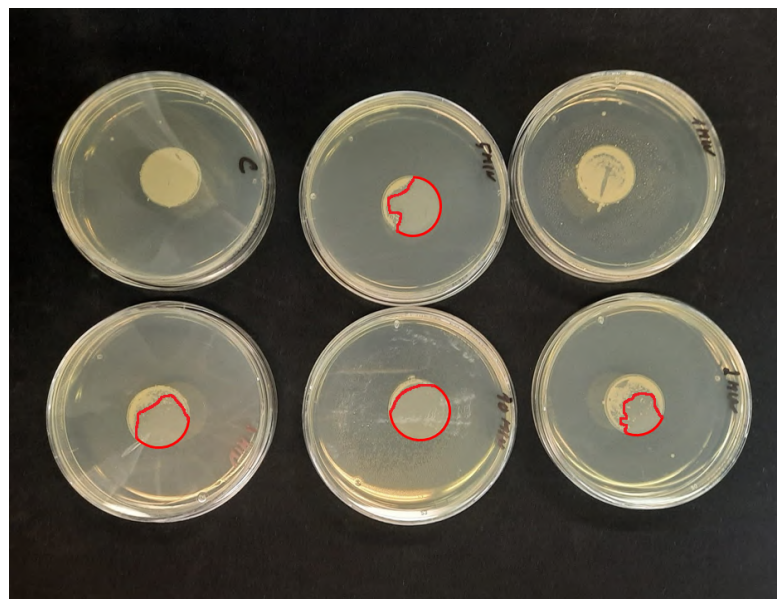


Figure 5.16: Example of treated full membranes of *Bacillus Subtilis* spores CFU/mL, directly plated on an agar Petri dish, depending on the duration of plasma exposure. The region inactivated by the plasma is highlighted in red, showing the bacteria surviving on the side of the membrane, where the plasma does not reach.

positioned in the center of the plasma discharge on top of the dielectric surface to ensure uniform treatments, as shown in Figure 5.14b.

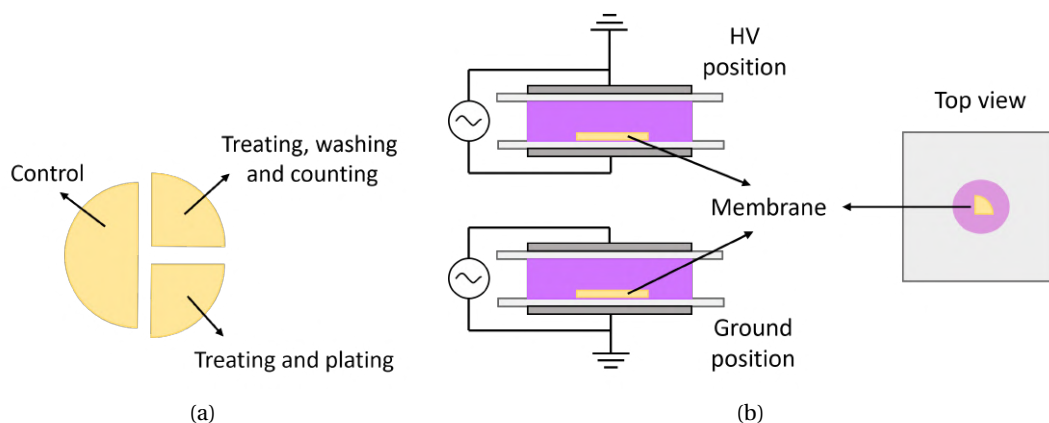


Figure 5.17: (a) Schematic of the cut membrane and different uses of the parts for a single plasma treatment. Half is used as a control, a quarter is treated, plated, and used for quality control, and the other quarter is treated, washed, and used for quantitative results. (b) Schematic of the membrane position inside the VDBD. The HV and Ground positions refer to the high-voltage and ground side of the VDBD.

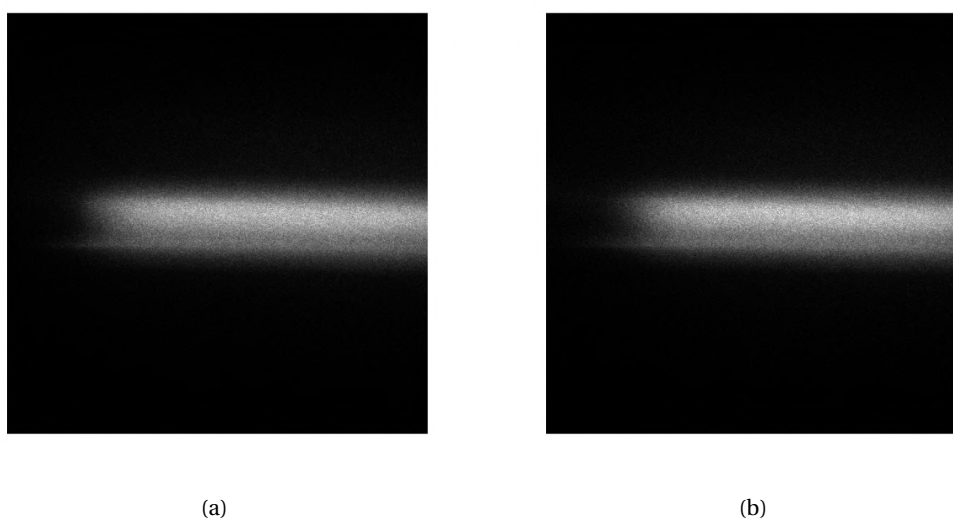


Figure 5.18: ICCD image of the first plasma discharge (a) without the membrane in the VDBD gap and (b) with a quarter of a membrane placed on top of the dielectric surface. All images are acquired with a gate time of 30 ns, for 100 on-ccd accumulations.

To examine the impact of a quarter of a membrane in comparison to the full membrane on the plasma discharge, an ICCD image of the plasma discharge was acquired with a quarter of the membrane in the VDBD gap. The results, presented in Figure 5.18, demonstrate the plasma stays diffused with the quarter of the membrane placed in the VDBD gap, and, differently from the full membrane, it does not change in size. A flow rate of 1000 sccm of saturated humid air was maintained, consistent with the conditions described in the ps EFISH measurements

detailed in Section 4.4, and the waveform parameters were held constant. To investigate the impact of the electric field and position within the plasma discharge on the spores, the membranes were initially placed on the dielectric on the ground side. Subsequently, they were positioned on the high-voltage side, mirroring the positioning of the ps EFISH measurements labeled "Ground" and "HV," as depicted in Figure 5.17b.

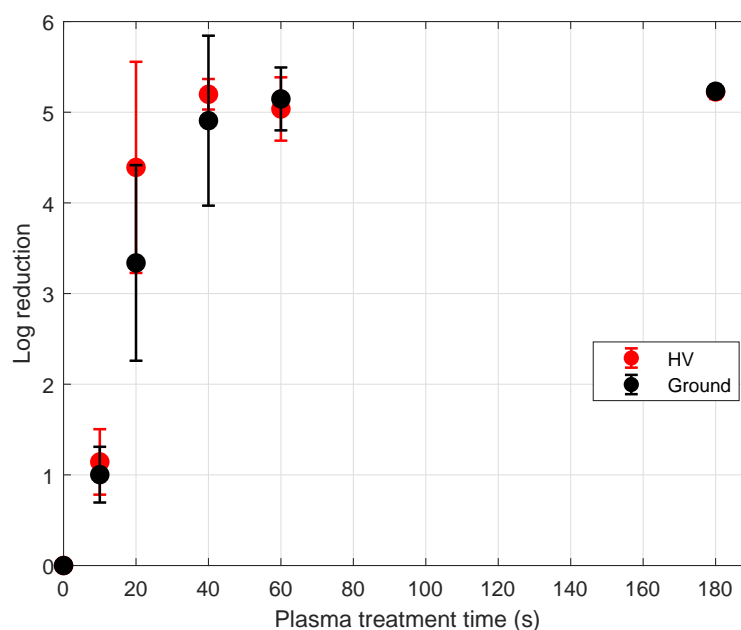


Figure 5.19: Log reduction of *Bacillus Subtilis* spores CFU/mL depending on the duration of plasma exposure. The mean and standard deviation of the log reduction for the triplicates are represented. The red data refers to the HV position, while the black data refers to the Ground position. Note that the errorbars of the data at 180 s are too small to appear on the plot.

This setup delivered more reproducible results. Figure 5.19 displays the mean and standard deviation of the log reduction obtained by direct plasma treatments of *Bacillus Subtilis* spores on membranes. The replicates exhibit much less variability compared to the case of full membranes, except for the 20-second treatment, likely due to its position on the steepest part of the log reduction curve. Nonetheless, the results show the same log reduction efficacy for the Ground and HV plasma treatments. The 20-second treatments show a more significant difference favoring the HV position for the 20-second treatments, however, the statistical significance is not enough to draw definitive conclusions about differences between the HV and Ground positions. The steepness of the log reduction curve between 10 and 40 seconds suggests the majority of the bacterial inactivation is occurring within this time window. Hence, a more accurate analysis of the time interval spanning from 10 to 40 seconds during these direct treatments might provide insight into whether or not the spore placement in the HV position yields more efficacious plasma treatments. Nevertheless, the treatments are remarkably effective and rapid. After just 40 seconds of treatment, nearly all *Bacillus Subtilis* spores are inactivated. It is easily possible that the inactivation efficacy is even stronger

than what is reported in this work, especially after 1 minute, since the maximum spore population being treated is approximately 10^5 . Moreover, the diffuse nature of the plasma enabled us to achieve consistent and uniform treatments, which can be challenging to attain with filamentary plasma. Additionally, these treatments can be characterized using other diagnostics, such as EFISH and LIF. It is important to note that the plasma treatments had an effect on the membrane material. The membrane, after exposure to plasma, exhibited signs of surface modification, resembling wrinkles, as evident in Figure 5.20. However, this surface modification did not compromise the membrane integrity, and the treatments were carried out without any issues. Nonetheless, it is essential to investigate the impact of plasma on the membrane surface.

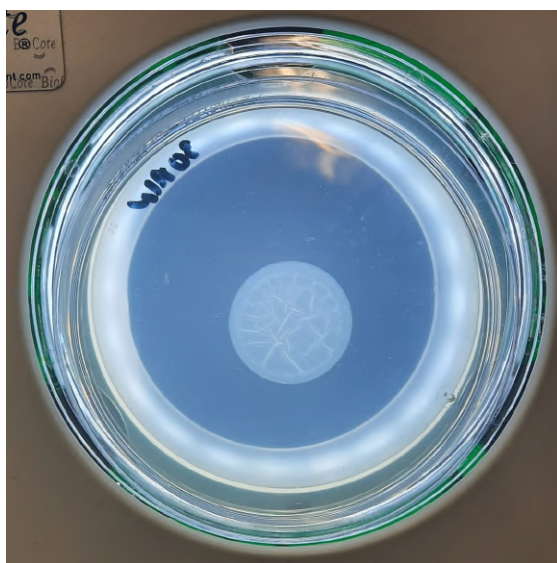


Figure 5.20: Picture of membrane after plasma treatments. The surface modification is clearly visible as "wrinkles" on the membrane.

Direct plasma treatments with membrane in the center of the gap

The ps EFISH measurements described in Section 4.4, revealed differences in the electric field depending on the position inside the plasma discharge, specifically in the center of the gap and in proximity of the dielectric surfaces. The electric field in the center was found to be less intense than the electric field close to the dielectric surfaces. To verify whether this would affect the direct plasma treatments, we conducted *Bacillus Subtilis* spore treatments with the membrane positioned in the middle of the plasma discharge. Nylon strings were used to secure the membrane in place at the center position, as depicted in Figure 5.21.

Only a single replicate was performed, since this method of keeping the membrane in place at the center position of the gap was not reliable. Despite this limitation, the preliminary results demonstrate a notably less efficient inactivation of the spores by the plasma treatments, as illustrated in Figure 5.22. In particular, the 20- and 40-second plasma treatments exhibit

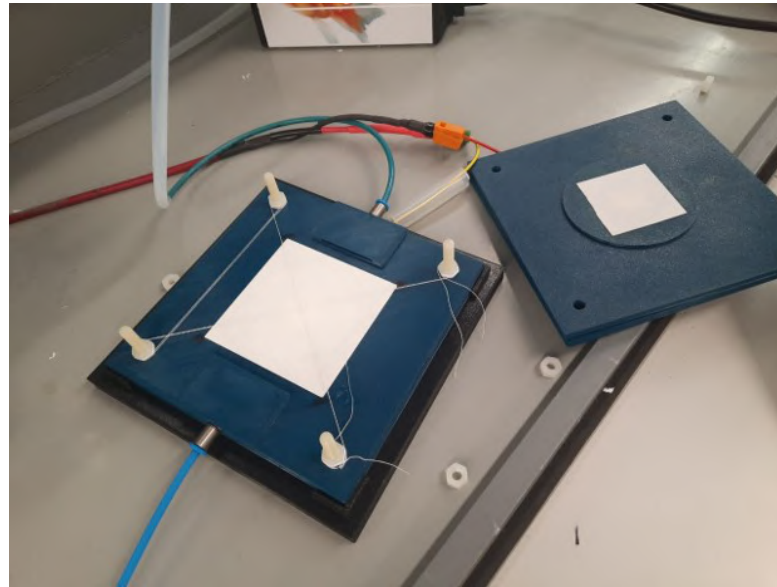


Figure 5.21: VDBD adapted for *Bacillus Subtilis* spores plasma treatments on membrane placed at the Center position. The nylon strings used to keep the membrane in place are visible.

significantly less effect on the spores. However, after 1 minute of treatment, all the spores have been inactivated, as observed in the other treatments (the lower log reduction value is attributed to the lower number of spores counted in the control group).

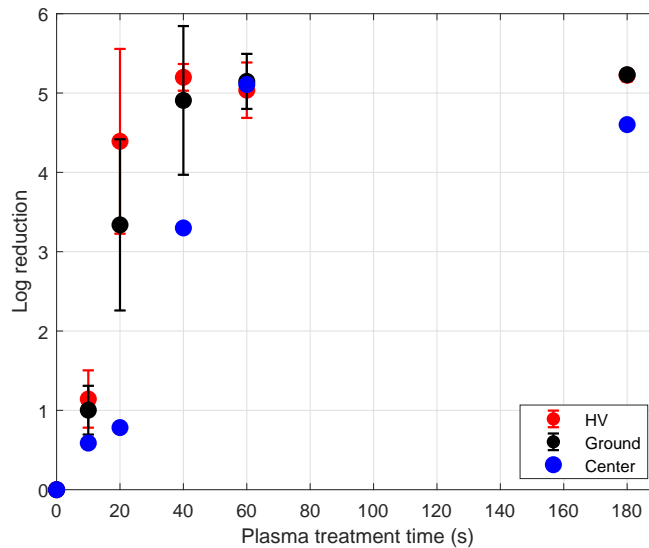


Figure 5.22: Log reduction of *Bacillus Subtilis* spores CFU/mL depending on the duration of plasma exposure. The blue data represent the treatments performed with the membrane in the Center position. The HV and Ground position are also plotted for reference.

To treat the membrane in the center of the plasma discharge requires a more dependable experimental configuration, and additional replicates are required to determine whether the position of the target within the plasma discharge affects the plasma treatments. Nevertheless, these initial findings suggest that the mechanisms underlying bacterial inactivation in LTPs may be less pronounced at the center of the plasma discharge. Further measurements are required to gain a more comprehensive understanding of how other plasma products vary within the plasma discharge. Nevertheless, these preliminary measurements underscore the importance of the biological target placement in relation to the plasma discharge and the significant variations in biological treatments based on the position within the plasma source.

5.3 Preliminary sterilization experiments with biological indicators

In the context of developing an application for this technology, we investigated the potential to achieve sterilization standards through low-temperature plasma treatments. These tests were conducted as part of the Solutions4Sustainability (S4S) proposal [182], aimed at developing a plasma-based method for use in the sterilization facility of the Sciences de la Vie (SV) department at EPFL.

5.3.1 BT96 biological indicator protocol

To evaluate the sterilization efficacy of well-established methods such as autoclaves, specific vials called biological indicators (BI) are routinely used. These BIs are designed to be permeable to steam and sensitive to heat, which is the mechanism responsible for bacterial inactivation in autoclave processes. However, since plasma technology is not a currently used sterilization method and the precise mechanism by which it inactivates bacteria is not fully understood, it was necessary to find an appropriate method to determine the sterilization efficacy of plasma treatments. For this purpose, we selected the biological indicator BT96 [183]. The BT96 BI is designed for monitoring plasma or vaporized hydrogen peroxide (H_2O_2) sterilization processes. This BI is intended for plasma-based methods that rely on the ionization of vaporized H_2O_2 , and as such, the vial is permeable to reactive species. This makes it a suitable preliminary method to assess the sterilization efficacy of air-based plasma treatments. The BT96 BI, depicted in Figure 5.23, is a polypropylene vial containing at least $\geq 10^6$ *Geobacillus stearothermophilus* ATCC 7953 spores.

As written in the instructions of the BT96 BI [183] "*An optional visual pH color change confirmation could be performed after 48 hours of incubation. If the sterilization process has not been successful, the culture medium will change to yellow during incubation at 60°C, thus showing the presence of living spores. If the sterilization process is successful, the culture medium will remain purple after the incubation process.*". Therefore, the vial was activated, subjected to plasma treatment, and then incubated for 48 hours, following which the color change was assessed.

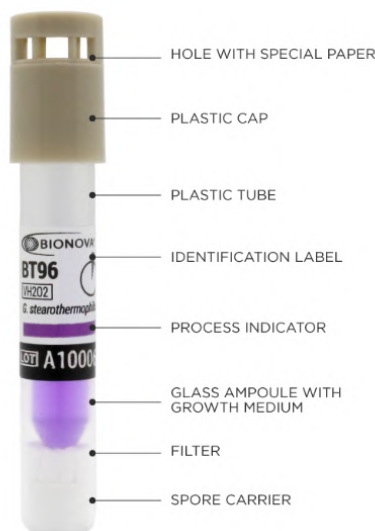


Figure 5.23: BT96 biological indicator used for the sterilizations experiments.

5.3.2 Plasma treatments of BT96 results

All the sterilization experiments were conducted using the perforated-disc SDBD described in Section 2.5, inside the reactor. An initial attempt to achieve sterilization was carried out with the setup we were already familiar with. We used the perforated-disc SDBD powered by the nanosecond-pulsed power supply at 8 kV, 400 ns long pulses, and 1 kHz, within the reactor without any flow, creating a static closed environment. Two BT96 BIs were utilized for each treatment: one placed at a distance of 2 cm from the plasma surface, as shown in Figure 5.24, and one at the bottom of the reactor at the edge. These BIs were subjected to 4 hours of continuous plasma exposure. However, these tests did not yield any positive results, as the vials turned yellow after 48 hours of incubation, indicating that the plasma treatments had no effect. Therefore, we decided to change the power supply to increase the plasma discharge power. To achieve this, the PAW power supply was employed to boost the plasma discharge power to approximately 39 W, as described in Section 2.1.3.

These treatments were carried out firstly in a static closed bio-plasma reactor and secondly with a 1000 sccm flow of saturated humid air and a passive exhaust, reaching a relative humidity of $\sim 70\%$ RH. The plasma treatments were conducted for 1 hour, consisting of repetitive cycles of 10 minutes of continuous plasma exposure followed by 5 minutes of pause to prevent the DBD from overheating. It is worth noting that the higher power delivered to the system could lead to DBD heating, even with the use of a cooling system.

The vials, examined after a 48-hour incubation period, are depicted in Figure 5.25. The successful treatments are indicated by the purplish vials, whereas the yellow ones denote unsuccessful results. The treatments were successful in the static case, both in proximity to the SDBD and at the bottom of the reactor, while, in the case of treatments conducted with a

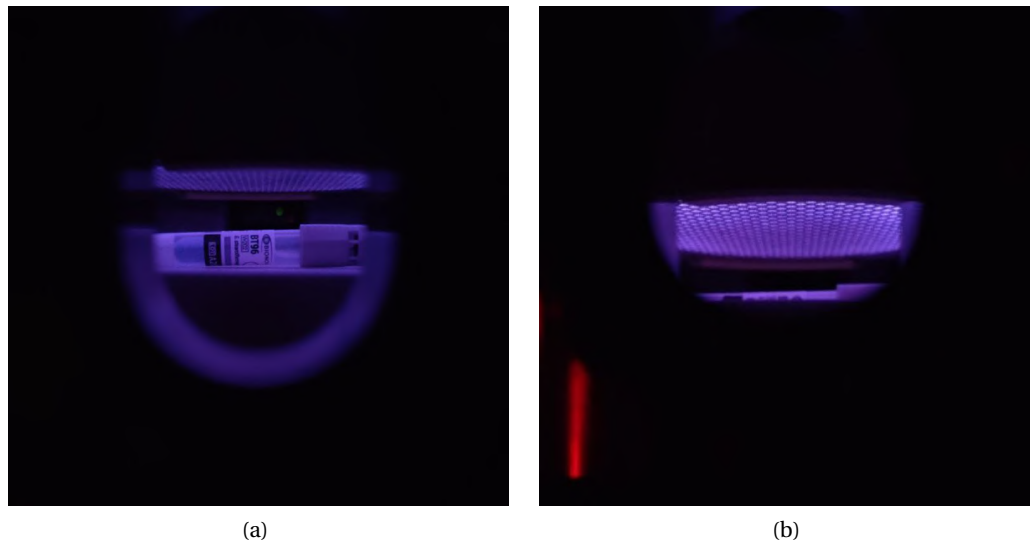


Figure 5.24: (a) Picture from the reactor window, showcasing the BT96 BI positioned inside the reactor, 2 cm away from the perforated-disc SDBD. (b) Better view of the plasma surface generated by the SDBD.



Figure 5.25: BT96 BI used for the sterilization experiments after 48 hours. The yellow vials correspond to unsuccessful treatments, while the purple ones are obtained after successful treatments.

relative humidity of approximately 70%, success was only achieved close to the SDBD. These preliminary results demonstrate the potential to attain sterilization standards under specific conditions. This area is worth further investigation to develop a plasma-based technology for sterilization, taking advantage of the numerous benefits this technique offers.

5.4 Conclusions

In this chapter, we explored the effects of low-temperature plasma treatments on a diverse range of bacteria, employing different treatment methods. Our exploration included both gram-positive bacteria in spore form and gram-negative bacteria in non-spore form. The plasma treatments were performed using different techniques, such as on agar Petri dish surfaces, on monolayer membranes, and with biological indicators. Additionally, various DBDs were used for both direct and indirect treatments. While promising results emerged regarding the efficacy of plasma treatments in bacterial disinfection, the experimental process revealed challenges and complexities.

The *E. coli* indirect plasma treatments were conducted using the PCB-fingers SDBD. The treatments demonstrated substantial log reductions in the bacterial population, with a significant impact observed even at low power settings. However, challenges arose in achieving reproducibility, primarily due to humidity-induced damage to the SDBD surface. The preliminary results not only demonstrated the significant impact of the biological target on altering plasma operation by influencing humidity and gas composition, but also highlighted an intriguing observation. Despite the indirect nature of the plasma treatments, with bacteria positioned up to 1 cm away from the plasma surface, a localized effect was evident. This was substantiated by the distinctive inactivation pattern observed on the Petri dishes. To address this issue, modifications were made, including introducing a dry airflow to minimize humidity, replacing the SDBD before each replicate and increasing the distance of the bacteria from the plasma surface up to 1.5 cm. These adjustments significantly improved reproducibility, enabling systematic studies of indirect plasma treatments. Notably, exposure to plasma for 10 minutes resulted in a remarkable 4-log reduction in the bacterial population. Furthermore, an investigation into the role of nitric oxide in the disinfection process was conducted. LIF measurements, described in Section 7.3, revealed a concentration of nitric oxide smaller than 1 ppm. To test the effect of this concentration of NO on *E. coli* we treated the bacteria with 1 ppm of NO. Direct exposure for 10 minutes did not exhibit discernible effects on the bacterial population. This led to the conclusion that NO, at this concentration, may not play a direct role in bacterial inactivation, emphasizing the importance of secondary reactive species generated during plasma treatments.

For *Bacillus Subtilis* spores, a different approach involving a monolayer membrane loaded with spores was adopted. This method allowed for direct plasma treatments without significantly altering plasma properties. Despite challenges in reproducibility related to the presence of the full membrane in the plasma gap, adaptations were made by dividing the membrane and conducting treatments on smaller sections. The results of these treatments demonstrated complete inactivation of the spore populations after only 1 minute of plasma exposure. The treatments were performed in the same experimental setup as the ps EFISH measurements to couple the bacteria treatments with the measured electric field. For this reason, the treatments were performed both on the ground and on the high-voltage side of the VDBD, showing not a significant difference. Since the log reduction curve is steeper between 10 and 40 seconds

treatments, differences in bacterial inactivation efficacy in this time window are more evident. Hence, a more precise examination of the time interval between 10 and 40 seconds could yield information regarding the impact of the target placement within the plasma discharge on the direct plasma treatments.

Finally, in the pursuit of practical applications for plasma technology, we delved into the prospect of achieving sterilization standards through low-temperature plasma treatments. To assess the sterilization efficacy of plasma treatments, we employed the BT96 biological indicator, containing at least $\geq 10^6$ *Geobacillus stearothermophilus* ATCC 7953 spores. The BT96 BI, permeable to reactive species, was chosen as a preliminary method to evaluate the sterilization effectiveness of air-based plasma treatments. The treatments were performed with the perforated-disc SDBD powered by the PAW power supply to increase the plasma discharge power and operate better in high humidity conditions. Encouragingly, the BI was successfully inactivated by 1-hour treatment within a closed bio-plasma reactor with no flow.

The findings presented in this chapter provide valuable insights into the intricate dynamics of plasma treatments on bacterial populations. Successful reductions in bacterial and spore populations under specific conditions underscore the potential of plasma technology for disinfection applications. Nevertheless, challenges related to reproducibility and environmental factors must be meticulously addressed for practical implementation. Importantly, these experiments highlight the need to consider the influence of the biological target on the plasma treatment setup and emphasize the necessity of reproducing the same conditions to accurately characterize the plasma under real application conditions. In conclusion, this chapter advances our understanding of plasma treatments on bacteria, paving the way for the development of efficient and reproducible disinfection methods with broad applications.

6 Chemical Characterization: FTIR Spectroscopy

This chapter delves into the chemical characterization of three distinct plasma setups using Fourier transform infrared (FTIR) spectroscopy. The aim is to unravel the dynamics of long-living reactive oxygen and nitrogen species (RONS) under various experimental conditions, providing crucial insights into the chemical composition and kinetics of these species. The same setups used for the biological treatments described in Chapter 5, namely, the PCB-fingers SDBD, perforated-disc SDBD, and VDBD, are meticulously analyzed through in-situ FTIR measurements, providing a comprehensive understanding of the production and dynamics of long-living RONS.

Section 6.1 begins with a brief introduction to the fundamentals of FTIR spectroscopy, showing the advantages of FTIR spectroscopy with respect to dispersive IR spectroscopy and providing insights into the calibration method employed based on the Beer-Lambert law.

In Section 6.2 the experimental setup used for the FTIR measurements is described in detail. The FTIR spectra are acquired in-situ, allowing for more direct measurements of the RONS produced by the plasma. The parameters for both the FTIR spectrometer and the HITRAN database, used to simulate the absorbance cross-sections, are presented.

Next, Section 6.3 discusses the results obtained from the different setups. The measurements are conducted under the exact conditions employed for the biological treatments detailed in Chapter 5, as well as under different conditions to assess the impact of small changes in setup parameters on the production of RONS. The PCB-fingers SDBD, perforated-disc SDBD and VDBD setups are all analyzed in detail, to investigate the RONS produced in these three configurations. Finally, a small summary of the main conclusions of this chapter is given in the last section.

6.1 Introduction to Fourier transform infrared spectroscopy

This section provides a general introduction to FTIR spectroscopy without attempting to be exhaustive. For more details, please refer to Ref. [184]. FTIR spectroscopy is widely recognized for its ability to deliver detailed molecular-level information on the composition and chemical dynamics of low-temperature plasma products [97, 185, 186]. Based on the interaction of infrared radiation with matter, this analytical technique enables the examination of vibrational and rotational modes of molecules, providing valuable insights into the presence of chemical species, their concentrations, and their temporal evolution. In the field of low-temperature plasmas, the unique advantages of FTIR spectroscopy have established it as an essential tool for investigating and comprehending the underlying physical and chemical processes.

The origins of infrared light discovery trace back to the 19th century, and since then, infrared absorption spectroscopy has been instrumental in determining molecular structures and measuring concentrations. The infrared spectrum encompasses wavelengths that excite the vibrational levels of molecules. When subjected to infrared radiation, sample molecules selectively absorb radiation at specific wavelengths, inducing a change in the electric dipole moment of the molecules. Consequently, the vibrational energy levels transition from the ground state to the excited state. The frequency of the absorption peak is dictated by the vibrational energy gap, and the number of absorption peaks correlates with the number of vibrational degrees of freedom of the molecule [184].

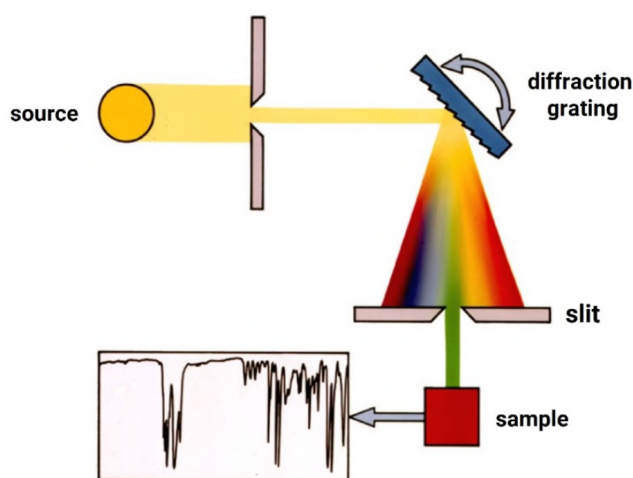


Figure 6.1: Basic schematics of dispersive IR spectroscopy (source: [187]).

The intensity of absorption peaks is related to the change in the electric dipole moment and the likelihood of the transition of energy levels. This means that homonuclear diatomic molecules such as O_2 , N_2 , and Cl_2 , which exhibit zero dipole change during vibration and rotation, are not infrared-active and cannot be detected with FTIR spectroscopy. The commonly used region for infrared absorption spectroscopy is $4000\text{--}400\text{ cm}^{-1}$, encompassing the absorption radiation of the majority of organic compounds and inorganic ions. Traditional IR spectroscopy is

performed by splitting the wavelengths of broad-spectrum IR light using a diffraction grating. The schematics of this approach, also called dispersion IR spectroscopy, are shown in Figure 6.1. By directing the resultant monochromatic IR light beam at the sample, it is possible to detect the absorbance of that particular wavelength. This procedure is iterated until the absorbance of all wavelengths of infrared light is measured. By plotting the resulting data, the IR spectrum can be obtained. This approach is tedious, and it has long acquisition times.

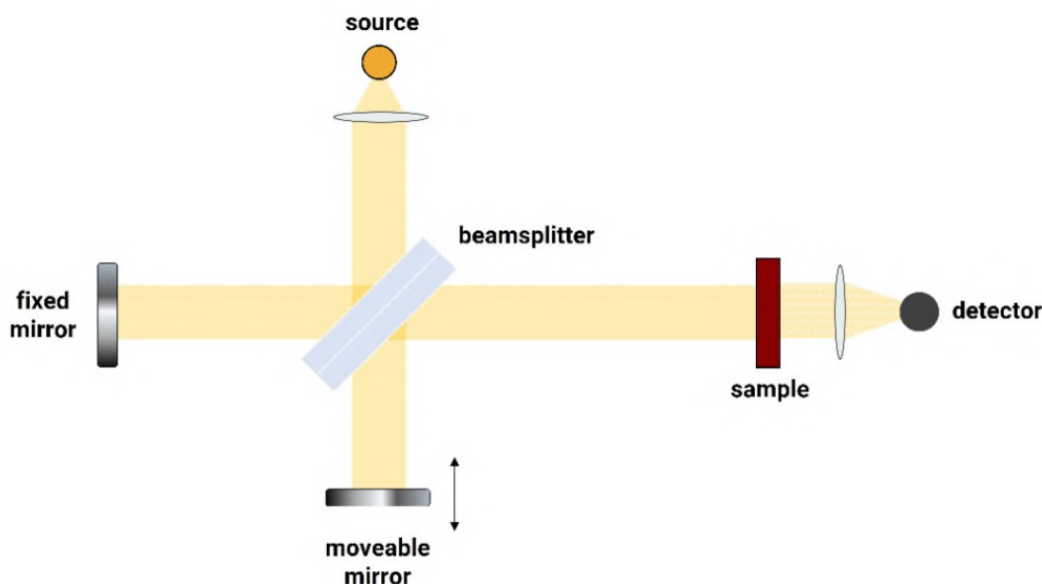


Figure 6.2: Basic schematics of FTIR spectroscopy, based on an interferometry system (source: [187]).

The main difference between dispersive IR spectroscopy and FTIR spectroscopy is the interferometer, shown in Figure 6.2, which, owing to a movable mirror, enables rapid measurements. The IR beam is split in half within the interferometer by a beam splitter before being directed towards two mirrors. After reflecting off the mirrors, the beams recombine at the beam splitter location. The moving mirror induces a phase mismatch between the two beams due to the different travel distances. An interference pattern is, then, produced when the two beams recombine. Each interference pattern causes distinct wavelengths of IR light to be present in the recombined beam, and by quickly moving the mirror through different positions, it is possible to cover the entire IR spectrum.

The resulting wave acquired by the detector is called an interferogram, shown in Figure 6.3a, and it is a function of the difference in optical length travelled by the IR beam in the two branches of the interferometer. Since the optical path is defined by the position in time of the moving mirror, the interferogram acquired by the detector is a time-domain spectrum. Finally, the application of the Fourier transform to the interferogram enables the extraction of the frequencies of infrared light that were absorbed by the sample, passing from the time domain to the frequency domain. In terms of ordinary frequency, ν , the Fourier transform is expressed as:

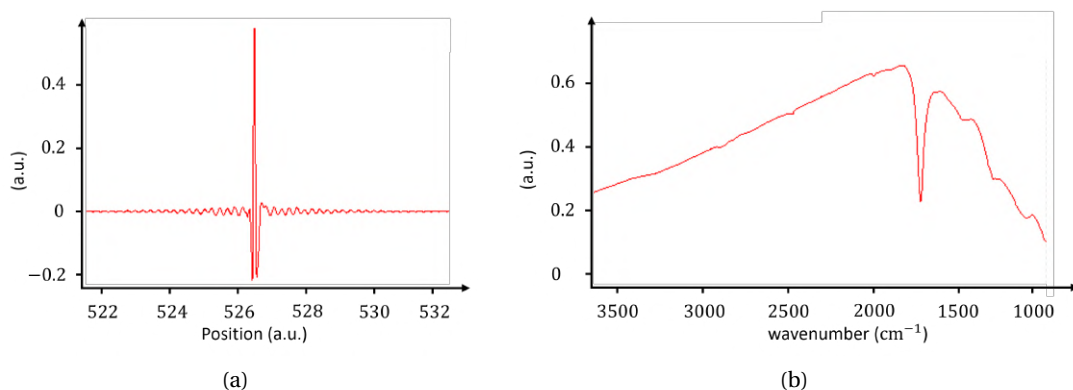


Figure 6.3: (a) Spatial-domain interferogram of the infrared (IR) signal. (b) Wavenumber-domain absorption spectrum obtained by Fourier-transforming the signal from the spatial domain of the interferogram.

$$f(\nu) = \int_{-\infty}^{\infty} f(t) e^{-i2\pi\nu t} dt. \quad (6.1)$$

The interferogram is then transformed into an IR absorption spectrum, as depicted in Figure 6.3b, commonly presented with absorption intensity or % transmittance plotted against wavelength or wavenumber. The transmittance, T , is the ratio of radiant power transmitted by the sample I to the radiant power of incident light on the sample I_0 . Absorbance, denoted as A , is the logarithm to the base 10 of the reciprocal of the transmittance T :

$$A = \log_{10} \frac{1}{T} = -\log_{10} T = -\log_{10} \frac{I}{I_0} = \log_{10} \frac{I_0}{I}. \quad (6.2)$$

To probe a particular molecule, it is essential to conduct background measurements. Typically, a standard FTIR spectrometer inherently accounts for this by computing the difference between the measured spectrum and a previously acquired background spectrum.

The result is a FTIR absorption spectrum that features peaks corresponding to the different radiation power absorbed by molecules whose concentration changed with respect to the background acquisition. The typical infrared spectrum is inherently presented with background subtraction, as illustrated in Figure 6.4.

6.1.1 FTIR spectrum absolute calibration

The absolute calibration of the FTIR signal is performed using the Beer-Lambert law [188]:

$$I(\nu) = I_0(\nu) e^{-n\sigma_i(\nu)L}. \quad (6.3)$$

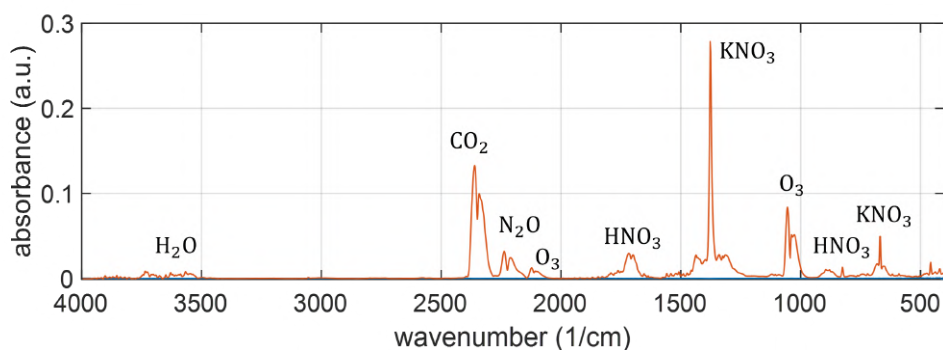


Figure 6.4: Example of a FTIR spectrum, featuring annotations indicating the corresponding molecule for each distinctive absorbance peak.

with $I_0(\nu)$ representing the radiant power of the incident light onto the sample and $I(\nu)$ the radiant power transmitted by the sample, both as a function of the frequency ν . Then, n denotes the density of the absorbing species, while $\sigma(\nu)$ is the absorption cross-section as a function of ν in $\text{cm}^2/\text{molecule}$, and L is the length of the absorbance pathway in cm. Rearranging the terms and recalling the definition of absorbance measured by the FTIR spectrometer from Equation 6.2, we obtain:

$$\ln \frac{I(\nu)}{I_0(\nu)} = -n\sigma(\nu)L;$$

$$A(\nu) = \frac{1}{\ln 10} n\sigma(\nu)L.$$

From the absorbance spectrum $A(\nu)$ measured by the FTIR spectrometer, it is possible to find the density n_i in molecules/ cm^3 :

$$n = \frac{A(\nu) \ln 10}{\sigma_i(\nu)L}. \quad (6.4)$$

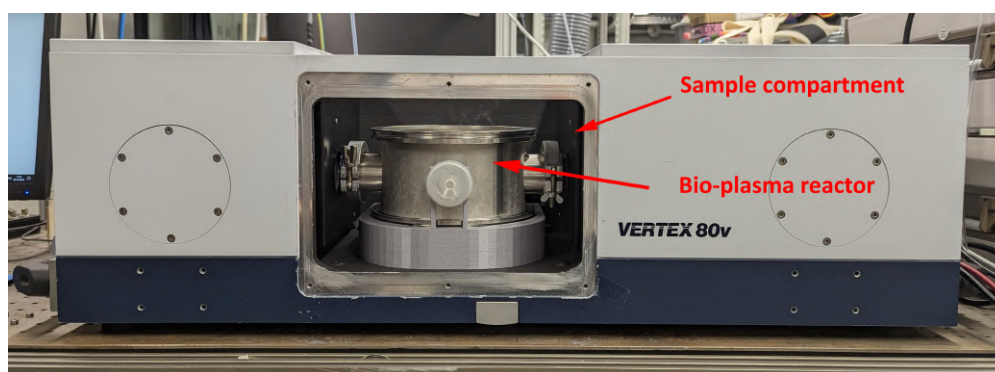
Considering the conversion to ppm as $n = n_0 n_i \times 10^{-6}$, where n_i is the density of species i in ppm and n_0 is the density of the gas, we can finally express the equation to determine the concentration in ppm of a specific molecule as follows:

$$n_i = \frac{A(\nu) \ln 10}{\sigma_i(\nu)L} \left(\frac{10^{12}}{n_0} \right), \quad (6.5)$$

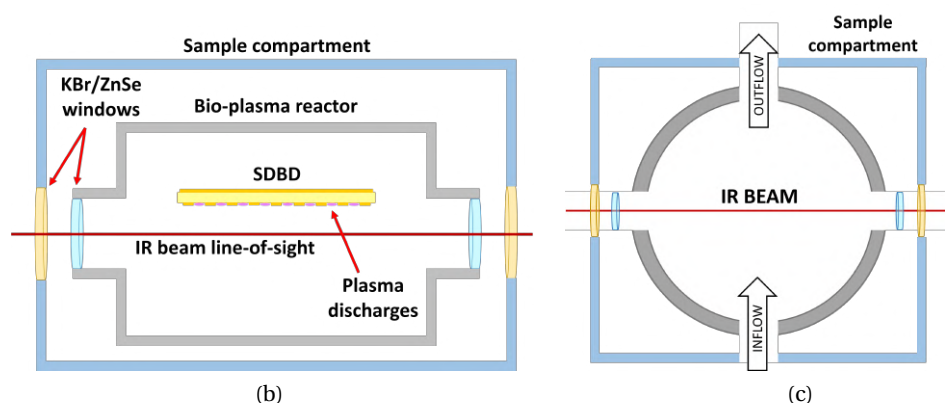
where $A(\nu) = \ln(I_0/I)$ represents the absorbance as a function of frequency ν . $\sigma_i(\nu)$ is the absorption cross-section of species i as a function of ν in $\text{cm}^2/\text{molecule}$. The last term $10^{12}/n_0$ is a conversion factor necessary to convert from molecule/ cm^3 to ppm.

6.2 In-situ FTIR spectroscopy experimental setup

In contrast to the more common methods, where FTIR spectroscopy is applied to the gas exhaust of the plasma source [97], our approach follows an in-situ methodology [129][185]. The significance of in-situ FTIR measurements lies in preventing changes in gas composition during the flow of the gas exhaust to a downstream FTIR spectrometer. In-situ measurements involve assessing molecules at their source, prior to any contact with surfaces, and immediately after their production, eliminating transit delays where reactive species could be modified by secondary gas reactions [129].



(a)



(b)

(c)

Figure 6.5: (a) Image of the bio-plasma reactor hosted within the sample compartment of the spectrometer. (b) Schematic representations illustrating the optical path of the IR beam within the bio-plasma reactor, presented from a side view and (c) top-down.

The in-situ FTIR measurements are performed employing a Bruker Vertex 80v spectrometer. The IR beam is focused within the sample compartment, as shown in Figure 6.5, converging at a point of maximum focus of approximately 8 mm, while the diameter of the beam is around 2.5 cm at the flap windows (see the Appendix for the FTIR schematic details). This has no impact on the measurements of the SDBDs. However, it is significant in the case of VDBDs since the diameter of the IR beam exceeds the VDBD gap, which is 1.75 mm. While this does not prevent the FTIR measurements, it does result in a decrease in signal strength,

hence affecting the signal-to-noise ratio. However, this issue did not significantly impact the measurements on the VDBD setup. The bio-plasma reactor is positioned within the sample compartment of the Vertex 80v, as depicted in Figure 6.5. Two flanges are employed to enable the entry and exit of the infrared beam in the bio-plasma reactor by using suitable IR windows along the optical path. The two flanges, positioned perpendicularly to the IR beam, are used instead for the inflow and outflow of the selected gas. The bio-plasma reactor can also operate in a closed configuration, referred to as "static," with no gas flow and no exhaust. A dedicated 3D-printed support has been custom-designed to securely position the bio-plasma reactor, guaranteeing accurate alignment and maintaining an optimal beam height with respect to the reactor windows.

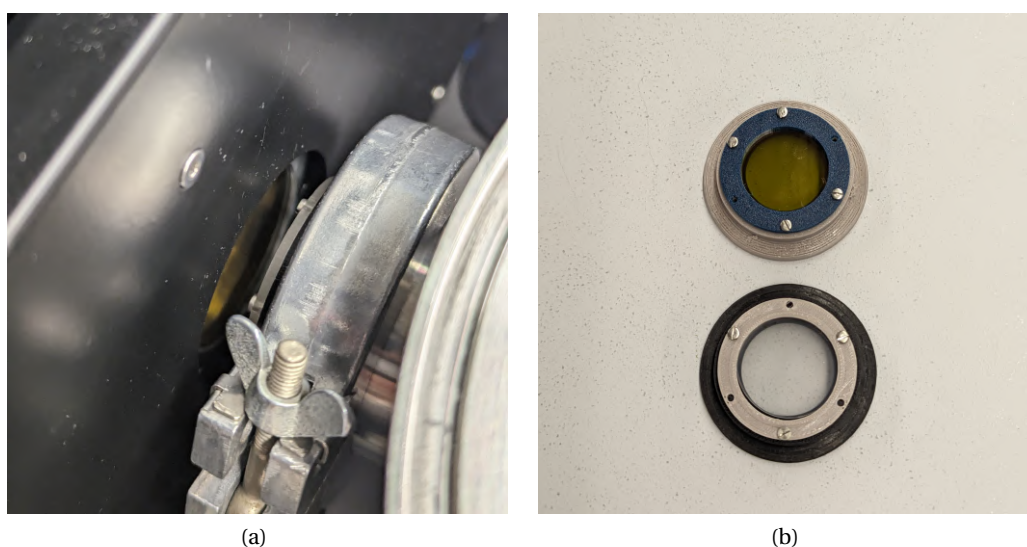


Figure 6.6: (a) Close-up view of one of the flap windows within the sample compartment, featuring ZnSe material. Note the gap between the flange of the bio-plasma reactor and the flap window. (b) Image showcasing the ZnSe window (in yellow) and the transparent KBr window mounted on 3D-printed adapters designed for the bio-plasma reactor.

To hermetically seal the bio-plasma reactor, two windows with a diameter of 30 mm are positioned along the line-of-sight of the IR beam. Custom-designed 3D adapters have been manufactured to match the flanges of the bio-plasma reactor, ensuring a sealed fit for the windows. Conversely, the optics bench of the vacuum FTIR spectrometer is sealed using 49.5 mm diameter windows, referred to as "flap" windows, on each side of the sample compartment, as depicted in Figure 6.6. The window materials consist of either potassium bromide (KBr) or zinc selenide (ZnSe), both known for their favorable infrared transmission characteristics within the range sampled by the FTIR spectrometer.

However, KBr is highly susceptible to humidity, leading to surface deterioration and reducing IR transmittance. Additionally, the reaction between reactive species produced by the plasma and the KBr window surface results in the formation of KNO_3 , a compound that is deposited

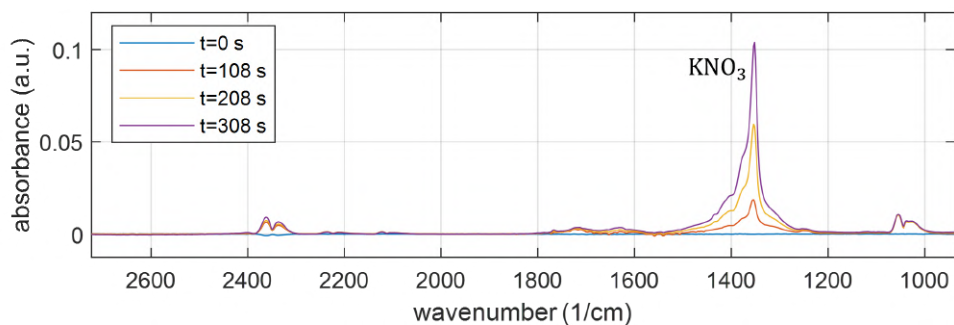
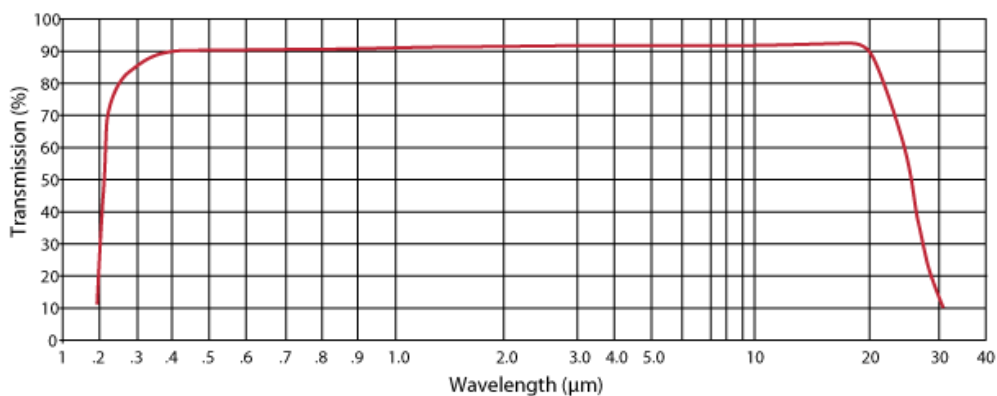
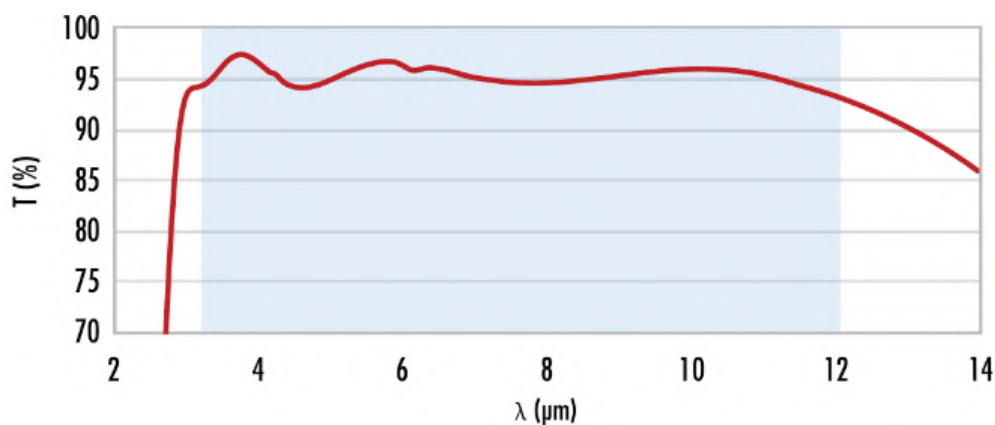


Figure 6.7: FTIR absorbance spectra example of a sequence of acquisition with plasma operating. The significant peak at 1352 cm^{-1} , increasing with time, is KNO_3 forming on the surface of the KBr windows.



(a) KBr



(b) ZnSe

Figure 6.8: Transmission spectra of the (a) KBr and (b) ZnSe material used for the FTIR measurements (source: [189, 190]).

on the window surface, causing an escalating peak during plasma operation at 1352 cm^{-1} , that obscures other molecular peaks within the same wavelength range. On the other hand, ZnSe, while not sensitive to humidity, exhibits a lower transmission coefficient and selectively

filters a portion of the IR spectrum (specifically between 700 and 400 cm^{-1}). Furthermore, unknown secondary peaks arise due to the reaction between ZnSe and plasma products. In this study, both materials were employed for the two sets of windows, as illustrated in Figure 6.5. However, KBr was predominantly chosen for the bio-plasma reactor windows due to both its superior transmission characteristics, shown in Figure 6.8, and our understanding of the peaks resulting from the interaction of KBr with plasma. The flap windows were provided by Bruker, while the bio-plasma reactor ZnSe windows were 30 mm diameter, 3 mm thickness, 3-12 μm coated, and the KBr windows were 32 mm diameter, 3 mm thickness, uncoated, both from Edmund Optics [190, 189], whose transmission spectra are reported in Figure 6.8.

It is important to note that due to the presence of electrical connections and gas tubing to the bio-plasma reactor, the sample compartment remained open. Consequently, the IR beam traversed the ambient air outside of the reactor over a short distance, approximately 2 cm in total, as seen in Figure 1a. This led to fluctuations in CO_2 and H_2O concentrations. Consequently, any conclusions regarding these two molecules in this setup are deemed invalid and are therefore disregarded. The Bruker Vertex 80v offers a broad spectrum of parameters; nonetheless, for the specific objectives of our experiments, a consistent setup was employed. The critical parameters, which are detailed in Table 6.1, were selected to reduce as much as possible the duration of a single acquisition (16 seconds) without compromising the quality of the spectra.

Table 6.1: Parameters used for FTIR spectroscopy measurements.

Resolution	4 cm^{-1}
Spectral range	400 to 4000 cm^{-1}
Number of scans	16
Detector	RT-DLaTGS
Aperture	8 mm
Scanner velocity	10 kHz

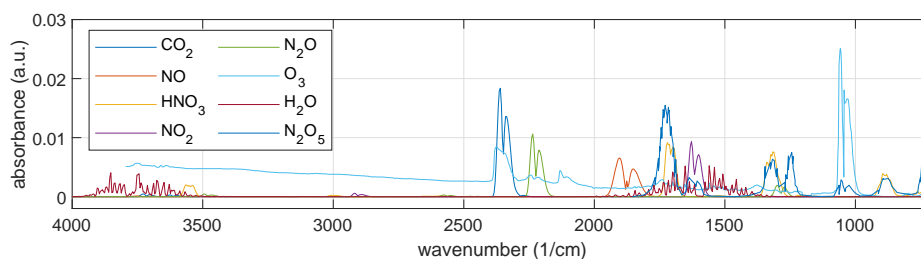


Figure 6.9: FTIR spectra of specific molecules expressed in arbitrary units, namely O_3 , NO , NO_2 , N_2O , N_2O_5 , HNO_3 , CO_2 and H_2O .

Each individual single FTIR spectroscopy measurement is averaged over a duration of 16 seconds, over 16 scans, allowing for individual measurements at 20-second intervals. Following acquisition, the spectra undergo analysis and correction for baseline drift, a common error in FTIR spectroscopy arising from mechanical vibrations in the optical path [191]. Subsequently,

the spectra are compared against reference spectra of specific gases, namely O₃, NO, CO, NO₂, N₂O, N₂O₅, HNO₃, CO₂, and H₂O, shown in Figure 6.9. These reference spectra are sourced from either Bruker or Hitran (High Resolution Transmission) databases [192] to identify the corresponding peaks of the molecules observed in FTIR measurements. Notably, the spectrum for N₂O₅ is obtained from [193].

6.2.1 Calibration of O₃, N₂O, NO₂ and HNO₃

After identifying the molecules corresponding to the peaks of the spectra detected by the FTIR measurement, the absorption spectrum is calibrated according to Equation 6.5. Given that the experiments are conducted at ambient temperature and atmospheric pressure, the gas density is equal to $n_0 = 2.5 \times 10^{25}$ molecules/m³. Regarding the path length, under the assumption that the species diffuse throughout the entire reactor on a timescale shorter than the 16 seconds required for a single spectrum acquisition, by taking $L = 23$ cm, the distance between the windows of the bio-plasma reactor, we are measuring the average concentration along the line-of-sight of the IR beam.

Among the reactive species detected by the FTIR, the absolute calibration can be obtained for O₃, NO₂, N₂O, and HNO₃, since their absorption cross-sections are available in the HITRAN database [192]. The HITRAN molecular spectroscopic database is a compilation of spectroscopic parameters used for simulating and analyzing the transmission and emission of light in gaseous media, with a focus on planetary atmospheres. Since all our experiments are conducted at atmospheric pressure and ambient temperature, the HITRAN database is an ideal tool for simulating the absorption cross-sections of the molecules of interest. Table 6.2 provides the precise parameters used to derive the absorption cross-sections for O₃, N₂O, N₂O and HNO₃.

Table 6.2: Parameters used for O₃, N₂O, NO₂ and HNO₃ absorption cross-section simulation on HITRAN.

Isotopologues	all
Spectral range	500 to 4000 cm ⁻¹
Cut-off intensity	1.0e-28 cm/molecule
Temperature	296 K
Pressure	1 atm
Line profile	Voigt
W	50 halfwidths
WN _{step}	0.00902 (default)
Device function	Gaussian
Resolution	0.1 cm ⁻¹
AW	< 50 (default)

The absorption cross-sections of O₃, N₂O, NO₂ and HNO₃, obtained with these parameters, are presented in Figure 6.10.

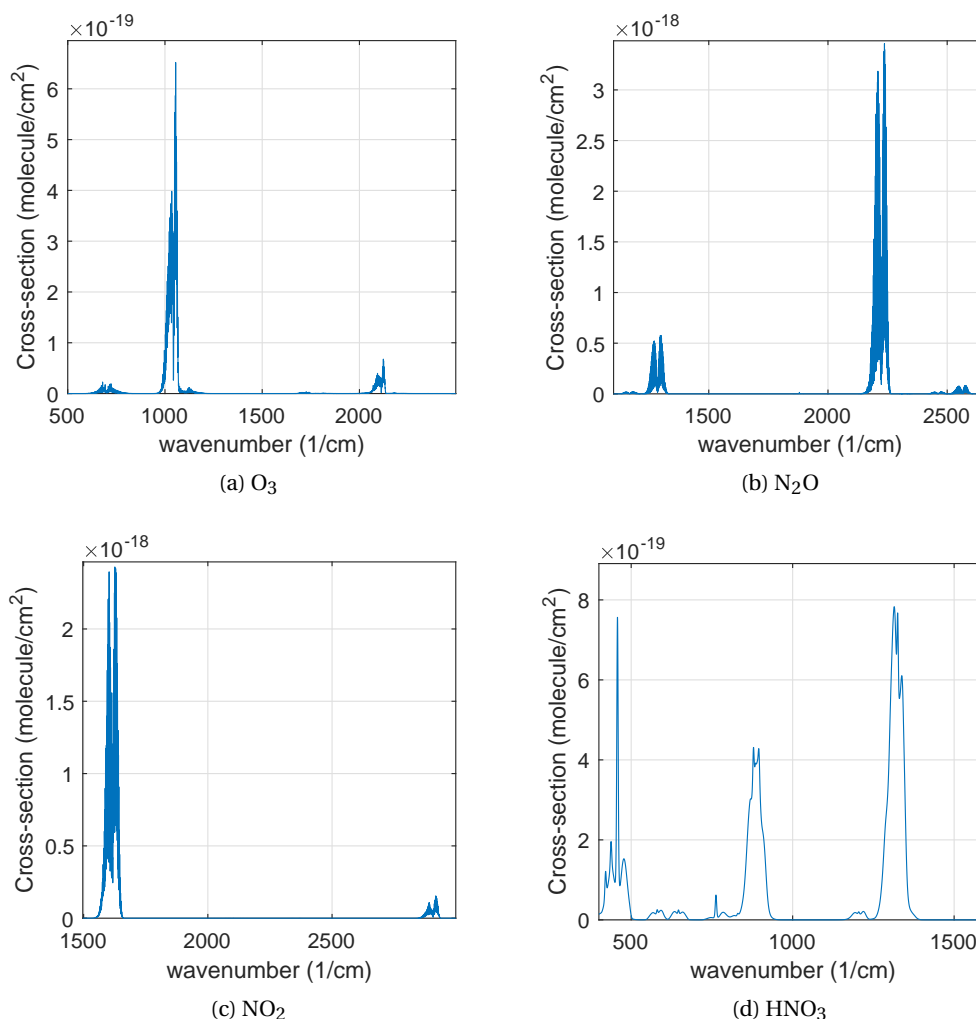


Figure 6.10: Absorption cross-section in $\text{cm}^2/\text{molecule}$ of (a) O_3 , (b) N_2O , (c) NO_2 and (d) HNO_3 , simulated with HITRAN, using the parameters in Table 6.2.

To calibrate the signal, a wavelength band has been defined for the three different molecules, corresponding to the highest peak of the absorption cross-section, as detailed in Table 6.3.

Table 6.3: Wavenumber range used for O_3 , N_2O , NO_2 and HNO_3 calibration.

O_3	1010 - 1065 cm^{-1}
N_2O	2194 - 2250 cm^{-1}
NO_2	1592 - 1600 cm^{-1}
HNO_3	850 - 920 cm^{-1}

The primary absorption peaks of NO_2 and HNO_3 at 1570-1650 cm^{-1} and 1670-1740 cm^{-1} , respectively, are partially overlapped by the water absorption peaks. Consequently, for the calibration process of NO_2 , the wavenumber range 1592-1600 cm^{-1} is selected to avoid the

H₂O absorption peaks, since in this range the absorption cross section of H₂O is null. To calibrate HNO₃, instead, a secondary absorption peak at 850 - 920 cm⁻¹ is used. The FTIR absorbance spectra and the absorption cross-section are integrated over their respective wavenumber ranges, as depicted in Figure 6.11. Finally, the integrated values are applied to Equation 6.5.

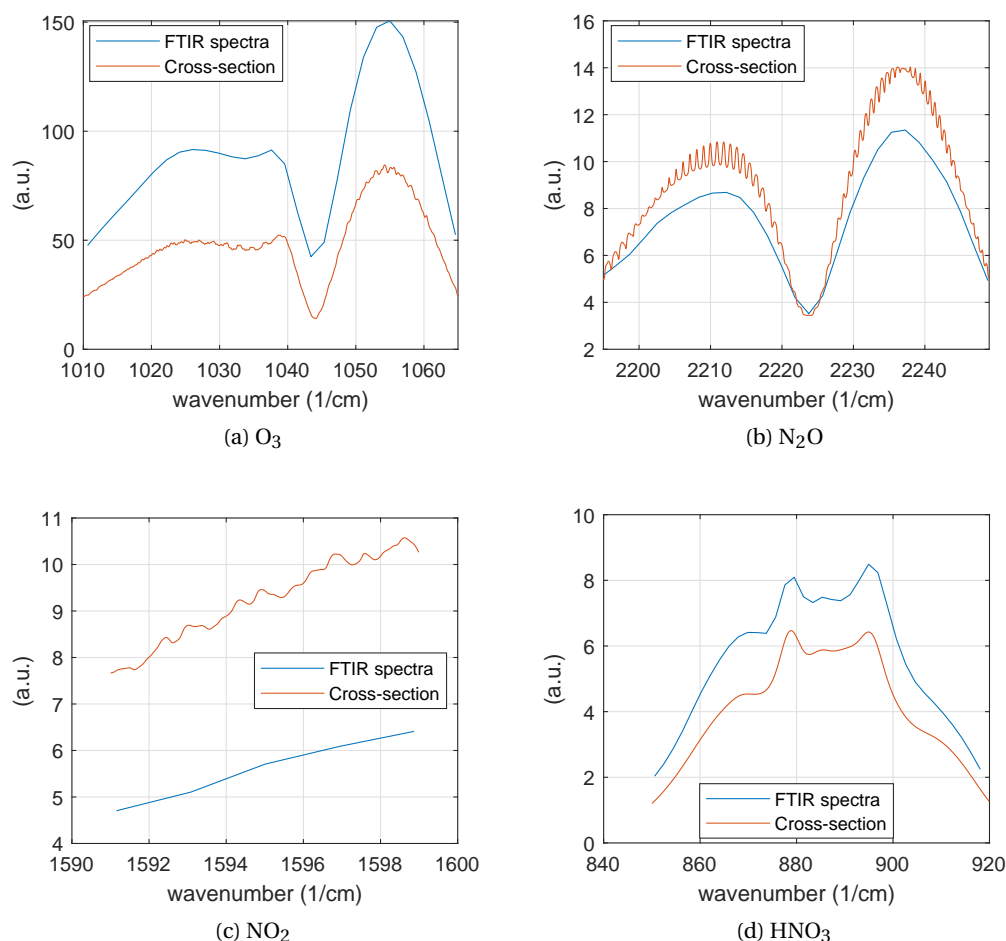


Figure 6.11: Absorption cross-section and example of measurement of FTIR absorbance spectra, for the wavelength range over which the signals are integrated for (a) O₃, (b) N₂O, (c) NO₂ and (d) HNO₃.

6.3 FTIR spectroscopy measurements

This section presents the in-situ FTIR measurements performed on the same DBD setups employed in the bacterial treatments detailed in Chapter 5, the EFISH measurements elucidated in Chapter 4, and the LIF measurements described in Chapter 7. Hence, the results can be robustly correlated with the rest of the results obtained in this thesis, assuring consistency throughout the investigation.

6.3.1 PCB-fingers SDBD FTIR measurements

The experimental arrangement employed in the plasma treatments of *E. coli*, as detailed in Section 5.1, was also characterized using FTIR spectroscopy. The PCB-fingers SDBD is operated at 4.7 kV, 400 ns long pulses at 1 kHz repetition frequency. A schematic representation of the setup for the in-situ FTIR measurements specific to this case is illustrated in Figure 6.13.

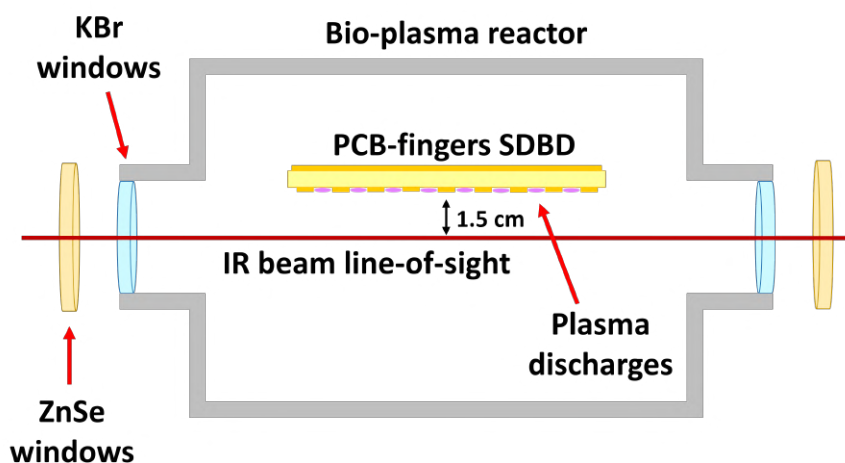


Figure 6.12: Schematics of the in-situ FTIR experimental setup of the PCB-fingers SDBD measurements.

The PCB-fingers SDBD is positioned upside down at a distance of approximately 1.5 cm from the IR beam so that the plasma is generated below the SDBD (as shown in Figure 6.13). The flap window material is ZnSe, and the windows for the bio-plasma reactor are made of KBr. Measurements are conducted at three distinct humidity levels, mirroring the conditions of the *E. coli* plasma treatments. The desired relative humidity is achieved through the gas flow system outlined in Section 2.5. This system is regulated by three Bronkhorst mass flow controllers: one for pure nitrogen (N_2), one for pure oxygen (O_2), and one for dry synthetic air. The latter, upon passing through a bubbler, generates saturated humid air, ideally at 100% RH. However, the tests performed on the flow setup demonstrated that the maximum achievable relative humidity with this configuration is approximately 90% RH. The gas mixture maintains a nitrogen-to-oxygen ratio of 4:1, while the total flow rate remains constant at 3000 sccm, with a passive exhaust. The study explores three distinct flow configurations:

- RH \approx 0%: 0 sccm humid synthetic air, 2400 sccm N_2 , 600 sccm O_2
- RH = 13% \pm 2%: 500 sccm humid synthetic air, 2000 sccm N_2 , 500 sccm O_2
- RH = 23% \pm 2%: 1000 sccm humid synthetic air, 1600 sccm N_2 , 400 sccm O_2

These three experimental conditions will be denoted as 0% RH, 13% RH and 23% RH. Fluctuations in RH result from slight temperature increase ($<10^\circ C$) in the gas during the plasma

discharge. FTIR spectra were acquired with a temporal resolution of 20 seconds over a duration of 10 minutes following the initiation of the plasma discharge for each of the three unique flow configurations.

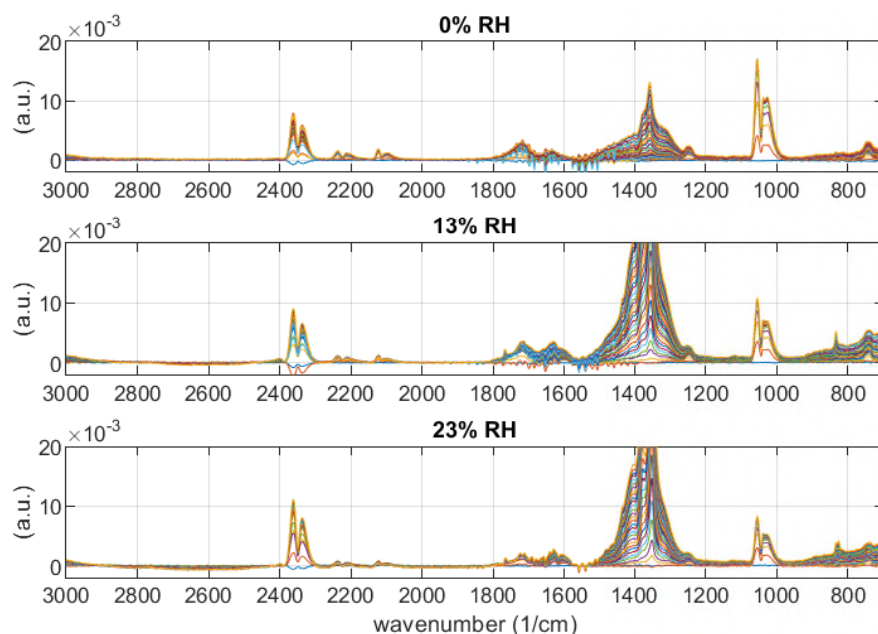


Figure 6.13: FTIR spectra, represented in arbitrary units, recorded during a 10-minute operation of the PCB-fingers SDBD under three distinct flow configurations: 0% RH, 13% RH, and 23% RH. Distinct colors represent the consecutive spectral acquisitions throughout the entire 10-minute data collection, illustrating the buildup of the detected species.

The evolving spectra for all three flow configurations are depicted in Figure 6.13. The large absorption peak of KNO_3 at around 1352 cm^{-1} is readily apparent. This peak is attributed to the irreversible surface transformation of the KBr windows, as elucidated in Section 6.2.

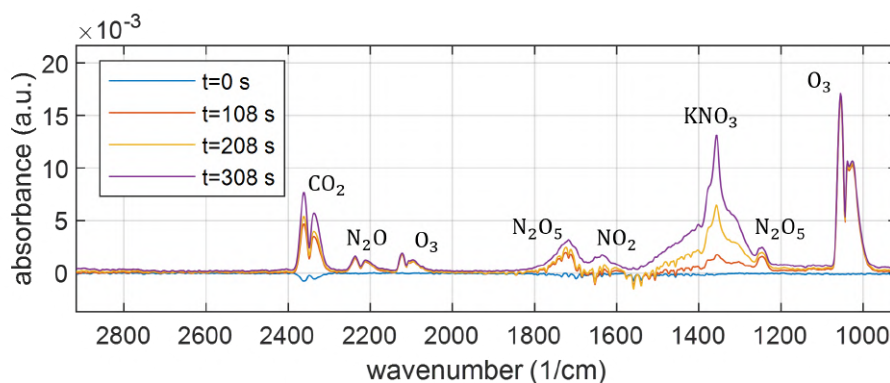


Figure 6.14: FTIR spectra obtained for the 0% RH flow setup of the PCB-fingers SDBD at 0 s, 108 s, 208 s and 308 s from the initiation of the plasma discharge.

In Figure 6.14, a subset of the spectrum series obtained for the 0% RH flow configuration is presented. The background spectrum at $t=0$ seconds was acquired before the initiation of the plasma discharge. Notably, distinct peaks corresponding to N_2O , NO_2 , N_2O_5 , and O_3 are observable. The characteristic peak of HNO_3 is situated around 1720 cm^{-1} , overlaying the primary peak of N_2O_5 at the same wavelength. However, all the bands associated with N_2O_5 are present at 743 , 1246 , and 1720 cm^{-1} [193]. In contrast, secondary peaks of HNO_3 are absent, indicating that the peak at 1720 cm^{-1} is entirely attributable to N_2O_5 .

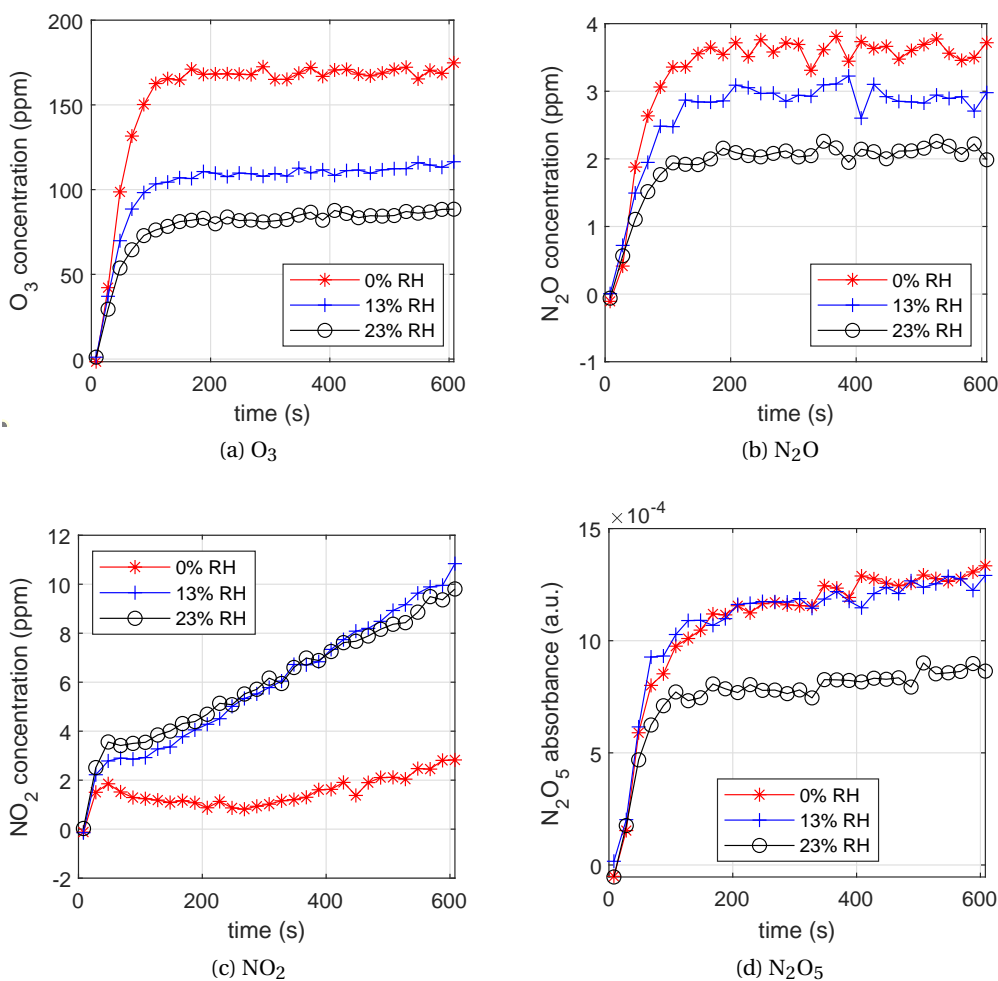


Figure 6.15: 10-minute evolution of the concentration of O_3 , N_2O , NO_2 in ppm and N_2O_5 in arbitrary units obtained from the FTIR absorption spectra. The measurements for the three different flow configurations are reported.

In Figure 6.15, the temporal evolution of O_3 , N_2O , and NO_2 concentrations in ppm is depicted (after absolute calibration), alongside the relative concentration of N_2O_5 , as its absorption cross-section is absent from the HITRAN database. The ozone concentration significantly surpasses that of the other species, attributed to the low surface power density of the SDBD plasma discharge. The power used in this setup, consistent with the bacteria treatments and

LIF measurements, is approximately ~ 1.3 W, at 4.7 kV, as detailed in Section 3.4.2. Assuming the plasma-covered surface corresponds to half the SDBD area ($8^2\pi/2 \sim 100$ cm²), the surface power density is approximately ~ 0.013 W/cm². This value is notably below the ~ 0.1 W/cm² threshold identified in [144], which distinguishes the so-called ozone-mode from the nitrogen oxides-mode. Hence, we expected ozone production to dominate over NO_x products in this experimental setup. The observed trends exhibit clear correlations between the dynamics of these species and RH. A decrease in ozone, N₂O, and N₂O₅ concentrations is found with increasing RH, while NO₂ displays the opposite trend. However, there is no significant difference between 13% RH and 23% RH for NO₂, and similarly, no substantial distinction between 0% RH and 13% RH for N₂O₅. It is crucial to note that while O₃ and N₂O, after an initial build-up phase, reach a dynamic equilibrium, N₂O₅, and especially NO₂, demonstrate a continuous linear increase. This behavior suggests that the flow intensity of 3000 sccm in this setup might not be sufficient to reach a dynamic equilibrium for all species. It is plausible that the increase in NO₂ is sustained by depleting N₂O and O₃. Nonetheless, the acquired spectra did not exhibit any discernible signal for NO due to its insufficient concentration for the FTIR to be detected. The Bruker Vertex 80V detection limit for NO falls below 10 ppm, as confirmed by injecting 1 and 10 ppm of NO inside the bio-plasma reactor. Figure 6.16 presents the spectra acquired for 1 ppm and 10 ppm of NO, together with the spectra of NO and H₂O for reference, showing the absorption spectrum of NO is barely recognizable at a concentration of 10 ppm, and completely indiscernible at a concentration of 1 ppm.

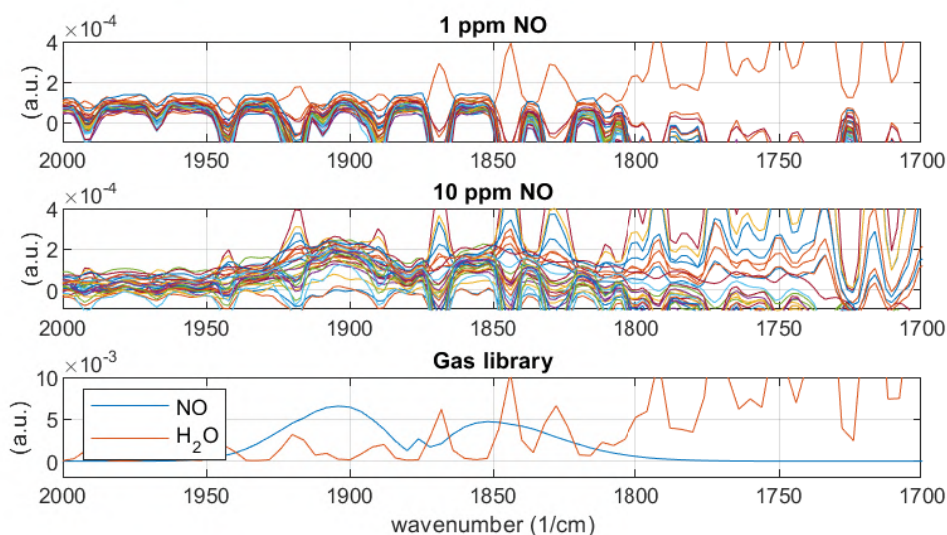


Figure 6.16: Absorbance FTIR spectra of 1 ppm of NO (top) and 10 ppm of NO (center), and absorption spectra of NO and H₂O (bottom) for reference. Nitric oxide is injected into the bio-plasma reactor using the same configuration as the PCB-fingers SDBD setup for the FTIR measurements. The absorption spectrum of NO is barely identifiable at a concentration of 10 ppm, and completely indistinguishable at a concentration of 1 ppm. This is mainly caused by the low signal intensity, while the water absorption peaks would prevent an accurate absolute calibration.

These results regarding the impossibility of detecting low concentrations of nitric oxide with FTIR spectroscopy led us to use alternative techniques with better sensitivity, as well as improved temporal and spatial resolution, to measure the presence of NO in our experimental setups, such as laser-induced fluorescence.

6.3.2 Perforated-disc SDBD FTIR measurements

FTIR measurements were also conducted on the perforated-disc SDBD setup utilized for the sterilization experiments, as detailed in Section 5.3. The DBD is powered by the PAW power supply, with a plasma discharge power of approximately 39 W.

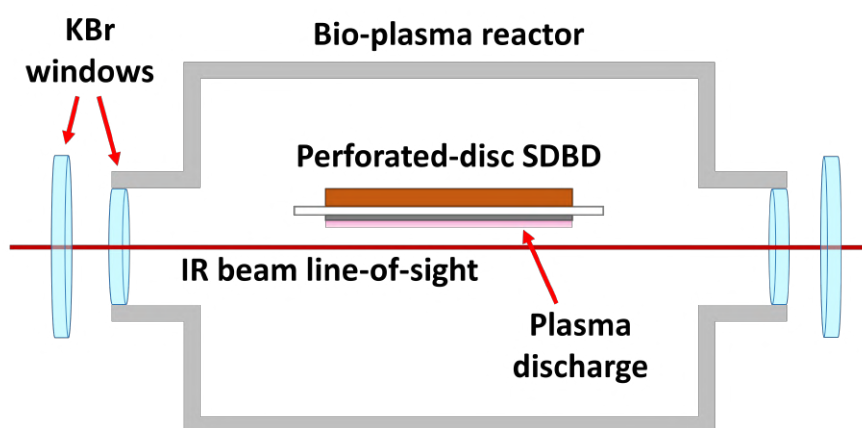


Figure 6.17: Schematics of the in-situ FTIR experimental setup of the perforated-disc SDBD measurements.

For the perforated-disc SDBD measurements, KBr windows were employed both for the bio-plasma reactor and the sample compartment. The perforated-disc SDBD was positioned within the bio-plasma reactor, as illustrated in Figure 6.17, under two distinct flow configurations employed for the sterilization experiments. The first configuration involved a flow of humid air at 1000 sccm with passive exhaust, achieving approximately $\sim 70\%$ RH. The second configuration operated with no flow and no exhaust, with the bio-plasma reactor closed. This configuration will be dubbed "static". To power the perforated-disc SDBD, the PAW power supply was used, delivering a larger power output with respect to the nanosecond-pulse powered DBDs. Owing to the higher power, we expected a different set of RONS produced by the plasma compared to the PCB-fingers SDBD results.

From Figure 6.18, it is immediately evident that in the static case, the peaks of the FTIR spectra are significantly larger compared to the $\sim 70\%$ RH flow case, as expected. In the static reactor scenario, species accumulate inside the reactor, as shown by the larger peak amplitudes. Another notable difference from the spectra obtained with the PCB-fingers SDBD in Section 6.3.1 is the prevalence of nitrogen oxides, namely N_2O , NO_2 , etc., over O_3 . Ozone is absent in these measurements, apart from an initial spike shown in Figure 6.20(a). This can be

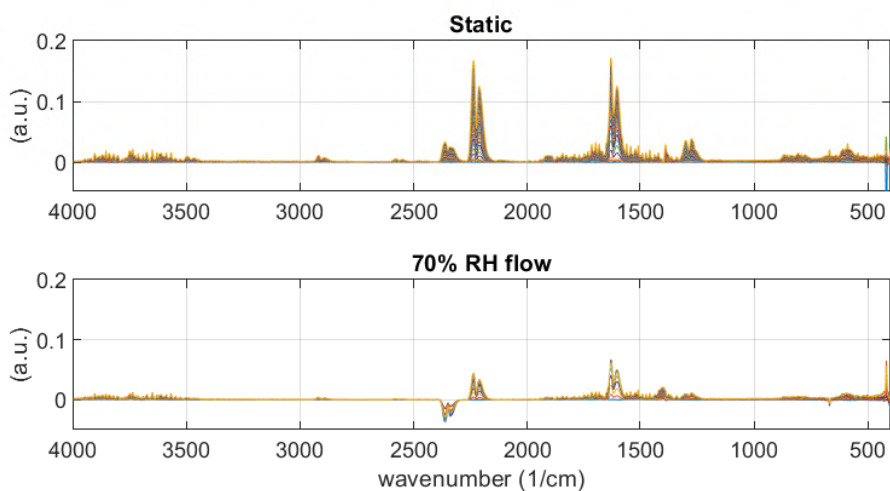


Figure 6.18: FTIR spectra, represented in arbitrary units, collected during a 10-minute operation of the perforated-disc SDBD under the static configuration and the $\sim 70\%$ RH flow configuration. Distinct colors represent the consecutive spectral acquisitions throughout the entire 10-minute data collection, illustrating the buildup of the detected species.

explained by the significantly higher power delivered to the plasma in this setup compared to the nanosecond-pulsed powered DBDs. Considering a plasma surface area of $\sim 200 \text{ cm}^2$, the surface power density is approximately 0.2 W/cm^2 , placing this setup in the nitrogen oxides-mode [144].

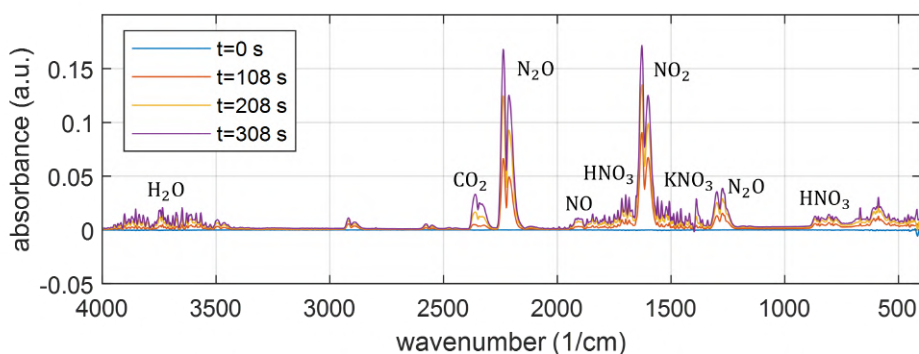


Figure 6.19: FTIR spectra acquired for the static configuration of the perforated-disc SDBD at different time points, specifically at 0 s, 108 s, 208 s, and 308 s from the initiation of the plasma discharge.

In Figure 6.19, the peaks of the molecules identified in the spectra are highlighted. The primary peaks of N_2O and NO_2 are particularly prominent, representing the molecules with higher density, reaching $\sim 140 \text{ ppm}$ and $\sim 200 \text{ ppm}$, respectively, in the $\sim 70\%$ RH flow case, and more than 500 ppm , in the static case. Although the peaks of HNO_3 and NO are also discernible, they are very small and entirely or partially covered by the water signal, hindering a precise analysis of these molecules. As previously noted, ozone is absent in both configurations, except for

a minor increase in the first minute after the plasma is initiated. Two additional peaks are clearly present in the 2500-3000 cm^{-1} region. However, we are unable to definitively attribute these peaks to any molecule. This wavelength range corresponds to the carboxylic acid O-H stretch, but it is a broad peak covering the entire 2500-3300 cm^{-1} range, suggesting that this is indeed not carboxylic acid. Nevertheless, the C-H bond and, to some extent, the N-H bond fall within this infrared absorption region [194]. This implies that there might be carbon sputtered by the stainless steel electrode of the perforated-disc SDBD reacting with H_2O , or, less likely, some nitrogen hydrogen compound.

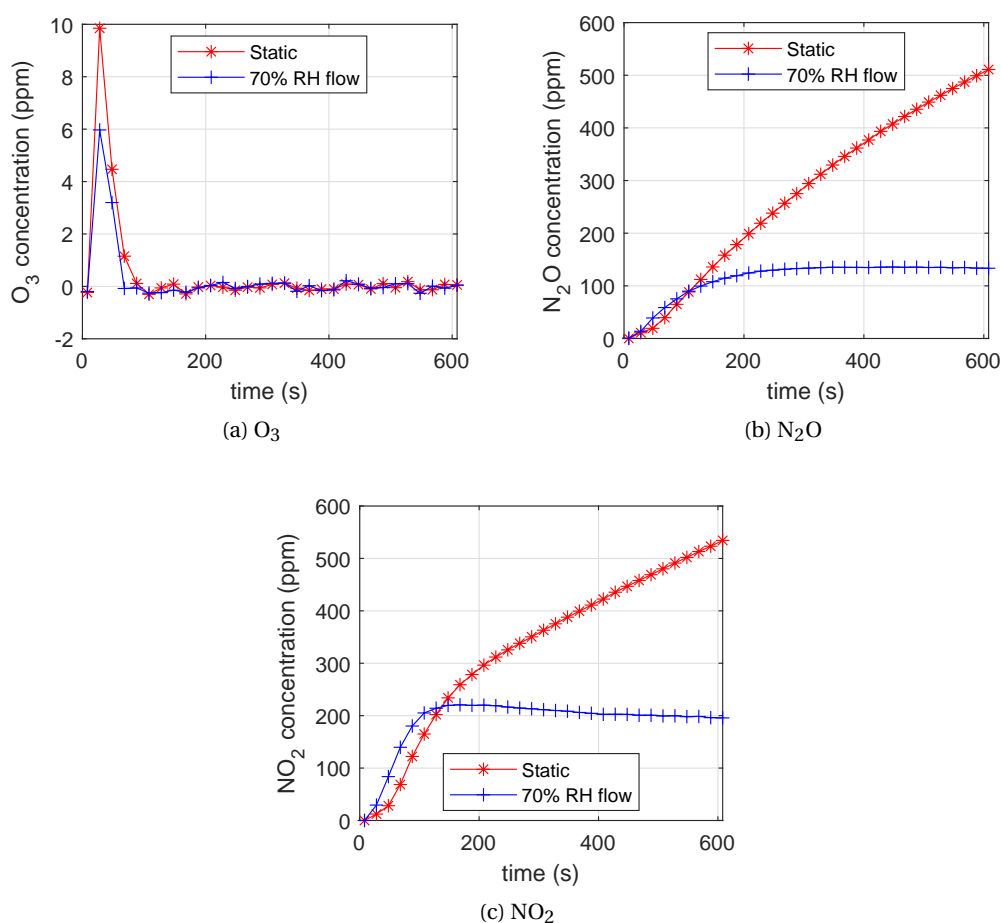


Figure 6.20: 10-minute evolution of the concentration of O_3 , N_2O and NO_2 in ppm obtained from FTIR absorption spectra of the perforated-disc SDBD. The measurements for the static configuration and the $\sim 70\%$ RH flow configuration are reported.

Comparing the two flow configurations reveals that in the static case, the concentration of reactive species is larger, both of RNS and ozone. It is clear that in the static case, N_2O and NO_2 continue to increase by accumulating in the closed bio-plasma reactor. In contrast, in the $\sim 70\%$ RH flow configuration, the concentration of N_2O and NO_2 stabilizes after a few minutes. The concentration of N_2O and NO_2 is notably higher than that of any other molecules detected

by FTIR, suggesting that these two molecules likely have the most significant impact in the sterilization tests detailed in Section 5.3.

6.3.3 VDBD FTIR measurements

The FTIR spectroscopy was also employed to analyze the setup used for the plasma treatments of *Bacillus Subtilis* spores on membranes, as detailed in Section 5.2. The VDBD was used with the same waveform characteristics, namely 11.6 kV applied voltage, 200 ns long pulses, and 1 kHz repetition frequency.

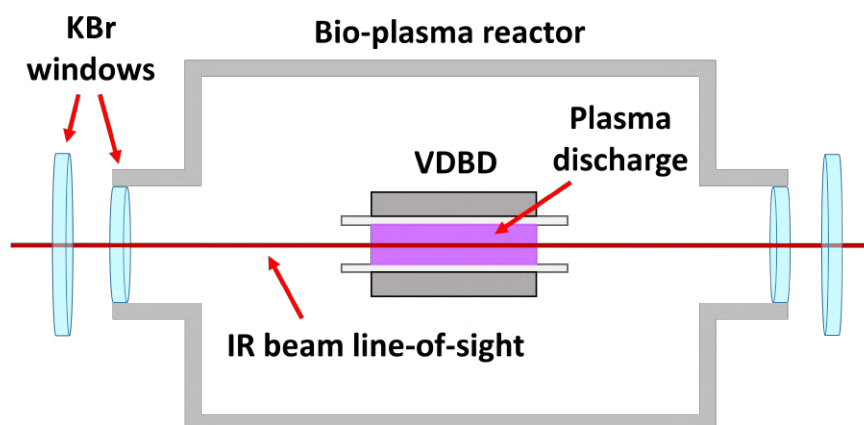


Figure 6.21: Schematics of the in-situ FTIR experimental setup of the VDBD measurements.

A schematics of the setup for the in-situ FTIR measurements is reported in Figure 6.21, for this particular case. Similarly to the perforated-disc SDBD measurements, KBr windows were used for both the bio-plasma reactor and the sample compartment. Three different flow configurations were tested:

- Static: no flow, no exhaust, closed bio-plasma reactor
- ~ 70% RH with passive exhaust: 1000 sccm humid synthetic air, passive exhaust
- ~ 70% RH with pump exhaust: 1000 sccm humid synthetic air, 6 l/min pump outflow

The third flow configuration corresponds to the one utilized for the ps EFISH measurements and plasma treatments of *Bacillus Subtilis* spores on membranes, as described in Sections 4.4 and 5.2. The evolution of the spectra obtained for the three different flow setups is presented in Figure 6.22. Similar to the perforated-disc SDBD measurements, the static case exhibits larger peaks due to the accumulation of species inside the bio-plasma reactor. However, in the VDBD setup, the magnitude of the difference between the static case and the other two configurations is remarkably high. Conversely, between the ~ 70% RH configurations with and without the pump in the outflow, the difference is less significant.

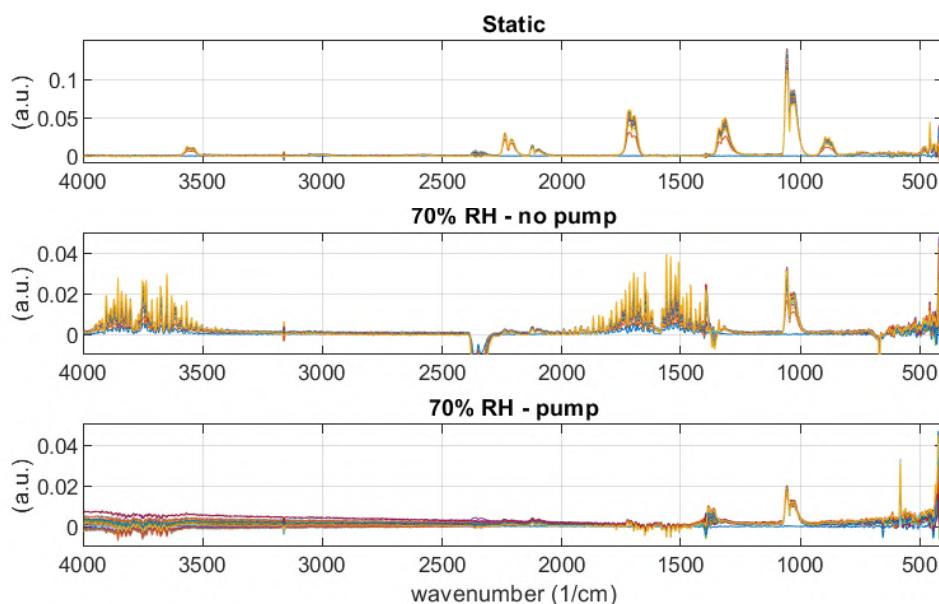


Figure 6.22: FTIR spectra, represented in arbitrary units, collected during a 10-minute operation of the VDBD under the three different flow configurations: static, $\sim 70\%$ RH flow without pump, and $\sim 70\%$ RH flow with pump. Distinct colors represent the consecutive spectral acquisitions throughout the entire 10-minute data collection, illustrating the buildup of the detected species. Please note the different scale between the static case and the two flow cases.

In Figure 6.23, the molecules identified by the IR absorption peaks in this setup are illustrated. In all three flow configurations, ozone and N_2O are easily recognizable. In the static case, a robust presence of HNO_3 is evident from the absorption peaks associated with HNO_3 , namely at 890 , 1320 , 1700 , and 3550 cm^{-1} . On the contrary, in the $\sim 70\%$ RH configurations, with and without the pump, if there is any trace of HNO_3 , it is too small to be distinguished from the water signal. Surprisingly, unlike the SDBD FTIR measurements, there is either no or too little trace of NO_2 to be analyzed.

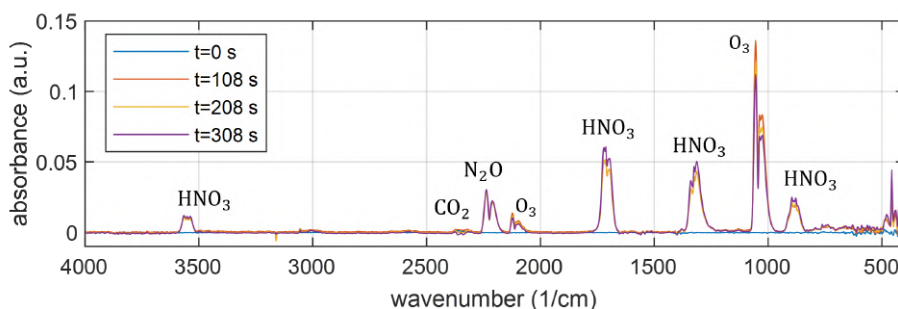


Figure 6.23: FTIR spectra acquired for the static configuration of the VDBD at different time points, specifically at 0 s, 108 s, 208 s, and 308 s from the initiation of the plasma discharge.

Given the substantial difference in order of magnitude between the static case and the $\sim 70\%$

RH cases, we will analyse the results of the static case separately from the other two flow configurations. Upon closer examination of the species kinetics in the static setup, as depicted in Figure 6.24, it becomes apparent that ozone is the most abundantly produced species, followed by HNO_3 and N_2O . Despite being confined in a closed reactor with no flow, the species do not keep accumulating, except for HNO_3 which keeps increasing, reaching ~ 220 ppm at 10 minutes. Ozone starts decreasing after reaching a maximum concentration of ~ 1700 ppm after 40 seconds, while N_2O achieves a stable equilibrium at ~ 90 ppm. The considerations made regarding power density for surface DBDs may also apply to volume DBDs, given that the power density of the VDBD in this setup is still relatively low due to the nanosecond-pulsed power supply used to power the VDBD. However, it is important to note that the results obtained in [144] pertain specifically to surface DBDs and are presented as a function of surface plasma power in W/cm^2 . Further investigation would be beneficial to ascertain whether the ozone-mode to nitrogen oxides-mode threshold remains the same for volume plasma discharges.

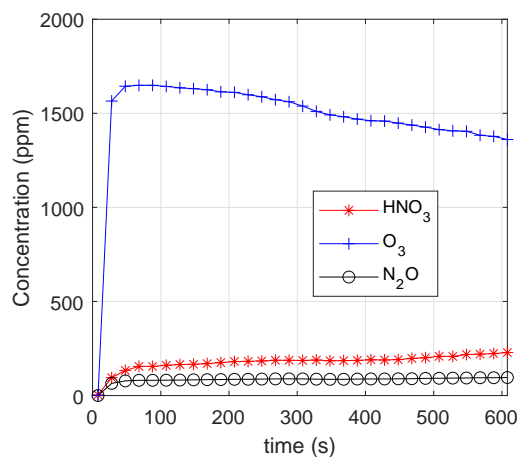


Figure 6.24: 10-minutes evolution of the absolute concentration of O_3 , N_2O and HNO_3 in ppm obtained from the FTIR absorption spectra in the static configuration of the VDBD setup.

The addition of 1000 sccm of humid synthetic air not only entirely alters the dynamics of reactive species but also significantly reduces the concentration of the RONS that are produced. The primary difference is the virtual disappearance of HNO_3 . While we cannot quantify the exact HNO_3 concentration, it can be safely assumed to be significantly lower than that found in the static case. Ozone and N_2O are still present, albeit at a lower concentration in comparison to the static case.

As expected, both O_3 and N_2O concentrations are lower in the case with the pump, as the reactive species are evacuated from the bio-plasma reactor by the pump flow. The concentration difference between the case with the pump and without the pump is a factor of 2 for ozone and a factor of 3 for N_2O . The results obtained in the VDBD setup clearly show that small changes to the setup abruptly change the RONS production and kinetics.

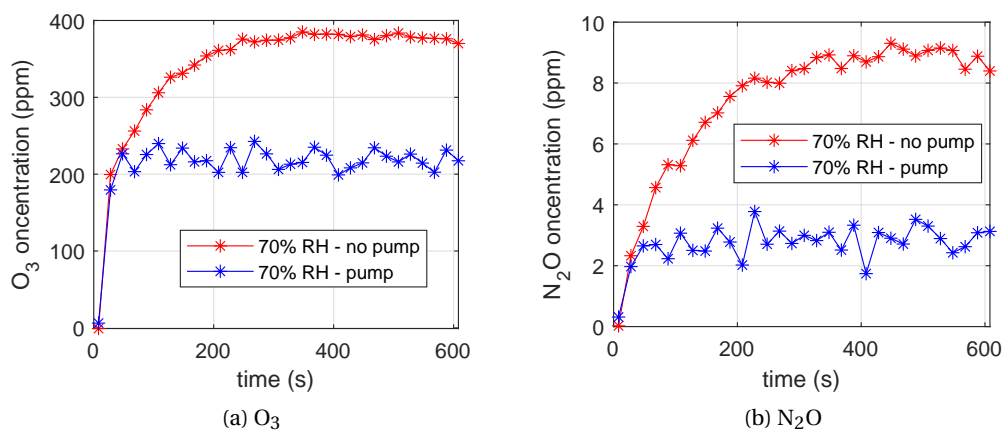


Figure 6.25: 10 minutes evolution of the concentration of O₃ and N₂O in ppm obtained from FTIR absorption spectra of the VDBD setup. The measurements for the ~ 70% RH flow configuration, with and without pump, are reported.

6.4 Conclusions

In summary, Chapter 6 provides a comprehensive chemical characterization of the three different setups used in this study through Fourier transform infrared (FTIR) spectroscopy. The evolving spectra for each configuration are meticulously analyzed, offering insights into the dynamics of reactive oxygen and nitrogen species under varying experimental conditions. The selection of experimental setups is carefully aligned with the conditions of the biological treatments detailed in Chapter 5. The in-situ measurements are particularly noteworthy as they capture the molecules at their source, precluding any contact with surfaces and minimizing transit delays where reactive species might undergo modification by secondary gas reactions.

In the case of the PCB-fingers SDBD used in the plasma treatments of *E. coli*, the FTIR spectra disclose the presence of key nitrogen oxides (N₂O, NO₂, N₂O₅) and ozone (O₃). Concentrations of these species exhibit distinct correlations with relative humidity (RH), with O₃, N₂O, and N₂O₅ showing decreasing trends as RH increases. Notably, NO₂ exhibits an opposite trend, increasing with respect to RH values. Moreover, the concentrations of N₂O₅ and particularly NO₂ show a continuous linear increase, suggesting that the flow intensity in this setup might not be adequate to achieve a dynamic equilibrium for all species. Based on the low surface power density of the plasma, the prevalence of ozone over nitrogen oxides is consistent with previous works [144].

In the perforated-disc SDBD, FTIR measurements highlight variations in species concentrations between static and ~ 70% RH flow configurations. Unlike the PCB-fingers SDBD, this setup operates in the nitrogen oxides-mode due to higher power dissipation in the plasma discharge, evidenced by the absence of ozone and high concentrations of N₂O and NO₂. The

static configuration results in even higher concentrations of nitrogen oxides, indicating the accumulation of species within the closed reactor. The larger concentration of N_2O and NO_2 , with respect to other species, in the static configuration suggests their potential significance in sterilization tests.

For the VDBD setup used in plasma treatments of *Bacillus Subtilis* spores, FTIR spectra demonstrate significant differences between static and $\sim 70\%$ RH flow configurations. Ozone, N_2O , and HNO_3 are prominent in the static case, reaching stable equilibrium after a few minutes. The introduction of humid air leads to a substantial reduction in the concentrations of these species, with a further decrease observed when a pump is added, highlighting the sensitivity of RONS production to experimental parameters. Not only do the concentrations of O_3 and N_2O differ by an order of magnitude between the static and $\sim 70\%$ RH flow configurations, but HNO_3 also completely disappears.

In conclusion, FTIR measurements provide valuable insights into the chemical composition and dynamics of reactive species in the studied plasma configurations. The findings highlight the importance of experimental parameters such as humidity, flow, gas composition, plasma discharge power, and DBD configuration when interpreting and comparing results. Minor alterations in these parameters can result in substantial variations in the production of reactive species, a consideration particularly relevant in real-world applications where the biological target may influence these parameters, thereby altering the chemistry of plasma products. These results lay the foundation for a better understanding of plasma-generated reactive species in diverse applications.

7 Chemical Characterization: Nitric Oxide LIF

This chapter explores the measurement of nitric oxide (NO) concentration using picosecond laser-induced fluorescence (LIF). NO is a well-known molecule for its bactericidal effect, which serves as a precursor for NO_x species. However, in the measurements of FTIR spectroscopy discussed in Chapter 6, it is not detected in any DBD setup. The objective here is to investigate the dynamics of nitric oxide in the same configurations used for the biological treatments described in Chapter 5, specifically the PCB-fingers SDBD and VDBD. The fast characteristics of the picosecond laser and the ICCD camera employed for these studies allow for high temporal and spatial resolution.

Section 7.1 begins with a concise overview of the basic principles of the laser-induced fluorescence technique, specifically emphasizing the application to nitric oxide. This section offers a description of the underlying mechanisms of LIF and the calibration methodology employed in this study.

The experimental setup used for the LIF measurements is thoroughly explained in Section 7.2. Minor differences in the configuration employed for the PCB-fingers and VDBD measurements are also documented. A comprehensive description of the methodology, equipment employed, and data analysis is provided.

Section 7.3 first presents the calibration and laser energy regime measurements and, secondly, the results obtained in the PCB-fingers SDBD setup. The investigation of the temporal evolution and spatial distribution of NO concentration in front of the SDBD is detailed. Then, the results of a study to investigate the variation of NO concentration while varying other parameters, such as plasma discharge power and frequency, are also discussed. NO LIF measurements during the plasma discharges are briefly described at the end of the section.

Section 7.4, provides an extensive description of the NO LIF measurements conducted on the VDBD plasma discharge. The measurements are performed within the plasma, as opposed to the SDBD scenario, and show the temporal evolution of NO. The concluding part provides a concise overview of the primary findings of this chapter.

7.1 Introduction to nitric oxide laser-induced fluorescence

Laser-induced fluorescence (LIF) is the emission of light from atoms or molecules excited by laser radiation. In this process, when an atom or a molecule resonantly absorbs a photon from the laser beam, it transitions to an excited energy state. This excited state, being unstable, spontaneously decays, releasing a photon. The photon is emitted in a random direction as the particle returns to a lower energy state, enabling the direct measurement of an absorption signal. In essence, LIF serves as an advanced method for measuring species absorption, offering an additional advantage. Traditional absorption spectroscopy, relying on transmitted light detection, frequently struggles with sensitivity limitations. Detecting a small amount of missing light in the transmitted beam poses challenges, particularly when employing pulsed lasers with intensity fluctuations from pulse to pulse. Fluorescence detection proves effective in addressing these concerns, as the signal can be distinguished above a background that, in favorable cases, approaches zero. Achieving single-photon-level detection is relatively straightforward. As elucidated in the earlier explanation, the LIF basic process involves two sequential radiative transitions: first, the absorption of a photon, followed by the emission of another photon.

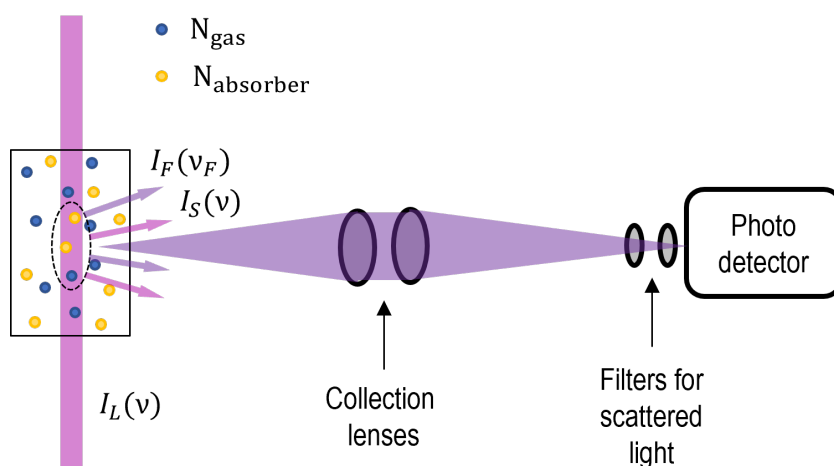


Figure 7.1: Basic representation of a LIF experiment. The laser beam, with intensity $I_L\nu$, excites the absorber molecules $N_{absorber}$ among the background gas N_{gas} molecules. The fluorescence $I_F(\nu_F)$ is then collected through collection lenses by the photo detector, while the scattered light $I_S(\nu)$ is filtered.

LIF presents several advantages with respect to other spectroscopy techniques. It can reach high temporal-resolution, since it is determined by the laser pulse length employed, and high spatial resolution. The imaging setup can define a very small focal volume reaching $<1 \text{ mm}^3$ spatial resolution. However, a significant caveat arises with fluorescence measurements, as they no longer provide a direct absolute measure of the absorbed radiation (and consequently, particle concentration). Several challenging or entirely unknown factors influence the observed signal. These factors encompass spectroscopic parameters like quenching and

experimental variables such as observation angle and optic transmission, among others. It is imperative to account for these factors in the methodology used for the absolute calibration of the fluorescence signal. Despite its analytical challenges, the exceptional sensitivity of LIF has promoted its widespread adoption in various fields. It has found extensive application in exploring chemical processes, establishing LIF as one of the main laser spectroscopic techniques for investigating molecules over many decades [195].

7.1.1 Theory of nitric oxide LIF

The fundamental processes in LIF can be schematized as illustrated in Figure 7.2. Upon resonant stimulation by the laser source, the molecule undergoes absorption of a photon with energy $h\nu = E_2 - E_1$, consequently transitioning to the excited state A. The deexcitation of the excited state includes both stimulated and spontaneous emissions, with the proportion between them being dictated by the intensity of the laser.

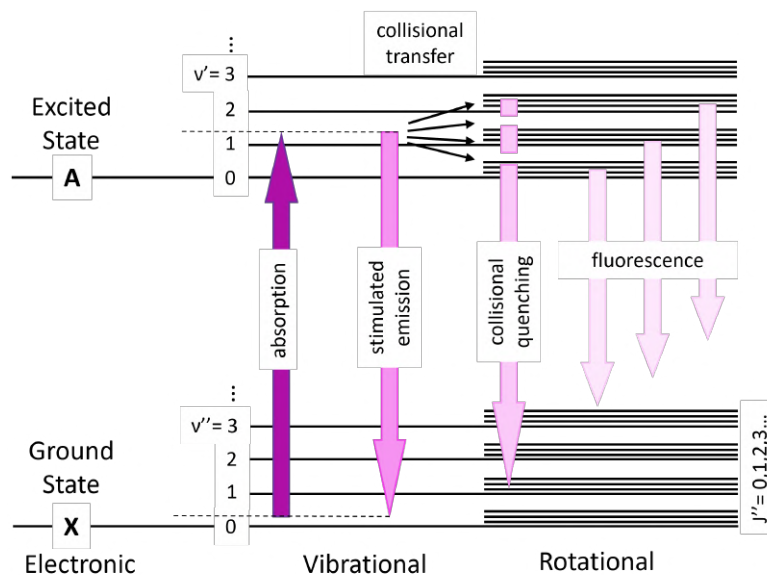


Figure 7.2: The diagram illustrates the various processes involved in the laser excitation of a molecular system, including radiative processes such as absorption, stimulated emission, and fluorescence, as well as non-radiative processes like collisional quenching. Additionally, elastic scattering is also shown as part of the excitation process. These processes occur within the electronic, vibrational, and rotational levels of the molecular system.

It is important to mention that the stimulated emission process acts as a mechanism for reducing the observation of LIF at right angles, as depicted in Figure 7.1, due to the fact that those photons travel in the same direction as the incoming laser beam. Another source of signal loss is attributed to the non-radiative quenching of the excited energy state, resulting in the absence of photon emission. Although quenching is generally not an issue in high-vacuum environments, as the period between collisions, depending on the gas density, is typically

longer than the radiative lifespan, it becomes a significant factor in experiments conducted in settings with considerable collisional quenching, such as at atmospheric pressure. In addition, if the fluorescence signal is observed at the same transition wavelength as the excitation, scattered light from the laser source may obscure it. A straightforward solution to this difficulty is to obtain background measurements, which can then be subtracted from the laser-induced fluorescence signal. Assuming molecules serve as LIF targets, the two electronic levels depicted in Figure 7.2 are additionally split into sub-levels according to the vibrational and rotational energies of the molecule. The quantum number ν is used to label vibrational levels, whereas the quantum number J is used to label rotational levels. In order to distinguish between distinct states, the lower ground-state levels are indicated by double primes, while the excited (upper) state levels are denoted by single-primed quantum numbers. Figure 7.2 depicts the primary mechanisms observed in the interactions between molecules and laser photons. Absorption begins at a certain rotational and vibrational level in the lower electronic (ground) state of the species being studied and then advances to a specific level in an electronically stimulated state. The difference in energy between these levels corresponds to the energy of the incident photon. Emission can occur from the excited quantum state to any lower energy level that is allowed according to the quantum selection rules for electronic dipole transitions. Hence, a plethora of emission lines are detected, and their intensities can be quantified either as a whole (by integrating the total light intensity) or separately.

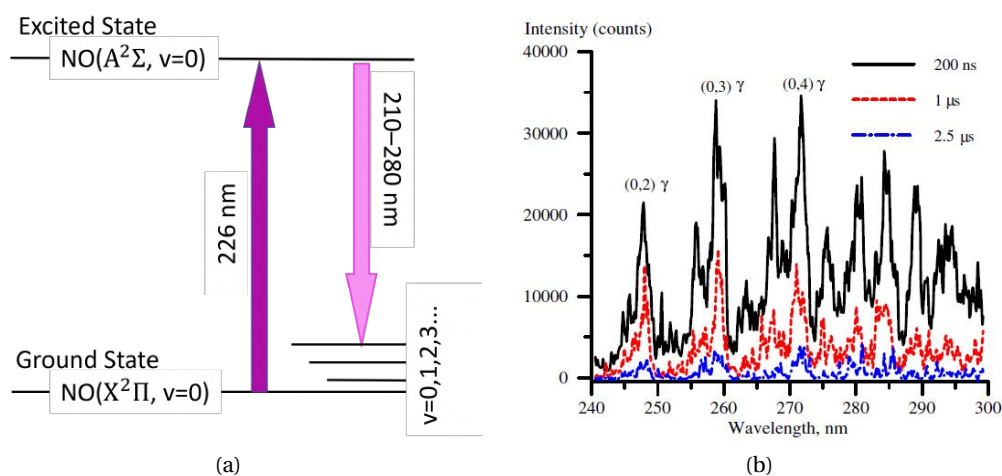


Figure 7.3: (a) The diagram illustrates the process of absorption and emission of nitric oxide during the $(A^2\Sigma) \rightarrow (X^2\Pi)$ transitions, commonly referred to as γ bands. (b) The emission spectra of nitric oxide in the range of 240–300, displaying the peaks of the γ bands for $X^2\Pi$, $\nu=2,3,4$ (source: [196]).

In the case of nitric oxide, the excitation wavelength is approximately around 226 nm [196], while the emission spectrum falls in the 210–410 nm wavelength region. It is important to take into account that both the excitation and emission wavelengths are in the ultraviolet (UV) range when choosing the optics for the LIF experimental setup. An especially noteworthy pattern can be seen in Figure 7.3b, which represents the regular progression in the 210–280

nm wavelength range. This pattern is attributed to the NO ($A^2\Sigma$) \rightarrow ($X^2\Pi$) transition, or γ bends, as schematized in Figure 7.3a [197].

The time-integrated LIF signal, denoted as $I(\lambda)$, is obtained by summing the contributions from all rotational transitions i excited by the laser wavelength λ [198]. Each rotational transition i is associated with a specific wavelength λ_i :

$$I(\lambda) = ClE \frac{A_{det}}{A_{tot} + Q} n \sum_i B_i f_i \Gamma(\lambda - \lambda_i), \quad (7.1)$$

where C represents a constant that accounts for the efficiency of the detection system and the collecting optics. The variable l represents the length of the detecting volume along the laser beam, while E denotes the energy of the laser pulse. The Einstein emission coefficient A_{det} corresponds to the fluorescence transition NO $A(v=0) \rightarrow X(v)$, measured by the detection equipment. The symbol A_{tot} represents the overall emission coefficient of the NO $A(v=0)$ state. The quenching rate of the NO $A(v=0)$ state, denoted as Q , is determined by the temperature and composition of the gas. The variable n represents the density of the ground state of NO $X(v=0)$. The symbol B_i represents the Einstein absorption coefficient associated with the transition i . The term $f_i(T_{rot})$ represents the Boltzmann factor associated with the rotating state of transition i , which is determined by the rotational temperature T_{rot} . Γ refers to the line profile that has been normalized." The derivation of Equation 7.1 is thoroughly explained in [198], and a comparable derivation is employed in [196]. In the case of temperature variations between 300 K and 600 K, such as the experiments performed in this thesis, the sum across the rotational transitions is constant [199], meaning the term

$$ClEA_{det} \sum_i B_i f_i \Gamma(\lambda - \lambda_i) \quad (7.2)$$

is constant for the plasma discharge measurement and the calibration measurements. LIF time-resolved measurements are conducted to quantify the quenching rate Q of the excited state of nitrogen oxide (NO) in its $A^2\Sigma$ electronic state. At atmospheric pressure in air, the collisional quenching term is the most significant factor compared to other non-radiative quenching processes. It has a considerable impact on the observed fluorescence signal. In order to consider this process, the LIF-integrated signal is normalized over the fluorescence decay time. Therefore, the fluorescence decay is fitted using an exponential function e^{-kt+b} , where $k = A_{tot} + Q = \tau^{-1}$ represents the decay time of the fluorescence. This technique is feasible only when employing a laser pulse that is shorter in duration than the average decay period of the fluorescence process under consideration. Consequently, the absorption occurs at a far quicker rate than the radiative and non-radiative processes, resulting in the absence of an absorption component during the fluorescence decay. In order to determine the absolute density n based on the time-integrated LIF signal I , the experimental arrangement necessitates calibration using a gas mixture that contains a known density of NO. The discrepancy in the

quenching of the LIF signal between the calibration and plasma measurement is corrected by considering the decay time τ . The laser power fluctuations are accounted for by monitoring the laser energy, denoted as E . The absolute density n of the ground state of NO X($v = 0$) can be determined using the following calculation:

$$n = \frac{n_{cal} E_{cal} \tau_{cal}}{I_{cal}} \frac{I}{E \tau}, \quad (7.3)$$

where the subscript *cal* denotes the values acquired from the calibration measurements.

7.2 Nitric oxide LIF experimental setup

Nitric oxide LIF measurements were conducted in both the PCB-fingers SDBD and VDBD setups, which were previously detailed in Chapter 2. This section presents the general experimental setup, which is common for both data campaigns. Minor adjustments will be explained in Sections 7.3 and 7.4. The LIF measurements of nitric oxide are performed using the picosecond laser described in Section 4.4.1. The nitric oxide molecule is excited at 226.1 nm. The optical configuration for the LIF measurements is shown in Figure 7.4.

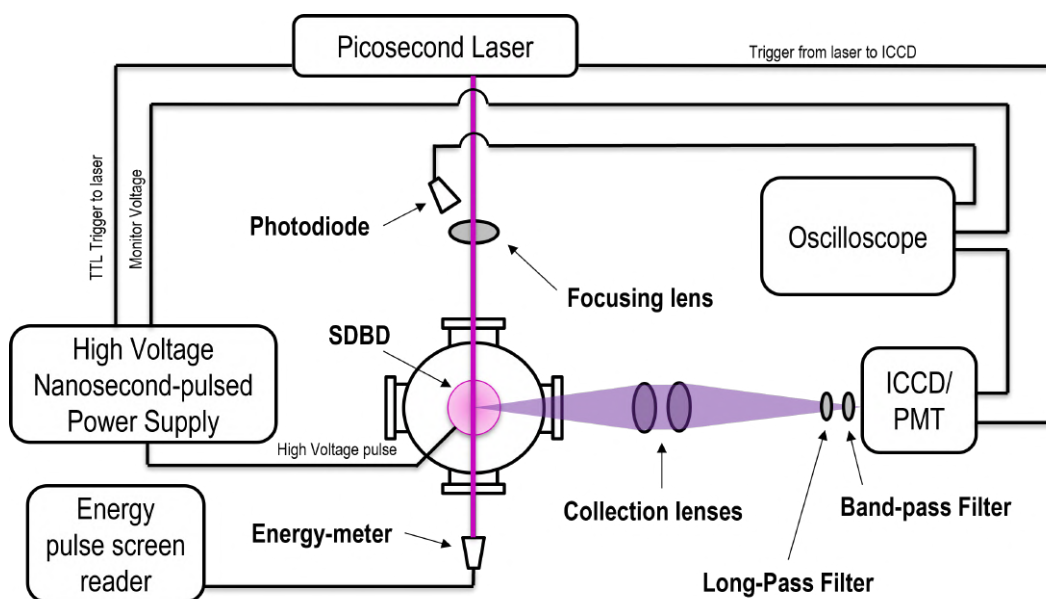


Figure 7.4: Schematics of the experimental setup used for the nitric oxide LIF measurements.

A photomultiplier tube (Hamamatsu Fast PMT, model H10721-20) was initially employed to detect the fluorescence. However, a strong electrical noise caused by the laser components polluted the PMT signal, thus preventing the precise exponential fitting of the fluorescence signal. The analysis of the outcomes achieved through the use of the PMT is elaborated upon in Section 7.3.4. Consequently, to solve this problem, we chose to work with a gated ICCD

camera (PM4-1024f-RB-PS-18-P43 by Teledyne Princeton Instruments [200]), whose main characteristics are shown in Table 7.1.

Table 7.1: ICCD main parameters.

Number of pixels	1024x1024
Pixel size	13 μm \times 13 μm
Intensifier	18 mm, Gen II, RB-fast gate
Minimum Gate Width (Optical FWHM)	\sim 500 ps
Repetition rate	Up to MHz
Quantum efficiency in the UV	\sim 12%

Figure 7.5 displays the quantum efficiency of the RB-fast gate intensifier of the ICCD camera along with additional options. The RB-fast gate intensifier was chosen over the other options due to its ability to achieve a gate time of approximately 500 ps and for its optimal quantum efficiency in the UV wavelength range, with the possibility to use the camera for other experimental setups such as atomic oxygen (O) or atomic hydrogen (H) two-photon laser-induced fluorescence (TALIF).

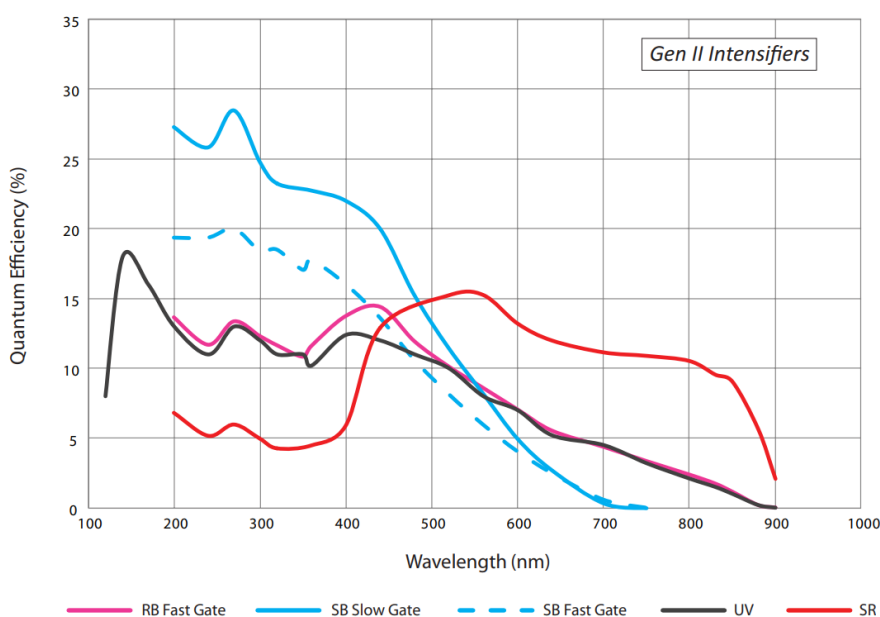


Figure 7.5: Quantum efficiency as a function of the wavelength of the Gen 2 intensifiers. The RB-fast gate (pink curve) is the one employed in this experimental setup.

To specifically capture the emission band of NO ($X^2\Pi$, $v=3$) at about 257 nm, we placed a 244 nm long-pass filter (Semrock LP02-244RS-25) in front of the ICCD to filter out any scattered light from the laser beam. In addition, following the long-pass filter in the optical path, we employed a 257/12 nm band-pass filter (Semrock FF01-257/12-25). To gather the fluorescence, we used two UV-grade fused silica plano-convex lenses with a focal length of $f = 300$ mm

(Thorlabs LA4855). Using another identical UV-grade fused silica plano convex lens, we focus the laser beam in the bio-plasma reactor. To monitor the synchronization of the ICCD, laser pulse, and plasma discharge, a photodiode (specifically the DET10A2 model manufactured by Thorlabs) detects the light of the laser beam reflected by the focusing lens. The energy of the laser beam is continuously measured using a pyroelectric detector (Gentec-eo QE8SP-B-MT-D0).

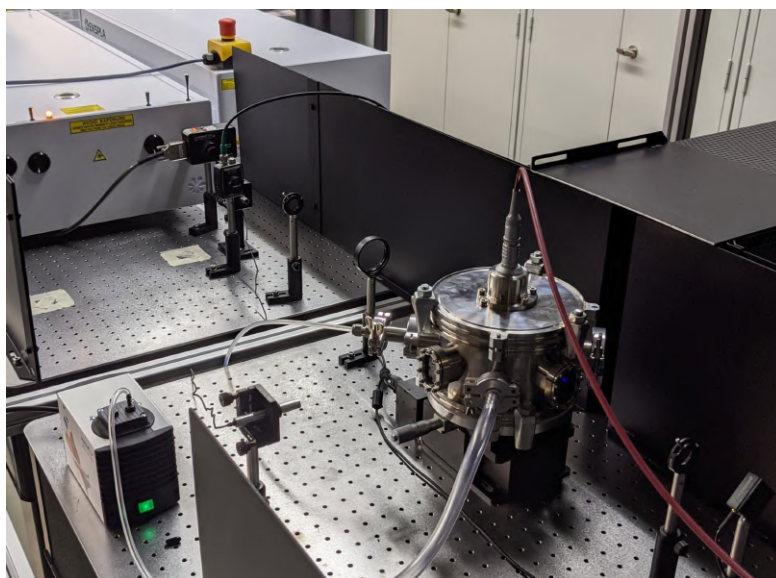


Figure 7.6: Picture of the NO LIF experimental setup.

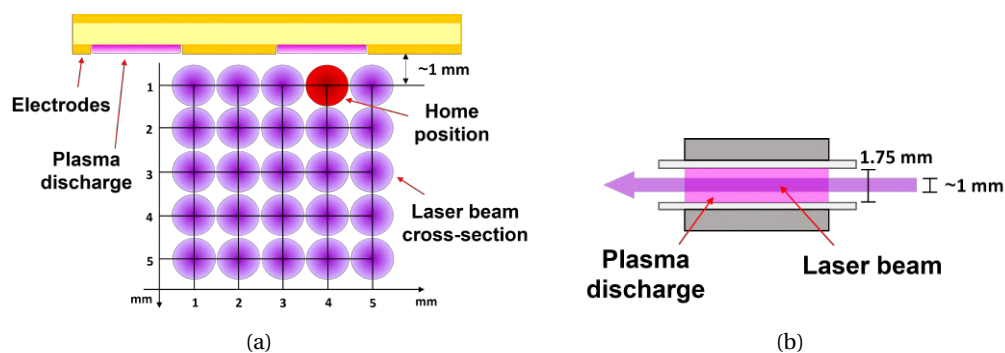


Figure 7.7: (a) SDBD setup: vertical section of the experimental setup showing the relative position between the laser beam and the SDBD plasma for the 2D LIF measurements. The position labeled home is the one used for the temporal evolution and power study of the NO concentration. (b) VDBD setup: schematics of the position of the laser beam setup for the NO LIF measurements.

The vertical section with the positions of the laser is reported in Figure 7.7a. The positioning of the DBD with respect to the laser beam is regulated using a motorized vertical translation stage (Thorlabs MLJ150/M) and a horizontal micrometer translation stage (see Figure 7.6). This translation mechanism enabled precise positioning of the laser beam relative to the

plasma discharge, achieving an accuracy of $\sim 50 \mu\text{m}$. The nitric oxide LIF measurements in the PCB-finger SDBD setup are performed in a $4 \times 4 \text{ mm}$ area in front of the DBD surface to measure the NO diffusion from the plasma surface. The position labeled "home" is the closest one to the plasma discharge and the one used for the temporal evolution, plasma discharge power, and repetition frequency studies. In the VDBD setup, the laser beam passes in the VDBD gap, where the plasma is generated, as shown in Figure 7.7b. The gas flow system was used to supply a controlled flow of gas to the reactor and to calibrate the LIF measurements by introducing a specific quantity of NO into the reactor. The flow rate employed for both the NO LIF measurements of the SDBD and VDBD is identical to the flow rate used for the EFISH and FTIR measurements. This is done to replicate the humidity and flow conditions of the bacterial treatments outlined in Chapter 5. In the PCB-fingers SDBD arrangement, the gas mixture is maintained with a fixed ratio of nitrogen to oxygen of 4:1, while the total flow rate remains constant at 3000 sccm, using a passive exhaust. This study investigates three distinct flow configurations:

- RH \approx 0%: 0 sccm humid synthetic air, 2400 sccm N₂, 600 sccm O₂.
- RH = 13% \pm 2%: 500 sccm humid synthetic air, 2000 sccm N₂, 500 sccm O₂.
- RH = 23% \pm 2%: 1000 sccm humid synthetic air, 1600 sccm N₂, 400 sccm O₂.

The three experimental conditions will be denoted as 0% RH, 13% RH and 23% RH. The fluctuations in relative humidity are a result of the little increase in gas temperature ($< 10^\circ\text{C}$) and the operation of the plasma discharge. In the VDBD system, a singular flow configuration was employed:

- RH \approx 70%: 1000 sccm humid synthetic air.

7.2.1 Triggering system for synchronization

The synchronization of the plasma discharge, ICCD, and laser is regulated by the nanosecond-pulsed power supply, as explained in Section 2.3. The laser is triggered by the TTL signal received from the nanosecond-pulsed power supply. Consequently, a TTL signal produced by the laser triggers the ICCD for the purpose of gate synchronization, as illustrated in Figure 7.8. The triggering technique is similar to the one used for the ps EFISH measurements. The sole distinction lies in our decision to forgo the pulse delay generator and instead settle for a minimum timestep of 50 ns. As previously stated in Section 4.4, a jitter of 11 ns is inevitable due to the external triggering of the laser. The value in question is irrelevant for the measurements conducted during the interval between voltage pulses. This is due to the fact that the dynamics of NO during this period, as well as the timescale of the measurements (about 100 microseconds), are significantly longer than 11 nanoseconds. However, this poses a challenge for the measurements conducted during the voltage pulse and plasma discharges.

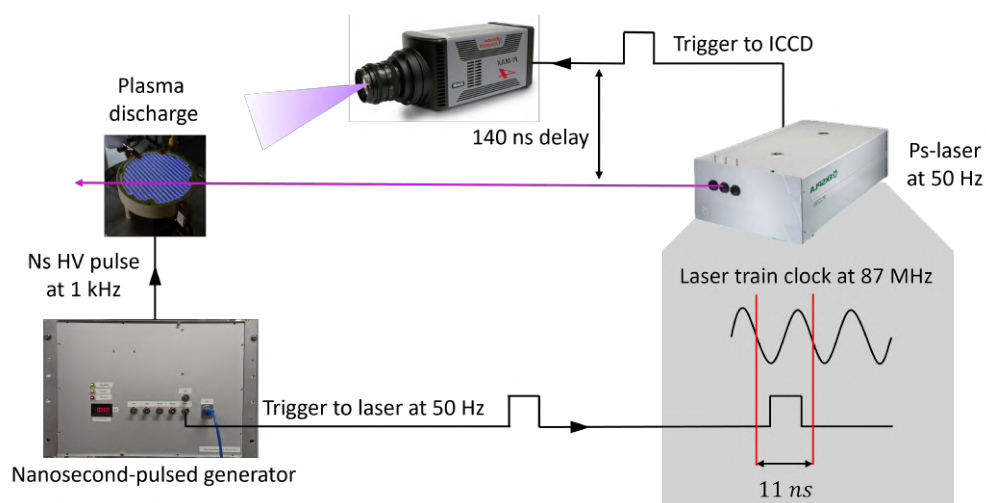


Figure 7.8: Schematics of the ps-laser LIF measurements triggering system.

7.2.2 ICCD ROI and data analysis for the SDBD setup

To determine whether the picture captured by the ICCD is accurately focused on the path of the laser, a millimeter paper has been positioned at the exact location where the laser beam passes. This paper is then illuminated with a backlight, and the position of the collection lenses and ICCD carefully adjusted to obtain a clear image. This process has been performed for both the SDBD and VDBD setups. This approach enabled us to evaluate the dimensions of the image captured by the camera as well. In addition, we verified the precise location and diameter of the laser beam by acquiring the laser light scattered by the mm-paper.

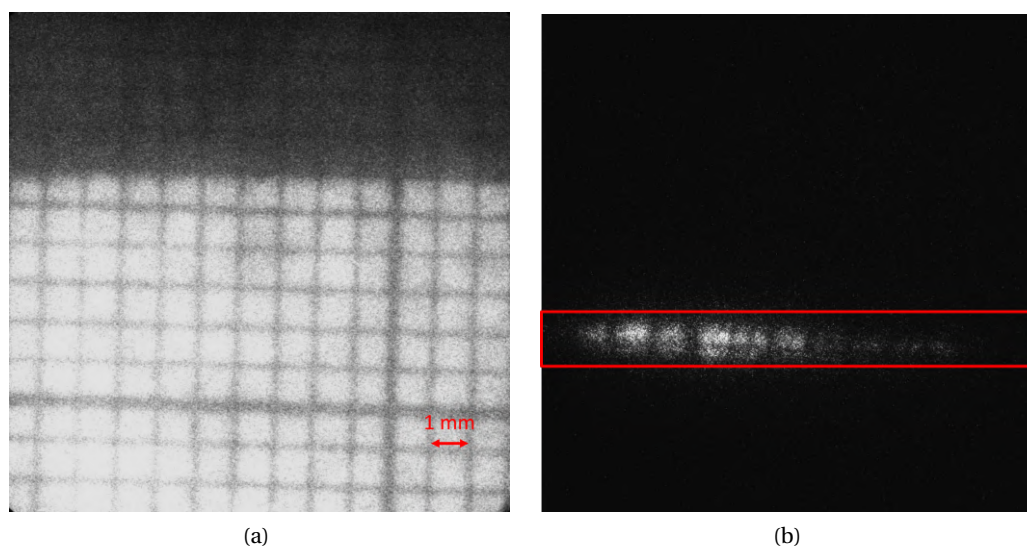


Figure 7.9: (a) ICCD-acquired full sensor image of the mm-paper illuminated with a backlight in the SDBD setup. (b) Scattered light from the laser hitting the mm-paper in the SDBD setup. The ROI selected for the data acquisition in the SDBD setup is highlighted in red.

A clear image of the millimeter paper is obtained in the SDBD setup as depicted in Figure 7.9a, showing correct focus on the laser position. Figure 7.9b displays the light scattered by the laser beam on the millimeter paper, showing an approximate beam diameter of 1 mm. To speed up the measurements, a specific area of the entire sensor, known as the region of interest (ROI), is chosen for the acquisition process. More precisely, a rectangular area measuring 100 x 1024 pixels that corresponds to the zone traversed by the laser is selected. This area measures roughly 1.3 x 13 mm. This measurement can be obtained directly from the mm-paper image or by considering that each pixel has a dimension of 13 x 13 μm . The pixels are binned vertically, resulting in an array of 1024 data points representing the total light intensity measured by the pixels horizontally, as depicted in Figure 7.10a. The system is symmetric in the x-direction due to the parallel alignment of the electrode fingers with the laser beam. This enables us to utilize the entire 1024 pixels to enhance the signal-to-noise ratio while simultaneously preserving the spatial resolution of the measurement (about 1 mm³), as the calibration measurements are conducted in a similar manner. The cumulative value of all 1024-pixel data yields the signal for a single acquisition of the ICCD camera. The ICCD settings used to obtain the temporal evolution of the fluorescence signal are the same for both the SDBD and VDBD setups.

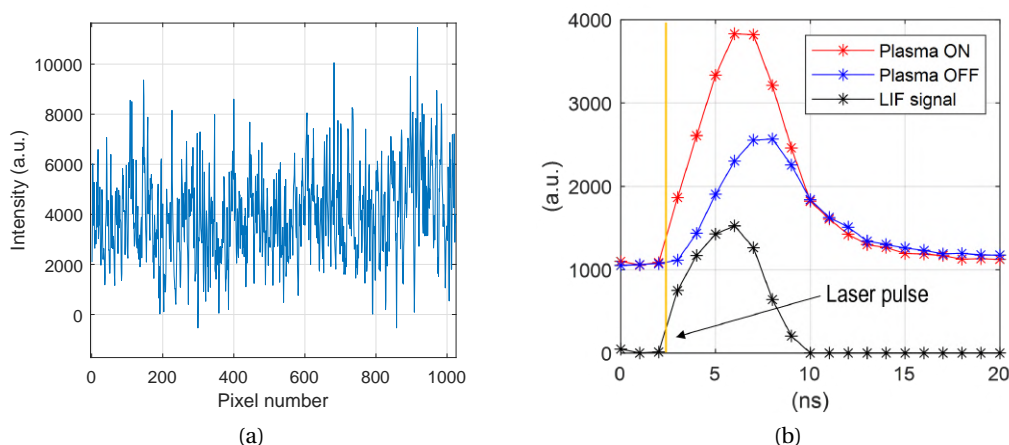


Figure 7.10: (a) Single ICCD acquisition of the ROI 1024 x 100 pixel, binned along the vertical direction. (b) Example of the ICCD signal acquired during plasma operation (red curve), the ICCD signal acquired in the absence of the plasma discharge (blue curve), and background-subtracted LIF signal (black curve), used for the analysis of the NO concentration. The laser pulse position (in yellow) is reported as a reference.

The gate time of the ICCD is set to 5 ns, since increasing the duration of the gate time did not enhance the accuracy of the measurements, whereas lower gate durations were inadequate for achieving a satisfactory signal-to-noise ratio. The ICCD gate is delayed with respect to the laser trigger from 138 ns to 148 ns, with time increments of 1 ns, for a total of 20 acquisitions per LIF signal. The 140 ns value is an internal delay between the laser trigger and the laser light pulse, as illustrated in Figure 7.8. The on-ccd accumulation is set at 1000, meaning photons from 1000 trigger events are accumulated on the sensor. The measurements are then performed

when the plasma is present and when it is absent. The ICCD signals acquired in these two scenarios are represented as plasma OFF and plasma ON in Figure 7.10b. The ICCD signal acquired when the plasma is absent is associated with the light scattered by the laser beam, while the baseline is the background electronic noise. The LIF signal is then obtained by subtracting the ICCD signal when the plasma is absent from the ICCD signal when the plasma is present. Likewise, for the calibration measurements, the ICCD signal when there is no nitric oxide inside the bio-plasma reactor is subtracted from the ICCD signal acquired when nitric oxide is injected in the bio-plasma reactor.

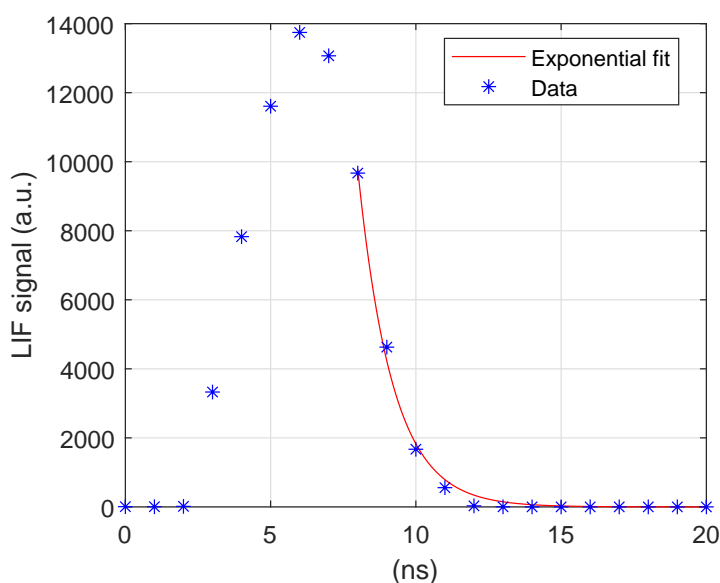


Figure 7.11: Example of a time-resolved data set of the LIF signal, showing the fluorescence decay timing and the exponential fit used to infer the quenching rate Q .

The LIF signal obtained with this process is then integrated, and the temporal decay of the signal is fitted with an exponential function e^{-kt+b} , as previously detailed in Section 7.1, to retrieve the time decay constant $\tau = 1/k$. Figure 7.11 displays the LIF signal as a function of time, along with the exponential fitting used to compute the quenching rate Q . The exponential fit of the temporal decay of the LIF signal is performed starting from the acquisition at 8 ns, to improve the fitting accuracy. The time decay constant τ is subsequently employed to normalize the integrated LIF signal, together with the laser energy, according to Equation 7.3.

7.2.3 Experimental setup modifications for the VDBD setup

The LIF experimental setup employed for the VDBD setup is identical to the one used for the PCB-fingers SDBD measurements, with a few minor modifications. The laser beam is guided using UV-graded fused silica right-angle prisms (Thorlabs PS609) to a more convenient location, and a UV-grade fused silica plano-convex lens (Thorlabs LA4184) with a focal length

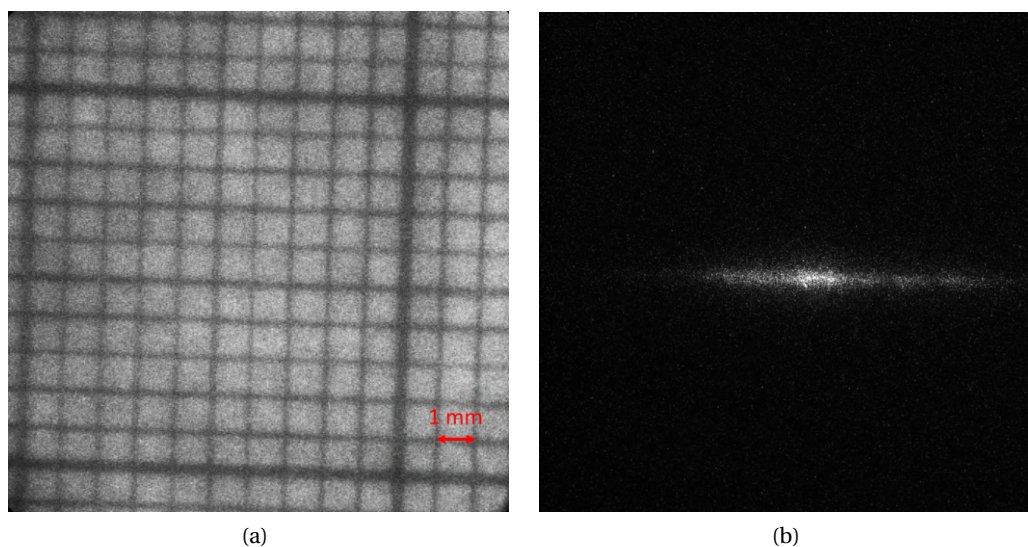


Figure 7.12: (a) ICCD-acquired full sensor image of the mm-paper illuminated with a backlight in the VDBD setup. (b) Scattered light from the laser hitting the mm-paper in the VDBD setup.

of 50 cm is employed instead of the 30 cm lens to focus the laser within the VDBD gap. These improvements do not entail any significant alteration to the system. Once again, in order to obtain accurate LIF measurements, the same process as the one used in the SDBD setup is employed to verify the accurate focus of the area across which the laser is traveling, as well as the precise alignment of the laser in relation to the camera image. Figure 7.12a displays an image of mm-paper illuminated by a white backlight, while Figure 7.12b shows the light scattered by the paper hit by the laser, revealing the position of the laser beam in the camera image. Differently from the SDBD setup, the dimensions of the VDBD (2 cm) are similar to the size of the full sensor image acquired by the ICCD, meaning care must be taken to be sure that we are imaging the center of the plasma discharge. For this purpose, a long gate (30 ns) acquisition of the first plasma discharge, shown in Figure 7.13 has been performed to select the correct ROI to be considered. The plasma discharge edge is visible on the left side of the ICCD image, meaning the ICCD is acquiring half of the plasma discharge, being the right side of the image the center of it since the plasma discharge is 2 cm long while the full sensor image length is 1.3 cm. Hence, instead of using the full horizontal length of the ICCD image, we only used a 77 x 100 pixel ROI on the right side of the ICCD image, as highlighted in Figure 7.13. This choice was two-fold. Firstly, it assured the LIF measurements were measuring the NO concentration at the center of the plasma discharge, and secondly, it kept the spatial resolution at 1 mm^3 . The ROI is vertically binned, and the data analysis is performed identically as the one described for the SDBD setup in Section 7.2.2.

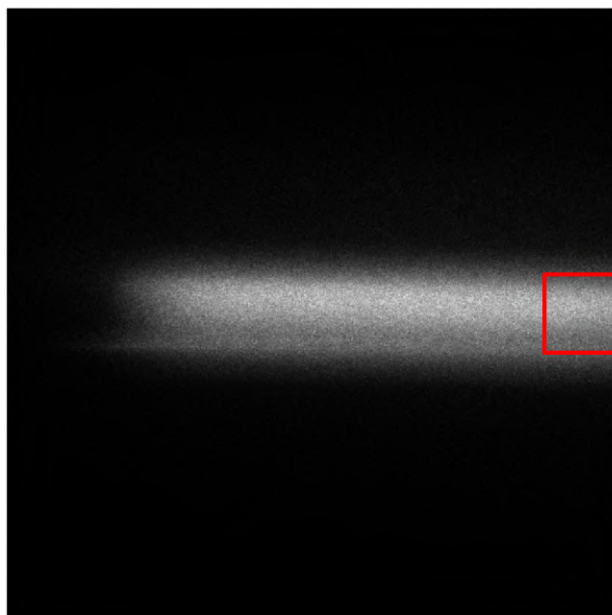


Figure 7.13: ICCD image of the plasma discharge, acquired with a 30 ns long gate. The ROI selected for the data acquisition in the VDBD is highlighted in red.

7.3 PCB-fingers SDBD nitric oxide LIF measurements

This section presents the results acquired in the PCB-fingers SDBD setup. The laser energy and calibration measurements are presented first, followed by the results.

7.3.1 Laser energy and calibration

To verify the linearity of the LIF signal with the energy of the laser pulse, we performed a scan of the LIF signal, incrementally increasing the laser pulse energy. The data shown in Figure 7.14a demonstrates that the relationship between the LIF signal and laser pulse energy is linear for the measured energy values. The laser energy used for the LIF measurements reported in this section is $\sim 40 \mu\text{J}$. The selection of this specific energy level for the laser pulse aims to maximize the signal-to-noise ratio.

To calculate the absolute density using the time-integrated LIF signal, the experimental setup requires calibration using a gas mixture that has a specific density of NO. The calibration process involves injecting NO at concentrations of 0.5, 0.6, 0.7, 0.8, and 0.9 ppm into the reactor and detecting the produced LIF signal. The accurate injection of NO into the reactor is carried out employing the gas flow system outlined in Section 2.5. The specific flow rates used to get the aforementioned quantities of NO concentration are listed in Table 7.2. The

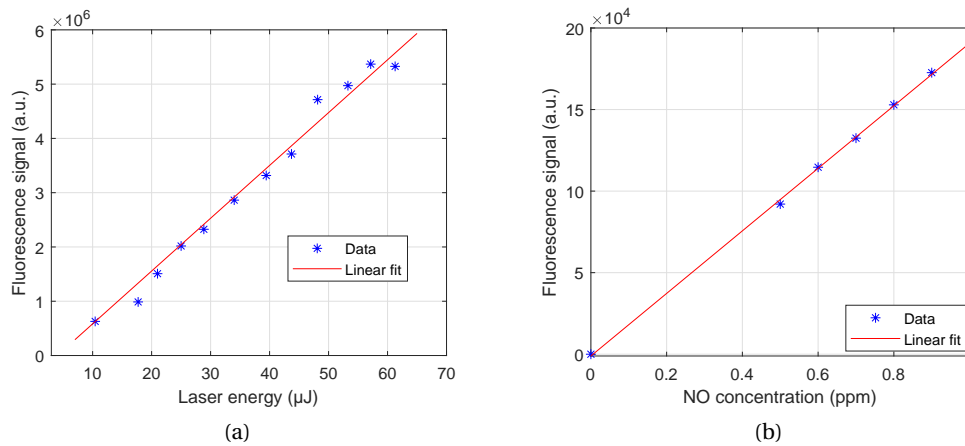


Figure 7.14: (a) LIF signal in arbitrary units at increasing laser pulse energy and linear fit of the data. (b) LIF signal emitted by different concentrations of NO for the absolute calibration of the LIF measurements. Raw data and linear fit are shown in the plot. The calibration constant extrapolated from the data is $C_{cal} = 1.41 \times 10^{-04}$.

overall flow rate remains constant at 3000 sccm to match the flow rate employed in the actual measurements. The data is then linearly fitted, as shown in Figure 7.14b, and the calibration constant is extrapolated. The value obtained in these specific measurements, defined as $C_{cal} = \frac{n_{cal}E_{cal}\tau_{cal}}{I_{cal}}$, is $C_{cal} = 1.41 \times 10^{-04}$.

Table 7.2: Flow rates for SDBD NO calibration measurements.

NO (ppm)	NO(100 ppm)/N ₂ (sccm)	N ₂ (sccm)	O ₂ (sccm)
0.5	15	2385	600
0.6	18	2382	600
0.7	21	2379	600
0.8	24	2376	600
0.9	27	2373	600

7.3.2 NO LIF results in the SDBD setup

To analyze the temporal changes in the concentration of nitrogen oxide, LIF measurements are performed in the "home" position, which is located closest to the plasma ignition area. This position is situated between the electrodes and is roughly 1 mm away from the DBD surface. The SDBD is operated at 4.7 kV, 400 ns long pulses and 1 kHz repetition frequency. Figure 7.16a displays the concentration of NO at various points in time following the plasma discharges. The time intervals are 100 μs, as shown in Figure 7.15. The measurements were taken at three different levels of relative humidity: 0% RH, 13% RH, and 23% RH.

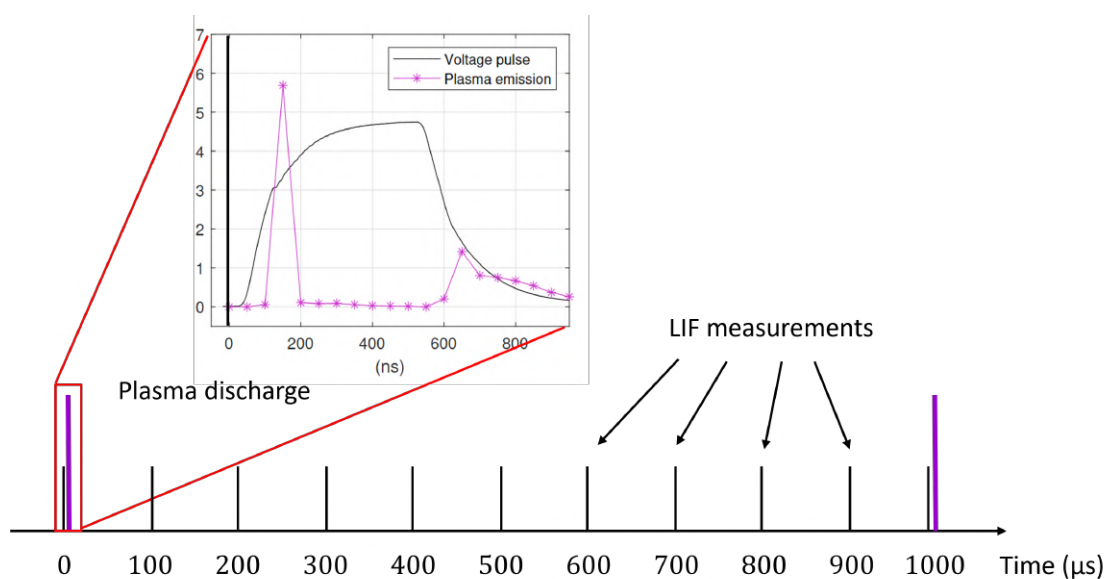


Figure 7.15: Schematics of the timing of the NO LIF measurements with respect to the plasma discharge (high-voltage pulse).

The error bar corresponds to the standard deviation of the decay constant obtained from the exponential fitting of the fluorescence decay. This variation is caused by minor fluctuations noticed throughout the individual measurements, which lasted for more than 6 minutes. The variations of RH and other quenchers during this time, particularly in the vicinity of the plasma region, could affect the time decay of the acquired signal, resulting in inaccuracies in the measured concentrations.

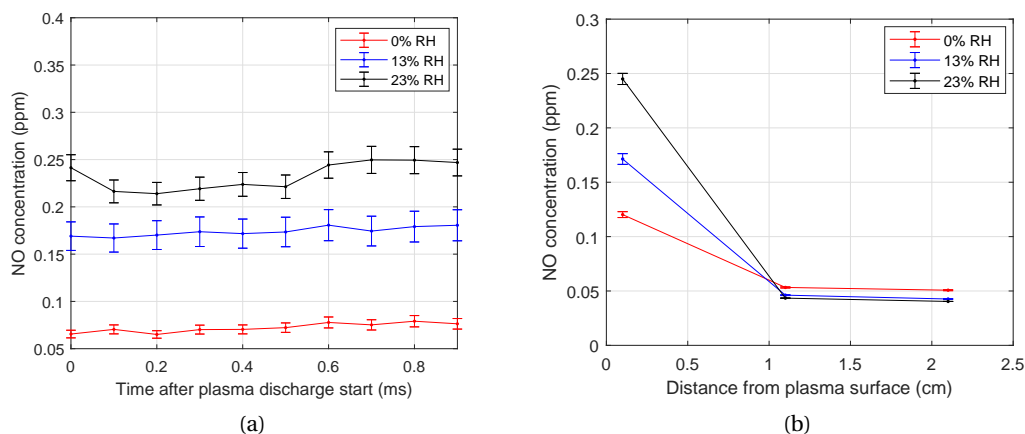


Figure 7.16: (a) NO concentration measured between high voltage pulses at a frequency of 1 kHz, 1 mm away from the DBD surface, at 0% RH, 13% RH, and 23% RH. (b) NO concentration between plasma discharges at varying distances from the plasma surface, at 0% RH, 13% RH and 23% RH, 500 μ s after the voltage pulse.

As shown in Figure 7.16a, the concentration of NO increases as the RH increases, and it is stable over time, during the intervals between high voltage pulses, throughout the operation of the SDBD. LIF measurements at different distances from the plasma discharge were performed to investigate the diffusion of nitric oxide from the plasma surface. Figure 7.16b shows the NO concentration rapidly decreasing at a distance of 1 cm, reaching approximately 50 parts per billion (ppb).

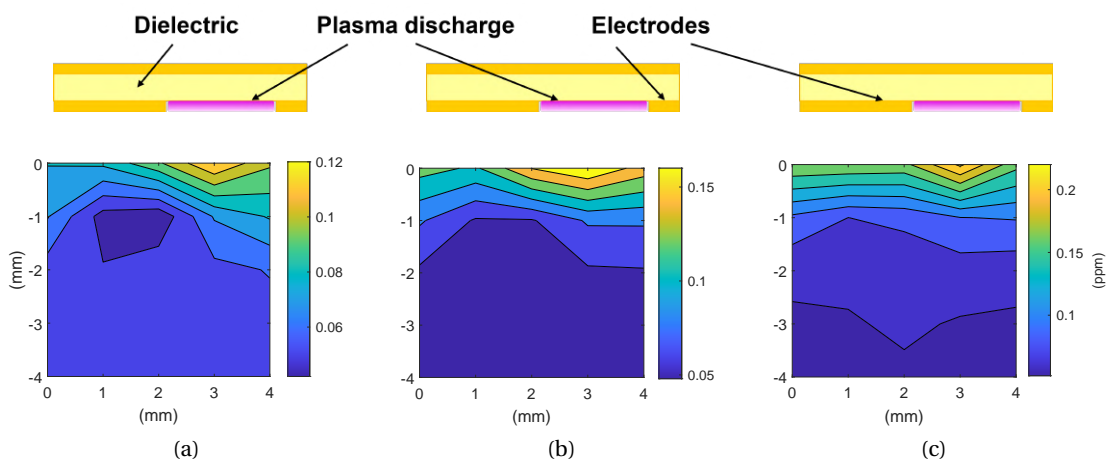


Figure 7.17: NO concentration in ppm over a 2D 4x4 mm area, perpendicular to the DBD surface, at 0% RH (a), 13% RH (b), and 23% RH (c), 500 μ s after the voltage pulse. Please note the different scales of the color bars for the three plots. A schematic of the SDBD is reported to show the position of the plasma discharge in pink.

To study the NO kinetics closer to the plasma surface, LIF measurements were conducted in the 2D region detailed in Figure 7.7a at a time interval of 500 μ s following the plasma discharge. This selection indicates the equidistant point between plasma discharges. The observations depicted in Figure 7.17 indicate that the concentration of NO follows the spatial arrangement of the electrodes, being primarily concentrated in the vicinity of the plasma and gradually spreading from the plasma surface.

To further our understanding of nitric oxide (NO) generation by atmospheric pressure LTP, NO concentration was measured at various plasma discharge powers by modifying the voltage applied to the SDBD, as illustrated in Figure 7.18a. The findings suggest that the concentration of NO rises as the power increases at 13% RH and 23% RH. However, it remains stable at 0% RH. An increase in NO production occurs even at lower power levels when the RH value is 23%. To provide additional evidence of the correlation between NO production and plasma discharge power, the measurements were taken at a frequency of 100 Hz. This meant reducing the power by a factor of 10 while maintaining a constant voltage of 4.7 kV. The NO concentration, as depicted in Figure 7.18b, has a comparable pattern in relation to RH but is larger at 100 Hz with respect to 1 kHz. The frequency of the plasma discharges has a significant impact on the concentration of NO, suggesting that the relationship with power is not straightforward. Temperature is another crucial variable that exerts a substantial influence on the generation

of NO [199].

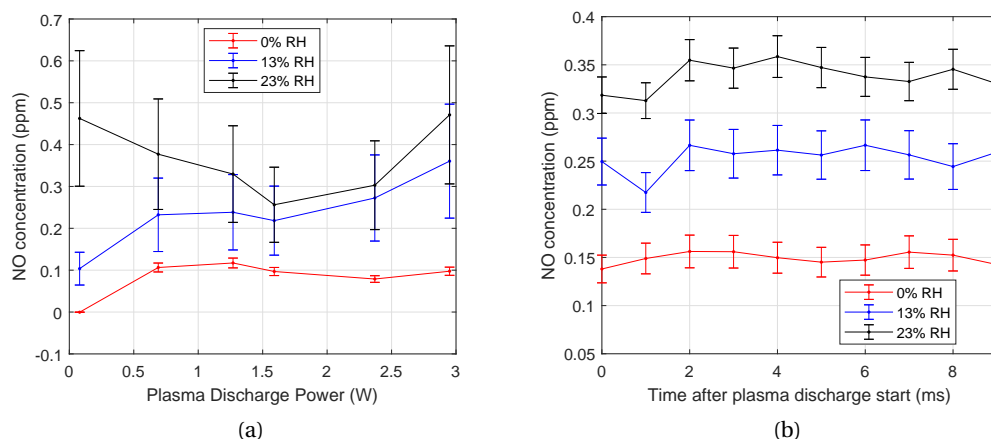


Figure 7.18: (a) NO concentration between plasma discharges at increasing plasma discharge power, 1 mm from the DBD surface, at 0% RH, 13% RH, and 23% RH, 500 μ s after the voltage pulse. The measured NO concentration is reported for increasing plasma discharge power obtained by varying the applied voltage to the SDBD at 2.7, 3.5, 4.4, 5.2, 6.0, and 6.8 kV. (b) NO concentration between plasma discharges at 100 Hz frequency, 1 mm from the DBD surface, at 0% RH, 13% RH and 23% RH. The applied voltage to the SDBD is 4.7 kV, resulting in a plasma discharge power of 0.13 W.

Nevertheless, the gas temperature had a minimal increase of less than 10 °C during the operation. Furthermore, at lower frequencies, the temperature rise was shown to be even more negligible. Therefore, it may be inferred that the slight variations in temperature do not significantly impact the concentration of NO in this specific scenario.

7.3.3 NO LIF measurements during the high-voltage pulse

An attempt has been made to measure the concentration of nitric oxide during the high-voltage pulse. Differentiating the fluorescence signal from the plasma optical emission is necessary due to the fact that the plasma emits light across the entire spectrum. To accomplish this, the plasma optical emission must be subtracted from the ICCD signal to isolate the fluorescence signal. To do so, the optical emission of the plasma is acquired without the laser beam. It is important to ensure that the background noise intensity, which is the signal acquired by the ICCD when there is no laser or plasma, is not subtracted twice. Thus, the measurements are conducted using the identical flow configurations previously described, with a time interval of 50 nanoseconds for a duration of 1000 nanoseconds. The PCB-fingers SDBD is powered at 4.7 kV, 400 ns long pulses, and 1 kHz repetition frequency. The results depicted in Figure 7.19 are in accord with the results outlined in the preceding section, although a number of factors must be elucidated. When attempting to measure the LIF signal during the voltage pulse, the uncertainty caused by the jitter between the laser pulse and the voltage pulse becomes

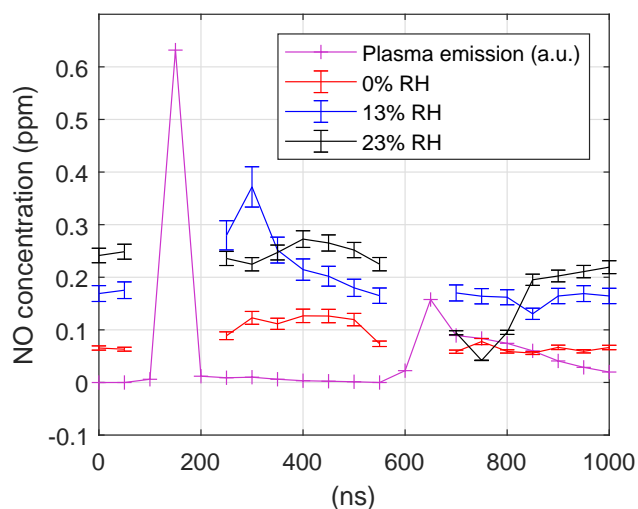


Figure 7.19: NO concentration during the high-voltage pulse at 4.7 kV, 400 ns long pulses, and 1 kHz repetition frequency at 0% RH, 13% RH, and 23% RH. The optical emission of the plasma is also reported for reference.

significant. This prevents us from measuring during the two plasma discharges because not only is the timescale for the dynamics of NO concentration potentially faster than 11 ns, but it is impossible to obtain the correct background for the specific LIF measurement. Another concern pertains to the stability of the optical emission of the plasma. Due to the varying intensity of the plasma discharge for subsequent voltage pulses, the plasma optical emission is not constant over time. As a result, it is not feasible to accurately isolate the fluorescence from the plasma optical emission. This hinders our ability to accurately measure the concentration of NO, as it may be confounded with optical emission. However, the preliminary observations depicted in Figure 7.19 show the LIF measurements as close as possible to the plasma discharges. The results do not exhibit a substantial increase in the NO concentration, indicating that the diffusion from the plasma surface is considerably slower than the production in the plasma discharge. To achieve more accurate measurements within the voltage pulse, it is necessary to reduce the jitter to a minimum of 1 ns. The most effective approach in our current setup is to utilize the laser as the "master" trigger and the nanosecond-pulsed generator as the "slave". However, due to constraints in both electronics and time, we were unable to implement this system during the time frame of this thesis.

7.3.4 Preliminary results obtained with the PMT

The initial measurements of NO LIF were conducted using a Hamamatsu fast PMT (model H10721-20) as a fluorescence detector. The main benefit of employing a photomultiplier tube (PMT) compared to a gated camera is that, provided the rise-time is sufficiently rapid, the PMT can capture the temporal evolution of the fluorescence light, including the time decay, in

a single acquisition. Nevertheless, the measurements were severely impacted by significant electrical interference associated with the laser electronic components. This interference had a particularly noticeable effect on the decay portion of the signal, as depicted in Figure 7.20.

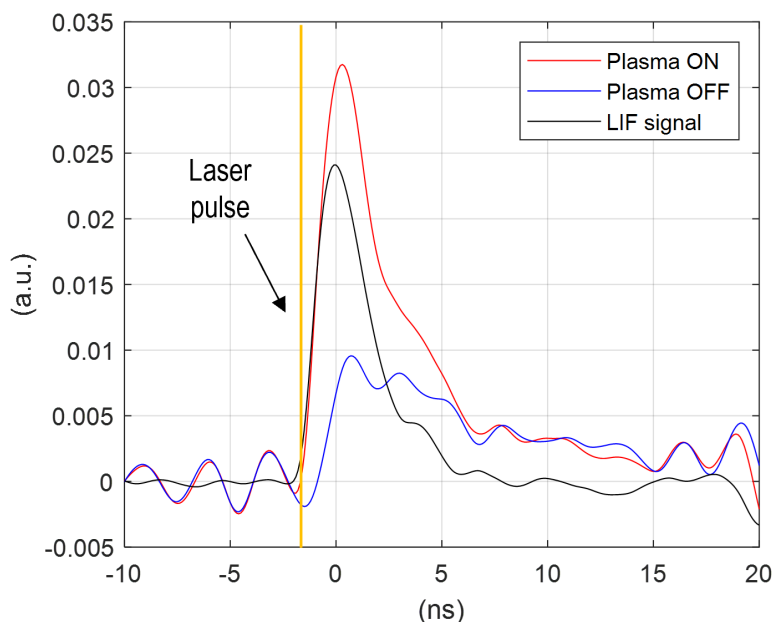


Figure 7.20: Example of the PMT signal acquired during plasma operation (red curve), the PMT signal acquired in the absence of the plasma discharge (blue curve), and the background-subtracted LIF signal (black curve), used for the analysis of the NO concentration. The laser pulse position (in yellow) is reported as a reference.

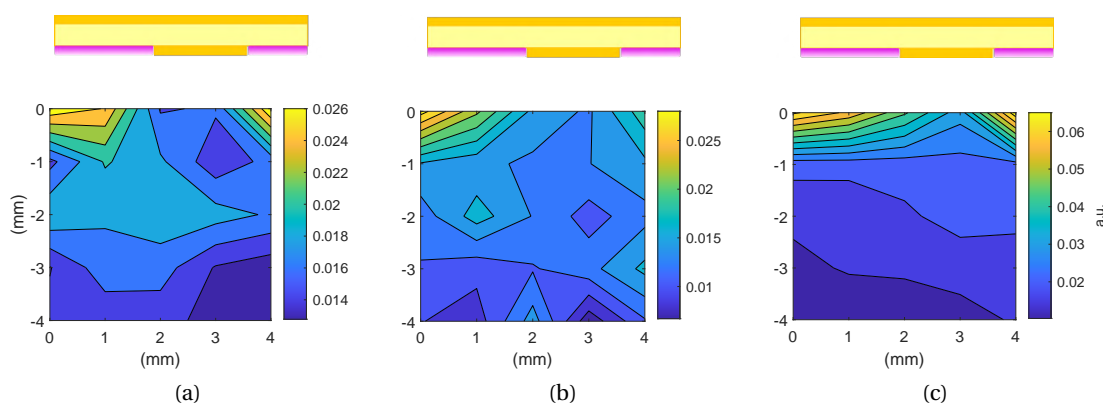


Figure 7.21: NO concentration in arbitrary units over a 2D 4x4 mm area, perpendicular to the DBD surface, at 0% RH (a), 1% RH (b) and 10% RH (c). These measurements are taken using a PMT in place of the ICCD, and despite not being calibrated, they show the same pattern found in the measurements obtained with the ICCD. Please note the different scales of the color bars for the three plots. A schematic of the SDBD is reported to show the position of the plasma discharge in pink.

The presence of this noise, along with the weak intensity of the fluorescence signal, hindered our ability to accurately fit the exponential decay of the fluorescence and determine the precise time decay constant. The motivation for switching to the ICCD camera was its immunity to the electronic noise generated by the laser. Although it was not possible to adjust the data according to the quenching rate Q , we obtained comparable outcomes, measured in arbitrary units, to those obtained using the ICCD camera. The tests were conducted using a slightly varied flow setup corresponding to relative humidities of 0% RH, 1% RH and 10% RH. Nevertheless, the NO concentration still follows the pattern of the electrode-fingers and rapidly decreases after a few millimeters away from the DBD surface, as shown in Figure 7.21.

7.4 VDBD nitric oxide LIF measurements

The measurements of NO concentration using LIF performed in the VDBD setup are presented in this section. First, the laser energy and calibration measurements are shown, and then the findings are presented.

7.4.1 Laser energy and calibration

Similarly to the LIF measurements performed in the SDBD setup, we first performed a study on the linearity of the LIF signal with the laser energy.

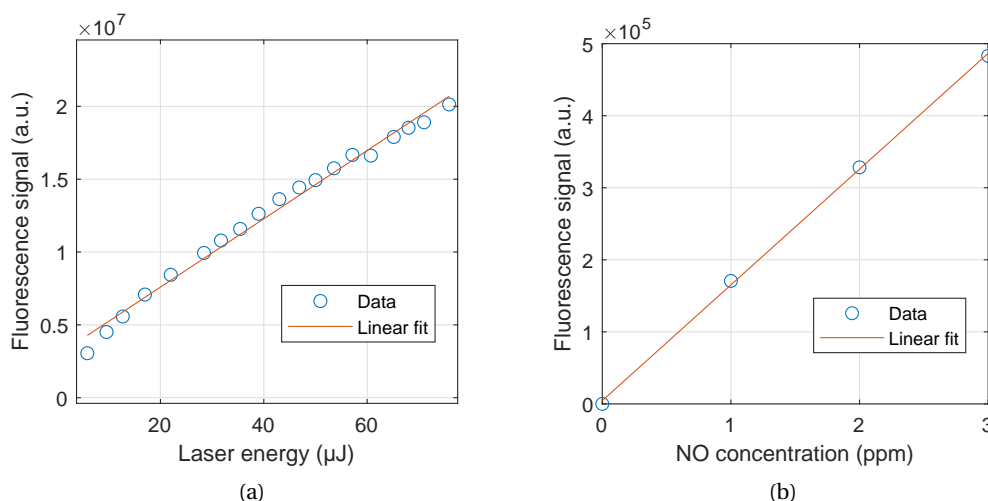


Figure 7.22: (a) LIF signal in arbitrary units at increasing laser pulse energy and linear fit of the data. (b) LIF signal emitted by different concentrations of NO for absolute calibration. Raw data and linear fit are shown in the plot.

To select the suitable laser energy and ensure that we avoid reaching the saturation region, we introduced 1 ppm of nitric oxide into the reactor with the following gas composition: 2370 sccm of N_2 , 600 of O_2 , and 30 sccm of NO/ N_2 at 100 ppm. Then, similarly to the LIF measurements

on the PCB-fingers SDBD, we acquired the LIF signal at progressively higher laser energies, as depicted in Figure 7.22a. We determined the optimal laser energy to be approximately $\sim 40 \mu\text{J}$. Afterwards, the calibration curve is obtained by performing measurements of the laser-induced fluorescence at increasing NO concentrations. Table 7.3 shows the flow rates that were used to add exact amounts of NO to the bio-plasma reactor.

Table 7.3: Flow rates for VDBD NO calibration measurements.

NO (ppm)	NO(100 ppm)/N ₂ (sccm)	N ₂ (sccm)	O ₂ (sccm)
1	30	2370	600
2	60	2340	600
3	90	2310	600

7.4.2 NO LIF results in the VDBD setup

Subsequently, LIF measurements are conducted to examine the temporal changes in NO concentration during the intervals between plasma discharges. These measurements are carried out using the flow setup detailed in Section 7.2, same as the EFISH measurements and spore plasma treatments.

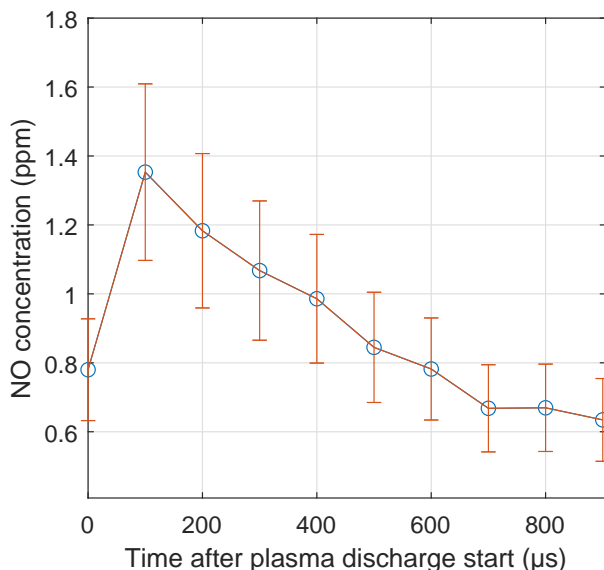


Figure 7.23: NO concentration in between plasma discharges at 11.6 kV, 200 ns long pulses and 1 kHz repetition frequency.

The VDBD operates at 11.6 kV, 200 ns long pulses, and at 1 kHz repetition frequency. The measurements are conducted at intervals of $100 \mu\text{s}$ between plasma discharges in order to track the synthesis and degradation of NO throughout time. Figure 7.23 presents the temporal

evolution of the NO concentration during plasma discharges. In contrast to the measurements on the PCB-fingers SDBD, there is a clear downward trend observed in the levels of nitric oxide over time, following its production in the plasma discharge, right after the measurement at time 100 μ s. The results in Figure 7.23 clearly show that the kinetics of NO production are faster than the diffusion and that the time decay of NO at atmospheric pressure is of the order of hundreds of microseconds. These results are promising, and they can be used together with the ps EFISH measurements for the validation of kinetic models.

7.5 Conclusions

This chapter summarizes the findings of our study on the nitric oxide (NO) laser-induced fluorescence (LIF) measurements performed in the PCB-finger SDBD and VDBD setups. This study is motivated by the absence of NO signatures in the FTIR spectra discussed in Chapter 6, despite the potential it holds as a bactericidal agent in plasma treatments of bacteria and its role as a precursor to NO_x molecules. The picosecond laser LIF technique provides valuable insights into the dynamics of NO by measuring its concentration under different experimental circumstances. The choice of the experimental settings is meticulously matched with the conditions of the biological treatments described in Chapter 5.

The concentration of NO generated in the PCB-fingers SDBD configuration has been thoroughly characterized by using first 2D spatially and time-resolved picosecond LIF measurements of NO. The results indicate a consistently low concentration (<1 ppm) of nitric oxide not decreasing in time. These results are in accord with the NO concentration anticipated by kinetic models [185], given that the diffusion time of NO is slower than its decay time. Nevertheless, we measured a significant rise in the concentration of NO in close proximity of the plasma surface. The production of NO also increases in response to the power of the plasma discharge. However, a complex relationship with power was observed, as lower frequencies result in larger concentrations of NO under the same relative humidity conditions.

Moreover, our research establishes a definitive correlation between the generation of nitric oxide and the level of relative humidity, where greater RH levels result in elevated quantities of NO. As the distance increases from the plasma surface, the level of nitric oxide decreases considerably. The NO concentration remains roughly 50 ppb at a distance of 1.5 cm from the plasma surface, which is where the *E.coli* treatments are undertaken. We conducted a preliminary assessment of the nitric oxide concentration during the plasma discharge. However, due to limitations in the triggering system, we were unable to perform LIF measurements during the formation of the plasma discharge. The findings obtained immediately before and after the plasma discharges, however, exhibited no significant change of the NO concentration, thereby confirming that the diffusion from the plasma discharge occurs over longer timescales.

This conclusion is further supported by the findings obtained in the VDBD configuration. The nitric oxide LIF measurements conducted in the VDBD gap, where the plasma is ignited, exhibit a distinct decrease in time between plasma discharges. This behavior supports the

conclusion that the decay time of nitric oxide is on the scale of hundreds of microseconds. The extremely promising results, coupled with the EFISH measurements, can be used to validate kinetic models of low temperature plasmas at atmospheric pressure.

Ultimately, the use of picosecond LIF measurements offers significant and valuable insights into the dynamics of nitric oxide within the examined plasma configurations. The findings emphasize the need of taking into account experimental conditions, such as humidity, plasma discharge power, and frequency, when analyzing and comparing data. The findings from the PCB-fingers SDBD experiments lead us to the conclusion that nitric oxide does not have a direct impact on the inactivation of bacteria in the *E.coli* treatments discussed in Section 5.1 due to its low concentration. Furthermore, the findings indicated that while FTIR is essential for quantifying the high concentrations of RONS generated in the plasma, it alone is inadequate for properly characterizing plasma discharges. Therefore, it must be supplemented with more sensitive techniques such as LIF.

8 Summary and Conclusions

This thesis investigates low-temperature plasmas (LTPs) used for disinfection and sterilization through a comprehensive physical, chemical, and biological characterization. Considerable attention has been dedicated to ensuring that the measurements are conducted in identical settings to those used during the biological treatments. This implies that the obtained results can be consistently linked with the bacteria plasma treatments. This aspect of the research in biological applications of low-temperature plasmas is often overlooked, and the effect of the biological target on the plasma discharge behavior neglected. We are specifically referring to the impact of the agar in a Petri dish on relative humidity (RH). We found in this thesis that the liquid-based substrate considerably increased the RH in the absence of flow, not only modifying the reactive oxygen and nitrogen species (RONS) generated within the plasma, but damaging the dielectric barrier discharge (DBD) as well. Furthermore, the location of the biological target with respect to the plasma is crucial, particularly in direct plasma treatments. Not only different locations inside the plasma present different plasma properties, but also the biological target itself modifies the plasma. This has been shown in this thesis, as the power dissipated into the plasma is influenced by the presence of the membranes inside the plasma discharge. Instead, the introduction of agar prevents accurate diagnostics by causing the plasma to become filamentary. Accounting for these observations, three particular DBD configurations were characterized and analyzed. Firstly, an indirect plasma treatment setup using a surface DBD (SDBD), then an upgraded version with the objective of achieving sterilization, and finally, a direct plasma treatment configuration employing a volume DBD (VDBD). Hence, the conclusions will be presented referring to the specific setup under consideration.

An investigation was conducted on *E. coli* to study the RONS involved in indirect plasma treatments using atmospheric pressure nanosecond LTP. An atmospheric pressure dielectric barrier discharge (DBD) powered by a nanosecond-pulsed power supply was employed to treat *Escherichia coli* bacteria located 1.5 cm away from the surface of the DBD. The treatments resulted in a reduction of 4 logarithmic units (4-log) in the bacteria population after 10 minutes of exposure to the plasma. The plasma discharge power, measured by Lissajous figures, was

~1.3 W, using a fixed voltage of 4.7 kV, 400 ns long pulses, and 1 kHz repetition frequency. Chemical characterization using FTIR and LIF spectroscopy was performed to determine the reactive species responsible for bacterial inactivation. Due to the indirect nature of the treatments, electric fields and charged particles are not considered as potential antibacterial agents. The bacteria treatments were conducted by introducing a flow of 3000 sccm of synthetic dry air into the reactor to maintain a stable relative humidity during the treatments. In the absence of flow, the agar in the Petri dish begins to release water, leading to a significant increase in RH. This increase not only alters the environmental conditions in bacteria treatments but also impairs the operation of the SDBD and prevents the uniform generation of plasma, hence compromising the reproducibility of the treatments. Implementing a controlled flow, corresponding to a RH level of 10-13% RH, greatly improved the reproducibility of the plasma treatments. Therefore, to investigate comparable levels of relative humidity, the chemical characterization was performed using the following three flow configurations: 0% RH, 13% RH, and 23% RH.

The results obtained with in-situ FTIR spectroscopy revealed the presence of various RONS that contribute to the antibacterial activity. Ozone is the most abundant reactive species, as expected from the low power surface density of the plasma discharge, and it reaches ~ 170 ppm at 0% relative humidity and decreases as the relative humidity increases. The nitric oxide molecules identified in the FTIR absorbance spectra are NO₂, N₂O, and N₂O₅. While N₂O₅ is not absolutely calibrated, NO₂ and N₂O exhibit concentrations ranging from 1 to 10 ppm. Nitric oxide (NO), which is a well-known bactericidal agent, is not detected by FTIR spectroscopy, despite being a precursor to the NO_x molecules identified using FTIR measurements, such as NO₂, N₂O, and N₂O₅. This absence indicates a NO concentration below the detection limit of the FTIR spectrometer.

To examine the NO kinetics, we performed 2D space- and time-resolved picosecond LIF measurements of the nitric oxide concentration generated by the nanosecond-pulsed SDBD plasma. The measurements indicate a consistently low concentration of nitric oxide, which amounts to 1 ppm. The results are in agreement with the NO concentration predicted by kinetic models [185], given that the diffusion time of NO is slower than its decay time. Nevertheless, a significant rise in the concentration of NO in the proximity of the plasma surface is measured. While NO production increases with plasma discharge power as well, this thesis revealed a nontrivial link between power and the NO concentration at lower frequencies under similar levels of RH. Moreover, our results demonstrate a direct correlation between relative humidity and NO production, with larger NO concentration associated with higher RH values. The NO concentration decreases dramatically with distance from the plasma surface. The measured NO concentration is approximately 50 ppb at a distance of 1.5 cm from the plasma surface, corresponding to the distance of the *E.coli* during the plasma treatments. Previous research has shown that this concentration is much below the recommended threshold of 160 ppm for efficient antibacterial action [201]. Indeed, this has been confirmed by exposing *E. coli* to a concentration of 1 ppm of nitric oxide for a duration of 10 minutes, which showed no discernible impact on the bacteria's viability. However, the notable 4-log decrease in *E.coli*

detected after LTP treatments implies that other reactive species play a major role in the inactivation mechanisms. Indirect plasma treatments for bacterial inactivation involve the participation of O₃ and by-products of NO, such as NO₂, N₂O, and N₂O₅, as indicated by in-situ FTIR measurements. Nevertheless, additional thorough investigations are necessary to completely verify and comprehend the role of these species in the inactivation process.

The impact of electric fields on direct plasma treatments of bacterial spores is another subject of this work. To generate a diffuse plasma discharge for the purpose of this study, a VDBD setup powered by a nanosecond-pulse power supply has been developed. The ps EFISH technique was used to measure the electric field evolution in three different locations inside the plasma discharge, specifically at the center of the VDBD gap and in the proximity of the dielectric surfaces on the ground and high-voltage side. The results showed that the electric field time evolution is different in these three positions. To determine whether the electric field variation has an impact on direct plasma treatments, we treated *Bacillus subtilis* spores in two distinct positions within the plasma discharge: on the ground and on the HV side. To increase treatment reproducibility and minimize the influence of the biological target on the plasma discharge, monolayer membranes were employed for the direct treatments rather than the more common agar Petri dish. If agar was used, the plasma discharge would become filamentary rather than diffuse, preventing the coupling of the EFISH measurements with the bacteria treatments. The electric field inside the plasma discharge is slightly altered by the membrane, according to the ps EFISH measurements conducted at the center of the gap with a membrane positioned on top of the dielectric. Further evidence for this comes from the variations in the power dissipated in the plasma discharge with and without a membrane positioned in the gap. Furthermore, the whole membrane prevented the accurate reproducibility of the spores direct treatments due to its larger size than the VDBD electrodes.

To overcome this issue, we only treated a fourth of the membrane instead of the entire membrane. This technique significantly increased the reproducibility of the treatments. The *Bacillus subtilis* spores were treated by placing the membrane on top of the dielectric on both sides of the VDBD, high-voltage and ground. The VDBD was driven by 11.6 kV and 200 ns long pulses at 1 kHz repetition frequency, resulting in a plasma discharge power of 1.5–2 W. After just one minute of direct plasma treatment, the results demonstrated the remarkable efficiency of the plasma treatments, completely inactivating the spores for a maximum treated dilution of $\sim 10^5$ spores. Although there were no statistically significant differences between the ground and HV positions for any of the treatments, there was a more significant difference favoring the HV position for the 20-second treatments. Although this data is insufficient to draw a firm conclusion, the steepness of the log reduction curve between 10 and 40 seconds suggests most bacterial inactivation is occurring within this time window. Therefore, a more precise investigation of the interval between 10 and 40 seconds of these direct treatments could aid in determining whether or not placing the spores on the HV position results in more effective plasma treatments. A preliminary test has been conducted by treating the spores on the membrane at the center of the VDBD gap. The results showed a less effective spores inactivation, hinting to a possible connection with the less pronounced electric field at the

center of the plasma, measured by ps EFISH. However, a better setup and more replicates are needed to draw reliable conclusions.

The electric field in the VDBD setup was measured both by ps and ns EFISH. This investigation aimed to compare the same diagnostic results using different pulse-length lasers. The ns EFISH investigations showed that laser pulse lengths longer than 1 ns can potentially achieve ns-level time resolution. To gain insight into the physics of nanosecond plasma discharges in humid air, the ps and ns EFISH measurement findings were compared to a simplified kinetic model. The presence of a strong and stable electric field after the initial plasma discharge is an essential difference from previous studies on nitrogen. This is due to the electronegativity difference between nitrogen and air, which is primarily caused by the oxygen and water molecules. Electrons rapidly transform into negative ions within a few nanoseconds following the breakdown, thereby sustaining the charge distribution in the gap and substantially limiting their motion. The kinetic model well predicts the evolution of the electric field as measured by the ns EFISH diagnostic. However, there are features of the electric field predicted by the model not observed in the ns EFISH data. A key element absent from the ns EFISH data is an overshoot of the electric field corresponding to the start of the first plasma discharge. This inconsistency is resolved, to some extent, by the improved spatial and temporal resolution of the ps EFISH measurements. However, the ps EFISH measurements only measure the overshoot in close proximity to the ground dielectric surface, whereas it is absent in the HV position and, similarly to the ns EFISH data, in the center of the gap. Investigations are ongoing to determine the cause of this behavior since the kinetic model predicts this feature in the center of the gap. The electric field dip caused by the breakdown of the plasma discharge is another noteworthy aspect. This characteristic is more pronounced in the ps EFISH data, with respect to the ns EFISH results, but only in close proximity to the high-voltage dielectric surface of the VDBD. The pattern is reversed in the event of the second plasma discharge, with a larger electric field on the HV side and a larger dip on the ground side.

The ns EFISH data does not reveal any discernible variation among the three positions in the plasma discharge. On the other hand, variations between the three locations are consistently shown by the ps EFISH measurements, which reveal that the temporal behavior of the electric field varies with the position within the plasma discharge. Furthermore, the ps EFISH measurements are performed on the ground and HV side at a distance of 270 μm from the dielectric surface. This suggests that electric field variations may be more pronounced at shorter distances from the dielectric surface.

Besides the plasma for sterilization purposes, the VDBD setup provides an ideal test bed for code validation. Hence, nitric oxide LIF measurements were also performed using the identical VDBD configuration as the ps EFISH measurements. Leveraging the initial results on the electric field and nitric oxide measurements, we started a collaboration with the Plasma Technology Laboratory (PTL) of the University of Bologna, where a complete model for simulating DBD plasma in air is presently being developed. This kinetic model overcomes the limitations of the kinetic model used in Ref. [145], allowing for a better understanding of

the physics of the nanosecond plasma discharges in humid air. The initial findings show great promise, but due to ongoing work, they cannot be included in this thesis.

Lastly, we explored the possibility of achieving sterilizing standards via low-temperature plasma treatments in our pursuit of biological applications of plasma technology. BT96 biological indicators, which contain $\geq 10^6$ *Geobacillus stearothermophilus* ATCC 7953 spores, were used to conduct a preliminary assessment on the possibility of achieving sterilization. The BT96 BI, which is reactive species permeable, was selected as an initial approach to assess the efficacy of air-based plasma treatments in sterilization. In order to increase the plasma discharge power and function better in high-humidity environments, the treatments were carried out using an SDBD driven by an AC power source able to deliver larger power (~40 W). Encouragingly, the BI was successfully inactivated in 1-hour treatments within a closed bio-plasma reactor with no flow. Further experiments to determine whether atmospheric pressure plasmas can be used to reliably sterilize a system are well worth the effort, given the extremely preliminary nature of these results.

Appendix

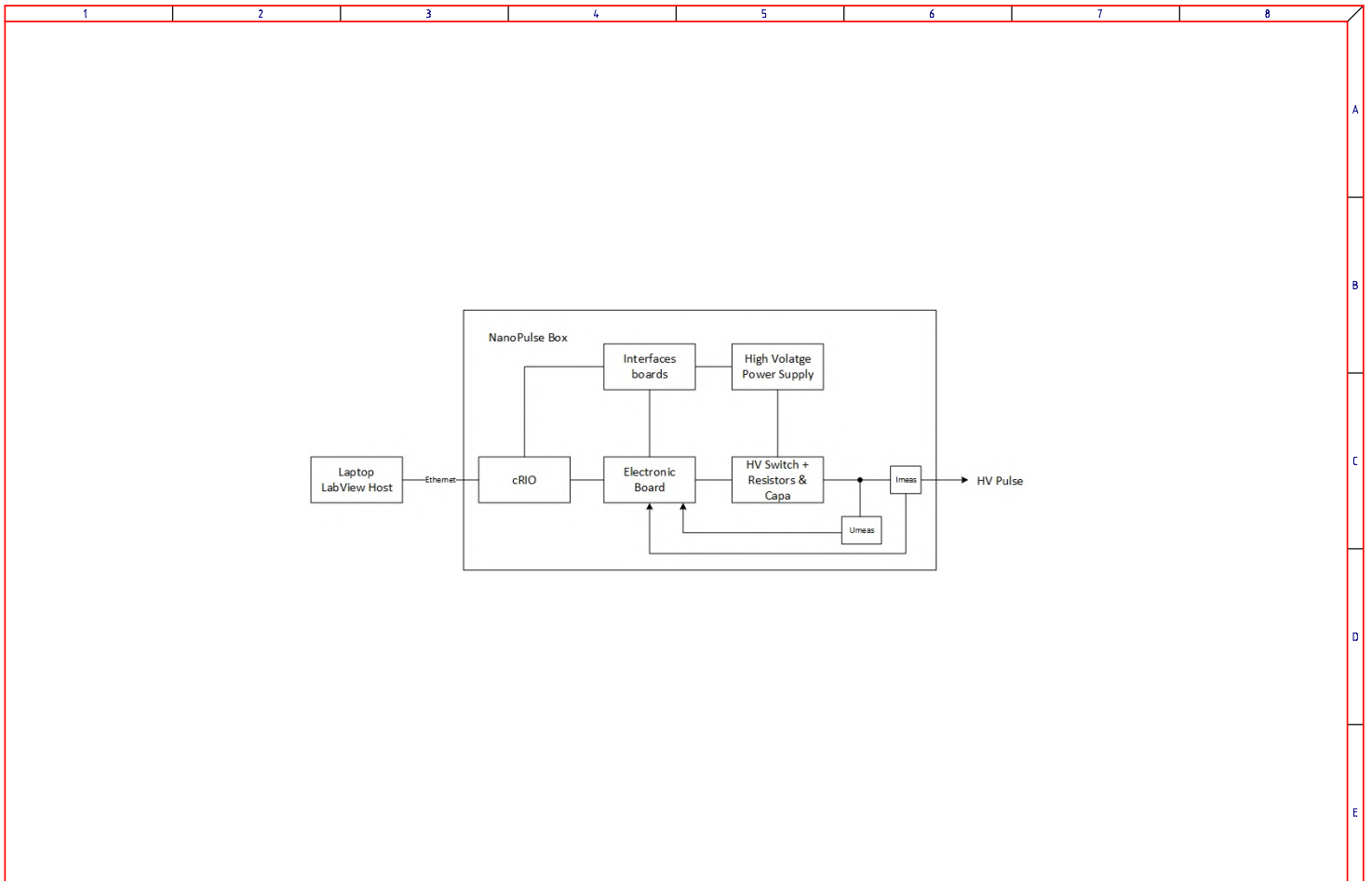
Nanosecond-pulsed high voltage power supply electric circuit schematics

In this section, the full electrical circuit schematics of the nanosecond-pulsed high-voltage power supply are reported.

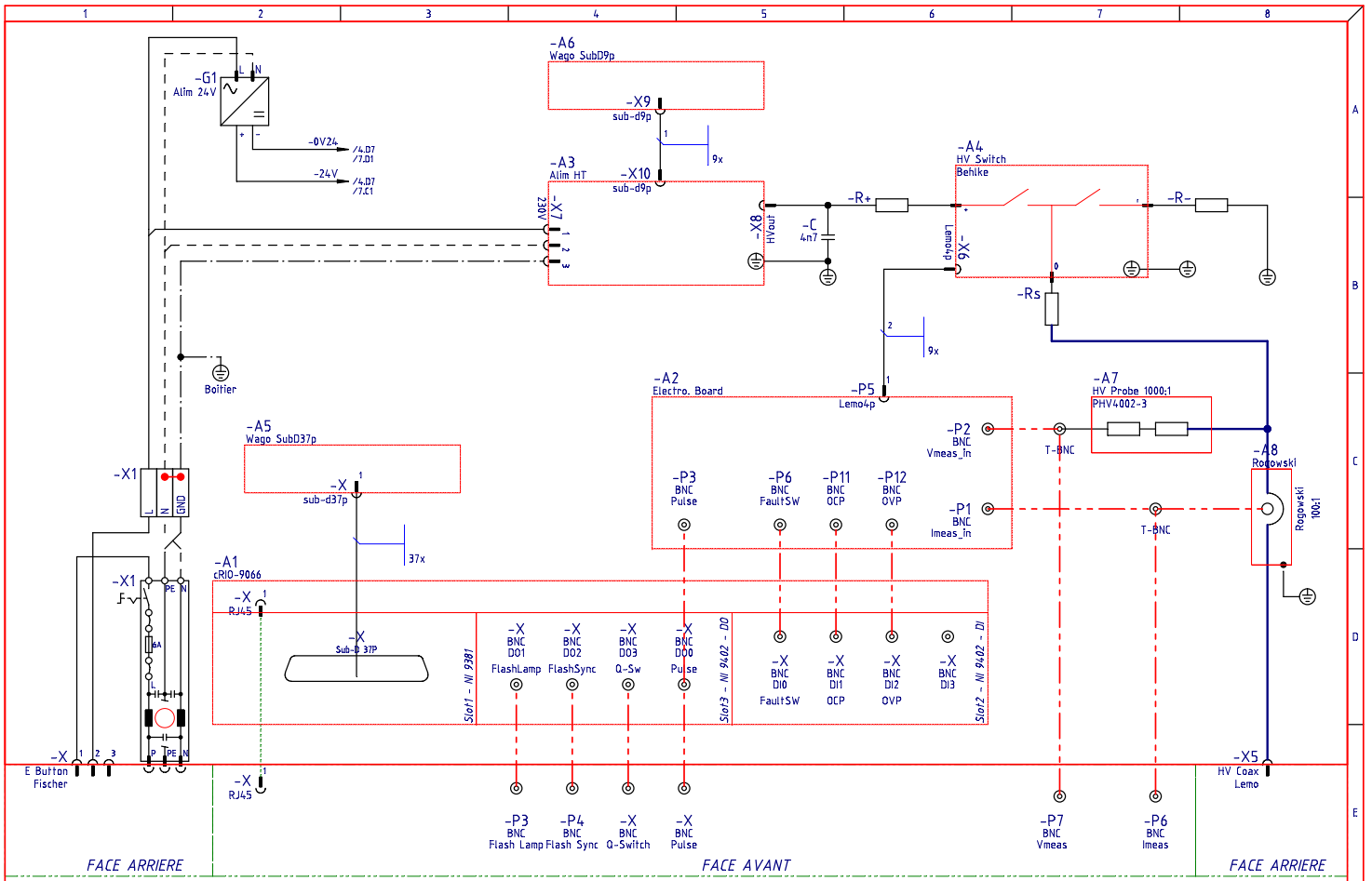


SWISS PLASMA CENTER

Dessiné	23.01.2019	0	30.07.2020	US	Projet	BioPlasma	Niv.1	Schema electrique	Usiné
Imprimé	24.03.2021	US			Nom	Plasma Industriel - BioPlasma	Niv.2	Boitier	Façon.
Contrôlé					Fichiers	BioPlasma.pro/000266	Logiciel:	Elcad 7.11.0	Lieu
							Niv.3	1. Photos du boitier	

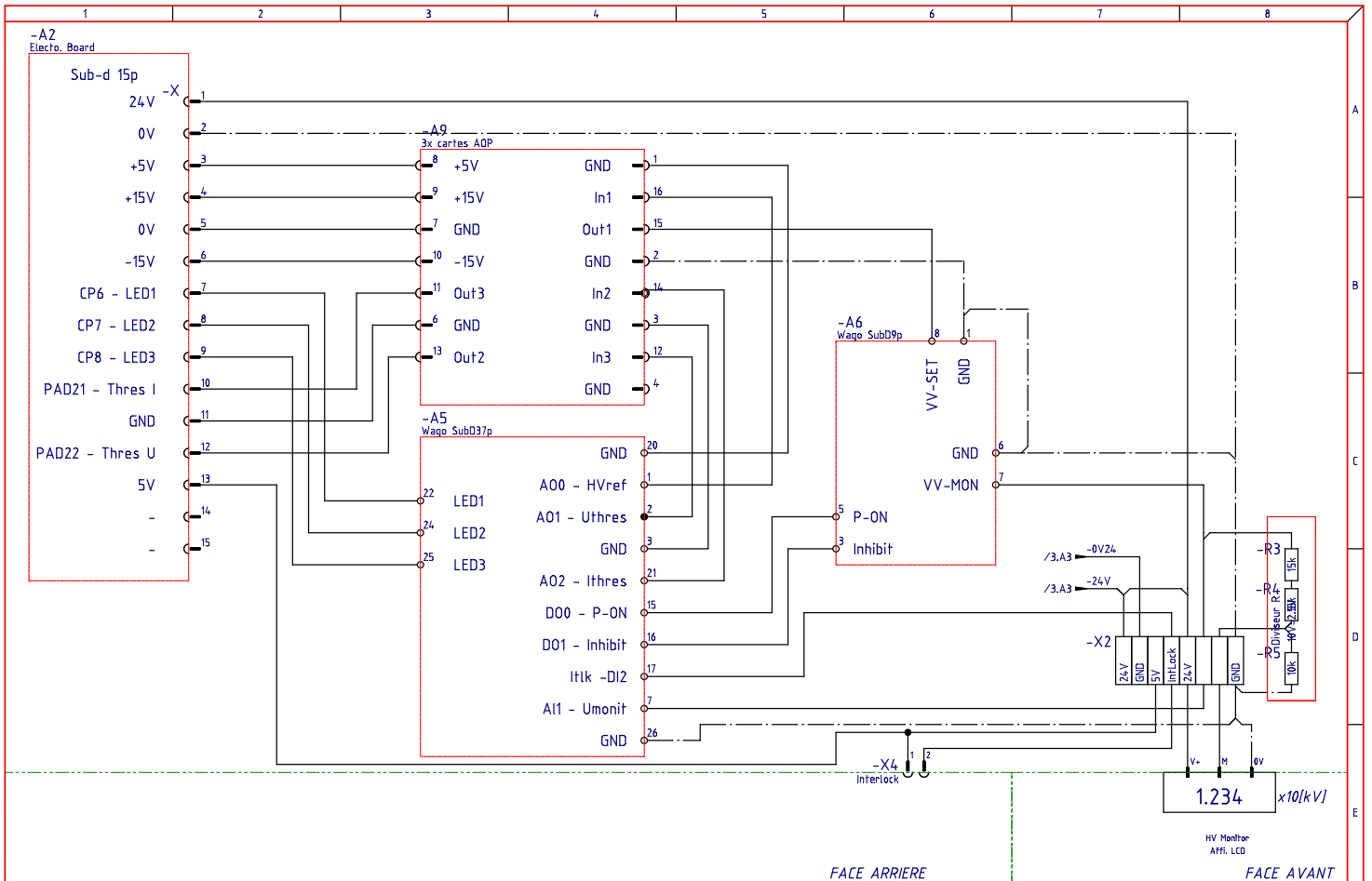


Dessiné	23.01.2019	0	30.07.2020	US	Projet	BioPlasma	Niv.1	Schema electrique	Unité
Imprimé	24.03.2021	US			Nom	Plasma Industriel - BioPlasma	Niv.2	Boitier	Fonct.
Contrôlé					Fichiers	BioPlasma.pro/000332	Niv.3	2. Schéma bloc	Lieu
					Logiciel	Elcad 7.11.0			



SWISS PLASMA CENTER

Dessiné	23.01.2019	0	30.07.2020	US	Projet	BioPlasma	Niv.1	Schema électrique	Unité
Imprimé	24.03.2021	US			Nom	Plasma Industriel - BioPlasma	Niv.2	Boitier	Fonct.
Contrôlé					Fichier	BioPlasma.pro/000343	Niv.3	3. Câblage interne	Lieu
					Logiciel	Elcad 7.11.0			



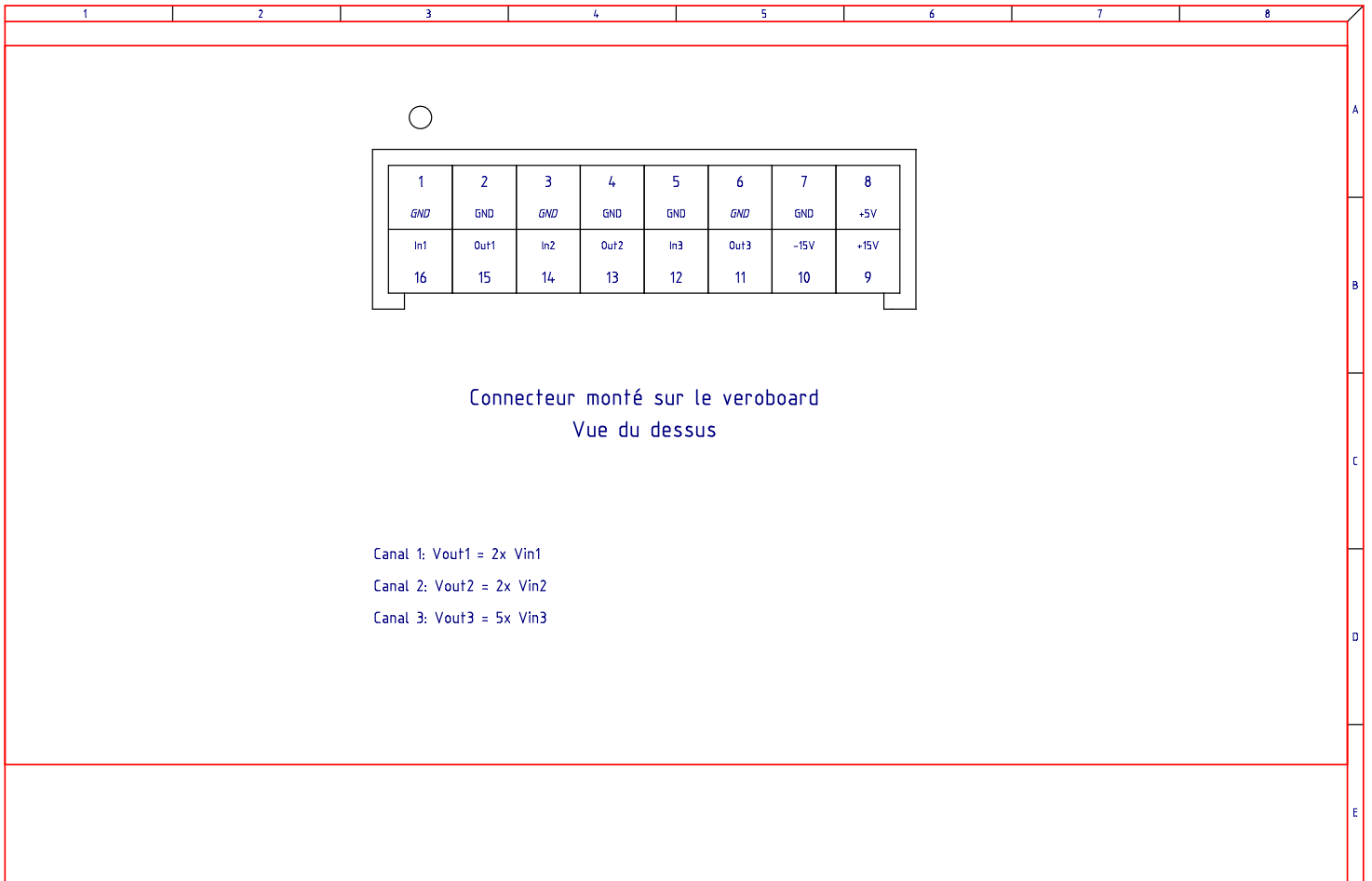
SWISS PLASMA CENTER

Dessiné	23.01.2019	0	30.07.2020	us
Imprimé	24.03.2021	us		
Contrôlé				

Projet	BioPlasma
Nom	Plasma Industriel - BioPlasma
Fichiers	BioPlasma.pro/000321
Logiciel	Elcad 7.11.0

Niv.1	Schema électrique
Niv.2	Boitier
Niv.3	4. Câblage entre circuits

Unité	
Fonct.	
Lieu	



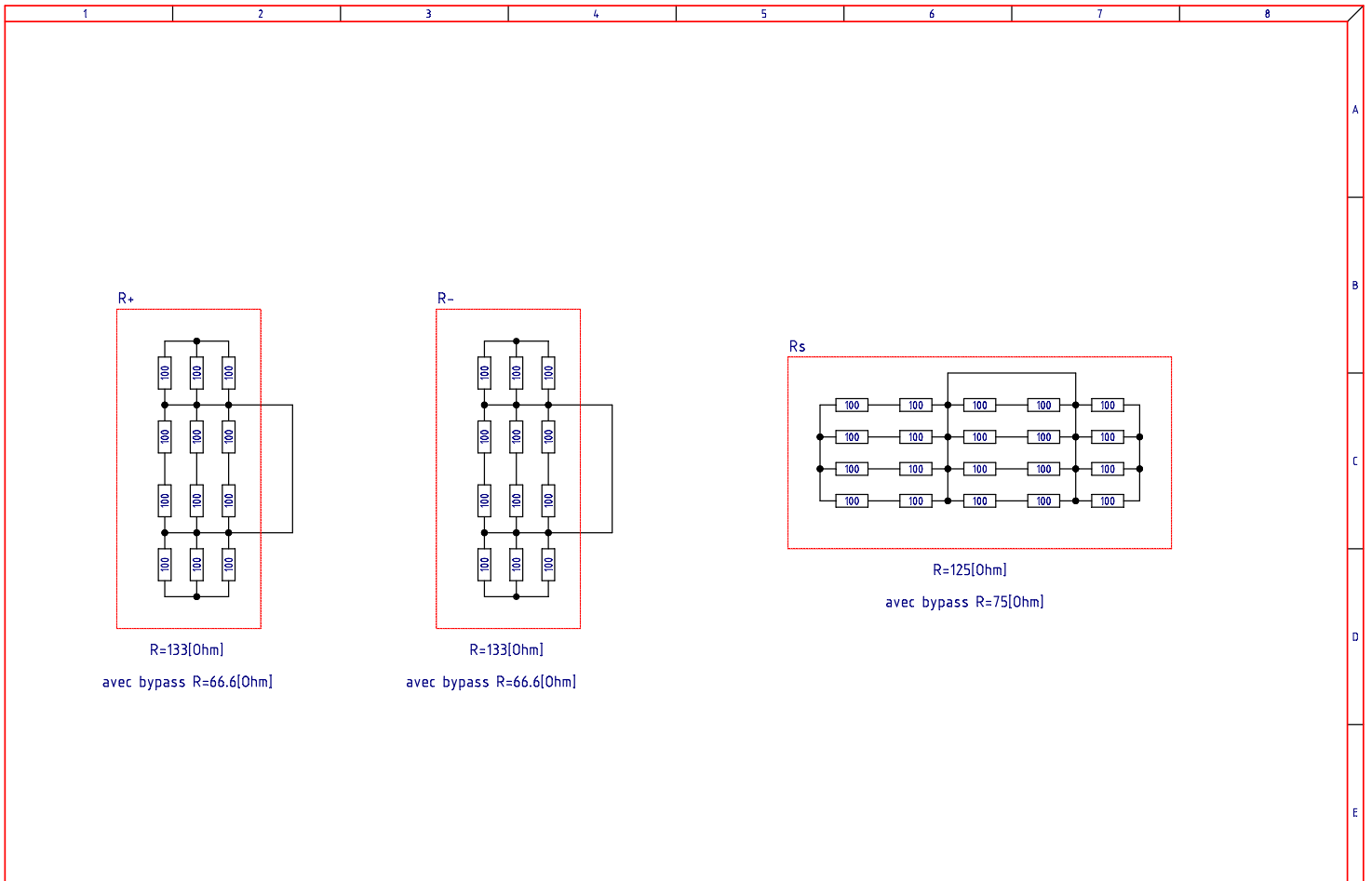
Connecteur monté sur le veroboard
Vue du dessus

Canal 1: Vout1 = 2x Vin1
 Canal 2: Vout2 = 2x Vin2
 Canal 3: Vout3 = 5x Vin3

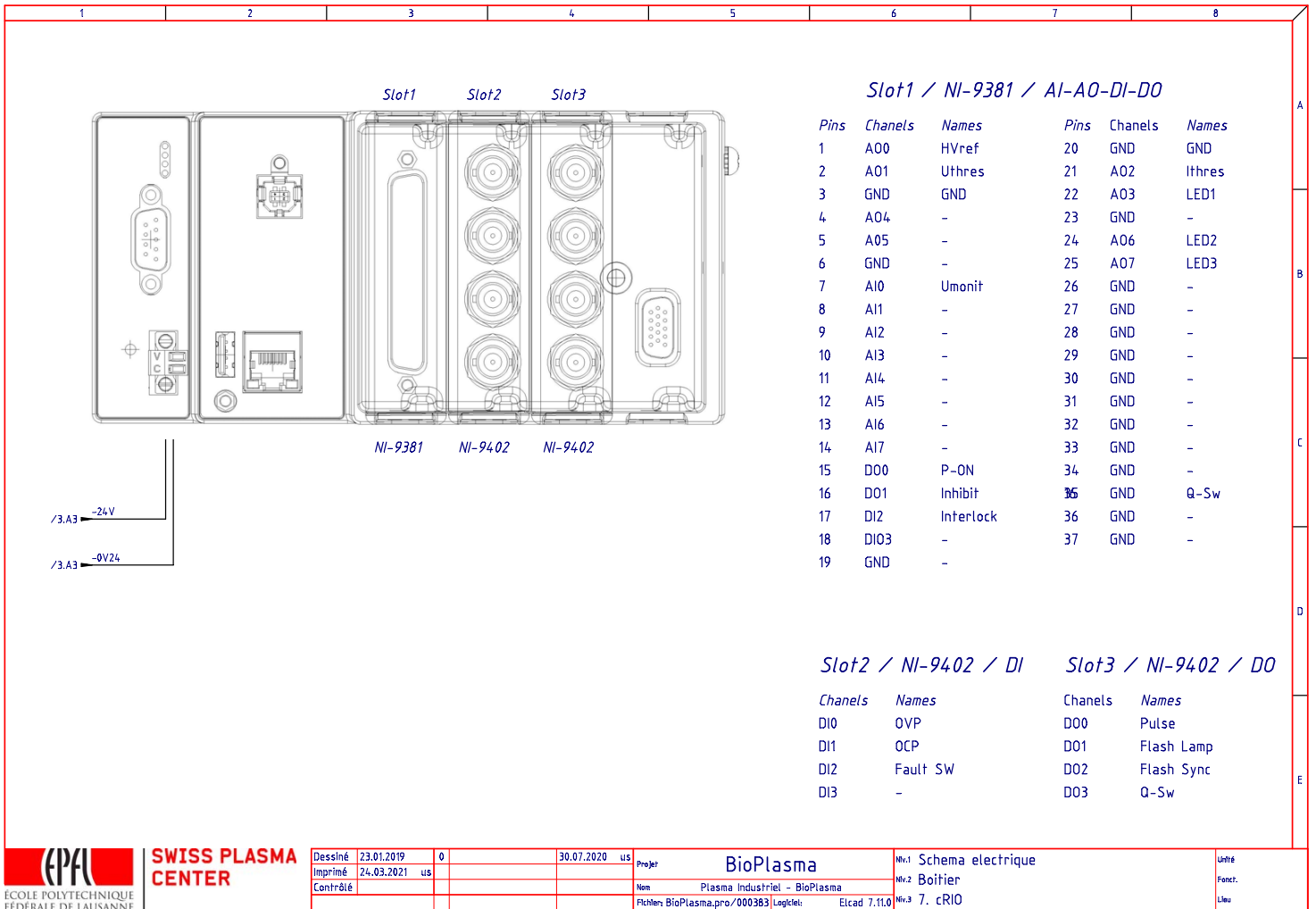


SWISS PLASMA CENTER

Dessiné	23.01.2019	0	30.07.2020	us	Projet	BioPlasma	Niv.1	Schema electrique	Unité
Imprimé	24.03.2021	us			Nom	Plasma Industriel - BioPlasma	Niv.2	Boitier	Fonct.
Contrôlé					Fichier	BioPlasma.pro/000344	Niv.3	5. AOP	Lieu
					Logiciel	Elcad 7.11.0			

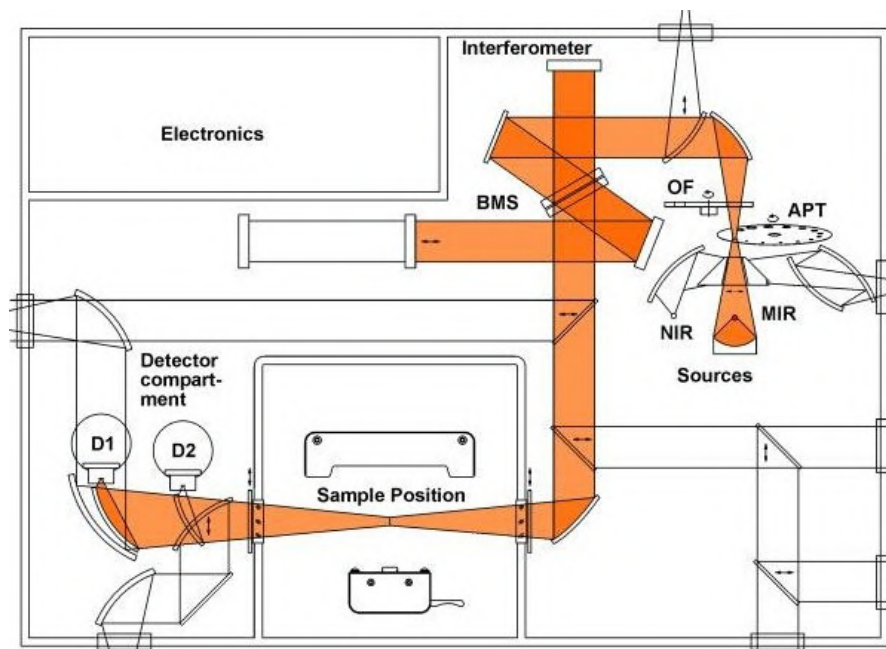


Dessiné	23.01.2019	0	30.07.2020	US	Projet	BioPlasma	Niv.1	Schema électrique	Unité
Imprimé	24.03.2021	US			Nom	Plasma Industriel - BioPlasma	Niv.2	Boitier	Fonct.
Contrôlé					Fichiers	BioPlasma.pro/000124	Niv.3	6. Mise en série/parallèle des R HT	Lieu
					Logiciel	Elcad 7.11.0			

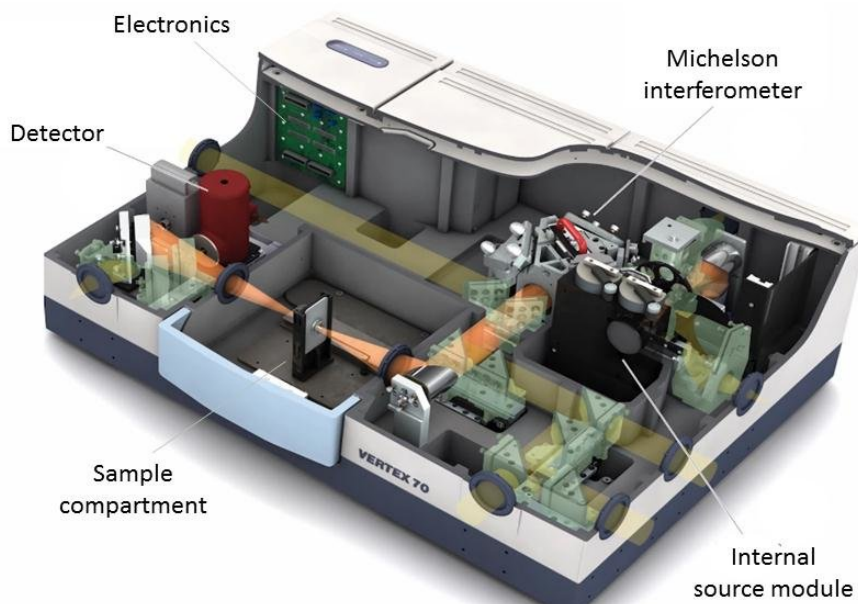


FTIR vertex 80v schematics

In this section, the detailed schematics of the FTIR vertex 80v spectrometers are reported.



(a)



(b)

Figure 1: (a) Representation of the optical path of the Bruker Vertex 80v, along with basic components of the spectrometer. (b) Three-dimensional illustration of the Bruker Vertex 80v spectrometer.

Bibliography

- [1] A. Fridman. *Plasma Chemistry*. Cambridge University Press, 2008. ISBN: 9781139471732. URL: <https://books.google.ch/books?id=ZzmtGEHCC9MC>.
- [2] Maher I. Boulos, Pierre L. Fauchais, and Emil Pfender. "The Plasma State". In: *Handbook of Thermal Plasmas*. Cham: Springer International Publishing, 2016, pp. 1–53. ISBN: 978-3-319-12183-3. DOI: 10.1007/978-3-319-12183-3_1-2. URL: https://doi.org/10.1007/978-3-319-12183-3_1-2.
- [3] P.K. Chu and X.P. Lu. *Low Temperature Plasma Technology: Methods and Applications*. Ebook Central Academic Complete Collection. CRC Press, 2013. ISBN: 9781466509917. URL: <https://books.google.ch/books?id=nzrSBQAAQBAJ>.
- [4] National Research Council. *Plasma Science: Advancing Knowledge in the National Interest*. Washington, DC: The National Academies Press, 2007. ISBN: 978-0-309-10943-7. DOI: 10.17226/11960. URL: <https://nap.nationalacademies.org/catalog/11960/plasma-science-advancing-knowledge-in-the-national-interest>.
- [5] Claire Tendero et al. "Atmospheric pressure plasmas: A review". In: *Spectrochimica Acta Part B: Atomic Spectroscopy* 61.1 (2006), pp. 2–30. ISSN: 0584-8547. DOI: <https://doi.org/10.1016/j.sab.2005.10.003>. URL: <https://www.sciencedirect.com/science/article/pii/S0584854705002843>.
- [6] M.I. Boulos, P. Fauchais, and E. Pfender. *Thermal Plasmas*. Advances in Experimental Medicine & Biology v. 1. Springer, 1994. ISBN: 9780306446078. URL: https://books.google.ch/books?id=psdRf_a9LKYC.
- [7] Kyoung-Jae Chung. "Electrical Breakdown in Gases". 2018. URL: https://ocw.snu.ac.kr/sites/default/files/NOTE/Lecture_06_Electrical%20breakdown%20in%20gases.pdf.
- [8] A Fridman, A Chirokov, and A Gutsol. "Non-thermal atmospheric pressure discharges". In: *Journal of Physics D: Applied Physics* 38.2 (Jan. 2005), R1. DOI: 10.1088/0022-3727/38/2/R01. URL: <https://dx.doi.org/10.1088/0022-3727/38/2/R01>.
- [9] Kevin Ollegott et al. "Fundamental Properties and Applications of Dielectric Barrier Discharges in Plasma-Catalytic Processes at Atmospheric Pressure". In: *Chemie Ingenieur Technik* 92 (Aug. 2020). DOI: 10.1002/cite.202000075.

- [10] Kogelschatz, U., Eliasson, B., and Egli, W. "Dielectric-Barrier Discharges. Principle and Applications". In: *J. Phys. IV France* 07 (1997), pp. C4-47-C4-66. DOI: 10.1051/jp4:1997405. URL: <https://doi.org/10.1051/jp4:1997405>.
- [11] Ronny Brandenburg. "Dielectric barrier discharges: progress on plasma sources and on the understanding of regimes and single filaments". In: *Plasma Sources Science and Technology* 26.5 (Apr. 2017), p. 053001. DOI: 10.1088/1361-6595/aa6426. URL: <https://dx.doi.org/10.1088/1361-6595/aa6426>.
- [12] F Avino et al. "Surface DBD degradation in humid air, and a hybrid surface-volume DBD for robust plasma operation at high humidity". In: *Journal of Physics D: Applied Physics* 56.34 (May 2023), p. 345201. DOI: 10.1088/1361-6463/acd2e4. URL: <https://dx.doi.org/10.1088/1361-6463/acd2e4>.
- [13] Valentin I Gibalov and Gerhard J Pietsch. "The development of dielectric barrier discharges in gas gaps and on surfaces". In: *Journal of Physics D: Applied Physics* 33.20 (Oct. 2000), p. 2618. DOI: 10.1088/0022-3727/33/20/315. URL: <https://dx.doi.org/10.1088/0022-3727/33/20/315>.
- [14] Ulrich Kogelschatz. "Filamentary, Patterned, and Diffuse Barrier Discharges". In: *Plasma Science, IEEE Transactions on* 30 (Sept. 2002), pp. 1400–1408. DOI: 10.1109/TPS.2002.804201.
- [15] B. Eliasson and U. Kogelschatz. "Modeling and applications of silent discharge plasmas". In: *IEEE Transactions on Plasma Science* 19.2 (1991), pp. 309–323. DOI: 10.1109/27.106829.
- [16] Mounir Laroussi. "Cold Gas Plasma Sources and the Science behind their Applications in Biology and Medicine". In: (June 2021).
- [17] F Massines et al. "Physics and chemistry in a glow dielectric barrier discharge at atmospheric pressure: Diagnostics and modelling". In: *Surface and Coatings Technology* 174-175 (2003), pp. 8–14. ISSN: 02578972. DOI: 10.1016/S0257-8972(03)00540-1.
- [18] S Okazaki et al. "Appearance of stable glow discharge in air, argon, oxygen and nitrogen at atmospheric pressure using a 50 Hz source". In: *Journal of Physics D: Applied Physics* 26.5 (May 1993), p. 889. DOI: 10.1088/0022-3727/26/5/025. URL: <https://dx.doi.org/10.1088/0022-3727/26/5/025>.
- [19] Denis Butscher. "Non-thermal plasma inactivation of microorganisms on granular food products". In: (). DOI: 10.3929/ethz-a-010626028. URL: <https://doi.org/10.3929/ethz-a-010626028>.
- [20] M. Laroussi et al. "Power consideration in the pulsed dielectric barrier discharge at atmospheric pressure". In: *Journal of Applied Physics* 96 (5 Sept. 2004), pp. 3028–3030. ISSN: 00218979. DOI: 10.1063/1.1777392.
- [21] J. L. Walsh, J. J. Shi, and M. G. Kong. "Contrasting characteristics of pulsed and sinusoidal cold atmospheric plasma jets". In: *Applied Physics Letters* 88 (17 2006). ISSN: 00036951. DOI: 10.1063/1.2198100.

- [22] James M. Williamson et al. "Comparison of high-voltage ac and pulsed operation of a surface dielectric barrier discharge". In: *Journal of Physics D: Applied Physics* 39 (20 Oct. 2006), pp. 4400–4406. ISSN: 00223727. DOI: 10.1088/0022-3727/39/20/016.
- [23] M. I. Lomaev and V. F. Tarasenko. "Uniform Action of Plasma of a Nanosecond Pulsed High-Voltage Discharge on the Surface of a Flat Anode". In: *Plasma Physics Reports* 49 (4 Apr. 2023), pp. 523–526. ISSN: 15626938. DOI: 10.1134/S1063780X2360007X.
- [24] E. Kh Baksht et al. "Dynamics of the spatial structure of pulsed discharges in dense gases in point cathodeplane anode gaps and their erosion effect on the plane electrode surface". In: *Plasma Physics Reports* 42 (9 Sept. 2016), pp. 876–886. ISSN: 1063780X. DOI: 10.1134/S1063780X16090014.
- [25] S. A. Stepanyan, V. R. Soloviev, and S. M. Starikovskaia. "An electric field in nanosecond surface dielectric barrier discharge at different polarities of the high voltage pulse: spectroscopy measurements and numerical modeling". In: *Journal of Physics D Applied Physics* 47.48, 485201 (Dec. 2014), p. 485201. DOI: 10.1088/0022-3727/47/48/485201.
- [26] U Kogelschatz et al. "Principle and Applications". In: *Journal de Physique IV Proceedings* (C4 1997), pp. 4–47. DOI: 10.1051/jp4:1997405. URL: <https://hal.science/jpa-00255561>.
- [27] A. Jay Palmer. "A physical model on the initiation of atmospheric-pressure glow discharges". In: *Applied Physics Letters* 25 (3 1974), pp. 138–140. ISSN: 00036951. DOI: 10.1063/1.1655412.
- [28] Pietro Ranieri et al. "Plasma agriculture: Review from the perspective of the plant and its ecosystem". In: *Plasma Processes and Polymers* 18.1 (2021), p. 2000162. DOI: <https://doi.org/10.1002/ppap.202000162>. eprint: <https://onlinelibrary.wiley.com/doi/pdf/10.1002/ppap.202000162>. URL: <https://onlinelibrary.wiley.com/doi/abs/10.1002/ppap.202000162>.
- [29] Evgeny M. Konchekov et al. "Advancements in Plasma Agriculture: A Review of Recent Studies". In: *International Journal of Molecular Sciences* 24 (20 Oct. 2023). ISSN: 14220067. DOI: 10.3390/ijms242015093.
- [30] Paolo F Ambrico et al. "On the air atmospheric pressure plasma treatment effect on the physiology, germination and seedlings of basil seeds". In: *Journal of Physics D: Applied Physics* 53.10 (Dec. 2019), p. 104001. DOI: 10.1088/1361-6463/ab5b1b. URL: <https://dx.doi.org/10.1088/1361-6463/ab5b1b>.
- [31] Alexandra Waskow, Alan Howling, and Ivo Furno. "Mechanisms of Plasma-Seed Treatments as a Potential Seed Processing Technology". In: *Frontiers in Physics* 9 (2021). ISSN: 2296-424X. DOI: 10.3389/fphy.2021.617345. URL: <https://www.frontiersin.org/articles/10.3389/fphy.2021.617345>.
- [32] Sapna Birania et al. "Cold plasma in food processing and preservation: A review". In: *Journal of Food Process Engineering* 45 (9 Sept. 2022). ISSN: 17454530. DOI: 10.1111/jfpe.14110.

- [33] Hao Jiang et al. "Food preservation by cold plasma from dielectric barrier discharges in agri-food industries". In: *Frontiers in Nutrition* 9 (Nov. 2022). ISSN: 2296861X. DOI: 10.3389/fnut.2022.1015980.
- [34] Denise Adamoli Laroque et al. "Cold plasma in food processing: Design, mechanisms, and application". In: *Journal of Food Engineering* 312 (Jan. 2022). ISSN: 02608774. DOI: 10.1016/j.jfoodeng.2021.110748.
- [35] Caterina Maccaferri et al. "Evaluation of the Antimicrobial Efficacy of a Large-Area Surface Dielectric Barrier Discharge on Food Contact Surfaces". In: *Plasma Chemistry and Plasma Processing* (Nov. 2023). ISSN: 15728986. DOI: 10.1007/s11090-023-10410-2.
- [36] Mounir Laroussi. "Cold Plasma in Medicine and Healthcare: The New Frontier in Low Temperature Plasma Applications". In: *Frontiers in Physics* 8 (2020). ISSN: 2296-424X. DOI: 10.3389/fphy.2020.00074. URL: <https://www.frontiersin.org/articles/10.3389/fphy.2020.00074>.
- [37] Zhitong Chen et al. "Cold atmospheric plasma delivery for biomedical applications". In: *Materials Today* 54 (2022), pp. 153–188. ISSN: 1369-7021. DOI: <https://doi.org/10.1016/j.mattod.2022.03.001>. URL: <https://www.sciencedirect.com/science/article/pii/S1369702122000608>.
- [38] Thomas Von Woedtke et al. "Plasma medicine: A field of applied redox biology". In: *In Vivo* 33 (4 2019), pp. 1011–1026. ISSN: 17917549. DOI: 10.21873/invivo.11570.
- [39] Gregory Fridman et al. "Blood coagulation and living tissue sterilization by floating-electrode dielectric barrier discharge in air". In: *Plasma Chemistry and Plasma Processing* 26 (4 2006), pp. 425–442. ISSN: 02724324. DOI: 10.1007/s11090-006-9024-4.
- [40] Krishna Priya Arjunan et al. "Non-thermal dielectric barrier discharge plasma induces angiogenesis through reactive oxygen species". In: *Journal of the Royal Society Interface* 9 (66 Jan. 2012), pp. 147–157. ISSN: 17425662. DOI: 10.1098/rsif.2011.0220.
- [41] Keping YAN et al. "Pulsed cold plasma-induced blood coagulation and its pilot application in stanching bleeding during rat hepatectomy". In: *Plasma Science and Technology* 20.4 (Mar. 2018), p. 044005. DOI: 10.1088/2058-6272/aa9b79. URL: <https://dx.doi.org/10.1088/2058-6272/aa9b79>.
- [42] Yudai Nomura et al. "Investigation of blood coagulation effect of nonthermal multigas plasma jet in vitro and in-vivo". In: *Journal of Surgical Research* 219 (Nov. 2017), pp. 302–309. ISSN: 10958673. DOI: 10.1016/j.jss.2017.06.055.
- [43] Zahra Shahbazi Rad, Fereydoun Abbasi Davani, and Gholamreza Etaati. "Determination of proper treatment time for in vivo blood coagulation and wound healing application by non-thermal helium plasma jet". In: *Australasian Physical and Engineering Sciences in Medicine* 41 (4 Dec. 2018), pp. 905–917. ISSN: 18795447. DOI: 10.1007/s13246-018-0686-z.
- [44] Seunghee Cha and Young Seok Park. "Plasma in dentistry". In: *Clinical Plasma Medicine* 2 (1 2014), pp. 4–10. ISSN: 22128166. DOI: 10.1016/j.cpme.2014.04.002.

- [45] Wilma Van Boxem et al. "Anti-cancer capacity of plasma-treated PBS: Effect of chemical composition on cancer cell cytotoxicity". In: *Scientific Reports* 7 (1 Dec. 2017). ISSN: 20452322. DOI: 10.1038/s41598-017-16758-8.
- [46] Fatemeh Faramarzi et al. "Cold Physical Plasma in Cancer Therapy: Mechanisms, Signaling, and Immunity". In: *Oxidative Medicine and Cellular Longevity* 2021 (2021). ISSN: 19420994. DOI: 10.1155/2021/9916796.
- [47] Milica Živanić et al. "Current State of Cold Atmospheric Plasma and Cancer-Immunity Cycle: Therapeutic Relevance and Overcoming Clinical Limitations Using Hydrogels". In: *Advanced Science* 10 (8 Mar. 2023). ISSN: 21983844. DOI: 10.1002/advs.202205803.
- [48] Tianhao Min et al. "Therapeutic Effects of Cold Atmospheric Plasma on Solid Tumor". In: *Frontiers in Medicine* 9 (May 2022). ISSN: 2296858X. DOI: 10.3389/fmed.2022.884887.
- [49] Dzohara Murillo et al. "Exploring the Use of Cold Atmospheric Plasma to Overcome Drug Resistance in Cancer". In: *Biomedicines* 11 (1 Jan. 2023). ISSN: 22279059. DOI: 10.3390/biomedicines11010208.
- [50] M. Keidar et al. "Cold plasma selectivity and the possibility of a paradigm shift in cancer therapy". In: *British Journal of Cancer* 105 (9 Oct. 2011), pp. 1295–1301. ISSN: 00070920. DOI: 10.1038/bjc.2011.386.
- [51] Dana Ziuzina et al. "Cold plasma inactivation of bacterial biofilms and reduction of quorum sensing regulated virulence factors". In: *PLoS ONE* 10 (9 2015), pp. 1–21. ISSN: 19326203. DOI: 10.1371/journal.pone.0138209.
- [52] Masakazu Tanino et al. "Sterilization using dielectric barrier discharge at atmospheric pressure". In: *Conference Record - IAS Annual Meeting (IEEE Industry Applications Society)* 2 (2005), pp. 784–788. ISSN: 01972618. DOI: 10.1109/IAS.2005.1518421.
- [53] Li Guo et al. "Microbial inactivation in model tissues treated by surface discharge plasma". In: *Journal of Physics D: Applied Physics* 53 (1 2020). ISSN: 13616463. DOI: 10.1088/1361-6463/ab4829.
- [54] Unggul Pundjung Juswono et al. "Bacterial Sterilization Using Non-Thermal Plasma Method Surface Dielectric Barrier Discharge (SDBD): Effect of Treatment Duration on Colony Count, DNA, Protease Enzymes, and Cell Morphology". In: *Trends in Sciences* 20 (7 July 2023). ISSN: 27740226. DOI: 10.48048/tis.2023.6760.
- [55] Paolo F. Ambrico et al. "Surface Dielectric Barrier Discharge plasma: a suitable measure against fungal plant pathogens". In: *Scientific Reports* 10 (1 Dec. 2020). ISSN: 20452322. DOI: 10.1038/s41598-020-60461-0.
- [56] Zlata Kelar Tučeková et al. "Multi-hollow surface dielectric barrier discharge for bacterial biofilm decontamination". In: *Molecules* 26 (4 Feb. 2021). ISSN: 14203049. DOI: 10.3390/molecules26040910.
- [57] Yiqian Li et al. "The Effect of Plasma on Bacteria and Normal Cells in Infected Wound". In: *Oxidative Medicine and Cellular Longevity* 2022 (2022). ISSN: 19420994. DOI: 10.1155/2022/1838202.

- [58] K. G. Kostov et al. "Bacterial sterilization by a dielectric barrier discharge (DBD) in air". In: *Surface and Coatings Technology* 204 (18-19 2010), pp. 2954–2959. ISSN: 02578972. DOI: 10.1016/j.surfcoat.2010.01.052. URL: <http://dx.doi.org/10.1016/j.surfcoat.2010.01.052>.
- [59] E. Leipold et al. "Decontamination of objects in a sealed container by means of atmospheric pressure plasmas". In: *Food Control* 22 (8 2011), pp. 1296–1301. ISSN: 09567135. DOI: 10.1016/j.foodcont.2011.02.003.
- [60] Janosch Schirmack et al. "Effects of low-temperature plasma-sterilization on mars analog soil samples mixed with deinococcus radiodurans". In: *Life* 6 (2 June 2016). ISSN: 20751729. DOI: 10.3390/life6020022.
- [61] Marcel Fiebrandt et al. "Inactivation of *B. subtilis* spores by low pressure plasma—influence of optical filters and photon/particle fluxes on the inactivation efficiency". In: *Journal of Physics D: Applied Physics* 51.4 (Jan. 2018), p. 045401. DOI: 10.1088/1361-6463/aa9f0a. URL: <https://dx.doi.org/10.1088/1361-6463/aa9f0a>.
- [62] Michael Beyrer et al. "Cold Atmospheric Plasma Inactivation of Microbial Spores Compared on Reference Surfaces and Powder Particles". In: *Food and Bioprocess Technology* 13 (5 May 2020), pp. 827–837. ISSN: 19355149. DOI: 10.1007/s11947-020-02438-5.
- [63] Katharina Stapelmann et al. "Utilization of Low-Pressure Plasma to Inactivate Bacterial Spores on Stainless Steel Screws". In: *Astrobiology* 13.7 (2013). PMID: 23768085, pp. 597–606. DOI: 10.1089/ast.2012.0949. eprint: <https://doi.org/10.1089/ast.2012.0949>. URL: <https://doi.org/10.1089/ast.2012.0949>.
- [64] Pradeep Puligundla and Chulkyoon Mok. "Inactivation of spores by nonthermal plasmas". In: *World Journal of Microbiology and Biotechnology* 34 (10 Oct. 2018). ISSN: 15730972. DOI: 10.1007/s11274-018-2527-3.
- [65] Hager Mohamed et al. "Non-Thermal Plasma as a Novel Strategy for Treating or Preventing Viral Infection and Associated Disease". In: *Frontiers in Physics* 9 (June 2021). DOI: 10.3389/fphy.2021.683118.
- [66] Ankit Moldgy et al. "Inactivation of virus and bacteria using cold atmospheric pressure air plasmas and the role of reactive nitrogen species". In: *Journal of Physics D: Applied Physics* 53.43 (Aug. 2020), p. 434004. DOI: 10.1088/1361-6463/aba066. URL: <https://dx.doi.org/10.1088/1361-6463/aba066>.
- [67] Malgorzata Z Pajak-Zajac et al. "Biofilm inactivation by cold plasma Antimicrobial efficacy of in-situ plasma-generated ozone against *Pseudomonas aeruginosa* biofilms in drains and water-submerged surfaces". In: (). DOI: 10.1101/2023.08.28.553206. URL: <https://doi.org/10.1101/2023.08.28.553206>.
- [68] Chandni Praveen et al. "Electron beam inactivation of selected microbial pathogens and indicator organisms in aerobically and anaerobically digested sewage sludge". In: *Bioresource Technology* 144 (2013), pp. 652–657. ISSN: 18732976. DOI: 10.1016/j.biortech.2013.07.034.

- [69] Charlotte Da Silva et al. "Bacterial Eradication by a Low-Energy Pulsed Electron Beam Generator". In: *Bioelectrochemistry* (Apr. 2023), p. 108593. ISSN: 15675394. DOI: 10.1016/j.bioelechem.2023.108593.
- [70] M Laroussi, D A Mendis, and M Rosenberg. "Plasma interaction with microbes". In: *New Journal of Physics* 5.1 (Apr. 2003), p. 41. DOI: 10.1088/1367-2630/5/1/341. URL: <https://dx.doi.org/10.1088/1367-2630/5/1/341>.
- [71] Francois Rossi and Ondřej Kylián. "Sterilization and decontamination of surfaces by plasma discharges". In: *Sterilisation of Biomaterials and Medical Devices* (Dec. 2012), pp. 117–150. DOI: 10.1533/9780857096265.117.
- [72] S Haberl et al. *Cell Membrane Electroporation-Part 2: The Applications*.
- [73] Gintautas Saulis. "Electroporation of cell membranes: The fundamental effects of pulsed electric fields in food processing". In: *Food Engineering Reviews* 2 (2 June 2010), pp. 52–73. ISSN: 18667910. DOI: 10.1007/s12393-010-9023-3.
- [74] Emanuele Simoncelli et al. "UV-VIS optical spectroscopy investigation on the kinetics of long-lived RONS produced by a surface DBD plasma source". In: *Plasma Sources Science and Technology* 28 (9 Sept. 2019). ISSN: 13616595. DOI: 10.1088/1361-6595/ab3c36.
- [75] M. Laroussi and F. Leipold. "Evaluation of the roles of reactive species, heat, and UV radiation in the inactivation of bacterial cells by air plasmas at atmospheric pressure". In: *International Journal of Mass Spectrometry* 233.1 (2004). Special Issue: In honour of Tilmann Mark, pp. 81–86. ISSN: 1387-3806. DOI: <https://doi.org/10.1016/j.ijms.2003.11.016>. URL: <https://www.sciencedirect.com/science/article/pii/S138738060400003X>.
- [76] P. Lukes et al. "Aqueous-phase chemistry and bactericidal effects from an air discharge plasma in contact with water: Evidence for the formation of peroxyxynitrite through a pseudo-second-order post-discharge reaction of H₂O₂ and HNO₂". In: *Plasma Sources Science and Technology* 23.1 (2014), p. 015019. ISSN: 09630252. DOI: 10.1088/0963-0252/23/1/015019.
- [77] Nazir Barekzi, M. Arda Akman, and Mounir Laroussi. "Inactivation pathways of reactive species generated by low temperature atmospheric pressure plasma". In: (2012), 2P-134-2P–134. DOI: 10.1109/PLASMA.2012.6383690.
- [78] Apurva Patange et al. "The Effect of Atmospheric Cold Plasma on Bacterial Stress Responses and Virulence Using *Listeria monocytogenes* Knockout Mutants". In: *Frontiers in Microbiology* 10 (2019). ISSN: 1664-302X. DOI: 10.3389/fmicb.2019.02841. URL: <https://www.frontiersin.org/articles/10.3389/fmicb.2019.02841>.
- [79] Renwu Zhou et al. "Plasma-activated water: Generation, origin of reactive species and biological applications". In: *Journal of Physics D: Applied Physics* 53.30 (2020), p. 303001. ISSN: 13616463. DOI: 10.1088/1361-6463/ab81cf.

- [80] V. S. Santosh K. Kondeti et al. “Long-lived and short-lived reactive species produced by a cold atmospheric pressure plasma jet for the inactivation of *Pseudomonas aeruginosa* and *Staphylococcus aureus*”. In: *Free Radical Biology and Medicine* 124 (Aug. 2018), pp. 275–287. ISSN: 18734596. DOI: 10.1016/j.freeradbiomed.2018.05.083.
- [81] S Lerouge et al. “Effect of gas composition on spore mortality and etching during low-pressure plasma sterilization”. In: (2000). DOI: 10.1002/(SICI)1097-4636(200007)51:1<128::AID-JBM17>3.0.CO;2. URL: <https://onlinelibrary.wiley.com/doi/10.1002/>.
- [82] Hong Sheng et al. “Microbicidal Activity of Artificially Generated Hydroxyl Radicals”. In: (2015). Ed. by Keiichi Sasaki, Osamu Suzuki, and Nobuhiro Takahashi, pp. 203–215.
- [83] Carles Corbella, Sabine Portal, and Michael Keidar. “Flexible Cold Atmospheric Plasma Jet Sources”. In: *Plasma* 6.1 (2023), pp. 72–88. ISSN: 2571-6182. DOI: 10.3390/plasma6010007. URL: <https://www.mdpi.com/2571-6182/6/1/7>.
- [84] W T Broadwater, R C Hoehn, and P H King. *Sensitivity of Three Selected Bacterial Species to Ozone*. 1973, pp. 391–393. URL: <https://journals.asm.org/journal/am>.
- [85] Oleg Lunov et al. “Cell death induced by ozone and various non-thermal plasmas: Therapeutic perspectives and limitations”. In: *Scientific Reports* 4 (Nov. 2014). ISSN: 20452322. DOI: 10.1038/srep07129.
- [86] A. Niveditha et al. *Application of cold plasma and ozone technology for decontamination of Escherichia coli in foods- a review*. Dec. 2021. DOI: 10.1016/j.foodcont.2021.108338.
- [87] Ahlem Mahfoudh et al. “Inactivation of vegetative and sporulated bacteria by dry gaseous ozone”. In: *Ozone: Science and Engineering* 32 (3 May 2010), pp. 180–198. ISSN: 01919512. DOI: 10.1080/01919511003791971.
- [88] Dick Zoutman, Michael Shannon, and Arkady Mandel. “Effectiveness of a novel ozone-based system for the rapid high-level disinfection of health care spaces and surfaces”. In: *American Journal of Infection Control* 39 (10 Dec. 2011), pp. 873–879. ISSN: 01966553. DOI: 10.1016/j.ajic.2011.01.012.
- [89] Jin Jeon et al. “Bactericidal agents produced by surface micro-discharge (SMD) plasma by controlling gas compositions”. In: *Plasma Processes and Polymers* 11 (5 2014), pp. 426–436. ISSN: 16128869. DOI: 10.1002/ppap.201300173.
- [90] Matthew J. Pavlovich, Douglas S. Clark, and David B. Graves. “Quantification of air plasma chemistry for surface disinfection”. In: *Plasma Sources Science and Technology* 23 (6 Dec. 2014). ISSN: 13616595. DOI: 10.1088/0963-0252/23/6/065036.
- [91] Ankit Moldgy et al. “To cite this article: Ankit Moldgy et al 2020”. In: *J. Phys. D: Appl. Phys* 53 (), p. 434004. URL: <https://doi.org/XXXX/XXXX>.
- [92] Majdi Shomali et al. “Nitrogen Dioxide Sterilization in Low-Resource Environments: A Feasibility Study”. In: *PLOS ONE* 10.6 (June 2015), pp. 1–11. DOI: 10.1371/journal.pone.0130043. URL: <https://doi.org/10.1371/journal.pone.0130043>.

- [93] Daiki Tsukidate et al. "Activation of plant immunity by exposure to dinitrogen pentoxide gas generated from air using plasma technology". In: *PLOS ONE* 17 (June 2022), pp. 1–21. DOI: 10.1371/journal.pone.0269863. URL: <https://doi.org/10.1371/journal.pone.0269863>.
- [94] David O. Schairer et al. "The potential of nitric oxide releasing therapies as antimicrobial agents". In: *Virulence* 3 (3 2012), pp. 271–279. ISSN: 21505608. DOI: 10.4161/viru.20328.
- [95] Muhammad Malik. "Nitric Oxide Production by High Voltage Electrical Discharges for Medical Uses: A Review". In: *Plasma Chemistry and Plasma Processing* 36 (May 2016). DOI: 10.1007/s11090-016-9698-1.
- [96] Victor N. Vasilets and Anatoly B. Shekhter. "Nitric Oxide Plasma Sources for Bio-Decontamination and Plasma Therapy". In: (2012). Ed. by Zdenko Machala, Karol Hensel, and Yuri Akishev, pp. 393–402.
- [97] Klaas De Baerdemaeker et al. "Non-Thermal Plasma Decontamination Using a Multi-Hollow Surface Dielectric Barrier Discharge: Impact of Food Matrix Composition on Bactericidal Efficacy". In: *Foods* 12.2 (2023). ISSN: 2304-8158. DOI: 10.3390/foods12020386. URL: <https://www.mdpi.com/2304-8158/12/2/386>.
- [98] Muhammad Arif Malik et al. "Ozone-free nitric oxide production using an atmospheric pressure surface discharge - A way to minimize nitrogen dioxide co-production". In: *Chemical Engineering Journal* 283 (Jan. 2016), pp. 631–638. ISSN: 13858947. DOI: 10.1016/j.cej.2015.07.092.
- [99] Moayyad Alharbi, Fahad Bakitian, and Ali Alenezi. "Evaluation of bactericidal effects of ultraviolet light C irradiation on cariogenic bacteria: An in vitro study". In: *BMC Oral Health* 21 (1 Dec. 2021). ISSN: 14726831. DOI: 10.1186/s12903-021-01767-x.
- [100] John C H Chang et al. "UV Inactivation of Pathogenic and Indicator Microorganisms". In: *APPLIED AND ENVIRONMENTAL MICROBIOLOGY* 49 (6 1985), pp. 1361–1365. URL: <https://journals.asm.org/journal/aem>.
- [101] Dai T Vrahas MS Murray CK Hamblin MR. "Ultraviolet C irradiation: an alternative antimicrobial approach to localized infections?" In: *Expert Rev Anti-Infect Ther* (2012). DOI: 10.1586/eri.11.166.
- [102] Gagik G Gurzadyan, Helmut Görner, and Dietrich Schulte-Frohlinde. "Ultraviolet (193, 216 and 254 nm) Photoinactivation of Escherichia coli Strains with Different Repair Deficiencies". In: *Radiation Research* 141 (3 1995), pp. 244–251. URL: <https://about.jstor.org/terms>.
- [103] Friederike Kogelheide et al. "The role of humidity and UV-C emission in the inactivation of B. subtilis spores during atmospheric-pressure dielectric barrier discharge treatment". In: *Journal of Physics D: Applied Physics* 53 (29 July 2020). ISSN: 13616463. DOI: 10.1088/1361-6463/ab77cc.

- [104] Nobuo Munakata, Mikio Saito, and Kotaro Hieda. "Inactivation action spectra of *Bacillus subtilis* spores in extended ultraviolet wavelengths (50-300 nm) obtained with synchrotron radiation". In: *Photochemistry and Photobiology* 54.5 (1991), pp. 761–768. DOI: <https://doi.org/10.1111/j.1751-1097.1991.tb02087.x>.
- [105] S Lerouge et al. "Sterilization by Low-Pressure Plasma: The Role of Vacuum-Ultraviolet Radiation". In: *Plasmas and Polymers* 5 (1 2000).
- [106] M K Boudam et al. "Bacterial spore inactivation by atmospheric-pressure plasmas in the presence or absence of UV photons as obtained with the same gas mixture". In: *Journal of Physics D: Applied Physics* 39.16 (Aug. 2006), p. 3494. DOI: 10.1088/0022-3727/39/16/S07. URL: <https://dx.doi.org/10.1088/0022-3727/39/16/S07>.
- [107] Butscher D Van Loon H Waskow A Rudolf von Rohr P Schuppler M. "Plasma inactivation of microorganisms on sprout seeds in a dielectric barrier discharge". In: *Int J Food Microbiol* (2016). DOI: 10.1016/j.ijfoodmicro.2016.09.006.
- [108] "Systematic review and meta-analysis of time-temperature pathogen inactivation". In: *International Journal of Hygiene and Environmental Health* 230 (2020), p. 113595. ISSN: 1438-4639. DOI: <https://doi.org/10.1016/j.ijheh.2020.113595>. URL: <https://www.sciencedirect.com/science/article/pii/S1438463920305411>.
- [109] V. G. Alder, Anne M. Brown, and W. A. Gillespie. "Disinfection of heat-sensitive material by low-temperature steam and formaldehyde". In: *Journal of Clinical Pathology* 19.1 (1966), pp. 83–89. ISSN: 0021-9746. DOI: 10.1136/jcp.19.1.83. eprint: <https://jcp.bmj.com/content/19/1/83.full.pdf>. URL: <https://jcp.bmj.com/content/19/1/83>.
- [110] M Moisan et al. *Low-temperature sterilization using gas plasmas: a review of the experiments and an analysis of the inactivation mechanisms*. 2001, pp. 1–21. URL: www.elsevier.com/locate/ijpharm.
- [111] Sarthak Das et al. "Role of cold atmospheric plasma in microbial inactivation and the factors affecting its efficacy". In: *Health Sciences Review* 4 (Sept. 2022), p. 100037. ISSN: 27726320. DOI: 10.1016/j.hsr.2022.100037.
- [112] Akikazu Sakudo, Yoshihito Yagyu, and Takashi Onodera. "Disinfection and sterilization using plasma technology: Fundamentals and future perspectives for biological applications". In: *International Journal of Molecular Sciences* 20 (20 Oct. 2019). ISSN: 14220067. DOI: 10.3390/ijms20205216.
- [113] Marcel Fiebrandt, Jan-Wilm Lackmann, and Katharina Stapelmann. "From patent to product? 50 years of low-pressure plasma sterilization". In: *Plasma Processes and Polymers* 15.12 (2018), p. 1800139. DOI: <https://doi.org/10.1002/ppap.201800139>. eprint: <https://onlinelibrary.wiley.com/doi/pdf/10.1002/ppap.201800139>. URL: <https://onlinelibrary.wiley.com/doi/abs/10.1002/ppap.201800139>.
- [114] Mounir Laroussi. "Low temperature plasma-based sterilization: Overview and state-of-the-art". In: *Plasma Processes and Polymers* 2 (5 June 2005), pp. 391–400. ISSN: 16128850. DOI: 10.1002/ppap.200400078.

- [115] S Lerouge, M R Wertheimer, and L ' H Yahia. "Plasma Sterilization: A Review of Parameters, Mechanisms, and Limitations". In: *Plasmas and Polymers* 6 (3 2001).
- [116] ISO: Global standards for trusted goods and services. *Sterilization of health care products - Vocabulary, ISO 11139, 2018*. 2018. URL: <https://www.iso.org/standard/66262.html>.
- [117] World Health Organization. *Safe management of wastes from healthcare activities. World Health Organization, 2014*. 2014. URL: <https://www.who.int/publications/i/item/9789241548564>.
- [118] Priorclave North America Inc. *The Thermodynamic Realities Of Medical-Grade Autoclaves*. 2013. URL: <https://www.priorclave.com/en-gb/wp-content/uploads/sites/2/2018/08/Is-it-Hip-to-be-Square.pdf>.
- [119] John Masefield, George R. Dietz, and William M. Owens. "Cobalt-60 contract gamma sterilization of medical devices". In: *Radiation Physics and Chemistry (1977)* 15.1 (1980), pp. 91–97. ISSN: 0146-5724. DOI: [https://doi.org/10.1016/0146-5724\(80\)90102-8](https://doi.org/10.1016/0146-5724(80)90102-8). URL: <https://www.sciencedirect.com/science/article/pii/0146572480901028>.
- [120] A. Booth. *Sterilization of Medical Devices*. Routledge, 1999. URL: <https://doi.org/10.1201/9780203738306>.
- [121] Md. Fakruddin, Khanjada Shahnewaj Bin Mannan, and Stewart Andrews. "Viable but Nonculturable Bacteria: Food Safety and Public Health Perspective". In: *ISRN Microbiology* 2013 (Sept. 2013), pp. 1–6. DOI: 10.1155/2013/703813.
- [122] Tobias G. Klämpfl et al. "Cold Atmospheric Air Plasma Sterilization against Spores and Other Microorganisms of Clinical Interest". In: *Applied and Environmental Microbiology* 78.15 (2012), pp. 5077–5082. DOI: 10.1128/AEM.00583-12. eprint: <https://journals.asm.org/doi/pdf/10.1128/aem.00583-12>. URL: <https://journals.asm.org/doi/abs/10.1128/aem.00583-12>.
- [123] T.C. Montie, K. Kelly-Wintenber, and J.R. Roth. "An overview of research using the one atmosphere uniform glow discharge plasma (OAUGDP) for sterilization of surfaces and materials". In: *IEEE Transactions on Plasma Science* 28.1 (2000), pp. 41–50. DOI: 10.1109/27.842860.
- [124] *Escherichia coli*. URL: https://en.wikipedia.org/wiki/Escherichia_coli.
- [125] H. Fremont, W. Horaud, and K. Weide-Zaage. "Measurements and FE-Simulations of Moisture Distribution in FR4 based Printed Circuit Boards". In: *EuroSime 2006 - 7th International Conference on Thermal, Mechanical and Multiphysics Simulation and Experiments in Micro-Electronics and Micro-Systems*. 2006, pp. 1–6. DOI: 10.1109/ESIME.2006.1643964.
- [126] J. Bortfeldt et al. "Study of hygroscopic expansion of anode readout boards of gaseous detectors based on FR4". In: *Journal of Instrumentation* 16.03 (Mar. 2021), P03016. DOI: 10.1088/1748-0221/16/03/P03016. URL: <https://dx.doi.org/10.1088/1748-0221/16/03/P03016>.

- [127] National instruments. *cRIO-9063*. URL: <https://www.ni.com/it-it/shop/model/crio-9063.html>.
- [128] Vaisala. *HUMICAP Handheld Humidity and Temperature Meter Series HM40*. URL: <https://docs.vaisala.com/v/u/B211064EN-F/en-US>.
- [129] Alexandra Waskow et al. “An In Situ FTIR Study of DBD Plasma Parameters for Accelerated Germination of Arabidopsis thaliana Seeds”. In: *International Journal of Molecular Sciences* 22.21 (Oct. 2021), p. 11540. ISSN: 1422-0067. DOI: 10.3390/ijms222111540. URL: <http://dx.doi.org/10.3390/ijms222111540>.
- [130] Hui Jiang et al. “Experimental study of Q-V Lissajous figures in nanosecond-pulse surface discharges”. In: *IEEE Transactions on Dielectrics and Electrical Insulation* 20.4 (2013), pp. 1101–1111. DOI: 10.1109/TDEI.2013.6571423.
- [131] Naoki Osawa et al. “Generation of high pressure homogeneous dielectric barrier discharge in air”. In: *The European Physical Journal - Applied Physics* 61.2 (2013), p. 24317. DOI: 10.1051/epjap/2012120398.
- [132] N. Gherardi and F. Massines. “Mechanisms controlling the transition from glow silent discharge to streamer discharge in nitrogen”. In: *IEEE Transactions on Plasma Science* 29.3 (2001), pp. 536–544. DOI: 10.1109/27.928953.
- [133] Y Liu et al. “Atmospheric-pressure diffuse dielectric barrier discharges in Ar/O₂ gas mixture using 200 kHz/13.56 MHz dual frequency excitation”. In: *Journal of Physics D: Applied Physics* 51.11 (Feb. 2018), p. 114002. DOI: 10.1088/1361-6463/aaac73. URL: <https://dx.doi.org/10.1088/1361-6463/aaac73>.
- [134] Sergey A. Starostin et al. “Formation and Expansion Phases of an Atmospheric Pressure Glow Discharge in a PECVD Reactor via Fast ICCD Imaging”. In: *IEEE Transactions on Plasma Science* 36.4 (2008), pp. 968–969. DOI: 10.1109/TPS.2008.924622.
- [135] Stollenwerk L. Amiranashvili Sh. Boeuf J.P. Purwins H.G. “Formation and stabilisation of single current filaments in planar dielectric barrier discharge”. In: *The European Physical Journal* 44 (2007). DOI: 10.1140/epjd/e2007-00168-7.
- [136] Floran Peeters and Tom Butterworth. “Electrical Diagnostics of Dielectric Barrier Discharges”. In: *Atmospheric Pressure Plasma*. Ed. by Anton Nikiforov and Zhiqiang Chen. Rijeka: IntechOpen, 2018. Chap. 2. DOI: 10.5772/intechopen.80433. URL: <https://doi.org/10.5772/intechopen.80433>.
- [137] E.J.J. Peeters. “The electrical dynamics of dielectric barrier discharges”. English. Proefschrift. Phd Thesis 1 (Research TU/e / Graduation TU/e). Applied Physics and Science Education, May 2015. ISBN: 978-90-386-3835-5.
- [138] David E. Ashpis, Matthew C. Laun, and Elmer L. Griebeler. “Progress Toward Accurate Measurement of Dielectric Barrier Discharge Plasma Actuator Power”. In: *AIAA Journal* 55.7 (2017), pp. 2254–2268. DOI: 10.2514/1.J055816. eprint: <https://doi.org/10.2514/1.J055816>. URL: <https://doi.org/10.2514/1.J055816>.

- [139] T. C. Manley. “The Electric Characteristics of the Ozonator Discharge”. In: *Transactions of the Electrochemical Society* 84 (1943), pp. 83–96.
- [140] Zoran Falkenstein and John J Coogan. “Microdischarge behaviour in the silent discharge of nitrogen - oxygen and water - air mixtures”. In: *Journal of Physics D: Applied Physics* 30.5 (Mar. 1997), p. 817. DOI: 10.1088/0022-3727/30/5/015. URL: <https://dx.doi.org/10.1088/0022-3727/30/5/015>.
- [141] J. Kriegseis, S. Grundmann, and C. Tropea. “Power consumption, discharge capacitance and light emission as measures for thrust production of dielectric barrier discharge plasma actuators”. In: *Journal of Applied Physics* 110 (1 2011). ISSN: 00218979. DOI: 10.1063/1.3603030.
- [142] Jochen Kriegseis et al. “Capacitance and power consumption quantification of dielectric barrier discharge (DBD) plasma actuators”. In: *Journal of Electrostatics* 69 (4 2011), pp. 302–312. ISSN: 03043886. DOI: 10.1016/j.elstat.2011.04.007. URL: <http://dx.doi.org/10.1016/j.elstat.2011.04.007>.
- [143] A. V. Pipa et al. “Experimental determination of dielectric barrier discharge capacitance”. In: *Review of Scientific Instruments* 83.7 (July 2012), p. 075111. ISSN: 0034-6748. DOI: 10.1063/1.4737623. eprint: https://pubs.aip.org/aip/rsi/article-pdf/doi/10.1063/1.4737623/14823180/075111\1\1_online.pdf. URL: <https://doi.org/10.1063/1.4737623>.
- [144] Tetsuji Shimizu et al. “The dynamics of ozone generation and mode transition in air surface micro-discharge plasma at atmospheric pressure”. In: *New Journal of Physics* 14.10 (Oct. 2012), p. 103028. DOI: 10.1088/1367-2630/14/10/103028. URL: <https://dx.doi.org/10.1088/1367-2630/14/10/103028>.
- [145] Paolo F Ambrico et al. “Breakdown development in a nanosecond pulsed dielectric barrier discharge in humid air in plane-to-plane geometry”. In: *Plasma Sources Science and Technology* 32.9 (Sept. 2023), p. 095008. DOI: 10.1088/1361-6595/acf6df. URL: <https://dx.doi.org/10.1088/1361-6595/acf6df>.
- [146] Lorenzo Ibba. “EFISH measurements in a Nanosecond-Pulsed Volume DBD plasma for Spores Treatments on Membranes”. In: (in preparation).
- [147] N. B. Anikin, S. M. Starikovskaia, and A. Yu Starikovskii. “Polarity effect of applied pulse voltage on the development of uniform nanosecond gas breakdown”. In: *Journal of Physics D Applied Physics* 35.21 (Nov. 2002), pp. 2785–2794. DOI: 10.1088/0022-3727/35/21/315.
- [148] T. L. Chng et al. “Electric field induced second harmonic (E-FISH) generation for characterization of fast ionization wave discharges at moderate and low pressures”. In: *Plasma Sources Science and Technology* 28 (4 Apr. 2019). ISSN: 13616595. DOI: 10.1088/1361-6595/ab0b22.
- [149] T. Darny et al. “Analysis of conductive target influence in plasma jet experiments through helium metastable and electric field measurements”. In: *Plasma Sources Science Technology* 26.4, 045008 (Apr. 2017), p. 045008. DOI: 10.1088/1361-6595/aa5b15.

- [150] K V Kozlov et al. "Spatio-temporally resolved spectroscopic diagnostics of the barrier discharge in air at atmospheric pressure". In: *Journal of Physics D: Applied Physics* 34.21 (Oct. 2001), p. 3164. DOI: 10.1088/0022-3727/34/21/309. URL: <https://dx.doi.org/10.1088/0022-3727/34/21/309>.
- [151] P Paris et al. "Intensity ratio of spectral bands of nitrogen as a measure of electric field strength in plasmas". In: *Journal of Physics D: Applied Physics* 38.21 (Oct. 2005), p. 3894. DOI: 10.1088/0022-3727/38/21/010. URL: <https://dx.doi.org/10.1088/0022-3727/38/21/010>.
- [152] J. Morrill et al. "Electron energy and electric field estimates in sprites derived from ionized and neutral N₂ emissions". In: 29.10, 1462 (May 2002), p. 1462. DOI: 10.1029/2001GL014018.
- [153] Petr Bilek et al. "Electric field determination in air plasmas from intensity ratio of nitrogen spectral bands: II. Reduction of the uncertainty and state-of-the-art model". In: *Plasma Sources Science and Technology* 27 (8 Aug. 2018). ISSN: 13616595. DOI: 10.1088/1361-6595/aad666.
- [154] Keegan Orr et al. "Measurements of electric field in an atmospheric pressure helium plasma jet by the E-FISH method". In: *Plasma Sources Science and Technology* 29.3 (Mar. 2020), p. 035019. DOI: 10.1088/1361-6595/ab6e5b. URL: <https://dx.doi.org/10.1088/1361-6595/ab6e5b>.
- [155] Arthur Dogariu et al. "Species-Independent Femtosecond Localized Electric Field Measurement". In: *Phys. Rev. Appl.* 7 (2 Feb. 2017), p. 024024. DOI: 10.1103/PhysRevApplied.7.024024. URL: <https://link.aps.org/doi/10.1103/PhysRevApplied.7.024024>.
- [156] Bangdou Huang et al. "Surface ionization wave propagation in the nanosecond pulsed surface dielectric barrier discharge: the influence of dielectric material and pulse repetition rate". In: *Plasma Sources Science and Technology* 29.4 (Mar. 2020), p. 044001. DOI: 10.1088/1361-6595/ab7854. URL: <https://dx.doi.org/10.1088/1361-6595/ab7854>.
- [157] Marien Simeni Simeni et al. "Electric field measurements in nanosecond pulse discharges in air over liquid water surface". In: *Plasma Sources Science and Technology* 27.1 (Jan. 2018), p. 015011. DOI: 10.1088/1361-6595/aaa06e. URL: <https://dx.doi.org/10.1088/1361-6595/aaa06e>.
- [158] Yingzhe Cui, Chijie Zhuang, and Rong Zeng. "Electric field measurements under DC corona discharges in ambient air by electric field induced second harmonic generation". In: *Applied Physics Letters* 115.24 (Dec. 2019), p. 244101. ISSN: 0003-6951. DOI: 10.1063/1.5129778. eprint: https://pubs.aip.org/aip/apl/article-pdf/doi/10.1063/1.5129778/14529907/244101\1\1_online.pdf. URL: <https://doi.org/10.1063/1.5129778>.
- [159] Maosheng He and Jeffrey M. Forbes. "Rossby wave second harmonic generation observed in the middle atmosphere". In: *Nature Communications* (2022). DOI: 10.1038/s41467-022-35142-3.

- [160] P. A. Franken et al. "Generation of Optical Harmonics". In: *Phys. Rev. Lett.* 7 (4 Aug. 1961), pp. 118–119. DOI: 10.1103/PhysRevLett.7.118. URL: <https://link.aps.org/doi/10.1103/PhysRevLett.7.118>.
- [161] J. F. Ward and Irving J. Bigio. "Molecular second- and third-order polarizabilities from measurements of second-harmonic generation in gases". In: *Phys. Rev. A* 11 (1 Jan. 1975), pp. 60–66. DOI: 10.1103/PhysRevA.11.60. URL: <https://link.aps.org/doi/10.1103/PhysRevA.11.60>.
- [162] Benjamin M. Goldberg et al. "Electric field measurements in a near atmospheric pressure nanosecond pulse discharge with picosecond electric field induced second harmonic generation". In: *Applied Physics Letters* 112.6 (Feb. 2018), p. 064102. ISSN: 0003-6951. DOI: 10.1063/1.5019173. eprint: https://pubs.aip.org/aip/apl/article-pdf/doi/10.1063/1.5019173/13304010/064102_1_online.pdf. URL: <https://doi.org/10.1063/1.5019173>.
- [163] Tat Loon Chng, Svetlana M Starikovskaia, and Marie-Claire Schanne-Klein. "Electric field measurements in plasmas: how focusing strongly distorts the E-FISH signal". In: *Plasma Sources Science and Technology* 29.12 (Dec. 2020), p. 125002. DOI: 10.1088/1361-6595/abbf93. URL: <https://dx.doi.org/10.1088/1361-6595/abbf93>.
- [164] Rudolf Penndorf. "Tables of the Refractive Index for Standard Air and the Rayleigh Scattering Coefficient for the Spectral Region between 0.2 and 20.0 μ and Their Application to Atmospheric Optics". In: *J. Opt. Soc. Am.* 47.2 (Feb. 1957), pp. 176–182. DOI: 10.1364/JOSA.47.000176. URL: <https://opg.optica.org/abstract.cfm?URI=josa-47-2-176>.
- [165] T L Chng et al. "Electric field evolution in a diffuse ionization wave nanosecond pulse discharge in atmospheric pressure air". In: *Plasma Sources Science and Technology* 28.9 (Sept. 2019), 09LT02. DOI: 10.1088/1361-6595/ab3cfc. URL: <https://dx.doi.org/10.1088/1361-6595/ab3cfc>.
- [166] Simin Feng and Herbert G. Winful. "Physical origin of the Gouy phase shift". In: *Opt. Lett.* 26.8 (Apr. 2001), pp. 485–487. DOI: 10.1364/OL.26.000485. URL: <https://opg.optica.org/ol/abstract.cfm?URI=ol-26-8-485>.
- [167] Ward JF, Bigio IJ, Finn RS. "Electric-field induced harmonic generation as a probe of the focal region of a laser beam." In: (1975). DOI: 10.1364/AO.14.000336.
- [168] Igor V Adamovich et al. "Nanosecond second harmonic generation for electric field measurements with temporal resolution shorter than laser pulse duration". In: *Journal of Physics D: Applied Physics* 53.14 (Jan. 2020), p. 145201. DOI: 10.1088/1361-6463/ab6790. URL: <https://dx.doi.org/10.1088/1361-6463/ab6790>.
- [169] Ekspla. *PL2230 series datasheet*. URL: https://ekspla.com/wp-content/uploads/products/picosecond-lasers/PL2230/Ekspla_PL2230-datasheet_-20230109.pdf.
- [170] Thorlabs. *Principles of Spatial Filters*. URL: https://www.thorlabs.com/newgrouppage9.cfm?objectgroup_id=14350.

- [171] Keegan Orr et al. "Formation and propagation of ionization waves during ns pulse breakdown in plane-to-plane geometry". In: *Plasma Sources Science and Technology* 29 (12 Dec. 2020). ISSN: 13616595. DOI: 10.1088/1361-6595/aba989.
- [172] NL Aleksandrov et al. "Kinetics of charged species in non-equilibrium plasma in water vapor-and hydrocarbon-containing gaseous mixtures". In: *Journal of Physics D: Applied Physics* 55.38 (2022), p. 383002.
- [173] Giacomo Pierotti et al. "A novel two-stage kinetic model for surface DBD simulations in air". In: *Plasma Sources Science and Technology* 32.6 (July 2023), p. 064005. DOI: 10.1088/1361-6595/acdea2. URL: <https://dx.doi.org/10.1088/1361-6595/acdea2>.
- [174] Arturo Popoli et al. "A Boltzmann Electron Drift Diffusion Model for Atmospheric Pressure Non-Thermal Plasma Simulations". In: *Plasma* 6.3 (2023), pp. 393–407. ISSN: 2571-6182. DOI: 10.3390/plasma6030027. URL: <https://www.mdpi.com/2571-6182/6/3/27>.
- [175] Guennadi Sezonov, Danièle Joseleau-Petit, and Richard D'Ari. "Escherichia coli physiology in Luria-Bertani broth". In: *Journal of Bacteriology* 189.23 (2007), pp. 8746–8749. ISSN: 00219193. DOI: 10.1128/JB.01368-07.
- [176] Stephen J. Hagen. "Exponential growth of bacteria: Constant multiplication through division". In: *American Journal of Physics* 78.12 (2010), pp. 1290–1296. ISSN: 0002-9505. DOI: 10.1119/1.3483278.
- [177] *CoStat - Software version 6.45*. URL: <http://cohortsoftware.com/costat.html>.
- [178] Harvey Motulsky. *Intuitive Biostatistics: A Nonmathematical Guide to Statistical Thinking*. Third. Oxford University Press, 2013.
- [179] Jin Shen et al. "Bactericidal Effects against S. aureus and Physicochemical Properties of Plasma Activated Water stored at different temperatures". In: *Scientific Reports* 6. March (2016). ISSN: 20452322. DOI: 10.1038/srep28505.
- [180] A Shaw et al. "A reference protocol for comparing the biocidal properties of gas plasma generating devices". In: *Journal of Physics D: Applied Physics* 48.48 (Nov. 2015), p. 484001. DOI: 10.1088/0022-3727/48/48/484001. URL: <https://dx.doi.org/10.1088/0022-3727/48/48/484001>.
- [181] Hao Wang et al. "Sterilizing processes and mechanisms for treatment of Escherichia coli with dielectric-barrier discharge plasma". In: *Applied and Environmental Microbiology* 86 (1 2020). ISSN: 10985336. DOI: 10.1128/AEM.01907-19.
- [182] *Solutions for Sustainability Initiative (S4S)*. URL: <https://www.epfl.ch/research/solutions-for-sustainability-initiative-s4s/>.
- [183] Terragene. *BT96, Self-Contained Biological Indicator*. URL: <https://terragene.com/wp-content/uploads/PD/biologicos/BT96/Product%20description%20-%20BT96%20rev.3.pdf>.

- [184] P.R. Griffiths, J.A. De Haseth, and J.D. Winefordner. *Fourier Transform Infrared Spectrometry*. Chemical Analysis: A Series of Monographs on Analytical Chemistry and Its Applications. Wiley, 2007. ISBN: 9780470106297. URL: https://books.google.it/books?id=C_c0GVe8MX0C.
- [185] Yukinori Sakiyama et al. "Plasma chemistry model of surface microdischarge in humid air and dynamics of reactive neutral species". In: *Journal of Physics D: Applied Physics* 45.42 (Oct. 2012), p. 425201. DOI: 10.1088/0022-3727/45/42/425201. URL: <https://dx.doi.org/10.1088/0022-3727/45/42/425201>.
- [186] M. Y. Naz et al. "Optical characterization of non-thermal plasma jet energy carriers for effective catalytic processing of industrial wastewaters". In: *Scientific Reports* 11 (1 Dec. 2021). ISSN: 20452322. DOI: 10.1038/s41598-021-82019-4.
- [187] Bruker. *FT-IR or IR Spectroscopy?* URL: <https://www.bruker.com/it/products-and-solutions/infrared-and-raman/ft-ir-routine-spectrometer/what-is-ft-ir-spectroscopy/difference-ir-vs-ftir.html#:~:text=FT%2DIR%20uses%20an%20interferometer,again%2C%20where%20they%20are%20recombined..>
- [188] Elise Vervloessem et al. "NH₃ and HNO_x Formation and Loss in Nitrogen Fixation from Air with Water Vapor by Nonequilibrium Plasma". In: *ACS Sustainable Chemistry & Engineering* 11.10 (2023), pp. 4289–4298. DOI: 10.1021/acssuschemeng.3c00208.
- [189] *Potassium Bromide (KBr) Windows*. URL: <https://www.edmundoptics.com/f/potassium-bromide-kbr-windows/14168/>.
- [190] *Zinc Selenide (ZnSe) Windows*. URL: <https://www.edmundoptics.com/f/zinc-selenide-znse-windows/13195/>.
- [191] "Origins of Baseline Drift and Distortion in Fourier Transform Spectra". In: *Molecules* 27 (13 July 2022). ISSN: 14203049. DOI: 10.3390/molecules27134287.
- [192] *HITRAN on the Web*. URL: <https://hitran.tsu.ru/>.
- [193] Haiqiang Wang et al. "Numerical evaluation of the effectiveness of NO₂ and N₂O₅ generation during the NO ozonation process". In: *Journal of Environmental Sciences (China)* 41 (Mar. 2016), pp. 51–58. ISSN: 10010742. DOI: 10.1016/j.jes.2015.05.015.
- [194] LibreTexts. *Infrared Spectroscopy Absorption Table*. URL: https://chem.libretexts.org/Ancillary_Materials/Reference/Reference_Tables/Spectroscopic_Reference_Tables/Infrared_Spectroscopy_Absorption_Table.
- [195] H.H. Telle, A.G. Ureña, and R.J. Donovan. *Laser Chemistry: Spectroscopy, Dynamics and Applications*. Wiley, 2007. ISBN: 9780470059401. URL: <https://books.google.ch/books?id=F9jZRse023QC>.
- [196] M Uddi et al. "Nitric oxide density measurements in air and air/fuel nanosecond pulse discharges by laser induced fluorescence". In: *Journal of Physics D: Applied Physics* 42.7 (Mar. 2009), p. 075205. DOI: 10.1088/0022-3727/42/7/075205. URL: <https://dx.doi.org/10.1088/0022-3727/42/7/075205>.

- [197] Guiyin Zhang, Weijia Jin, and Haiming Zheng. “Dynamic mechanism about the fluorescence emission of NO dielectric barrier discharge plasma”. In: *Journal of Quantitative Spectroscopy and Radiative Transfer* 127 (2013), pp. 90–95. ISSN: 0022-4073. DOI: <https://doi.org/10.1016/j.jqsrt.2013.04.031>. URL: <https://www.sciencedirect.com/science/article/pii/S0022407313001908>.
- [198] A F H van Gessel et al. “Temperature and NO density measurements by LIF and OES on an atmospheric pressure plasma jet”. In: *Journal of Physics D: Applied Physics* 46.9 (Jan. 2013), p. 095201. DOI: 10.1088/0022-3727/46/9/095201. URL: <https://dx.doi.org/10.1088/0022-3727/46/9/095201>.
- [199] A F H van Gessel, K M J Alards, and P J Bruggeman. “NO production in an RF plasma jet at atmospheric pressure”. In: *Journal of Physics D: Applied Physics* 46.26 (June 2013), p. 265202. DOI: 10.1088/0022-3727/46/26/265202. URL: <https://dx.doi.org/10.1088/0022-3727/46/26/265202>.
- [200] Teledyne Princeton Instruments. *PI-MAX®4: 1024f datasheet*. URL: https://www.princetoninstruments.com/wp-content/uploads/2020/04/PIMAX4_1024f_datasheet.pdf.
- [201] Jackson R. Hall et al. “Mode of Nitric Oxide Delivery Affects Antibacterial Action”. In: *ACS Biomaterials Science and Engineering* 6 (1 Jan. 2020), pp. 433–441. ISSN: 23739878. DOI: 10.1021/acsbiomaterials.9b01384.



Lorenzo Ibba

Applied Physicist / R&D Engineer / Data analyst / Research Engineer / Scientist

Experienced and dedicated research engineer with a passion for driving innovation. Bringing forth expertise in hand-on laboratory work, as well as data analysis and code developing. Equipped with a diverse and promising skill-set, including plasma physics, laser physics and optics, data analysis, image processing, Python, Matlab and C++. Able to effectively self-manage during independent projects, as well as collaborate in a team setting.

✉ lorenzo.ibba@outlook.com

📍 Chavannes-près-Renens, Switzerland

📞 0786900619

🌐 [linkedin.com/in/lorenzo-ibba](https://www.linkedin.com/in/lorenzo-ibba)

WORK EXPERIENCE

PhD Researcher in Applied Physics EPFL - Swiss Plasma Center

07/2019 - Present

Achievements/Tasks

- Developed and characterized plasma-based sterilization prototypes for industrial applications
- Successfully implemented complex laser-based diagnostics: Laser-Induced Fluorescence and EFISH
- Developed complex data analysis scripts in Matlab and Python
- Responsible for the maintenance and testing of complex machines, including picosecond laser, FTIR spectrometer and Nanosecond-pulsed High Voltage power supply
- Laser safety responsible of the Bio-Lab at the SPC, EPFL
- Teaching assistant for Physics I and Physics II for Engineering

Contact : Ivo Furno - ivo.furno@epfl.ch

Software Developer Intern Vidinoti SA

03/2017 - 07/2017

Achievements/Tasks

- Successfully developed a C++ code for real-time 3D object recognition, based on point-cloud data taken with IR depth-sensor devices

EDUCATION

Master of Science (MSc) in Applied Physics EPFL, Ecole Polytechnique Fédérale de Lausanne

09/2015 - 02/2019

Courses

- Developed and characterized plasma dielectric barrier discharges for sterilization purposes
- Characterized an interferometry technique for measuring plasma density in low pressure plasmas

Bachelor of Science in Physics (BSc) UNIMIB, Università di Milano Bicocca

09/2013 - 09/2015

Courses

- Designed a Langmuir probe for temperature and density measurement in a linear gyrotron machine
- Explored the link between gamma emission and alpha particle dynamics in JET tokamak simulations

SKILLS

Hand-on Laboratory skills

Data Analysis

Plasma technologies

Plasma Physics

LIF

EFISH

FTIR

Spectroscopy

Bio-plasmas

Atmospheric/low-pressure plasmas

Microbiology

High-Voltage Technology

HV Pulsed Generators

Dielectric Barrier Discharges

Programming

Computational Physics

Scientific Modelling

Python

Matlab

C/C++

Laser Physics

Optics

Computer Vision

3D Object Recognition

Image Processing

Linux

CAD softwares

3D printing

Research

Innovation

Ability to Work in a Team

Versatility

Strong Communication Skills

Adaptability

Quick Learner

Critical Thinking

Problem Solving

ACHIEVEMENTS

ECPD 2023 Poster Award Winner

S4S 2023 - Solutions4Sustainability Grant Group Winners

LANGUAGES

English

Full Professional Proficiency

French

Limited Working Proficiency

Italian

Native or Bilingual Proficiency

INTERESTS

Kitesurf

Sail

Ski

Piano Player

Volleyball

Football

Tennis